Centro Brasileiro de Pesquisas Físicas

Doctoral Thesis

CP violation studies and test of CPT symmetry in three-body charmless B decays

Author:
Laís Soares Lavra

Supervisor:
Prof. Ignácio Alfonso de Bediaga e Hickman

A thesis submitted in fulfilment of the requirements for the degree of Doctor of Philosophy in Physics in the Brazilian Center for Research in Physics (CBPF)

Rio de Janeiro, 2019

CENTRO BRASILEIRO DE PESQUISAS FÍSICAS

Abstract

CP violation studies and test of CPT symmetry in three-body charmless B decays

by Laís Soares Lavra

This thesis describes two analyses performed on charmless three-body B decays. The first study concerns the measurement of the inclusive CP violation in four decays channels: $B^{\pm} \to K^{+}K^{\pm}K^{-}$, $B^{\pm} \to \pi^{+}K^{\pm}\pi^{-}$, $B^{\pm} \to K^{+}\pi^{\pm}K^{-}$ and $B^{\pm} \to \pi^{+}\pi^{\pm}\pi^{-}$ using Run II (2015-2016) LHCb dataset, which corresponds to an integrated luminosity of 0.328 fb^{-1} in 2015, 1.665 fb^{-1} in 2016 recorded at centre-of-mass energy of 13 TeV. Also, a qualitative study was performed in the phase-space of these four decay channels, with the combination of the Run I and Run II data samples. The second analysis describes the measurement of the lifetime difference between B^{+} and B^{-} in $B^{\pm} \to K^{+}K^{\pm}K^{-}$ and $B^{\pm} \to K^{+}\pi^{\pm}K^{-}$ decays. It exploits the Run I (2011-2012) LHCb dataset, corresponding to an integrated luminosity of 1.0 fb^{-1} in 2011 and 2.0 fb^{-1} in 2012 at centre-of-mass energy of 7 TeV and 8 TeV, respectively.

Apart from the analysis side, this thesis also presents quality assurance tests developed to monitor the performance of some components of the new LHCb tracking detector, the SciFi tracker.

Keywords: LHCb, Charmless three-body $B^{\pm}$ decays, CP asymmetry, B lifetime, CPT symmetry, Scintillating Fiber Tracker

Contents

List of Figures

List of Tables

Chapter 1

Introduction

The concept of the fundamental structure of matter dates from ancient times when Leucippus and Democritus in the 5th century BC devised the idea of an indivisible building block of matter. The idea, however, remained as only a theoretical concept until 1897, when J.J. Thomson discovered the electron as the first elementary particle. Over decades of scientific progress, experiments have revealed the existence of many other fundamental particles and the interaction between them.

Currently, the best theory that describes the nature of fundamental particles is known as the Standard Model (SM) of particle physics. It states that matter is made up of very tiny and indivisible particles called quarks and leptons, which constitute all observed matter in the Universe. In addition to the quarks and leptons, there also are the equivalent of antimatter for each of them - the antiquarks and antileptons. Antimatter particles have identical properties to matter particle, but with opposite charge and quantum numbers.

The existence of antimatter was first predicted by Paul Dirac. In 1920s he managed to combine the theory of special relativity and quantum mechanics in an equation that describes the electron. The by-product, however, was the prediction of the existence of antiparticle of the electron: the positron. The insight leads us into a new description of a Universe made of matter and antimatter.

The Big Bang is the most widely accepted theory to explain how our Universe began and evolved. This theory predicts that matter and antimatter should have been created in equal amounts at the beginning of the Universe. However, essentially all mass observed is made up of matter and there is no evidence of antimatter in the cosmological scale. Therefore there must exist a mechanism during its evolution that led to generating the observed matter-antimatter asymmetry.

In the 1960s, Andrei Sakharov proposed three conditions to explain this imbalance [1]:

1. an interaction capable of changing quarks into leptons (violation of the baryonic number).
2. loss of thermal equilibrium during the early expansion of the Universe.
3. matter-antimatter difference, i.e. violation of C and CP symmetry.

Although the phenomena CP violation is described within the SM, it is insufficient to account for the predominance of matter over antimatter in the Universe today, thus there must exist extra sources of CP violation.

In this context, B meson decays provide the ideal environment to study and investigate new sources of CP violation, since B decays involve rare processes that could reveal new physics. Also, a large CP violation is foreseen in several B decay channels. Thus the study of B decays can provide insight into the question of whether the observed CP violation is sufficient to explain the excess of matter. In this thesis, it is analysed four charmless three-body: $B^{\pm} \to \pi^{+}K^{\pm}\pi^{-}$, $B^{\pm} \to K^{+}K^{\pm}K^{-}$, $B^{\pm} \to \pi^{+}\pi^{\pm}\pi^{-}$ and $B^{\pm} \to K^{+}\pi^{\pm}K^{-}$, with the purpose to study *CP* violation effects. In the course of this thesis, these four decay channels are referred to $B^{\pm} \to h^{+}h^{\pm}h^{-}$, where $h^{\pm}$ stands for charged kaon ($K^{\pm}$) or charged pion ($\pi^{\pm}$).

The first observation of *CP* violation with B decays happened in 2001, when *BABAR* and *BELLE*, experiments dedicated to producing B meson, observed *CP* violation in neutral B decays. Nowadays, B meson decays have been produced in high energy proton-proton collisions at LHC (Large Hadron Collider). This collider has 4 collision points, where are located 4 different experiments. One of the experiments is the LHCb (Large Hadron Collider beauty), dedicated to the production of b and c-hadrons with the purpose to study *CP* violation and find rare decays. Recent results from the LHCb experiment have measured *CP* violation in the B sector. In particular, it was measured the inclusive *CP* violation in $B^{\pm} \to \pi^{+}K^{\pm}\pi^{-}$, $B^{\pm} \to K^{+}K^{\pm}K^{-}$, $B^{\pm} \to \pi^{+}\pi^{\pm}\pi^{-}$ and $B^{\pm} \to K^{+}\pi^{\pm}K^{-}$ with significance of 2.8 standard deviations (σ), 4.3σ, 4.2σ and 5.6σ [2]. It has been the first observation of *CP* violation in three-body B decays to date. Also, the *CP* asymmetry was found not to be uniformly distributed in the phase space of these decays. Indeed, large *CP* asymmetries were observed in certain phase-space regions. Phenomenological studies performed with those results have indicated the existence of new mechanisms responsible for generating the *CP* asymmetry [3]. In this thesis, it is performed an update of the measurement of *CP* violation in the four charmless B decays by using the new dataset collected by the LHCb. Besides, an inspection in the phase-space of the four modes is made to localize regions with high asymmetry.

The observed *CP* violation in B decays lead us to consider about a possible violation of other symmetries. The *CPT* invariance [1] is a fundamental symmetry in physics as any local Lorentz invariant field theory is invariant under *CPT*. Thus, the Standard Model of particle physics is also a theory *CPT* invariant. It predicts that for each *CP* violation effect there must be a corresponding T violating effect in such way to preserve *CPT* symmetry. Although the T violation is expected in decays with *CP* violation, it is hardly observed, mostly because its observation is not experimentally viable to attempt [4]. By exploring the connection between *CPT* and Lorentz invariance, we propose to investigate violation of these symmetries in decays with observed *CP* violation. This search is based on the framework of some models with explicit Lorentz violation, which motivate us to investigate *CPT* and Lorentz invariances through the measurement of the lifetime difference between B^{+} and B^{-}. In this thesis, measurements of the lifetime difference are presented using $B^{\pm} \to K^{+}K^{\pm}K^{-}$ and $B^{\pm} \to \pi^{+}K^{\pm}\pi^{-}$ with the purpose to investigate other violation of invariance in weak decays.

Precision measurements are crucial to claim discovery and test models, such as on testing predictions of the SM for *CP* violation. However, it can only be achieved with large statistics, that come with the increasing of b-hadron production in parallel with the improvement of detection techniques. Thus, the LHCb experiment during its Long ShutDown 2 (2019-2021) will be upgraded to increase substantially the event yield. For hadronic channels, it is expected to achieve a factor 20 large compared to the current detector. For this, many of its sub-detector will be replaced to deal with the new environment. In particular, the tracker system will be replaced by a new technology made by scintillating fibres. In this thesis we present some quality test performed to ensure a good performance of the new tracking detector.

[1] Combination of the charge symmetry C, parity symmetry P and temporal symmetry T.

Overview of this Thesis

This thesis consist of three parts, comprised in 6 chapters. The first and second parts concern the measurement of physical quantities of B charmless decays using data from the LHCb experiment. Whereas the third part is dedicated to my contribution to the LHCb upgrade.

Chapter 2 covers the theoretical concepts related to the LHCb analyses performed in the thesis. The study of B meson decays is motivated, main mechanism of CP violation generation in B decays is discussed, the role of final state interaction in charged B decays as well as the decay formalism for the modes studied are presented.

Chapter 3 is dedicated to an overview of the LHCb experiment. A description of which LHCb subdetectors as well as the trigger system are given.

Chapter 4 details the measurement of the global CP asymmetry in the decays modes $B^{\pm} \to K^{+}K^{\pm}K^{-}$, $B^{\pm} \to \pi^{+}K^{\pm}\pi^{-}$, $B^{\pm} \to K^{+}\pi^{\pm}K^{-}$ and $B^{\pm} \to \pi^{+}\pi^{\pm}\pi^{-}$. It covers the strategy to select the decay channels, background suppressing, fit to the invariant mass to extract the signal yields and the correction of efficiency across the phase space. The analysis is performed using LHCb dataset collected in 2015 and 2016 (Run II).

Chapter 5 shows an inspection performed in the Dalitz of the four decays channels analysed in the chapter 3, with the purpose to localise CP violation sources. The inspection is performed combining all Run I and Run II data (2011, 2012, 2015 and 2016).

Chapter 6 is devoted to the measurement of the lifetime difference between B^{+} and B^{-} in the $B^{\pm} \to K^{+}K^{\pm}K^{-}$ and $B^{\pm} \to \pi^{+}K^{\pm}\pi^{-}$ decays. The lifetime difference is obtained in order to probe violation of CPT symmetry. This analysis is performed using LHCb dataset collected in 2011 and 2012 (Run I).

Finally, the chapter 7 discusses the upgrade of the LHCb detector. The current LHCb tracker system will be replaced by the SciFi tracker, a new detector made of scintillating fibres and read-out by silicon photomultipliers. In this part is presented an introduction of the Scifi Tracker followed by the descriptions of the experimental setups used to perform quality test in some of its components.

Chapter 2

Theoretical overview

The purpose of this chapter is to provide an overview of the theoretical aspects which involve charmless B decays. The focus will be on brief approach of the theoretical models related to the study of the CP violation in charged B decays, such as the role of Final State Interaction.

2.1 C, P and T symmetry

In the Standard Model there are three discrete symmetries which are of interest here: the charge conjugation C, parity P and time reversal T. The charge conjugation C does not change space-time quantities but instead interchanges particle and antiparticle. The effect of the operation of parity P is to invert all coordinates space, i.e. $x \to -x$. Momentum, p, is reversed while angular momentum is unchanged under parity. Thus spin, σ, is unchanged but helicity[1] ($h = \sigma \cdot p/|p|$) changes the sign. Whereas the time reversal, T, reverses the time coordinate $t \to -t$.

C and P symmetries are known to be violated in the weak interactions. The combined CP symmetry was thought to be conserved until 1964, when CP violation was first discovered in neutral kaon sector [5]. At the time there was no known mechanism that could accommodate the observation. Such mechanism was introduced by Kobayashi and Maskawa in 1973. They postulated the existence of a third generation of quarks, before the quark c to be discovered, by introducing a 3×3 unitary matrix [6].

The combination of those three symmetries, CPT, however has been checked to be conserved. By construction, any quantum field theory is invariant under the CPT symmetry, and therefore it is a fundamental symmetries in physics. Some of its consequences that can be experimentally studied are:

- Equality of masses for particle and antiparticle.
- The equality of total widths or lifetimes for particle and antiparticle.

In quantum field theory the combination CPT is always conserved, thus if CP is violated, T must be violated in such that the overall CPT is preserved.

2.2 CKM matrix

Within the framework of the Standard Model, CP violation arises from a single complex phase in the mixing matrix of quarks, the Cabibbo-Kobayashi-Maskawa (CKM) matrix [7], which connects the eletroweak eigenstates (d',s',b') with their mass eigenstates (d,s,b) through the following unitarity transformation:

[1] Projection of the spin of a particle onto its direction of motion.

$$\begin{pmatrix} d' \\ s' \\ b' \end{pmatrix} = \begin{pmatrix} V_{ud} & V_{us} & V_{ub} \\ V_{cd} & V_{cs} & V_{cb} \\ V_{td} & V_{ds} & V_{tb} \end{pmatrix} \begin{pmatrix} d \\ s \\ b \end{pmatrix} = V_{CKM} \begin{pmatrix} d \\ s \\ b \end{pmatrix}$$

The elements of the V_{CKM} matrix describe couplings of the $W^{\pm}$ bosons to quark pairs, the element V_{ud} describes the transition from a down quark to an up quark ($d \rightarrow W^- + u$). Those elements are not fixed by theory and are evaluated experimentally.

From the unitarity constraint and phases redefinition, V_{CKM} is reduced to be dependent on four parameters: three mixing angles and one phase, which is the only source of CP violation. The CKM matrix can be parametrized in a number of ways. The most common are the standard parametrization recommended by the Particle Data Group [8]:

$$V_{CKM} = \begin{pmatrix} c_{12}c_{13} & s_{12}c_{13} & s_{13}e^{-i\gamma} \\ -s_{12}c_{23} - c_{12}s_{23}s_{13}e^{i\gamma} & c_{12}c_{23} - s_{12}s_{23}s_{13}e^{i\gamma} & s_{23}c_{13} \\ s_{12}s_{23} - c_{12}c_{23}s_{13}e^{i\gamma} & -c_{12}s_{23} - s_{12}c_{23}s_{13}e^{i\gamma} & c_{23}c_{13} \end{pmatrix}$$

where $s_{ij} \equiv \sin\theta_{ij}$ and $c_{ij} \equiv \cos\theta_{ij}$. The angles θ_{ij} are the three mixing angles between the i-th and j-th generation and γ is the phase responsible for all CP-violating phenomena in the Standard Model.

According to the experimental evidence there is a hierarchy among the CKM matrix elements. This hierarchical structure can be used to derive an alternative parametrization suggested by Wolfenstein [9], which turns out to be very useful for estimating the size of flavour violating transitions. It exhibits the hierarchy in a transparent manner by expanding each element in power of the parameter $\lambda = |V_{us}| \approx 0.22$:

$$V_{CKM} = \begin{pmatrix} (1-\lambda^2/2) & \lambda & A\lambda^3(\rho - i\eta) \\ -\lambda & (1-\lambda^2/2) & A\lambda^2 \\ A\lambda^3(1-\rho-i\eta) & -A\lambda^2 & 1 \end{pmatrix} + \mathcal{O}(\lambda^4)$$

The quantities A, ρ and η are defined by using the parameters from the standard parametrization:

$$\lambda = s_{12} \tag{2.1}$$

$$A\lambda^2 = s_{23} \tag{2.2}$$

$$A\lambda^2(\rho - i\eta) = s_{13}e^{-i\gamma} \tag{2.3}$$

Those are real numbers and determined experimentally. As the Wolfenstein parameter λ is associated with CKM factors, all B-decays amplitudes have at least two power of λ. Amplitudes with higher powers are called CKM-suppressed.

According to the standard model (SM), the CP violation is due to a complex phase in the CKM matrix. Within the Wolfestein parametrization of the CKM matrix, the only elements which have non-negligible phases are V_{td} and V_{ub}. These two complex matrix elements are conventionally parametrized as $V_{td} \equiv |V_{td}| \exp -i\beta$ and $V_{ub} \equiv |V_{td}| \exp -i\gamma$. The phase information can be displayed using the unitary triangle, which is due to the orthogonality of the first and third columns of CKM matrix. [10].

Unitarity triangle

The unitarity of the matrix ($V_{CKM}V^{\dagger}_{CKM}$=$\mathbb{1}$) leads to the following six relations among its elements:

$$V_{ud}V^*_{cd} + V_{us}V^*_{cs} + V_{ub}V^*_{cb} = 0 \tag{2.4}$$

$$V_{ud}V^*_{td} + V_{us}V^*_{ts} + V_{ub}V^*_{tb} = 0 \tag{2.5}$$

$$V_{cd}V^*_{ud} + V_{cs}V^*_{us} + V_{cb}V^*_{ub} = 0 \tag{2.6}$$

$$V_{cd}V^*_{td} + V_{cs}V^*_{ts} + V_{cb}V^*_{tb} = 0 \tag{2.7}$$

$$V_{td}V^*_{ud} + V_{ts}V^*_{us} + V_{tb}V^*_{ub} = 0 \tag{2.8}$$

$$V_{td}V^*_{cd} + V_{ts}V^*_{cs} + V_{tb}V^*_{cb} = 0 \tag{2.9}$$

The relations are know as orthogonality conditions. Each relation above represents a triangle in a complex plane (see Figure 2.1). The equation 2.4 have a particular interest as it applies directly to b-hadron decays. In the Wolfenstein parametrization, this implies the sum of terms that are each $\mathcal{O}(\lambda^3)$. The relation in 2.4 defines the angles α, β and γ, given by:

$$\alpha = arg\left(\frac{-V_{td}V^*_{tb}}{V_{ud}V^*_{ub}}\right), \beta = arg\left(\frac{-V_{cd}V^*_{cb}}{V_{td}V^*_{tb}}\right), \gamma = arg\left(\frac{-V_{ud}V^*_{ub}}{V_{cd}V^*_{cb}}\right) \tag{2.10}$$

Since the top quark mass is large, B mesons are the only mesons containing quarks of the third generation and thus their decay provide a unique opportunity to study CP violation.

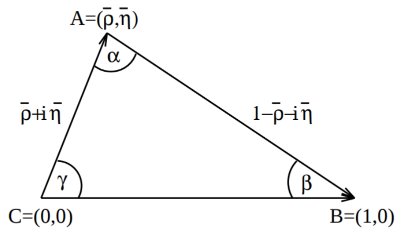

FIGURE 2.1: Unitarity triangle. Figure taken from [11].

2.3 CP violation in B meson decays

The study of CP violation has fundamental importance in physics due to its connection with the observed baryon asymmetry in the universe. In 1967, Andrei Shakarov [1] postulated three necessary conditions to observe baryon asymmetry:

1. CP violation in fundamental processes in the early universe.
2. C and baryon number violation.
3. A departure from thermal equilibrium.

However, in the Standard Model, the complex phase in the CKM matrix cannot provide sufficient *CP* violation to account the magnitude of the baryon asymmetry, therefore other sources of *CP* violation must exist [12].

CP violation has been observed in B system since 2001 and appears to conform to the expectation of the Standard Model. The study of the *CP* violation in the B sector is the great interest not only to test Standard Model parameters but also to uncover evidences of new physics, which is typically connected to new sources of *CP* violation.

In addition, it is also essential to have complete phenomenological understanding of the *CP* violation arising in the framework of the Standard Model. The key problem for the theoretical understand is related to strong interactions, i.e. hadronic uncertainties. In this context charged charmless B system can provide experimentally rich phenomenological information about the strong interactions.

2.3.1 B mesons

The B mesons are pseudoscalar meson and are composed of a b quark and a light anti-quark. While the binding is provided by the strong interaction B mesons can only decay by weak interaction [12]. As the t quark is too have to produce hadrons, B mesons are the heaviest mesons. A list of known B meson states is shown in Table 2.1.

Particle	Quark content	Charge	Mass (GeV/c^2)	Lifetime (ps)
B^+	$\bar{b}u$	+1	5.279	1.638
B^-	$b\bar{u}$	-1	5.279	1.638
B^0	$\bar{b}d$	0	5.279	1.519
$\bar{B}^0$	$b\bar{d}$	0	5.279	1.519
B_s^0	$\bar{b}s$	0	5.366	1.527
$\bar{B}_s^0$	$b\bar{s}$	0	5.366	1.527
B_c^+	$\bar{b}c$	+1	6.274	0.510
B_c^-	$b\bar{c}$	-1	6.274	0.510

TABLE 2.1: List of B meson states with their quark content, charge, mass and lifetime as reported in Ref. [8].

There are also further excited states of B mesons, usually labelled B^*, that exist at higher energies (masses) but with identical quark content [13].

Neutral B mesons have an interesting property: they can oscillate between particle and antiparticle states. This phenomenon is known as B *oscillation* or B *mixing* and can only occur in neutral particles. The oscillation happen as a consequence of the difference between the flavour (B^0 and $\bar{B}^0$) and the mass eingstates. Thus, we can define two mass eigenstate for neutral meson: B_H and B_L, where H stands heavy mass and L light or less heavy mass. The two states are defined to be [14]:

$$B_H = pB^0 + q\bar{B}^0 \tag{2.11}$$

$$B_L = pB^0 - q\bar{B}^0 \tag{2.12}$$

where the coefficients p and q represent the relative strength of B^0 $\bar{B}^0$, respectively and obey $|p|^2 + |q|^2 = 1$. In the case $|p| = |q|$ the mass eigenstates are *CP* eingestates and *CP* is conserved.

2.3.2 Tree and Penguin processes

Hadronic B decays are mediated by $b \to q_1 \bar{q}_2 d(s)$ quark level transitions, with q_1,q_2 $\in \{u, d, c, s\}$. The topologies of weak decay Feynman diagram that can contribute to B decays are generally divided into two classes, *tree* and *penguin* diagrams.

Tree diagrams are process that emits a $W^{\pm}$ boson, which decays into two new quarks. This process does not involve internal loops. The penguin process is one which involve internal loops, a W boson is reabsorbed on the same quark line from which it was emitted. The virtual $W^{\pm}$ boson and a gluon emitted in which decays into two quarks. The transition is classified depending on the flavour content of their final state [15]:

- $q_1 \neq q_2 \in \{u, c\}$: only tree diagrams contribute.
- $q_1 = q_2 \in \{u, c\}$: tree and penguin diagrams contribute.
- $q_1 = q_2 \in \{d, s\}$: only penguin diagrams contribute.

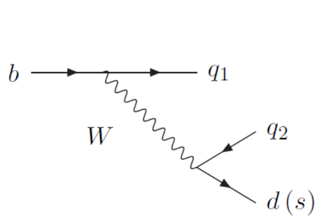

(A) Tree diagram.

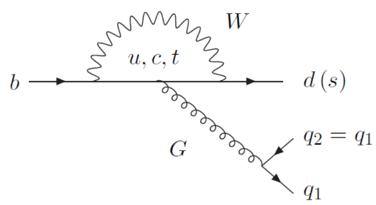

(B) Penguin diagram.

FIGURE 2.2: Tree and Penguin process. Figures taken from [15].

The most dominant decay for B meson are charmed decays, such as D mesons, because the $b \to c$ transition is CKM favoured. Other transitions such as $b \to u$ transitions are CKM suppressed by $|V_{ub}|$. For this reason, charmless decays are less frequent than the charmed and charmonium decays. Such decays are tree level process. Whereas decays of the b quarks to s or d quarks can only take place via penguin diagrams. Charmless hadronic decays such as the subject of this thesis have contribution from both penguin and tree-level process.

2.3.3 CP violation manifestation

The CP violation in the Standard Model is the result of a phase, and is therefore only observable in processes involving interfering amplitudes [6]. The mechanisms for generating interference in B decays fall into three classes [16]:

1. **Direct CP violation**, which occurs when the amplitude for a decay and its CP conjugate have different magnitude. It can occur in both neutral and charged decays.

2. **CP violation in mixing**, also called indirect CP violation, occurs when two neutral mass eigenstates cannot be chosen to be CP eigenstates, i.e. in the Eq. 2.11 and 2.12 $|q/p| \neq 1$. It implies that $B^0 \to \bar{B}^0$ and $\bar{B}^0 \to B^0$ have different probabilities to occur.

3. *CP* **violation in the interference between decays and mixing**, which occurs in decays into final state that are common to B^0 and $\bar{B}^0$. This type of *CP* violation is due to the fact that B^0 can either directly decay to the state f or first oscillate to $\bar{B}^0$ and then decay to the same state f, that is *CP* violation occur if the following condition is satisfied:

$$\Gamma(B^0 \to \bar{B}^0 \to f) \neq \Gamma(\bar{B}^0 \to B^0 \to f)$$

All three types can be observed in neutral B decays, but only the first type (direct *CP* violation) can occur in B charged mesons. As this thesis concerns about charged B decays, here the focus is on direct *CP* violation, in which a more detailed discussion is given in the following.

2.3.4 Direct CP violation

By considering the decay of a particle B into a final state f, $B \to f$ and its CP conjugated $\bar{B} \to \bar{f}$. The decay amplitude A_f can be defined as follow:

$$A = A(B \to f) = \langle f | \mathcal{T} | B \rangle \, , \bar{A} = \bar{A}(\bar{B} \to \bar{f}) = \langle \bar{f} | \mathcal{T} | \bar{B} \rangle \tag{2.13}$$

where $\mathcal{T}$ is the weak transition matrix. The amplitude can be expressed as a linear combination of all possible intermediate processes $B \to i \to f$. For each process i there are complex quantities associated each consisting of magnitude A_i and phase. The phase can be split in two contributions, ϕ and δ, and the amplitudes take the following form:

$$A = \sum_i A_i e^{i(\delta_i + \phi_i)}, \bar{A} = \sum_i A_i e^{i(\delta_i - \phi_i)} \tag{2.14}$$

The two kinds of phases that appear in the amplitudes are referred as *weak* (ϕ) and *strong* (δ) phases. In principle their designation do not necessarily mean that the phases are in weak and in strong interactions [17]. A weak phase is defined as the one which changes sign when passes to the *CP*-conjugate process (CP-odd) and the strong phase is defined as the one which does not change the sign under *CP* operation (*CP*-even).

The B meson decays via weak interaction and after that the final state particles interact through the strong interaction, which introduces the scattering phase $e^{i\delta}$ in the amplitude of each intermediate process i.

In this context, the origin of the ϕ phase is from the Cabbibo-Kobayashi-Maskawa (CKM) matrix [16]. Whereas the physical source of the phase δ is that there may be multiple real intermediate states which can contribute to the process in question via rescattering effects. The origin of strong phases are may from final-state interactions (FSI) (see section 2.4), which allow the various final states of the weak decay to scatter elastically or inelastically via strong interaction (or eletromagnetic).

The definition of direct CP violation is that $|A|^2 \neq |\bar{A}|^2$, and the typical CP violating observable is defined in terms of decay rates Γ:

$$\mathcal{A}_{CP} \equiv \frac{\Gamma(B \to f) - \Gamma(\bar{B} \to \bar{f})}{\Gamma(\bar{B} \to \bar{f}) + \Gamma(\bar{B} \to \bar{f})} = \frac{|A(\bar{B} \to \bar{f})|^2 - |A(B \to f)|^2}{|A(B \to f)|^2 + |A(\bar{B} \to \bar{f})|^2} \tag{2.15}$$

By writing the equation above considering that the amplitude A has two intermediate processes contributing:

$$A = A_1 e^{i(\delta_1+\phi_1)} + A_2 e^{i(\delta_2+\phi_2)} \tag{2.16}$$

$$\bar{A} = A_1 e^{i(\delta_1-\phi_1)} + A_2 e^{i(\delta_2-\phi_2)} \tag{2.17}$$

The direct CP asymmetry $\mathcal{A}_{CP}$ is given by

$$\mathcal{A}_{CP} = \frac{-2|A_1||A_2| \sin(\delta_1-\delta_2)\sin(\phi_1-\phi_2)}{|A_2|^1 + |A_2|^2 + 2|A_1||A_2|\cos(\delta_1-\delta_2)\cos(\phi_1-\phi_2)} \tag{2.18}$$

It can be seen that in any process where there is only a single contribution term in the decay amplitude, $A_2 = 0$, or $\delta_1 = \delta_2$ or $\phi_1 = \phi_2$, then $|A| = |\bar{A}|$ and no CP violation can be observed. Therefore, one immediately concludes that to have direct CP violation the transition amplitude must be the sum of two or more interfering amplitudes and satisfies two conditions simultaneously:

- there has to be a relative *CP*-violating weak phase between the two amplitudes contributing to $B \to f$.
- there has to be a relative *CP*-conserving strong phase generated by strong final state interaction.

Although the strong interaction phases can not generate *CP* violation by themselves, they are essential for the weak phase differences to show up as observable CP asymmetries [17].

In the literature, it is commonly stated that the two conditions above are enough to produce a non-vanishing *CP* asymmetry. However, the constraint from *CPT* is not apparent and must be taken into account. Together with the unitary of the scattering matrix, *CPT* invariance imposes an important restriction on direct *CP* violation: without re-scattering processes direct *CP* asymmetries cannot occur, even if there are weak phases [18].

Thus, a non zero direct CP asymmetry for a particular decay ($B \to f$) requires contributions from final state interaction related to the re-scattering process ($B \to f' \to f$), where the decay ($B \to f'$) is weak, and the state f' subsequently scatters into f via the strong interaction, producing *CP*- conserving complex phases in the decay amplitude. The next section is dedicated to a discussion about the implications of the *CPT* theorem on direct *CP* violation.

2.4 Final State Interaction (FSI)

In the decay of the hadronic B mesons, quarks produced interact strongly after the weak transition and still continuous interacting after the hadron formation. Such interactions are called Final State Interactions (FSI).

In high energy physics, FSI can be classified into "hard" and "soft" scattering. Hard scattering occurs at the quark level before the hadronisation takes place and it is described as a short-distance effect. Collisions involving hard scattering are interpreted as interactions between the quark and gluons of QCD. On the other side, soft scattering occurs at the hadronic level and it is described as a long-range process [16]. After weak decays of a heavy meson, the hadrons produces can re-scatter into other particles states through non-pertubative strong interaction (or electromagnetic) among themselves through different FSI processes.

As an example, consider the weak process $b \to u\bar{u}s$. This process can be generated through the penguin process $b \to c\bar{c}s$ decay, where a quark re-scattering process $c\bar{c}$ into $u\bar{u}$ occurs. This process can generate a FSI phase in the penguin loop through the hard re-scattering process. After that, the quarks in the final state group themselves into hadrons. Those hadrons can interact with each other and the same process can be viewed in another way. The $b \to c\bar{c}s$ process can give rise to $B \to \bar{D}_s D$ decay for example, and the final state charmed meson can re-scatter into other hadrons, such as $D_s D \to \pi\bar{K}$. This process also generate FSI phase, now due to the soft re-scattering [16]. Even though FSI processes are classified according to the type of re-scattering, i.e. soft and hard, both mechanism can not be separated. The expectation is that one of the them dominate in a certain process.

2.4.1 FSI in the context of *CP* violation

From the Eq. 2.14, it can be seen that direct *CP* violation arises from the interference effects between two amplitudes that have different weak phases, as well as different strong phases due to final state interaction phase. It was first recognised in the pioneer work of Bander, Silverman, and Soni [19]. In the paper is introduced the so called BSS mechanism, which states that the asymmetries in B charged decays may come from the interference between tree and penguin quark level diagrams owning different weak and strong phases. The weak phase provided by the CKM matrix and the strong phase generated by FSI at the quark level (hard rescattering). In other words, the *CP* violation in charged B decays would arise mainly due to the contributuion of short-distance effects governed by penguin transitions.

For a long time the traditional discussions have centered around the asymmetries that come from the BSS mechanism and the common believe was that in B decay soft FSI are expected to play only a minor role. The argument was that in hadronic B decay with a large energy, the hadrons produce in the final state would travel fast enough to leave the interaction region without have adequate time for getting involved in final state rescattering [20].

However, by analysing the implication of the BSS mechanism of *CP* violation in B system, the work of Gerard and Hou [21] suggested that scattering at the hadronic level (soft FSI rescattering) actually grows with energy. In addition, they showed that BSS mechanism by only considering short distance amplitudes could violate CPT theorem at the quark level process.

By following this work, Wolfenstein in his paper [18] showed the implications on *CP* violation when taking into account the *CPT* constraint and the unitarity of scattering matrix $\mathcal{S}$. Such work is resumed in the following.

2.4.2 Impact of *CPT* invariance on direct *CP* violation

Regardeless of the existence of *CP* violation in a process, the CPT theorem implies the total decay rate of a particle B and its antiparticle $\bar{B}$ are identical:

$$\Gamma_{tot}(B) = \Gamma_{tot}(\bar{B}) \tag{2.19}$$

which does not mean that the partial decay rate to a specific final state $\Gamma(B \to f)$ is the same as its CP conjugate $\Gamma(\bar{B} \to \bar{f})$. By looking at the Eq. 2.15, it can be seen that if $\Delta\Gamma \neq 0$ the *CP* is clearly violated but *CPT* need not be. Therefore, in order to preserve *CPT* all of the different partial rate asymmetries present in a given decay must cancel.

Under this assumption *CPT* implies not only the total sum of all partial decay rates be the same for particles and antiparticles. It can actually tells us that the sum over subsets of all decay rates have to coincide for particles and antiparticles [22].

It can be understood by considering a decay of a particle B. The weak interaction cause B to decay to several final states f_α, which can be connected among themselves by strong FSI [2]. The final state interactions in $B \to f$ arise as a consequence of the unitarity of the full $\mathcal{S}$-matrix, $\mathcal{S}\mathcal{S}^\dagger = 1$, which involves rescattering of physical particles in the final state [23]. Therefore, in order to have FSI phases, the occurrence of intermediate states is necessary, such as $B \to i \to f$, where B decay weakly into i followed by a strong rescattering of i into the final state f.

The decay channels can be divided into classes F_j (defined by their quantum numbers) containing final states f^j_α that emerge from intermediate processes $i_\alpha \to f_\alpha$, which the final states f_α are linked to each other through the strong final state interactions. Thus, for processes which are linked by FSI, *CPT* invariance together with the unitarity of the scattering matrix implies a very deep restriction; it states that the sum of all partial decay rates over certain subsets connected by FSI has to be equal for particles and antiparticles [22]:

.

$$\sum_{f^j_\alpha \in F_j} \Gamma(B \to f^j_\alpha) = \sum_{\bar{f}^j_\alpha \in \bar{F}_j} \Gamma(\bar{B} \to \bar{f}^j_\alpha) \tag{2.20}$$

From this relation, it can be seen that to have *CP* violation in a given decay, at least two different states with equal quantum number must exist which can be connected by strong re-scattering.

Another consequence of the Eq. 2.20 can be realised by looking at the two-pion and three-pion decays of the charged kaon. Due to G-parity conservation, which is a combination of C symmetry and isospin symmetry, a pair of pions can only scatter into an even number of pions. In other words, an initial state of two pions can produce either two pions or two kaons. Thus two-pion final state are disconnect from three-pion final states and by using the equation 2.20, *CPT* implies:

$$\Gamma(K^+ \to \pi^+\pi^0) = \Gamma(K^- \to \pi^-\pi^0) \tag{2.21}$$

and no *CP* violation can occur in the decay $K^+ \to \pi^+\pi^0$. On the other hand, *CP* violation in the three-pion decays may occur, but only under CPT condition:

$$\Gamma(K^+ \to \pi^+\pi^0\pi^0) - \Gamma(K^- \to \pi^-\pi^0\pi^0) = \Gamma(K^- \to \pi^+\pi^-\pi^-) - \Gamma(K^+ \to \pi^-\pi^+\pi^+) \tag{2.22}$$

Therefore in order to preserve *CPT* the sum of the partial rate asymmetry of the three-pion decay for K^+ must be equal but with opposite sign in the other channels connected by FSI for the K^- [17].

As a consequence, whether there is *CP* violation in one channel, it must exchange partial rate asymmetry with some other coupled channels in order to satisfy the *CPT* constraint. This exchange will depend fundamentally on the mechanism which gives rise to the partial rate asymmetry in the first place. Based on this, Atwood and Soni [24] proposed the existence of two types of *CP* violation which can give rise to the exchange of the partial rate asymmetries: *simple* (type I) and *compound* (type

[2] In this context to be connected means different final states with the same quantum number which can mix with each other by FSI. Thus, final states with different quantum numbers are not connected by the FSI to the other possible final states.

II) *CP* violation. The simple *CP* violation is governed by the effects at the quark level transitions, i.e. short-distance rescattering, and asymmetries arise due to the interference between the tree and penguin diagram (BSS model). The compound *CP* violation arises from the interaction between the hadrons in the final state, long-distance rescattering effects.

2.5 Direct *CP* violation in charmless three-body $B^{\pm}$ decays

The inclusive *CP* violation (integrated over the phase-space) have been recently measured in the decays $B^{\pm} \to K^{+}K^{\pm}K^{-}$, $B^{\pm} \to \pi^{+}K^{\pm}\pi^{-}$, $B^{\pm} \to K^{+}\pi^{\pm}K^{-}$ and $B^{\pm} \to \pi^{+}\pi^{\pm}\pi^{-}$ for the first time by the LHCb Collaboration [2]. The origin of those asymmetries may come from different nontrivial sources. It will be shown later that $B^{\pm} \to h^{+}h^{\pm}h^{-}$ decays are dominated by intermediate processes, which can interfere with each other producing *CP* violation with different signs in specific regions of the phase-space. Thus, the asymmetries produced in localised regions, when sum over all phase-space, can cancel out and produce the integrated asymmetries observed.

In the next section is introduced three-body phase space formalism, which can be useful to contextualise the understanding of *CP* asymmetries in the phase space of those decays.

2.6 Three-body decay phase space

In this thesis, all decays involved are decays of the B charged meson into three final state particles ($B^{\pm} \to h^{+}h^{\pm}h^{-}$). Three-body decays can be described by nine degrees of freedom. Applying kinematics constraint such as momentum and energy conservation and take into account the initial and final state particles all have spin zero (pseudoscalares), only two degrees of freedom remain. It means that three body decays can be described by two independent variables. There is a freedom in choice of which two variables to use to describe a tree-body decay, whereas the pair parameters have a phase-space term constant in the kinetically allowed region [25]. In 1953, Richard Dalitz proposed the use of the Mandelstam variables to study the decay of charged kaons into three pions, which has been used in most analyses nowadays to describe three-body decays.

2.6.1 Dalitz Plot

Considering a particle of mass M and momentum P decaying into three daughter particles a, b and c with masses $m_{a,b,c}$ and four-momentum $p_{a,b,c}$. The three-body mass invariant combination (Mandelstam variables) are defined as

$$s_{ab} \equiv m_{ab}^2 = (p_a + p_b)^2 \tag{2.23}$$

$$s_{ac} \equiv m_{ac}^2 = (p_a + p_c)^2 \tag{2.24}$$

$$s_{bc} \equiv m_{bc}^2 = (p_b + p_c)^2 \tag{2.25}$$

By applying four-momentum conservation, it can be shown that the invariant masses of pairs of final-state are related in the following way:

$$M^2 + m_a^2 + m_b^2 + m_c^2 = m_{ab}^2 + m_{bc}^2 + m_{ac}^2 \tag{2.26}$$

Therefore, the decay kinematics is completely described by two independent pair of invariant mass combination. The total four-momentum conservation leads that the three-particle final states lie in a plane and the events to be restricted in a certain phase-space region. The two-dimensional plot of the event distribution defined in terms of any two the pair masses defined above is called Dalitz plot.

To establish the Dalitz plot contour, i.e. the kinematically allowed region of the Dalitz plot, consider that m_{ab}^2 and m_{bc}^2 as the variables chosen to describe a certain decay. For a given value of m_{ab}^2, the kinematics accessible ranges of the m_{bc}^2 variable can be written as [25]:

$$(m_b + m_c)^2 \leq (m_{bc}^2) \leq (M - m_a)^2 \tag{2.27}$$

The Dalitz plot region of kinematically allowed phase space is shown in Figure 2.6. The three corners of the Dalitz plot correspond the maximal value of m_{bc}^2 or m_{ac}^2, where one of the particle is in the frame of the decaying particle. Whereas, the configuration for minimum values occur when two particles are produced in the same direction, whereas the third particle in the opposite direction.

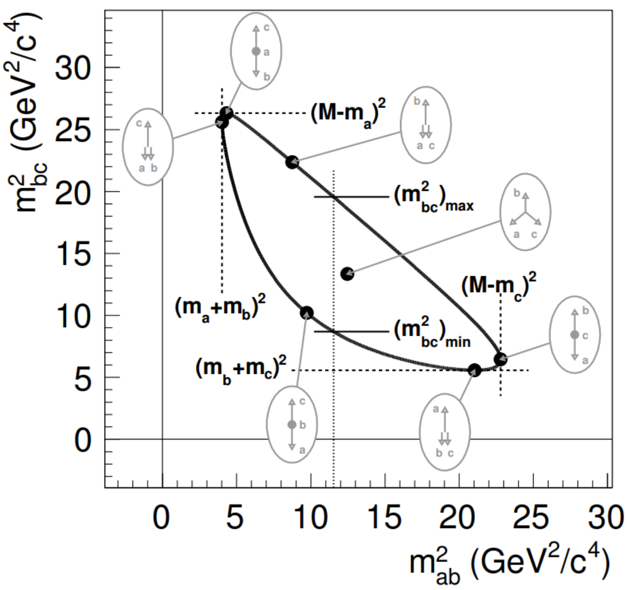

FIGURE 2.3: Kinematic boundaries of the three-body decay phase space and illustrastion of various kinemactic configurations. Copied from [25].

Another feature of the Dalitz plot approach is due to its relation to the decay rate (Γ) of the process. From the Fermi's Golden Rule, the differential decay rate can be calculated through the product of two quantities. The amplitude $\mathcal{M}$ of the process, which contains all dynamics information and the phase space available of the process, that only depends on kinematics factors such as momenta, masses and energies of the particles involved [26]. For a three-body decay in which all particles involved are spinless, the differential decay rate can be writen in terms of the Dalitz variables [8]:

$$d\Gamma = \frac{1}{(2\pi)^3}\frac{1}{32M^3}|\mathcal{M}|^2 dm_{ab}^2 dm_{bc}^2 \tag{2.28}$$

Thus the Dalitz plot gives the $|\mathcal{M}|^2$ variation over the kinematically accessible phase space of a particular decay (m_{ab}^2, m_{bc}^2). As a consequence, if $|\mathcal{M}|^2$ is constant the decays events will be uniformly distributed in the allowed region of the Dalitz plot. In contrast, any non-uniform structure in the Dalitz plot will give information about the dynamics of the decay [3]. Those structures can arise when a three-body decay proceeds via intermediate states, such as resonances.

2.6.2 Three-body $B^{\pm}$ decays

Three body $B^{\pm}$ decays can proceed direct to the three-body final state or via intermediate state. In general, such intermediate states come from resonance contributions. An illustration of both decay types is shown in Figure 2.4. If a B decay proceeds via resonant state, it can be considered a decay via quasi-two-body intermediate state. For example, $B \to abc$, could proceed via $B \to Rc$, where R is the resonance which can decay $R \to ab$. Any decay that does not proceed via an intermediate resonance is termed non-resonant decay.

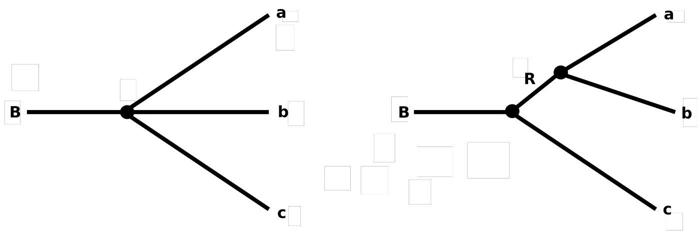

FIGURE 2.4: An illustration of a non-resonant (on the left) and resonant (on the right) decay for $B \to abc$.

Resonances are particles with extremely small lifetime because they decay via strong interaction. The different types of resonances are classified according to its spin J of and its parity P, by using the notation J^P [25]:

- scalars ($J^P = 0^+$) : f_0, χ_c
- pseudoscalars ($J^P = 0^-$) : π, K, B
- vectors ($J^P = 1^-$) : ϕ, ρ^0, ψ
- tensors ($J^P = 2^+$): K_2^*, $f_2(1270)$

Three-body B decays are generally dominated by resonances, more specific the $B^{\pm} \to h^+h^{\pm}h^-$ decays have contributions from many types of resonances which are studied with the help of Dalitz Plot analyses. It will be discussed later that those contributions are particular important in the study of CP violation. The main characteristics of resonances that can be observed in Dalitz plot are [25]:

- Resonances appear as bands of events in the Dalitz Plot.
- The position and size of the band are related to the mass and width of the resonance.

[3] give information on final state interaction in the decay.

- The spin of the resonance governs the distribution of events along the band.
- The exact pattern of events in the Dalitz plot is determined by interference between the various contributing states.

Each resonance in the Dalitz plot has a shape according to its angular distribution, which can be observed as a function of helicity angle. If the particles in the decay are labelled 1,2 and 3, the helicity angle is defined as the angle between the momentum vector of particle 1 and the momentum of particle 3 in the rest frame of a resonance formed by particles 1 and 2. Take as an example that the B meson decays into a pion (particle 1), the opposite-sign kaon (particle 2) and a bachelor pion (particle 3), it is illustrated in Figure 2.5.

The resonance bands in a Dalitz plot show information about the spin of the resonance involved, in terms of helicity angle, a spin zero resonance (scalar) will be uniform across the Dalitz plot band; a spin one resonance (vector) will be distributed according to $\cos^2\theta_H$ and a spin two resonance (tensor) distributed according to $|3\cos^2\theta_H - 1|^2$. Figure 2.6 illustrates how various resonance states appear in the Dalitz plot. The uniform distribution of the phase-space decay in (a). Scalar resonances appear as bands in the Dalitz plot, as shown in Figure (b-d) for resonances in bc, ac and ab channels respectively. Angular distributions for vector and tensor intermediate states introduce valeys along the resonance bands Figure (e,f). The region where the amplitudes of two resonances overlap is sensitive to the phase difference between the two amplitudes Figure (g,h).

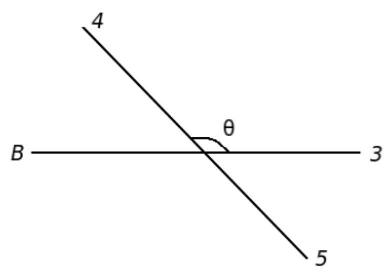

FIGURE 2.5: The helicity angle

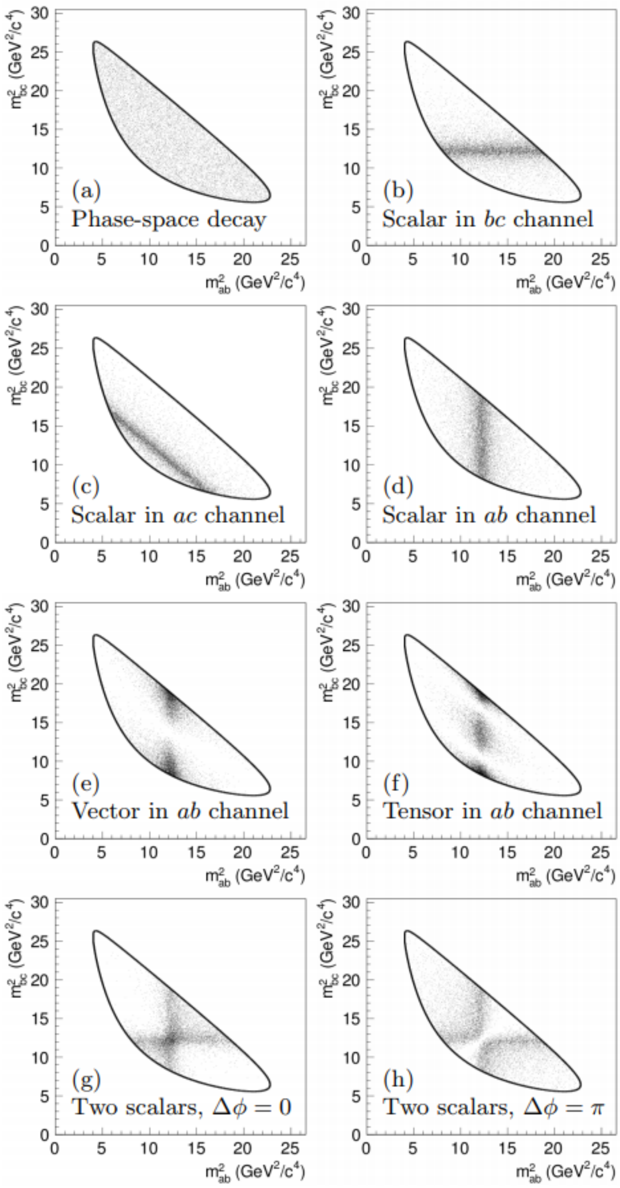

FIGURE 2.6: Dalitz plot examples of uniform distribution (a), scalar resonance (b-d), vector (e) and tensor (f) resonances, and (g,h) the interference of two scalar resonances with different relative phase. Taken from [25].

2.7 Phase-space of $B^{\pm} \to h^{+}h^{\pm}h^{-}$ decays

Charmless B hadronic decays such as the subject of this thesis: $B^{\pm} \to K^{+}K^{\pm}K^{-}$, $B^{\pm} \to \pi^{+}K^{\pm}\pi^{-}$, $B^{\pm} \to K^{+}\pi^{\pm}K^{-}$ and $B^{\pm} \to \pi^{+}\pi^{\pm}\pi^{-}$ are suppressed due to both contributions of the tree level transition $b \to u$ and the penguin $b \to s(d)$ processes. The latter, can be the dominated contribution in the $B^{\pm} \to K^{+}K^{\pm}K^{-}$ and $B^{\pm} \to \pi^{+}K^{\pm}\pi^{-}$ decays, thus providing an environment to study penguin process. The tree-level processes can be the dominated contribution in the $B^{\pm} \to K^{+}\pi^{\pm}K^{-}$ and $B^{\pm} \to \pi^{+}\pi^{\pm}\pi^{-}$, which may provide an environment to the phenomenological understanding related to strong interactions in the Standard Model. In addition, CPT invariance group those decays into two distinct classes containing final states that are mutually distinct under the strong interactions. Thus *CPT* connect the decay $B^{\pm} \to K^{+}K^{\pm}K^{-}$ to $B^{\pm} \to \pi^{+}K^{\pm}\pi^{-}$ and $B^{\pm} \to K^{+}\pi^{\pm}K^{-}$ to $B^{\pm} \to \pi^{+}\pi^{\pm}\pi^{-}$.

The Dalitz plot variables of interest in this thesis are pair of two opposite charge combinations (m^2_{bc},m^2_{ac}):

- $B^{\pm} \to \pi^{+}K^{\pm}\pi^{-}$: $(m^2_{\pi^+\pi^-},\, m^2_{K^+\pi^-})$
- $B^{\pm} \to K^{+}\pi^{\pm}K^{-}$: $(m^2_{K^+K^-},\, m^2_{K^+\pi^-})$

In the case of the decays with two final state particles not distinguishable, such as $B^{\pm} \to K^{+}K^{\pm}K^{-}$ and $B^{\pm} \to \pi^{+}\pi^{\pm}\pi^{-}$ channels, the resulting phase-space must be simmetrized in order to avoid to account the same resonant state in $m^2_{K^{\pm}K^{\mp}}$ and $m^2_{K^{\mp}K^{\pm}}$ projections. Thus the Dalitz plot is defined in terms of two independent variables:

- $B^{\pm} \to K^{+}K^{\pm}K^{-}$: $(m^2_{(K^+K^-)low},\, m^2_{(K^+K^-)high})$
- $B^{\pm} \to \pi^{+}\pi^{\pm}\pi^{-}$: $(m^2_{(\pi^+\pi^-)low},\, m^2_{(\pi^+\pi^-)high})$

where m^2_{high} and m^2_{low} are respectively the highest and the lower value between m^2_{bc} and m^2_{ac}.

The Dalitz plot of the four decays modes obtained in Ref. [2] is shown in Figure 2.9. It can be seen that for all channels the event distribution is concentrated at low mass region, as expected due to the dominance of intermediate contributions.

2.7.1 $B^{\pm} \to K^{+}K^{\pm}K^{-}$ and $B^{\pm} \to \pi^{+}K^{\pm}\pi^{-}$ decays: penguin-dominated

The $B^{\pm} \to K^{+}K^{\pm}K^{-}$ and $B^{\pm} \to \pi^{+}K^{\pm}\pi^{-}$ decays have branching fraction of the order of 10^{-5} and proceed through similar diagrams. In Figure 2.7 are shown two possible quark diagrams for both processes. For the $B^{\pm} \to K^{+}K^{\pm}K^{-}$ decay, on the bottom left is shown for the decay $B^{\pm} \to \phi(1020)K^{\pm}$, driven by the penguin process $b \to s\bar{s}s$ which are the dominated contribution and on the bottom right the tree-level process $b \to u\bar{u}s$ which arises from $B^{\pm} \to f_x K^{\pm}$ decay [4]. As can be seen from the Figure, the tree diagram is suppressed (λ^4) in relation to the penguin contribution (λ^2).

The Dalitz plot for the $B^{\pm} \to K^{+}K^{\pm}K^{-}$ decay is shown in Figure 2.9(a), the region of $m^2(K^+K^-)_{low}$ around 1.0 GeV/c^2 correspond to the $\phi(1020)$ and that around 11.5 GeV/c^2 to the $\chi_{c0}(1P)$. In the region 2-3 GeV/c^2, there are clusters that could correspond to the $f_2'(1525)$ or the $f_0(1500)$ resonances observed by BABAR. Also, the $B^{\pm} \to J/\psi K^{\pm}$ with $J/\psi \to K^+K^-$ is visible around 9.6 GeV/c^2.

[4] f_x is refereed to different f states.

Resonance	$I^G(J^{PC})$	Mass(MeV)	Width(MeV)
$\phi(1020)$	$0^{-}1^{--}$	1019.461 ± 0.019	4.266 ± 0.031
$f_0(980)$	$0^{+}0^{++}$	990 ± 20	10 to 100
$f_0(1500)$	$0^{+}0^{++}$	1504 ± 6	109 ± 7
$\chi_{c0}(1P)$	$0^{+}0^{++}$	3414.75 ± 0.31	10.5 ± 0.6
$f_2'(1525)$	$0^{+}2^{++}$	1525 ± 5	73^{+6}_{-5}
$f_0(1710)$	$0^{+}0^{++}$	1723^{+6}_{-5}	139 ± 8

TABLE 2.2: Masses and widths of resonances components that contributes for $B^{\pm} \to K^{+}K^{\pm}K^{-}$ based on Belle model Ref. [27].

Resonance	$I^G(J^{PC})$	Mass(MeV)	Width(MeV)
$f_0(980)$	$0^{+}0^{++}$	990 ± 20	10 to 100
$\rho^0(770)$	$1^{+}1^{--}$	775 ± 0.25	149.1 ± 0.8
$\chi_{c0}(1P)$	$0^{+}0^{++}$	3414.75 ± 0.31	10.5 ± 0.6
	$I(J^P)$		
$K^*(892)^0$	$\frac{1}{2}(1^-)$	895.81 ± 0.19	47.4 ± 0.6
$K^{*0}(1430)^0$	$\frac{1}{2}(0^+)$	1425 ± 50	270 ± 80

TABLE 2.3: Masses and widths of resonances components that contributes for $B^{\pm} \to \pi^{+}K^{\pm}\pi^{-}$ based on Babar/Belle model [28].

For the $B^{\pm} \to \pi^{+}K^{\pm}\pi^{-}$, the decay is described by the transition $b \to u\bar{u}s$, which can receive contribution from tree and penguin processes. Two possible quarks diagrams are shown on the top of the Figure 2.7, where the penguin one is the dominated process.

In the Tables 2.2 and 2.3 shown a list of the main resonant contribution to $B^{\pm} \to K^{+}K^{\pm}K^{-}$ and $B^{\pm} \to \pi^{+}K^{\pm}\pi^{-}$, respectively.

The Dalitz plot for the $B^{\pm} \to \pi^{+}K^{\pm}\pi^{-}$ decay is shown in Figure 2.9(b). The resonances contributions observed are $K^{*0}(892)$,$\rho^0(770)$,$f_0(980)$ and $K^{*0}_{0,2}(1430)$ in both $K^{\mp}$ and $\pi^{+}\pi^{-}$ spectra, and the region of $m^2(\pi^{+}\pi^{-})_{low}$ around 11 GeV/c^2 the $\chi_{c0}(1P)$ resonance.

2.7.2 $B^{\pm} \to \pi^{+}\pi^{\pm}\pi^{-}$ and $B^{\pm} \to K^{+}\pi^{\pm}K^{-}$ decays: tree-dominated

The $B^{\pm} \to K^{+}\pi^{\pm}K^{-}$ and $B^{\pm} \to \pi^{+}\pi^{\pm}\pi^{-}$ have branching fractions of the order of 10^{-6}. The $B^{\pm} \to \pi^{+}\pi^{\pm}\pi^{-}$ decay can receive contributions from both penguin and tree diagrams, as shown in Figure 2.8. However the dominated contribution comes from the tree-level $b \to u$ transition [29]. The most common resonant contribution is the $B^{\pm} \to \rho^0(770)\pi^{\pm}$ mode, although ρ^0 and f states also contribute, as listed in Table 2.4.

In the Figure 2.9(c) the $B^{\pm} \to \pi^{+}\pi^{\pm}\pi^{-}$ Dalitz plot is shown. The resonances are $\rho^0(770)$ at $m^2(\pi^{+}\pi^{-})_{low} < 1$ GeV/c^2. In the region of $1.5 < m^2(\pi^{+}\pi^{-})_{low} < 2$ GeV/c^2, there are clusters that could correspond to the $\rho^0(1450)$, the $f_2(1270)$ and $f_0(1370)$ resonances.

On the bottom of the Figure 2.8 are presented two possible quarks diagrams for the $B^{\pm} \to K^{+}\pi^{\pm}K^{-}$ decay. On the right, the one dominated by $b \to u\bar{u}d$ tree transition, where the main contribution may comes from f states. In addition, the penguin transition $b \to s\bar{s}d$ is also present, mostly may due to resonances such as $K^{*0}(892)$. There are other resonant states which contribute to the decay, as listed in Table 2.5.

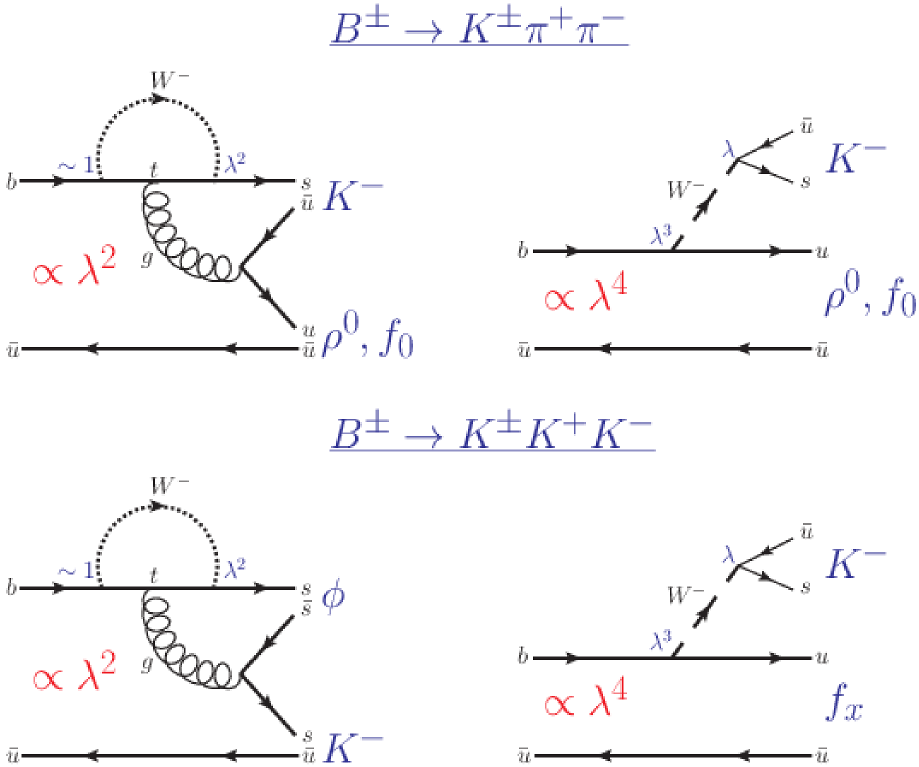

FIGURE 2.7: Tree and penguin diagrams for $B^{\pm} \to \pi^{+}K^{\pm}\pi^{-}$ (top) and $B^{\pm} \to K^{+}K^{\pm}K^{-}$ (bottom) with their dependencies on the Wolfenstein λ parameter. The f_x holds for any resonance decaying into two kaons in the final state.

Resonance	$I^G(J^{PC})$	Mass(MeV)	Width(MeV)
$\rho^0(770)$	1^+1^{--}	775 ± 0.25	149.1 ± 0.8
$\rho^0(1450)$	1^+1^{--}	1465 ± 25	400 ± 60
$f_0(980)$	0^+0^{++}	990 ± 20	10 to 100
$f_2(1270)$	0^+2^{++}	1275.5 ± 0.8	$186^{+2.2}_{-2.5}$

TABLE 2.4: Masses and widths of resonances components for $B^{\pm} \to \pi^{+}\pi^{\pm}\pi^{-}$. Based on LHCb model [30].

In the Figure 2.9(d) is shown the Dalitz plot for the $B^{\pm} \to K^{+}\pi^{\pm}K^{-}$ decay, there is a cluster of events at $m^2(K^{\pm}\pi^{\mp})_{low} < 2$ GeV/c^2, which could correspond to the resonances $K^{*0}(892)$ and $K^{*0}_{0,2}(1430)$.

Resonance	$I^G(J^{PC})$	Mass(MeV)	Width(MeV)
m_{KK}			
$\rho^0(1450)$	1^+1^{--}	1465 ± 25	400 ± 60
$f_0(980)$	0^+0^{++}	990 ± 20	10 to 100
$f_2(1270)$	0^+2^{++}	1275.5 ± 0.8	$186^{+2.2}_{-2.5}$
$f_0(1370)$	0^+0^{++}	1200 to 1500	200 to 500
$m_{K\pi}$	$I(J^P)$		
$K^*(892)^0$	$\frac{1}{2}(1^-)$	895.81 ± 0.19	47.4 ± 0.6
$K^{*0}(1430)^0$	$\frac{1}{2}(0^+)$	1425 ± 50	270 ± 80

TABLE 2.5: Masses and widths of resonances components for $B^{\pm} \to K^+\pi^{\pm}K^-$. Based on LHCb model [31].

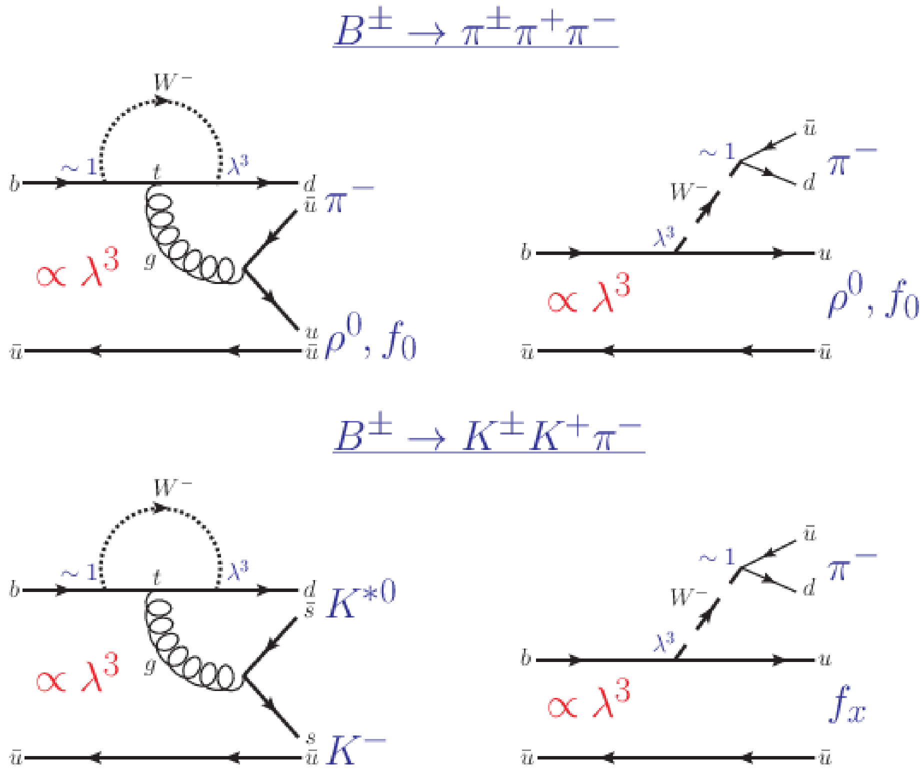

FIGURE 2.8: Tree and penguin diagrams for $B^{\pm} \to \pi^+\pi^{\pm}\pi^-$ (top) and $B^{\pm} \to K^+\pi^{\pm}K^-$ (bottom) with their dependencies on the Wolfenstein λ parameter. The f_x holds for any resonance decaying into two kaons in the final state.

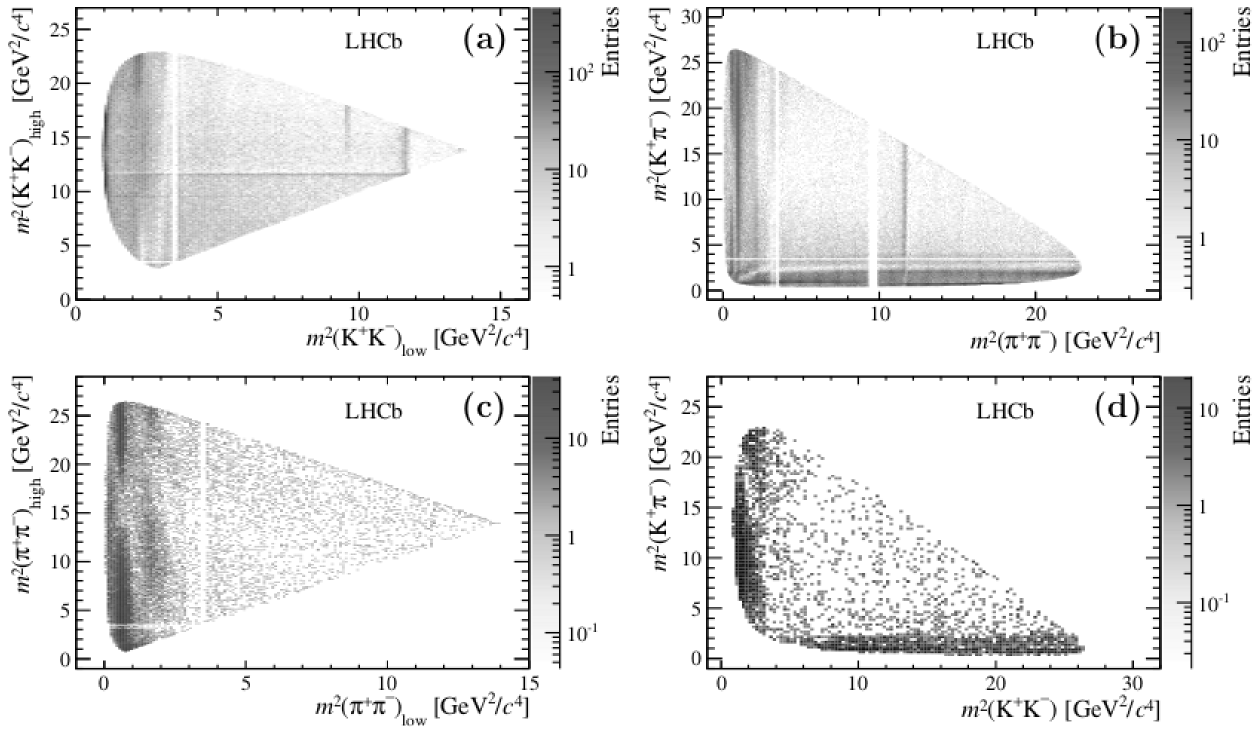

FIGURE 2.9: Dalitz Plot of $B^\pm \to K^+K^\pm K^-$ (a) , $B^\pm \to \pi^+K^\pm\pi^-$ (b), $B^\pm \to \pi^+\pi^\pm\pi^-$ (c) and $B^\pm \to K^+\pi^\pm K^-$ (d). Taken from [2].

2.8 Final comments

In this chapter, it was shown that in B decays the CP violation can be manifested in three ways. However, only one type can occur in charged B decays, the direct CP violation. The direct CP violation can only be observed if there are two or more processes that provide a relative weak phase and a relative strong phase generated by final state interaction. In addition, CPT theorem requires the existence of re-scattering processes as an additional constraint on direct CP violation.

The three-body charmless B decays, due to the predominance of intermediate states, provide an ideal environment to observe CP violation effects. Since those decays can produce many sources of strong phase and processes that involve re-scattering effects.

The theoretical approach for these decays has been based on two different models: the BSS model[19] and the Wolfenstein approach[18]. The BSS model assumes that the CP violation comes from the interference between tree and penguin amplitudes, and it predicts a small CP violation effect in $B^\pm \to h^+h^\pm h^-$ decays. Whereas the Wolfenstein approach, by taking into account the CPT theorem implications on direct CP violation, emphasises the role of soft re-scattering in producing CP violation effects.

The recent results from LHCb experiment have measured direct CP violation in $B^\pm \to \pi^+K^\pm\pi^-$, $B^\pm \to K^+K^\pm K^-$, $B^\pm \to \pi^+\pi^\pm\pi^-$ and $B^\pm \to K^+\pi^\pm K^-$ with significances of 2.8σ, 4.3σ, 4.2σ and 5.6σ [2]. In addition, large CP asymmetries were observed in certain phase-space regions, including regions not related to any resonance, recently attributed to the final state hadronic rescattering produced by the strong interaction.

These measurements also have revealed that may there is a correlation among asymmetries in the coupled channels. The inclusive asymmetry was found to be positive for $B^\pm \to \pi^+K^\pm\pi^-$ and $B^\pm \to \pi^+\pi^\pm\pi^-$ decay channels and negative for $B^\pm \to K^+K^\pm K^-$ and $B^\pm \to K^+\pi^\pm K^-$ decay channels. The same characteristic was observed in the regions with high asymmetry associated with the hadronic rescattering. This feature may be explained by taking into account the implications of CPT constraint on direct CP violation [3]; it states that the sum of all partial decay rates over certain subsets with same quantum numbers and connected by strong interactions have to be equal for particles and antiparticles. As a consequence, in decay with CP violation, there must be another channel connected by strong interaction in which has CP violation with opposite sign in such a way to fulfil the CPT condition. This exchange between partial rates depends on the underlying mechanism that gave rise to the asymmetry [24]. In the case of the three-body charge B decays, the underlying mechanism has been attributed to the hadronic rescattering. Therefore, the rescattering of the final state particles would be responsible for the *flow* of CP violation among the coupled decay channels.

Thus, those experimental results have indicated that final state rescattering may play a prominent role in $B^\pm \to h^+h^\pm h^-$ decays. However, such interactions occur at the nonperturbative QCD regime, and it can not be reliably evaluated with a well-established theoretical model. As a consequence, the study of those processes rely on phenomenological approaches, which uses experimental data results to analyse the role of such effects in the CP violation. Therefore, it is crucial to provide precise measurements of the CP asymmetry in those decays. In this thesis, we present CP violation studies involving $B^\pm \to h^+h^\pm h^-$ decays. We aim to update the recent measurements by using new data collected by the LHCb.

Chapter 3

The LHCb experiment

The Large Hadron Collider beauty (LHCb) is one of the four main experiment of the Large Hadron Collider (LHC) located at CERN. LHCb was designed to study B decays and investigate CP violation phenomena. This chapter gives a short description of the experiment. It begins with an introduction of the LHC machine, followed by an overview of the LHCb experiment, where a brief description of its sub-detectors is given. Last, a summary of the trigger and LHCb software system are presented.

3.1 CERN - the path for the LHC

CERN (*Conseil Européen pour la Recherche Nucléair*) is an European organisation for particle physics research locate at Switzerland. It was founded in 1954 with the mission towards to the fundamental research on nuclear physics unliked to military proposal. The idea of creating CERN came after the Second World War as an effort of important scientists to create an international scientific collaboration to bring together scientists around the world [32].

The CERN's first accelerator was the Synchrocyclotron(SC), built in 1957, providing beam of 600 MeV for CERN's first experiments in particle physics. In 1959, the Proton Synchrocyclotron (PS) was built to accelerate protons and reach a beam energy of 28 GeV. The PS was responsible for the first observation of an antinuclei. In 1971 the PS was used to feed two interconnected rings in order to be used to collide beams of protons, called Intersecting Storage Rings (ISR). It was responsible for producing the world's first proton-antiproton collisions, paving the way for proton-antiproton collisions in the Super Proton Synchrotron (SPS).

The SPS, built in 1976, was the first of CERN's giant underground rings. It is still running nowadays, has 7 kilometres circumference and runs with energy up to 450 GeV. The SPS was responsible for producing many important results, such as inner structure of protons and the discovery of W and Z particles.

In 1989, CERN started the Large Electron-Positron (LEP), the world's highest energy electron-positron collider. Located at CERN's underground in the Franco-Swiss border, between 45 and 170 metres bellow the surface, it has a circumference of 26.7 km and reached an energy up to 209 GeV. During many years of research, LEP provided a detailed study of the eletrectweak interaction and proved that there are three generations of particles of matter. In 2000, LEP was closed to liberate the tunnel to built the Large Hadron Collider (LHC) [33].

3.2 The LHC

The Large Hadron Collider (LHC) is an accelerator and proton-proton (pp) collider installed in the existing 26.7 km tunnel that was constructed the LEP accelerator

Ref.[34]. The pp collision can achieve energy up to 14 TeV in the centre of mass collision and instantaneous luminosity of $10^{34}\text{cm}^{-2}s^{-1}$. The beams goes from one ring to another and interact in four point situated around the LHC, at these points the are the four main experiments: ATLAS and CMS designed for general purpose and LHCb and ALICE, designed to the study of c and b-hadron physics and quark-gluon plasma, respectively. A schematic layout of the LHC is shown in Figure 3.1.

The number of events per second generated in the LHC collisions is given by:

$$N_{event} = L\sigma_{event} \tag{3.1}$$

where σ_{event} is the cross section for the event and L the instantaneous luminosity L defined as [35] [34] :

$$L = \gamma \frac{n_b N^2 f_{rev}}{4\pi\epsilon_n\beta^*} R \tag{3.2}$$

where,

- γ is the proton beam energy in unit of rest mass: 7460,6
- n_b is the number of bunches per beam: 2808 for 25 ns bunch spacing.
- N is the number of particles per bunch: 1.15^{11} protons
- f_{rev} is the revolution frequency: 11.2 kHz
- ϵ_n the normalised transverse beam emittance: 3.75 μm
- β^* the beta function at the collision point: 0.55 m
- R the geometric luminosity reduction factor due to the crossing angle at the interaction point: 0.85

With the nominal parameter values shown above, the accelerator can operate with luminosity up to $10^{34}\text{cm}^{-2}s^{-1}$. ATLAS and CMS were designed to operate with high luminosity (with peak of $L(ATLAS\&CMS) = 10^{34}\text{cm}^{-2}s^{-1}$). Whereas LHCb and ALICE with low luminosity, $L(LHCb) = 10^{32}\text{cm}^{-2}s^{-1}$ and $L(ALICE) = 10^{27}\text{cm}^{-2}s^{-1}$).

The first LHC collisions occurred in 2010 at a reduced centre of mass energy of 7 TeV, in 2011-2012 data taking it achieved 8 TeV and during 2015-2018 energy of 13 TeV in the centre of mass of the proton collisions. It is expected that in 2021, after the second long shutdown, LHC machine will reach its total energy of 14 TeV.

3.3 The LHCb detector

The Large Hadron Collider beauty (LHCb) is an experiment dedicated to the study of heavy flavour physics. It is designed for precise measurements of CP violation and rare decays containing b and c quarks. The LHCb detector is a single-arm forward spectrometer, which is a geometry similar to a fixed-target experiment. The geometry choice was motivated by the fact that the $b\bar{b}$ pair produced in the pp collision at LHC, predominately fly in the same forward (or backward) direction.This is demonstrated in in Figure 3.2 where a simulation of the angular correlation of the produced B meson is shown. About one third of produced $b\bar{b}$ decay within the LHCb acceptance [37].

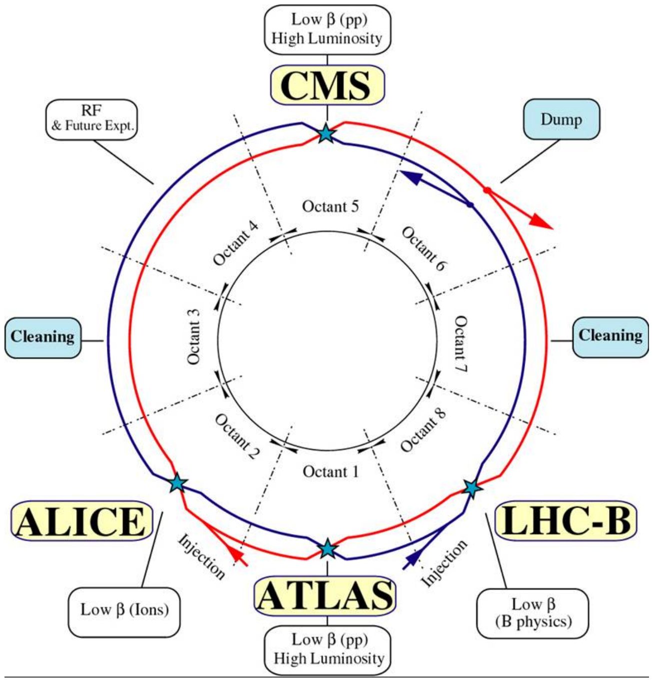

FIGURE 3.1: Schematic layout of the LHC and positions of the four main experiments [36]

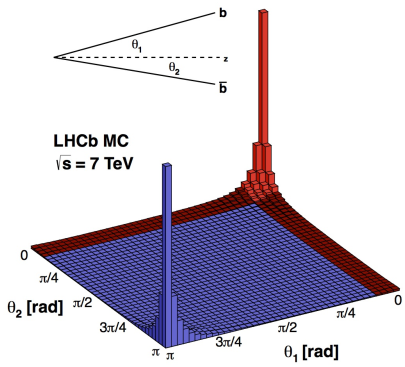

FIGURE 3.2: Simulation of the angular distribution for the $b\bar{b}$ produced at the LHC.

The LHCb acceptance is defined by a polar angle with respect to the z axis (along the beam). In the horizontal plane the acceptance lies between 10-300 mrad and in the vertical plane between 10-250 mrad horizontal plane.

The detector consists of several subsystems, as shown in Figure 3.3, that can be classified into two categories. The first one is the tracking system which consists of three sub-detectors: The Vertex Locator(VELO), the Tracker Turicensis (TT) located in front of magnet and the tracking stations T-stations (T1-T3) located behind the magnet, implemented as Inner Tracker(IT) and Outer Tracker(OT). They are used for reconstruction and determination of vertices and momentum of the particles. The category is the sub-detectors which provide particle identification. They are composed of two Ringing Imaging Cherenkov detectors (RICH), RICH1 situated in front of TT and RICH2 situated behind T-stations. Calorimeter system, composed of different sub-detectors, which the main components are the eletrocmagnetic calorimeter (ECAL) and hadronic calorimeter (HCAL). In addition, five muon stations (M1-M5), one placed before the calorimeters and the others are the outermost sub-detector of LHCb.

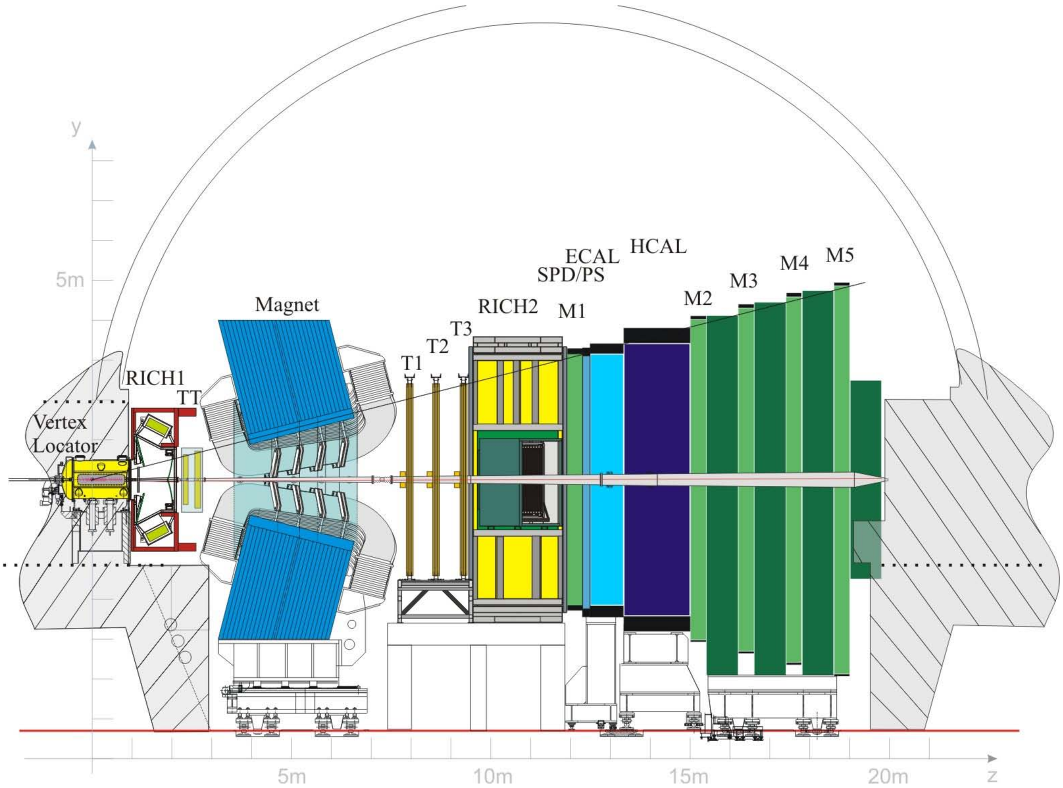

FIGURE 3.3: Schematic layout of the LHCb experiment [38].

It is known that B hadrons decays always result in secondary vertices, therefore it is crucial for the LHCb experiment be able to distinguish primary and secondary vertices. At LHC luminosity, the number of pp collisions in a single bunch crossing increases, the vertex reconstruction becomes more complicated and multiple collisions also increase the radiation damage to the detector. Given these considerations, LHCb was chosen to operate at an average luminosity much lower than maximum design luminosity of the LHC, in which the number of interactions per crossing is dominated by single interactions thus facilitating the triggering and reconstruction by assuring low channel occupancy.

The LHCb detector was designed to operate at an instantaneous luminosity of $L = 2 \times 10^{32}\text{cm}^{-2}\text{s}^{-1}$. The experiment successfully collected collision data since 2010 and has to date (2018) collected more than 6 fb^{-1} of integrated luminosity. For the data taking period of 2011 and 2012 (Run I), the LHCb could collect data at an instantaneous luminosity of $L = 4 \times 10^{32}\text{cm}^{-2}\text{s}^{-1}$, twice the design value total luminosity and total luminosity of 3 fb^{-1} of pp collisions at 7 and 8 TeV centre-of-mass energy. This was possible thanks to excellent performance of the detector. For the second data taking period (Run II, 2015-2018), the centre-of-mass energy delivered by the LHC was increased to 13 TeV, leading to a increase in the $b\bar{b}$ and $c\bar{c}$ cross-sections of about 60%. At this period, the experiment collected data at total luminosity of 0.328 fb^{-1} in 2015, 1.665 fb^{-1} in 2016 and 1.609 fb^{-1} in 2017 and 2.19

fb^{-1} in 2018[39]. The evolution for the integrated luminosity for various data taking years is shown in Figure 3.4.

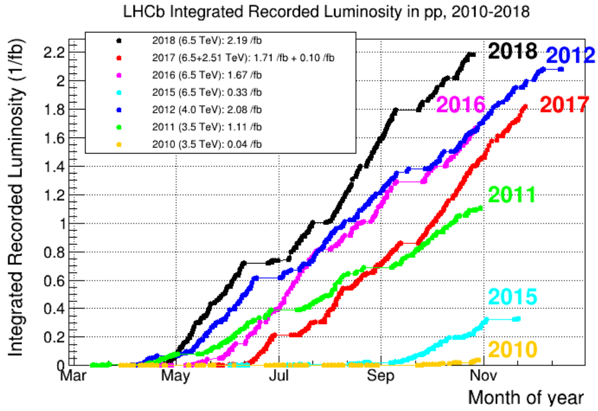

FIGURE 3.4: The evolution for the LHCb integrated luminosity for various data taking years[39].

3.3.1 Magnet

The LHCb magnet [38] is a warm dipole placed close to the interaction region, between TT and T tracking station. Its purpose is for charged particle separation and momentum measurement by using the deflection of the trajectories as the particles traverse the magnet. It consists of two trapezoidal aluminium coils bent by 45° which produces an integrated field of 4 Tm, where the main field is oriented vertically (y axis) and has a maximum value of 1 Tm. A photography of the LHCb magnet is shown in Figure 3.5. The magnet field polarity changes between *up* and *down* during operation in order to reduce systematic errors in the measurements that could result from left-right asymmetry of the detector.

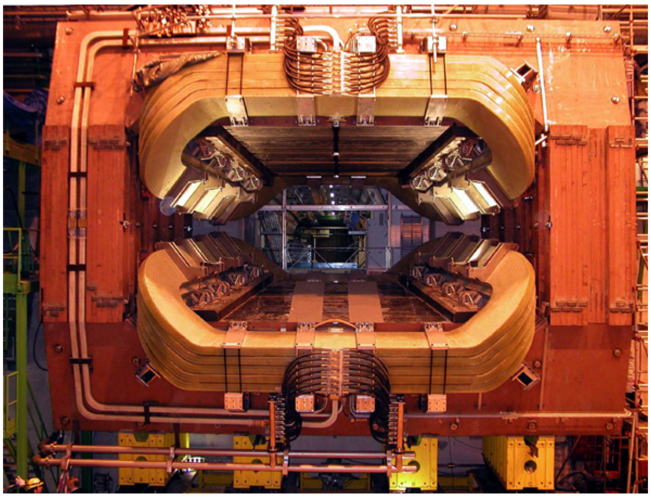

FIGURE 3.5: The LHCb magnet. Taken from [40].

3.3.2 Tracking System

The trajectories of charged particles in the LHCb are reconstructed combining information of tracking system, which consists of the vertex locator system (VELO) and four tracking station: the Tracker Turicensis (TT) located before the magnet and T-stations (T1-T3) placed behind the magnet. The VELO detector is responsible for providing precise vertex measurements while the tracking stations is required to reconstruct tracks and measure the momentum of charge particles. A brief description of each subsystem is given below.

Vertex Locator detector

The VErtex LOcator (VELO) [41, 38, 42] is a detector dedicated to provide precise measurement of trajectories of charged particles close to the interaction region, which are used to determine the primary interaction vertices and the secondary vertices that are a distinctive feature of b- and c-hadron. Those hadrons have a lifetime of the order of pico seconds, and fly a distance of around 1 cm before decay. From the measurement of the flight distance (distance between primary and secondary vertex) of the particle in the VELO, the decay time can be obtained.

The VELO is a silicon micro-strip detector positioned around the pp interaction region. It consists of two movable halves, allowing it to retract during LHC injection. Each half contains 21 modules, where each module has two semi-circular silicon micro-strip sensors that provide measurements of the radial coordinate (R sensor) and the azimuthal angle (ϕ sensor).

In addition to the 42 VELO modules there are 4 pile-up veto modules, which contain only an R sensor located in the most upstream positions. The pile-up modules are used in the Level-0 trigger to suppress events containing multiple pp interactions in a single bunch-crossing. During injection and adjustment of the beams each half of the VELO is retracted by 2.9 cm, while during the data taking the halves are moved 7 mm from the LHC beam. In Figure 3.6 is shown a layout of the VELO system.

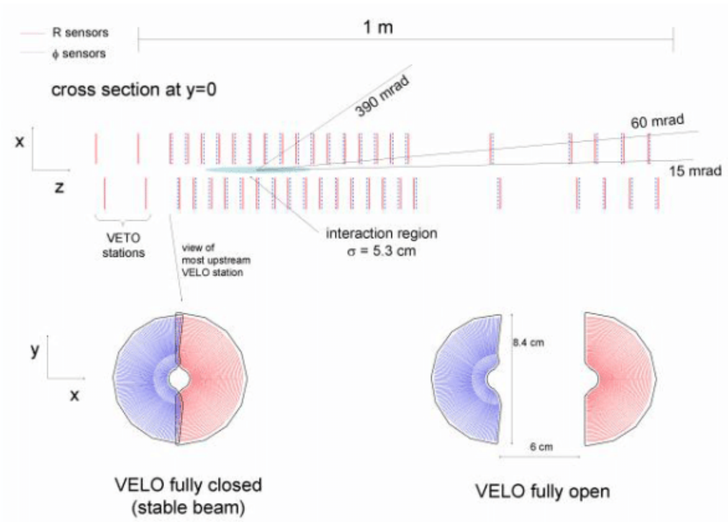

FIGURE 3.6: Cross-sections of the LHCb vertex locator. On top is the top view in the yz-plane of the VELO sensors, in red lines are the R sensors and blue lines are ϕ sensors. On bottom the xy-plane views of the first two modules in both closed (left) and open (right) positions [38].

Tracker Turicensis (TT) station

The Tracker Turicensis (TT) is placed between RICH 1 and the magnet. The detector mainly used to reconstruct low momentum tracks (which are bent out of the LHCb acceptance by the magnet) as well as long-lived neutral particles, which may decay outside of the VELO acceptance. In the region of the TT detector, the integrated magnetic field is low ($\approx$ 0.15 Tm) which enables the detector provide information about the momentum of charged particles which is later used in the trigger decision. The TT station consists of four detection layers which covers the full acceptance. The four detection layers are arranged in an $(x - u - v - x)$ configuration with vertical strips in the first and the last layer and the second layer strips rotated by -5 around the beam axis and by +5 in the third layer. A schematic layout is shown in Figure 3.7.

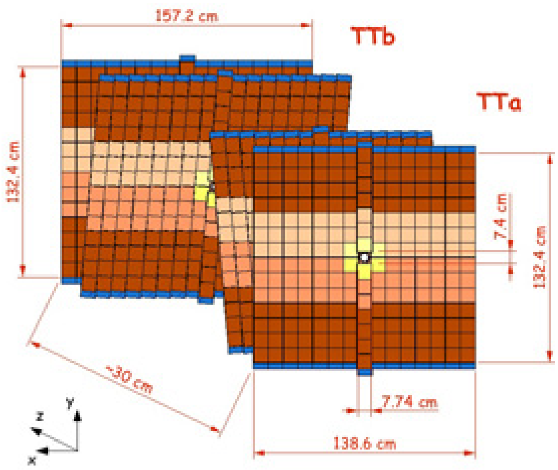

FIGURE 3.7: Layout of the Tracker Turicensis station [38].

T-stations

The T-stations (T1,T2,T3) are placed behind the magnet and is composed of two detector types. The inner region, close to the beam line, made of silicon strip detectors, called Inner Tracker (IT). The outer region, which is covered by straw tube chambers, called Outer Tracker (OT).

In the IT detector, each of the three stations has the same $(x - u - v - x)$ configuration as in the TT station, four detection layers with two layers rotated by $\pm 5°$. The area covered by the IT is small, it is a cross-shaped area of 125 cm wide and 40 com height, which corresponds to 1.5% of the total surface area of one T station. A layout of one of the three T-stations is shown in Figure 3.8. The choice of the silicon detector was motivated by the requirements of low occupancy and 50μm spacial resolution as in the IT region the flux of charged particles is high (about 30%) [43].

Each station contains four detection layers in the same $x - u - v - x$ configuration as in the IT and TT.

The outer part of the three T-stations (OT) detect charged particles with gas-filled straw tube detector. Each station contains four detection layers in the same $x - u - v - x$ configuration as in the IT and TT. The spatial resolution for a single cell is around 200 μm and hit efficiency of 99%. In Figure 3.8 (on top) shows a layout of the OT station.

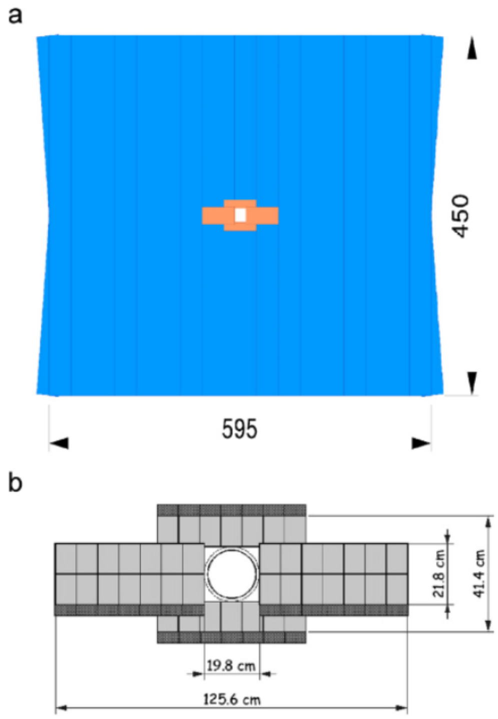

FIGURE 3.8: On top a layout of the OT station, with IT station in the centre region. On bottom a layout of the IT station, which is surrounded by the beam pipe and covered by silicon strip detector [44].

3.3.3 Particle Identification System

Particle Identification (PID) is a fundamental requirement for LHCb. It is essential the separation of pions and kaons in B hadron decays.

The PID system consist of two Ring Imagining Cherenkov detectors (RICH), the calorimeter system and the muon detector. For the common charged particle types (e, μ, K, p): electrons are primarily identified using the electromagnetic calorimeter; muons with the muon detector; the identification of kaons, pions and protons are provided by the RICH system and hadrons in general have their energy measured by the hadronic calorimeter.

RICH detectors

The RICH detectors in the LHCb use the information of particle trajectory and momentum estimated by the tracking system to identify charged particles [45]. The working principle is based on the Cherenkov radiation which occurs when a charged particle traverses a medium with a speed higher than the speed of light in that medium. As the particle traverse the medium with velocity v in medium with refractive indice n , emits photons in a cone with angle $\alpha = \frac{c}{nv}$, where c is the speed of light. The RICH principle is based on the measurement of the velocity v.

The RICH system is divided into two detectors to cover full momentum range. The RICH 1 is situated before the magnet, covers the full LHCb acceptance and was designed to detect low momentum particles (up to 60 GeV/c) that are swept out of the LHCb acceptance. It is a detector with both a silica aerogel and a C_4F_{10} gas radiator. The RICH 2 is located after the magnet and cover a smaller acceptance where high momentum particles are produced, 15 mrad to 120 mrad in the horizontal plane and to 100 mrad in vertical plane. It is filled with CF_4 gas radiator has to detect particles with high momentum (15-100 GeV/c^2) [38].

In both RICH detectors, the Cherenkov radiation is focused by using a combination of spherical and flat mirrors to be read out by Hybrid Photon Detectors (HPDs). The optical layout is vertical for RICH 1 and horizontal for RICH 2. A layout of both RICH detector is presented in Figure 3.9.

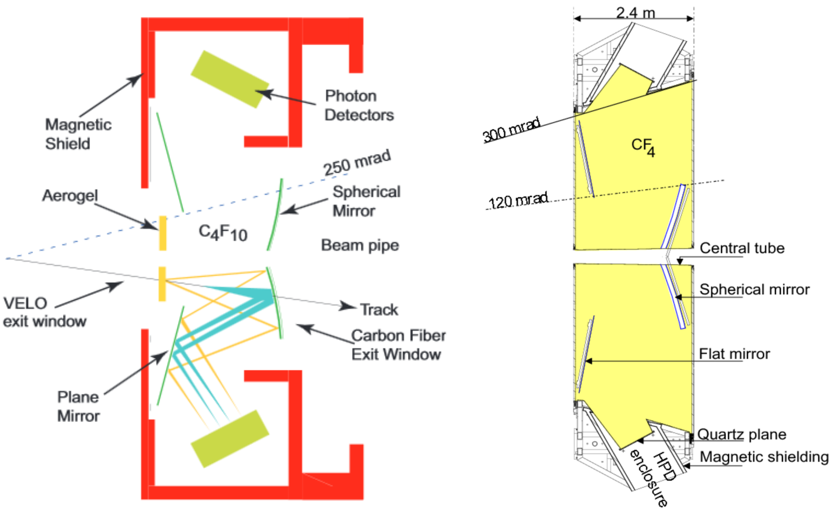

(A) (B)

FIGURE 3.9: (A) schematic layout of the RICH 1 detector and (B) top view schematic of the RICH 2 detector [38].

Calorimeters

The calorimeter system is composed of a Scintillating Pad Detector (SPD), a Preshower (PS), a electromagnetic calorimeter (ECAL) and a hadronic calorimeter (HCAL), shown in Figure 3.10. The main purpose of the system is to provide information with measurements of position and energy of electrons, hadrons and photons as well as contribution to the particle identification in the offline analysis and select candidates with high transverse energy for the trigger decision.

All calorimeters adopted the same energy detection principle: incident particles pass trough the calorimeter and interact with the scittilanting material producing a cascade of secondary particles. Those particles are absorbed by the scittilanting material which then emits scintillation light. The light is transmitted via wavelenght-shifting fibres to photomultipliers tubes. The total amount of scintillation light detected by the tubes is used to measure the energy of the particles.

The SDP and PS are a double detector made by three layers placed just after the ECAL. The upstream detector layer, SPD, helps to identify charged particles, and improves separation of electrons and protons, while the upstream layer, the PreShower detector, to identify electromagnetic particles. The SDP and PS are two planes of 15 mm thick scintillator pads separated by a lead 12 mm converter with a thickness of 2.5 radiation lengths (X_0) [46].

The ECAL is made of sampling structure with 66 layers of 4 mm thick scintillanting pads separated by 2 mm thick lead absorbers (total thickness of 25 X_0). Its main tasks are to measure the energy and position of electrons and photons and provide information of high tranverse momentum of electrons, photons and π^0 candidates to the trigger system. The ECAL provides a measurement of the energy resolution $\sigma(E)/E(GeV)$ of $10\%\sqrt{E} \oplus 1\%$[47].

The HCAL is a sampling device made from 16 mm thick iron plates and 4 mm thick scinttilanting pads, as absorber and active material, respectively. Its main purpose is to provide information to the trigger system through the measurement of the energy of protons, neutrons, pions and kaons. The energy is measured with a resolution on the level of $80\%/\sqrt{E} \oplus 8\%$ [48].

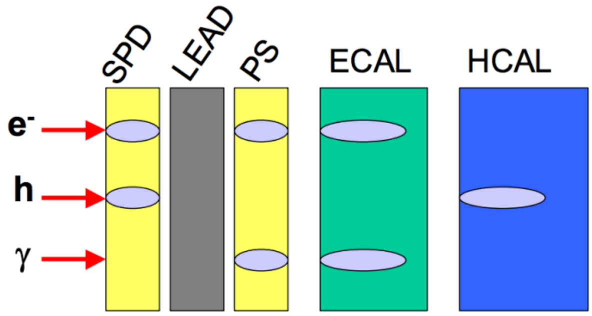

FIGURE 3.10: Signal deposited on the different parts of the calorimeter by an electron, a hadron and a photon [46].

Muon detector

Muons are in the final state of many *B*-decays sensitive to new physics and *CP* violation, therefore its identification is crucial to the experiment. As muons penetrate the full calorimeter system, the LHCb has a separated system to detected them.

The muon detector is the largest and the furthest subdetector of the LHCb and provides information for the high-p_T muon trigger at the Level-0 trigger and muon identification for the high-level trigger (HLT) and offline analysis. It consist of four stations M2-M5 and a special station M1 placed in front of the calorimeter system. A side view of the muon detector is shown in Figure 3.11. The full system comprises 1380 chambers and covers a total area of 435 m^2. Two technologies are used, the Gas Electron Multiplier (GEM) in the inner region of M1 station and for the other chambers the Multi-wire Proportional Chambers (MWPC), both filled with a mixture of $Ar/CO_2/CF_4$ gases.

3.4 Trigger system

In the LHC collision, approximately 10^{11} bunch of protons collide every 25 ns (40 MHz). In each collision, approximately 25 pair of proton collisions occur, but only 1 per million is used for physics. As the LHCb experiment operates with luminosity lower than the maximum design luminosity of LHC, in 2011 (resp. 2012, 2015 and 2016) the detector had 13 MHz (resp. 13.5,) frequency of crossings with visible interactions, defined as interactions that produce at least two charged particles with sufficient hits to be reconstructed [49].

In order to be able to not only select the interesting events but also to reduce the high events rate (to make possible the data storage) the LHCb uses a trigger system compound of three levels: the first stage is implemented in hardware and is known as L0 level trigger, which reduces the visible crossing rate to 1 MHz. This is followed by software *High Level Triggers* (HLT), subdivided into two stages: HLT1

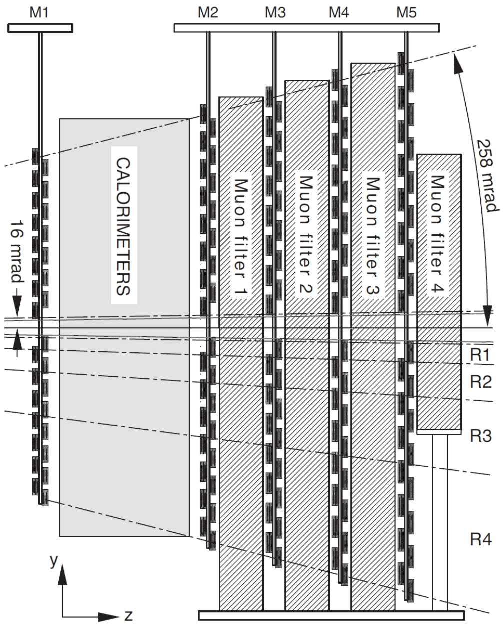

FIGURE 3.11: Schematic figure of the LHCb muon detector showing the five stations M1-M5 [38].

and HLT2, reducing the rate to 50 kHz and 2 kHz respectively. In Figure 3.13 shows an illustration of the LHCb trigger system.

The L0 level trigger reduces the visible crossing rate to 1 MHz. At this rate the entire detector can be read out. The L0 produces decision based on information from the calorimeters and muon system. Events with either high transverse momentum or large transverse energy are selected by L0 level [50]. L0 algorithms select candidates through different *lines*. A *trigger line* is composed of a sequence selections and of reconstruction algorithms made to build a candidate (hadrons, photons, electrons or muons) in a particular trigger level. The trigger line can accept or reject a decision. An event will be accepted by L0, HLT1 or HLT2 if it is accepted by at least one of its trigger lines at the relevant stage [51]. The L0 trigger line of interest here is the `L0Hadron` in which select the hadron candidate with the highest transverse energy, E_T, in the calorimeters. Muons, electrons and photons are triggered through other dedicated lines, such as the `L0Muon` trigger line, which is used in the analysis of the $B^0 \to \mu^+\mu^-$ decay. This line uses information from the muon system to reconstruct the two highest muon momentum.

The second stage, HLT, consists of software algorithms. At the first level, HLT1 algorithms refine candidates found by the Level-0 trigger and divide them into independent *alleys*, one for each L0 trigger line, as illustrated in Figure 3.12. The concept of *trigger alleys* is explained in details in Ref. [52].

The HLT1 applies a progressive partial reconstruction through different trigger lines, each one seeded by a L0 candidate. To reduce the event rate, HLT1 performs the partial reconstruction by using information from the VELO and tracking stations. If at least one track is found that satisfies strict quality and transverse momentum criteria for a line, then the event is passed to the second level of the software trigger (HLT2). Requiring candidate tracks with a combination of high p_T and/or large impact parameter reduces the rate to about 30 kHz [50]. There are around 38 HLT1 trigger lines [53], the one of interest in this thesis is the `Hlt1TrackAllL0` line, which

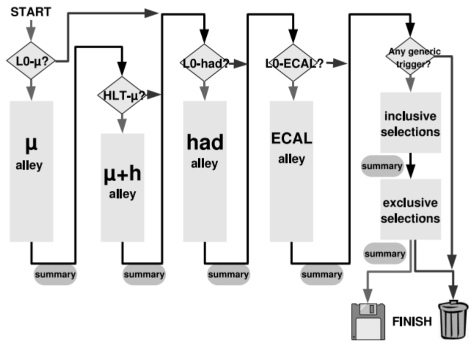

FIGURE 3.12: An illustration of trigger alleys in HLT1. For each type of Level-0 trigger decision, a different alley is executed.[52].

uses the **L0Hadron** line as a seed and select tracks with large transverse momentum and impact parameter.

In the second level, HLT2 reconstructs all tracks in the event with transverse momentum greater than 300 MeV/c. After the reconstruction, a set of exclusive and inclusive selections reduces the trigger rate to 5 kHz in which can be saved to offline analysis. There are some lines which are used to select the $B^{\pm} \to h^{+}h^{\pm}h^{-}$ candidates, such *topological* trigger lines as the **HLT2Topo**, which is specifically designed to select all b-hadrons with at least two charged particles in the final state and a displaced decay vertex [51].

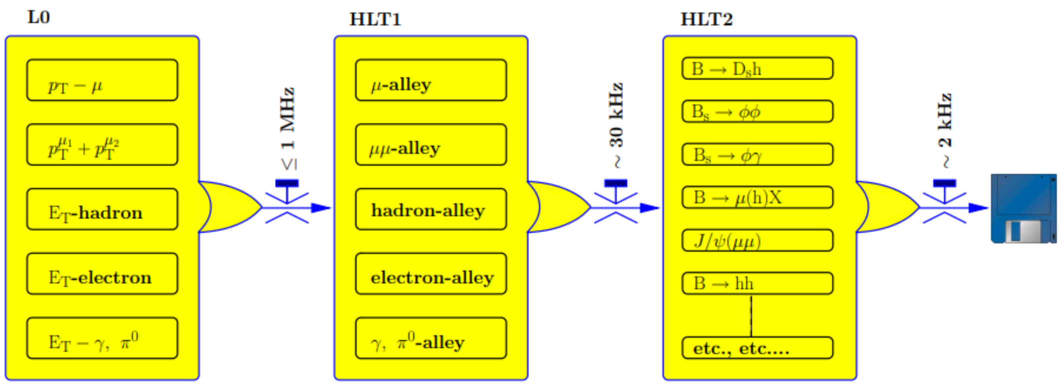

FIGURE 3.13: Overview of the LHCb trigger system [54].

3.4.1 TOS and TIS events

Each trigger line decision can be categorised as triggered-on-signal (TOS), if the candidate/tracks come from the signal decay fired the trigger, i.e. meet the selection requirement to be accept in a certain trigger line. Or triggered-independent-of- signal (TIS) if the rest of the event, i.e. candidates/tracks from other particles rather the ones from the signal, were sufficient to fire the trigger line. Thus, for a TIS decision, the presence of the signal candidate is not necessary for the trigger line to trigger the event. A trigger line that was not categorised neither TIS nor TOS, that is, when neither signal decay events nor the rest of events are sufficient to fire the trigger, but both events, the decision is categorised as trigger-on-both (TOB) [55][56]. In Figure 3.14 illustrates how those three categories are classified.

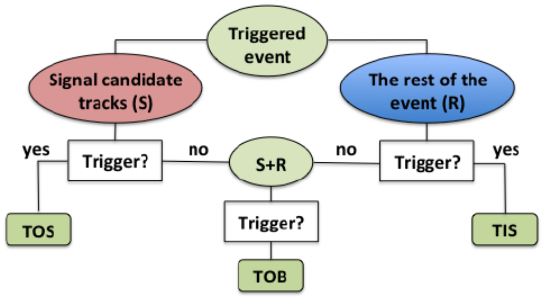

FIGURE 3.14: Diagram illustrating how Triggered On Signal (TOS), Triggered Independent of Signal (TIS) and Triggered on Both (TOS) events are classified [56].

3.4.2 Trigger in $B^{\pm} \to h^{+}h^{\pm}h^{-}$ analysis

The trigger lines used to select the signal channels $B^{\pm} \to h^{+}h^{\pm}h^{-}$ are at the first level trigger (L0): `L0Hadron` and `L0Global`. The `L0Hadron` select decays with hadrons on the final state, only the candidate with the highest energy transverse ($E_T > 3.5$) measured on calorimeters is selected for the trigger decision. The `L0Global` has all the L0 trigger lines merged. The HLT1 processes the events accepted by L0 trigger. The events used in the $B^{\pm} \to h^{+}h^{\pm}h^{-}$ are triggered by the trigger line `Hlt1TrackAllL0`, this line will be executed for all L0 accepted events and selects good quality track candidates based on their transverse momentum ($p_T > 1.6$ GeV) and displacement from the primary vertex. The relevant HLT2 line for $B^{\pm} \to h^{+}h^{\pm}h^{-}$ analysis is topological lines `HLT2Topo(2-,3-,4-Body)`, which is designed to select all partially reconstructed b-hadron decays with two, three or four charged particles in the final state and a displaced decay vertex.

3.5 Stripping

Once the data is triggered and stored, it is reconstructed and further transformed into a format suitable for the offline analysis. The data is separated into streams with similar selections and then into specific stripping lines that are used for analysis project, through a process called *stripping*. The various stripping lines are created by individual groups in the LHCb collaboration.

The $B^{\pm} \to h^{+}h^{\pm}h^{-}$ decay modes was processed using the inclusive stripping line `StrippingBu2hhh` with different versions, which depend on the year and running data taking.

Chapter 4

Measurement of the *CP* violation in $B^\pm \to h^+h^\pm h^-$ decays

In this chapter is presented an analysis performed using data collected by LHCb during 2015 and 2016 (Run II) at centre-of-mass energy of 13 TeV, corresponding to an integrated luminosity of 1.9 fb^{-1}. This chapter report the measurement of the direct *CP* asymmetries in the $B^\pm \to K^+K^\pm K^-$,$B^\pm \to K^+\pi^\pm K^-$,$B^\pm \to \pi^+K^\pm\pi^-$ and $B^\pm \to \pi^+\pi^\pm\pi^-$ decays[1], defined in terms of the decay rate (Γ):

$$A_{CP}(B^\pm \to h^+h^\pm h^-) = \frac{\Gamma(B^- \to h^-h^+h^-) - \Gamma(B^+ \to h^+h^+h^-)}{\Gamma(B^- \to h^-h^+h^-) + \Gamma(B^+ \to h^+h^+h^-)} \tag{4.1}$$

The analysis undertaken here is an update of the measurement performed in Ref.[2].

4.1 Introduction

The inclusive *CP* asymmetries, $\mathcal{A}_{CP}$, of the four $B^\pm \to h^+h^\pm h^-$ decay channels were measured by the LHCb experiment by using 2011 and 2012 data (Run I) [2] to be:

- $\mathcal{A}_{CP}$ $(B^\pm \to \pi^+K^\pm\pi^-)$ = +0.025 ± 0.004 ± 0.004 ± 0.007.
- $\mathcal{A}_{CP}$ $(B^\pm \to K^+K^\pm K^-)$ = -0.036 ± 0.004 ± 0.002 ± 0.007.
- $\mathcal{A}_{CP}$ $(B^\pm \to \pi^+\pi^\pm\pi^-)$ = +0.058 ± 0.008 ± 0.009 ± 0.007.
- $\mathcal{A}_{CP}$ $(B^\pm \to K^+\pi^\pm K^-)$ = -0.123 ± 0.017 ± 0.012 ± 0.007.

where the first uncertainty is statistical, the second systematic and the third comes from the PDG value of $\mathcal{A}_{CP}$ $(B^\pm \to J/\psi K^\pm)$. In additional to the significant inclusive *CP* asymmetry measured, large *CP* asymmetries were found in localized regions of the phase-space (discussed in the next chapter).

Most of these channel have branching ratios of the order of 10^{-6} to 10^{-5} and thereby large statistics are needed to provide precision measurement. The 2015 and 2016 data from LHCb provide samples with amount of data approximately 30% greater than the ones from Run I data (2011+2012).

The analysis aims to update the measurement quoted above, by obtaining the global *CP* asymmetry in $B^\pm \to h^+h^\pm h^-$ decays and study the *CP* asymmetry in phase space of these channels. The measurement of the *CP* violation in $B^\pm \to h^+h^\pm h^-$ decays is provided by the global charge asymmetry $\mathcal{A}_{CP}$, defined as [57]:

[1] those four decays will be refereed as $B^\pm \to h^+h^\pm h^-$ along the chapter

$$\mathcal{A}_{CP} = \frac{N_{B^-} - N_{B^+}}{N_{B^-} + N_{B^+}}, \tag{4.2}$$

where N_{B^-} and N_{B^+} are the number of negative and positive of B candidates, respectively.

The charge asymmetry obtained from the mass fit signal yields is the raw asymmetry $\mathcal{A}_{raw}$, which can be interpreted as:

$$\mathcal{A}_{raw} = \mathcal{A}_{CP} + \mathcal{A}_{P} + \mathcal{A}_{D}(h = \pi, K) \tag{4.3}$$

where:

- $\mathcal{A}_{CP}$ is the asymmetry from physical CP violation.
- $\mathcal{A}_{P}$ is the asymmetry of B^-/B^+ production during the proton-proton collisions and it is defined as

$$\mathcal{A}_{P} \equiv \frac{\sigma(B^-) - \sigma(B^+)}{\sigma(B^-) + \sigma(B^+)} \tag{4.4}$$

  where σ represents the production cross-section within the acceptance detector. The $B^{\pm}$ production asymmetry at LHCb has been previously measured using 2011 and 2012 data of the $B^{\pm} \to J/\psi K^{\pm}$ decay and was determined to be [58]:

$$\mathcal{A}_{P}{}_{=}^{2011} - 0.0023 \pm 0.0024(stat) \pm 0.0037(syst) \tag{4.5}$$

$$\mathcal{A}_{P}{}^{2012} = -0.0074 \pm 0.0015(stat) \pm 0.0032(syst) \tag{4.6}$$

  As at the present moment there is no measurement of the $\mathcal{A}_{P}$ on 2015 and 2016 data, thus in this analysis the 2012 measurement is used.

- $\mathcal{A}_{D}$ (h) is the asymmetry due to detector instrumentation, which is the detection asymmetry for pions $\mathcal{A}_{D}$ (π) and kaons $\mathcal{A}_{D}$ (K). Those asymmetries come from differences between negative and positive particle interaction with matter, acceptance and reconstruction and were obtained by the LHCb [58, 59] as a function of the kaon/pion momentum. The asymmetries are implemented as a correction when constructing the acceptance model, discussed in section 4.13.

4.2 Data and Simulation

The measurement of the inclusive *CP* violation described in this thesis is based on the data collected by the LHCb in 2015 and 2016 at centre-of-mass energy $\sqrt{s} = 13$ TeV and an integrated luminosity of 1.9 fb^{-1}.

The LHCb Monte Carlo simulated (MC) samples of $B^{\pm} \to h^{+}h^{\pm}h^{-}$ events were generated with similar conditions as during the data taking. Two different 2015 and 2016 signal MC samples are used: a *small* MC sample, referred as only MC signal, and a large MC sample. The MC signal of 2015 and 2016 are used for the background estimation, particle identification requirements and to define cuts based multivariate analysis study. These samples were generated without *CP* violation and flat in the Squared Dalitz plot representation (described in section 4.13.1). Their size are summarised in Table 4.1.

Decay	Magnet Polarity	2015	2016
$B^{\pm} \to K^{+}K^{\pm}K^{-}$	MagDown	257787	504110
	MagUp	250485	514017
$B^{\pm} \to K^{+}\pi^{\pm}K^{-}$	MagDown	257693	500810
	MagUp	250811	500269
$B^{\pm} \to \pi^{+}K^{\pm}\pi^{-}$	MagDown	250231	500222
	MagUp	255345	500123
$B^{\pm} \to \pi^{+}\pi^{\pm}\pi^{-}$	MagDown	251197	605977
	MagUp	257717	500831

TABLE 4.1: MC signal statistics.

Decay	Magnet Polarity	2015(Gen./Reco.)	2016 (Gen/Reco.)
$B^{\pm} \to K^{+}K^{\pm}K^{-}$	MagDown	30,518,065/1,003,521	75,289,768/2,681,054
	MagUp	33,146,247/1,086,364	74,122,045/2,635,843
$B^{\pm} \to K^{+}\pi^{\pm}K^{-}$	MagDown	32,783,983/1,032,844	76,907,591/2,637,534
	MagUp	32,319,470/1,016,462	76,569,578/2,620,096
$B^{\pm} \to \pi^{+}K^{\pm}\pi^{-}$	MagDown	34,433,974/1,005,999	81,766,408/2,593,777
	MagUp	35,343,049/1,032,185	78,779,571/2,495,577
$B^{\pm} \to \pi^{+}\pi^{\pm}\pi^{-}$	MagDown	38,249,997/1,053,830	86,522,036/2,509,959
	MagUp	36,592,823/1,007,250	83,500,285/2,421,863

TABLE 4.2: Large MC signal statistics

The large MC samples of $B^{\pm} \to h^{+}h^{\pm}h^{-}$ signal MC are used to study the acceptance effects after each step of the selection. The samples are also generated flat in Squared Dalitz plot representation and without *CP* violation. The size of the generated and reconstructed large MC samples are summarised in Table 4.2.

4.3 Analysis strategy to select $B^{\pm} \to h^{+}h^{\pm}h^{-}$ events

The selection of $B^{\pm} \to h^{+}h^{\pm}h^{-}$ candidates is divided in several steps. It begins with the choice of trigger lines that selects the interesting events from the *pp* collision, described in section 4.4. It is followed by a general pre-selection, named *stripping*, presented in section 4.5, which is a common selection for many B decays into three hadrons in the final states that can be used in different analyses. The trigger and stripping selection are mostly based on track quality variables thus, both selection steps are very efficient in removing candidates with low track reconstruction quality.

After the trigger and stripping selection a set of selection specific for each channel is performed in order to reduce the physical background sources. A set of additional loose requirements constitutes the preselection described in section 4.7. After these preliminary steps, the selection aims on reducing as much as possible the two main background contribution that affect the separation of each $B^{\pm} \to h^{+}h^{\pm}h^{-}$ decays: the combinatorial background and the peaking background. The combinatorial background originates from random combinations of tracks faking the signal, and to reduce its contamination, it is used selection cuts based on multivariate analysis technique, described in section 4.8. The peaking background mostly comes from B decays that are not correctly reconstructed and populate the signal region: dedicated particle-identification criteria and invariant mass cuts (vetoes) are performed to reduce those contributions, as shown in section 4.9.

Thus, the strategy to select the $B^{\pm} \to h^{+}h^{\pm}h^{-}$ modes can be summarised according to the following sequence:

1. **Trigger selection**: Generic selection to pick interesting events of B hadronic decays from pp collision.
2. **Stripping selection**: Generic selection to group three-body hadronic B decays.
3. **Pre-selection**: Specific loose requirements for each $B^{\pm} \to h^{+}h^{\pm}h^{-}$ channel applied on particle identification variables and two-body invariant mass to reduce the peaking background and reduce the samples for the multivariate analysis.
4. **Multivariate Analysis selection**: Aims to suppress significantly the combinatorial background in each decay channel.
5. **Particle Identification selection**: Final particle identification requirement to reduce as much as possible the background contribution due to the misidentification of pions and kaons.

4.3.1 Selection variables

The variables used for the selection requirements are mainly based on the topological feature of three-body B hadron decays. An illustration of the $B^{\pm} \to h^{+}h^{\pm}h^{-}$ topology is shown in Figure 4.1. The main variables are described below.

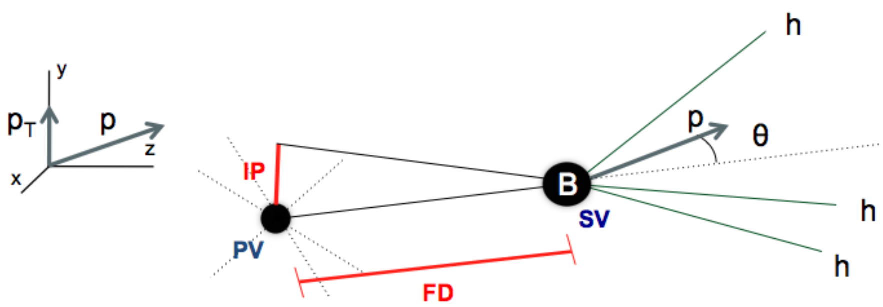

FIGURE 4.1: Schematic view of the topology of three-body B charmless decay.

Transverse momentum-energy (p_T-E_T) : The transverse momentum (Figure 4.1) is the momentum component in the plane transverse to the beam direction (z-axis). The transverse energy is the measured energy converted into a transverse momentum measurement.

Primary and Secondary vertex (PV-SV) : The primary vertex (PV) of a particle is the interaction point of the pp collision where the particle originates. Secondary vertex is the point where the particle decays into the final state.

Impact parameter (IP) : The impact parameter (IP) of a track in the LHCb is defined as the distance of closest approach between a reconstructed track and the primary vertex. The IP variable is used to distinguish particles that was produced at the primary vertex and particles produced at the secondary vertex. Typically, final state particles from a B meson have higher impact parameter than the particles that do not originate from the primary vertex.

Flight Distance (FD) : It is the distance between the production point where the proton beams collide (PV) and the decay vertex into the three final state tracks (SV).

Cosine of θ ($\cos\theta$) : The angle θ is the angle between the B momentum vector and the flight direction. For a $B^{\pm}$ candidate, the $\cos\theta$ is expected to be approximately 1.

Distance of Closest Approach (DOCA) : It is defined as the shortest distance between two pair of tracks from the final state particles. For a decay with three final state particles, this distance is computed from three possibilities of pair combination.

Particle Identification (PID) variables :

The particle identification information obtained from the calorimeters, RICH and muon system are combined to provide a single set of PID variables. The LHCb uses extensively PID variables as selection criteria in the analyses to discriminate pions, kaons, protons, electrons, and muons. In this thesis, the PID variables `ProbNN` are used. This quantity is the output of multivariate techniques created by combining tracking and PID information. This results in a single probability values for each particle hypothesis [60].

4.4 Trigger selection

The LHCb trigger system (described in 3.4) has the task to select events of interest for the physics analysis out of all events produced in the pp collisions at the LHC. The LHCb trigger reduces significantly the high events rate through three different levels, one at the hardware level (L0) and two at the software level (HLT1 and HLT2). By reducing the data and keeping only interesting events, the trigger makes possible the data storage for the offline analysis. To select $B^{\pm} \to h^{+}h^{\pm}h^{-}$ candidates, trigger requirements were imposed in all levels. At the first level, L0, the trigger uses dedicated line to select photons, electrons, muons and hadrons. To select the $B^{\pm} \to h^{+}h^{\pm}h^{-}$ candidates, it was required the event to be triggered-on-signal (TOS) by the `L0Hadron` line. The `L0Hadron` line is dedicated to select hadrons and candidates only fire this trigger line if it has high transverse energy E_T in the calorimeters ($E_T > 3.5$ GeV). Thus, select `L0Hadron_TOS` candidates means that the events triggered met the selection requirement imposed by `L0Hadron` line. At the L0 trigger is also imposed that events are triggered-independent-of-signal (TIS) in the `L0Global` line. This line has all the trigger lines merged. Hence, a TIS decision on `L0Global` means to select candidates from all lines in which presence of the signal candidate was not necessary to trigger the event. Summarising, at the L0 level trigger, $B^{\pm} \to h^{+}h^{\pm}h^{-}$ candidates are accepted only if they were triggered by `L0Hadron_TOS || L0Global_TIS`, where `||` is logical operator *or*. This trigger removes most of charmonium events such as $B^{\pm} \to J/\psi K^{\pm}$ decays.

The first stage of high level trigger (HLT1) performs partial reconstruction and select very high transverse momentum. To select $B^{\pm} \to h^{+}h^{\pm}h^{-}$ candidates at this level, it is used the `HLT1TrackALL_TOS` line, which is an inclusive beauty and charm trigger line that selects good quality track candidates based on their transverse momentum p_T ($p_T > 1.6$ GeV) and significant displacement from the primary vertex. It is the dominant trigger line for most physics channels that do not contain leptons in the final state [61]. At the second stage (HLT2), the full reconstruction is performed and the selection of decay candidates of interest is based on an inclusive topological selection: `HLT2Topo(2-,3-,4-Body)_TOS` line[62], based on multivariate techniques, this trigger line select B decays with two, three or four charged particles in the final state and a with significant displaced decay vertex and transverse momentum.

4.5 Stripping selection

After the trigger selection the data is storage and separated into many categories of decays. These categories select candidates based on very loose requirements in such way to group them into only decays that share common features. This pre-selection stage is known as *stripping*, and each category of decays is associated a stripping line, as mentioned in section 3.5. To select $B^{\pm} \to h^{+}h^{\pm}h^{-}$ decays, it is used the stripping line called `StrippingBu2hhh_KKK_inclLine`, which is an inclusive selection approach that aims to select all three-body hadronic B decays. An inclusive selection means reconstruct the B meson decay by attributing all three daughter mass particles to kaon mass hypothesis within a large three-body invariant mass window (4 - 7 GeV/c^2)[2]. This is done in order to include all relevant final states. For example, the invariant mass distribution of $B^{\pm} \to K^{+}\pi^{\pm}K^{-}$ decay mode will not appear as a Gaussian distribution in the mass spectra but as a wider distribution above the true B mass. After this stage, the $B^{\pm}$ invariant masses are recalculated by assigning the correct mass hypothesis separately for each decay channel.

The stripping selection criteria is based on kinematic variables and exploit the fact that three-body B hadron decays share similar topology. An illustration of the $B^{\pm} \to h^{+}h^{\pm}h^{-}$ topology is shown in Figure 4.1.

The B meson originates in the interaction point of the pp collision called primary vertex (PV). Due to its large mean lifetime (order of picoseconds), the B meson travels approximately 1 cm before decaying in its secondary vertex (SV), producing the three final state tracks. Thus, a requirement on the variable characterised by the separation between the PV and SV (i.e. flight distance (FD)) have to be done to select the B candidates. The B meson is produced with large transverse momentum, therefore the B candidate has to satisfy a minimum requirements on p_T. In addition, its momentum vector points to the primary vertex, resulting typically in a small impact parameter (IP) and angle θ between the B momentum direction and the line connecting the B vertex and primary vertex. In contrast, the final states particles (also referred as daugther particles) tend to have larger impact parameters as they do not originate from the primary vertex. A common requirement is to impose that the daughters have high IP in relation to the PV, which can be very efficient for the signal. However, low momentum daughters tend to travel in the same direction of the B meson, which points to the primary vertex. As a result, when applying cuts on high IP of tracks, it can remove low momentum daughter and introduce inefficiencies in the border of the Dalitz Plot [63]. In order to avoid this effect it is used cuts in χ^2 per degree of freedom of the tracks and quality of the reconstructed vertex refine selection, which reduce the combinatorial background and refine the selection. Another useful requirement is to use the sum of the daughter tracks $\mathrm{P_T}$ and P as this technique allows the daughter track "accesses" any Dalitz plot region. A summary of the selections cuts imposed by the stripping line `StrippingBu2hhh_KKK_inclLine` are listed in Tab. 4.3.

[2]variable $B^{\pm}$ candidate M_{KKK}

Variables	Selection cuts	Description
Tracks P_T	> 0.1 GeV/c	daughters transverse momentum
Tracks P	> 1.5 GeV/c	daughters momentum
Tracks IP χ^2	> 1	χ^2 distance of the particle trajectory to PV
Tracks χ^2/n.d.f.	< 3	χ^2 per degree of freedom of the track fit
Tracks GhostProb	< 0.5	Ghost track probability
$\sum P_T$ of tracks	> 4.5 GeV/c	Sum of momentum of tracks
$\sum$ P of tracks	$> 20.$ GeV/c	Sum of daugher transverse momentum
$\sum$ IP χ^2 of tracks	> 500	Sum of χ^2 distance of the particle trajectory to PV
P_T of the highest-P_T track	> 1.5 GeV/c	Transverse momentum of the leading P_T
Maximum DOCA	< 0.2 mm	Maximum distance of closest approach between the two tracks
$B^{\pm}$ candidate M_{KKK}	$5.05 - 6.30$ GeV/c^2	Mass of combination of 3 charged kaon
$B^{\pm}$ candidate M^{COR}_{KKK}	$4 - 7$ GeV/c^2	B candidate corrected mass under KKK hypothesis
$B^{\pm}$ candidate IP χ^2	< 10	Difference in the vertex-fit χ^2 of the PV reconstructed with and without B candidate
$B^{\pm}$ candidate P_T	$> 1.$ GeV/c	Transverse momentum of the $B^{\pm}$ candidate
Flight Distance	> 3 mm	Distance from SV to any PV
Secondary Vertex χ^2	< 12	Quality of the secondary vertex
$B^{\pm}$ candidate $\cos(\theta)$	> 0.99998	Cosine of the angle between the direction of the B candidate and z-axis
$B^{\pm}$ Flight Distance χ^2	> 500	Distance between PV and SV.

TABLE 4.3: The stripping selection requirements for charmless $B^{\pm}$ decays into three light hadrons.

4.6 Background from B decays

This section describes the types of background from B hadrons decays that passes the trigger and stripping selection criteria. These backgrounds usually enter the signal region due to a wrong mass assumption, partially reconstructed decays and Cabibbo-favoured channels. The main background contribution are:

- Intermediate charmed decays
- Peaking background
- Partially reconstructed background
- Combinatorial background

4.6.1 Intermediate charmed decays

The most dominant decays for B meson are charmed and charmonium decays, such as D and J/ψ mesons, because the $b \to c$ transition is more frequent than $b \to u(d)$ transition. Therefore charmed decays are the main background contribution.

In the $B^{\pm} \to h^+h^{\pm}h^-$ mass spectrum, charmed background can be either due to an intermediate charm decay ($B^{\pm} \to Dh^{\pm}$) or misidentified charmonium state ($B^{\pm} \to J/\psi K^{\pm}$). To remove this type of background, invariant mass cuts and tight particle identification requirements need to be applied in the region of those charmed decays.

Charmonium resonances

The branching fraction of $B^{\pm} \to J/\psi K^{\pm}$ makes it a significant background. Topologically, $B^{\pm} \to J/\psi K^{\pm}$, $J/\psi \to \mu^+\mu^-$ has similar properties as the signal. The mass difference between π and μ is small, so this kind of background will occupy the same range as the signal. To eliminate contamination from $J/\psi \to \mu^+\mu^-$, where muons are misidentified as pions from $J/\psi \to \pi^+\pi^-$, it is required that hadron tracks not to be muon, through a variable for muon identification called `isMuon`. The remaining J/ψ contribution is removed by applying invariant mass cuts around its mass.

Charmed mesons

Another type of fully reconstructed modes is when a B meson decays into two-body $D^0 h$ combination, and D^0 decaying into KK,$\pi\pi$ or $K\pi$. To remove these contributions, mass vetoes under each hypothesis are applied, as described in section 4.10.

4.6.2 Signal cross-feed

Cross-feed are the background due to three-body B decays which are reconstructed with misidentified final state particles. Thus the wrong mass assumption is attributed to misidentified particles which leads the formation of mass peak lower or higher than the B mass. The most relevant background of this type are the signal cross-feed contribution, which are the cross-feed contribution from $B^{\pm} \to h^{+}h^{\pm}h^{-}$ modes other than one considered as signal with a single or double mis-identified pion or kaon particle.

In Figure 4.2 is shown the simulation of the signal cross-feed for each $B^{\pm} \to h^{+}h^{\pm}h^{-}$ decay channel, where it is shown the reconstructed invariant mass for a single, double and triple misidentified final state particle. It can be seen at the bottom left of the Figure 4.2 the invariant mass distribution of cross-feed contributions for the $B^{\pm} \to K^{+}\pi^{\pm}K^{-}$ decay, where the $B^{\pm} \to \pi^{+}\pi^{\pm}\pi^{-}$ decay (in red) appears as mass peak in the right side of the invariant B mass distribution in the $B^{\pm} \to K^{+}\pi^{\pm}K^{-}$ spectrum (in magenta). The $B^{\pm} \to \pi^{+}\pi^{\pm}\pi^{-}$ is reconstructed as $B^{\pm} \to K^{+}\pi^{\pm}K^{-}$ by assuming the two pion as kaons leading the formation of mass peak lower than the B mass as $m_{\pi} < m_{K}$.

Since the decays under study have final states purely hadronic, it is crucial to apply particle identification (PID) requirements that are able to distinguish very well kaons and pions. In particular, the use of LHCb particle identification variables (described in section G.3) reduce significantly the signal cross-feed in the mass spectrum and the remaining ones are modelled in the invariant B mass fit. As can be seen from Figure 4.2, each type of cross-feed background has a specific and non-uniform distribution in the B mass spectrum, thus the determination of yield and shape of each background component is essential to take into account their contribution in the extraction of signal yield (discussed in the section 4.12.3).

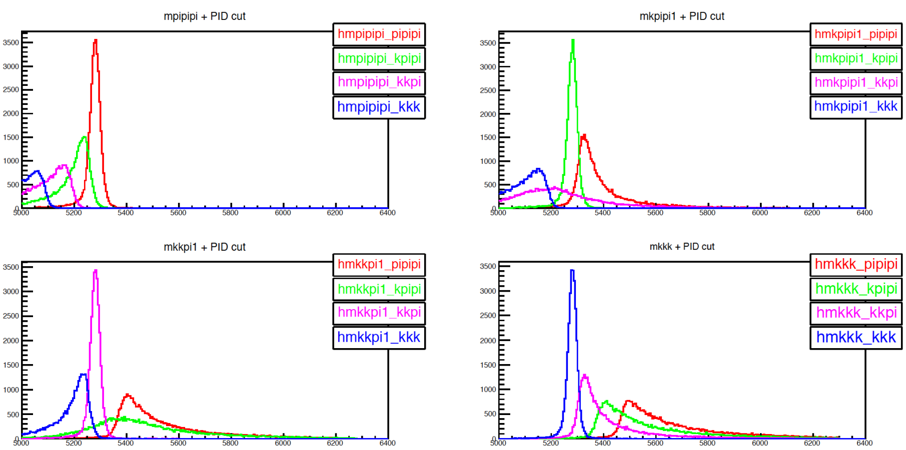

FIGURE 4.2: Simulation of the signal cross-feed contribution for each decay channel. At the left side, on the top the $B^{\pm} \to \pi^{+}\pi^{\pm}\pi^{-}$ and on the bottom $B^{\pm} \to K^{+}\pi^{\pm}K^{-}$. At the right side, on the top the $B^{\pm} \to \pi^{+}K^{\pm}\pi^{-}$ and on the bottom $B^{\pm} \to K^{+}K^{\pm}K^{-}$.

4.6.3 Partially reconstructed four-body B decays

Partially reconstructed background appear in the spectrum when a neutral (π^0 or photon) particle from the B decay into four particles in the final state is missed. This type of background populate the low side band region in the mass spectrum and are modelled in the invariant B mass fit.

4.6.4 Combinatorial background

This type of background is due to the random combination of tracks (both real and ghost particles) that form fake B candidates. Due to the large number of combinations, combinatorial background is expected to be almost constant shape along the B mass spectrum. It will be shown later that this type of background is highly reduced through multivariate analysis selection and remaining background is modelled by an exponential function in the B mass fit.

4.7 Pre-selection

After the stripping and trigger selection, the $B^{\pm} \to h^{+}h^{\pm}h^{-}$ candidates are required to satisfy other criteria in order to reduce the physical background. In contrast with the stripping selection, which is a set of loose requirements common to many channels, this pre-selection is specific for this analysis and applies selection cuts more specific to each $B^{\pm} \to h^{+}h^{\pm}h^{-}$ decay mode.

At this stage, the samples have not had any particle identification requirements of the final state particles applied and hence contains all combinations of pions and kaons which lead to a very high cross-feed contribution from other B decays. The main contribution is the signal cross-feed due to the mis-identification of pion as kaon. This contribution leads the formation of mass peak around the B mass in the four $B^{\pm} \to h^{+}h^{\pm}h^{-}$ channels, as already shown in Figure 4.2.

In order to reduce the cross-feed background from other $B^{\pm} \to h^{+}h^{\pm}h^{-}$ channels, loose PID requirements are performed, which are applied to the four decay modes and require that kaon and pion candidates have `ProbNNk`>0.1 and `ProbNNpi`>0.1, respectively.

Additionally, the loose requirements include particle identification requirements to remove contributions from muons and electrons in all tracks. Also, invariant mass cuts are performedin the region around D^0 mass (1865 MeV/c^2), in the range [1830,1900] MeV/c^2, and in the region around J/ψ mass (3096 MeV/c^2), in the range [3050,3150] MeV/c, to exclude the contribution of $B^{\pm} \to Dh^{\pm}$ and $B^{\pm} \to J/\psi K^{\pm}$ decays, respectively.

4.8 Multivariate Analysis selection

The combinatorial background comes from a random combination of tracks that form a fake signal of B candidates and populate uniformly the whole B mass spectrum. Due to the fact that it has a characteristic exponential function shape along the spectrum, cuts on variables with high discrimination power between signal and background can be applied to reduce the combinatorial background contribution. The simple approach is to apply rectangular cuts on these variables, but due to a large number of tracks and correlation between the variables it is necessary to adopt a more powerful approach to select the events with high signal efficiency. The Multivariate Analysis

(MVA) selection explore the correlation between variables and combine them to obtain a single discriminant. There are many multivariate analysis methods available such as *Boost Decision Tree* (BDT) and Neural Network, which is based on machine learning technique, that roughly consists of three steps: *training* on the simulation samples to learn the differences between signal and background, *testing* on independent simulation samples to evaluate the results and *evaluation* of the output result on data samples. The MVA selection performed in this thesis uses the BDT method.

4.8.1 BDT training

For the BDT training, it was used the data and simulation samples describe in section 4.2. It was chosen ten variables with good discrimination power between signal and background as input in the BDT training, common for the four channels. Before training, the samples pass through stripping cuts, trigger, J/ψ and D^0 vetoes and loose PID requirements. In the latter, weights from PIDCalib (see section 4.13.3) are applied on the simulation samples instead of applying the PID cuts. It is performed since the agreement between data and simulation of the PID variables are not well represented.

It was performed two types of training: (i) one specific for each channel and (ii) common to all channels. Specific for each channel means that the optimization was performed using its own MC samples as a signal and the high side band region of the B mass spectrum data sample (> 5.4 GeV)[3] as background. Common to all channels means merging all MC samples (from the four channels) to use as a signal and data from the $B^{\pm} \to \pi^{+}\pi^{\pm}\pi^{-}$ channel in the high side band (> 5.4 GeV) as background. It is used similar number of events for background and signal samples in the training.

The training is performed using the BDT implementation in the TMVA package [64]. Figure 4.3 shows for each decay channel the distribution of the BDT output variables, comparing the two optimizations type (i) and (ii). As can be seen from the figures, for all channels there are a good distinction between signal and background.

4.8.2 BDT optimisation

In order to optmise the BDT output, the optimal cut on the BDT output is obtained by calculating the statistical significance for each signal mode:

$$Significance_{BDT} = \frac{S_{MC}}{\sqrt{(S+B)_{Data}}} \tag{4.7}$$

where the S_{MC} in the numerator is the number of events taken from MC signal sample and $(S+B)_{Data}$ is the number of events in the signal region $|(B_m - 5284\ MeV/c^2)| < 40\ MeV/c^2$ taken from the data for a given BDT cut, after applying the final PID requirements. In the Appendix A the Figure A.1 and Figure A.2 show the significance and signal efficiency for each decay channel, indicating the location of the cut on the BDT output variable we choose, for both optimization. The signal efficiency is obtained through ratio between MC signal events before and after applying all selection requirement. The BDT value was chosen as the value close to the maximum significance that gives good signal efficiency.

Each channel mode has its own BDT output, and therefore its own optimal cut. In Table 4.4 is listed the cuts for the optimizations performed: specific and common to all channels. By analysing both specific and common BDT output cuts on data, it

[3]In this region, combinatorial background is predominant.

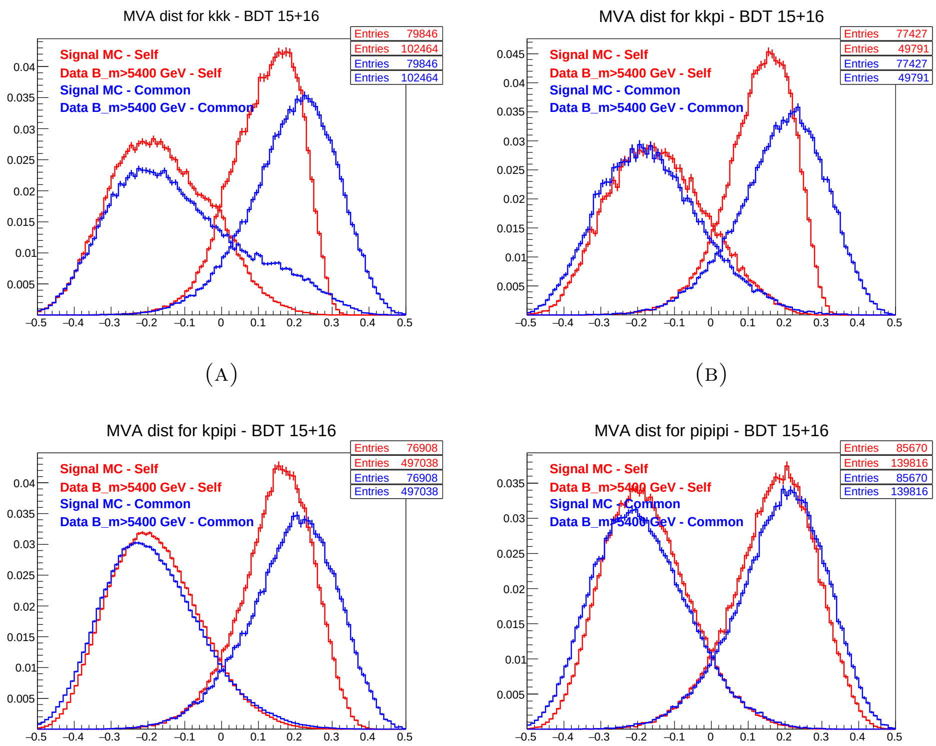

(A) (B) (C) (D)

FIGURE 4.3: In each plot, left curves are background and right ones are signal. Red lines are for the optimization type (i) and and blues lines for the optimization type (ii). (A) $B^{\pm} \to K^{+}K^{\pm}K^{-}$ mode, (B) $B^{\pm} \to K^{+}\pi^{\pm}K^{-}$, (C) $B^{\pm} \to K^{+}\pi^{\pm}K^{-}$ and (D) $B^{\pm} \to \pi^{+}\pi^{\pm}\pi^{-}$.

was found that the BDT output specific for each channel has the better performance. In Figure 4.4 is shown the $B^{\pm} \to h^{+}h^{\pm}h^{-}$ invariant mass before, i.e. with trigger, stripping, preselection cuts applied, and after apply the BDT selection for the optimization specific for each channel. As can be seen, the combinatorial background is significantly reduced. The result for common optimization will be used in the future for the systematic calculation.

4.9 Particle Identification selection

For the particle identification (PID) requirements, it is done by using "affirmative" and "negative" requirements on the following PID variables:

- `ProbNNk`: probability value for the hypothesis of the particle is a kaon (K).
- `ProbNNpi`: probability value for the hypothesis of the particle is a pion (π).

The affirmative requirement means the probability of a particle being identified as its true type, for example a pion candidates being identified as a pion. Whereas in the negative requirement, means the probability that a particle is not identified as another particle, for example, a pion candidate not identified as kaon.

The PID requirements are defined with the help of the $B^{\pm} \to Dh^{\pm}$ modes, when it is possible.

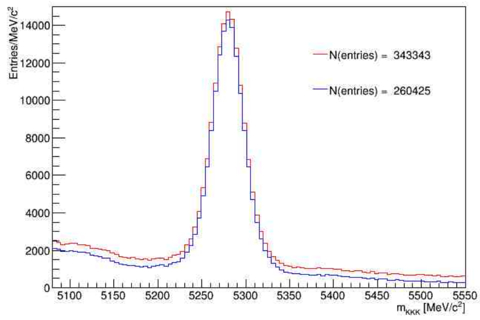

(A)

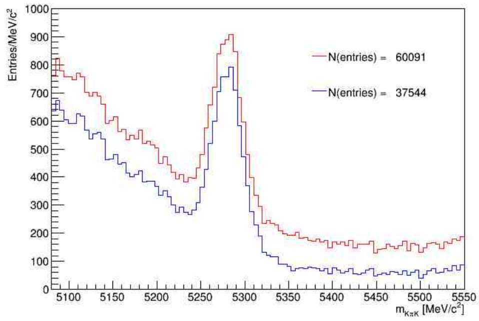

(B)

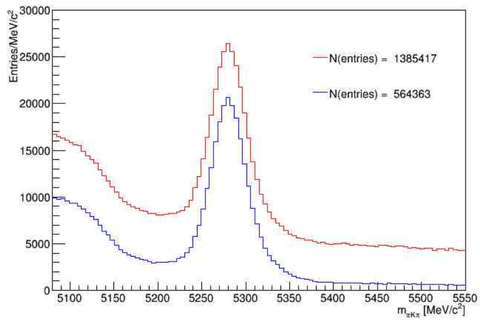

(C)

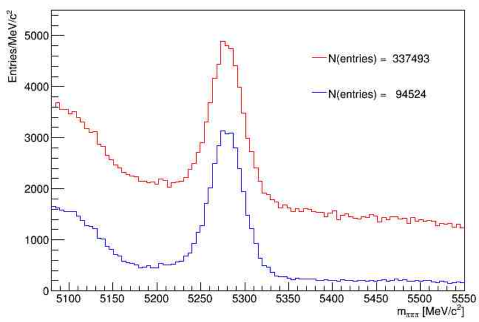

(D)

FIGURE 4.4: Invariant B mass distribution before (red line) and after (blue) the BDT selection for the optimization specific for each channel in (A) $B^{\pm} \to K^{+}K^{\pm}K^{-}$, (B) $B^{\pm} \to K^{+}\pi^{\pm}K^{-}$, (C) $B^{\pm} \to K^{+}\pi^{\pm}K^{-}$ and (D) $B^{\pm} \to \pi^{+}\pi^{\pm}\pi^{-}$.

4.9.1 $B^{\pm} \to K^{+}K^{\pm}K^{-}$

This mode has the second largest branching fraction in comparison with the four $B^{\pm} \to h^{+}h^{\pm}h^{-}$ decays channel, and only with the BDT requirement the signal is very clean, as can be seen in Figure 4.4(a). The main cross-feed comes from the $B^{\pm} \to \pi^{+}K^{\pm}\pi^{-}$ mode, but only tiny fraction of these misidentified candidates lie within the signal region. For this reason, there is no need of stringent PID requirement and the same PID requirement used in the Run I analysis [2] is kept, which is applied `ProbNNk`>0.2 for the three final state particles. The $B^{\pm} \to K^{+}K^{\pm}K^{-}$ final spectrum is shown in Figure 4.5(a).

4.9.2 $B^{\pm} \to K^{+}\pi^{\pm}K^{-}$

The main cross-feed contributions in this mode are:

- cross-feed from $B^{\pm} \to K^{+}K^{\pm}K^{-}$: when the pion is mis-identified as a kaon.
- cross-feed from $B^{\pm} \to \pi^{+}K^{\pm}\pi^{-}$: when one of the kaons is mis-identified as a pion.

To suppress the $B^{\pm} \to \pi^{+}K^{\pm}\pi^{-}$ cross-feed negative requirements have to be made on the pion hypothesis variable, `ProbNNpi`, to all kaon candidate. Whereas to reduce the $B^{\pm} \to K^{+}K^{\pm}K^{-}$ cross-feed, negative requirements have to be made on the kaon hypothesis variable, `ProbNNk`, to the pion candidate.

Channel	BDT selection cuts
$B^{\pm} \to \pi^{+}\pi^{\pm}\pi^{-}$	$>$ -0.03
$B^{\pm} \to \pi^{+}K^{\pm}\pi^{-}$	$>$ -0.03
$B^{\pm} \to K^{+}\pi^{\pm}K^{-}$	$>$ -0.07
$B^{\pm} \to K^{+}K^{\pm}K^{-}$	$>$ -0.15
common	$>$ -0.05

TABLE 4.4: Cuts on the BDT output variable for each cannel specific optimization and for the optimization common to all channels.

To determine the negative requirements, the $B^{\pm} \to K^{+}\pi^{\pm}K^{-}$ sample is used. To evaluate PID cuts to reduce the $B^{\pm} \to K^{+}K^{\pm}K^{-}$ contribution, $B^{+} \to K^{+}K^{+}K^{-}$ sample from $B^{\pm} \to K^{+}\pi^{\pm}K^{-}$ is used. By applying various negative PID requirements on the variable `ProbNNk` to pion candidate and analysing the evolution of the sample with cuts, it was found that the requirement `ProbNNk`<0.1 eliminates most of $B^{\pm} \to K^{+}K^{\pm}K^{-}$ contribution. Plot showing the impact of each tested negative cut on the sample is presented in Figure B.1 in Appendix B.

$B^{+} \to \bar{D}^{0}(\to K^{+}\pi^{-})\pi^{+})$ from $B^{\pm} \to K^{+}\pi^{\pm}K^{-}$ is used to determine the PID requirement in order to control the $B^{\pm} \to \pi^{+}K^{\pm}\pi^{-}$ cross-feed. This contamination is controlled by applying various negative PID requirements on the variable `ProbNNpi` to the kaon candidates. After test a set of requirements it was found that `ProbNNpi`< 0.2 is the most efficient to reduce the $B^{\pm} \to \pi^{+}K^{\pm}\pi^{-}$ contribution. A plot showing the impact of each cut on the sample is presented in Figure B.2 in Appendix B.

For the affirmative requirements, the $B \to \bar{D}^{0}(\to K^{+}K^{-})\pi^{+})$ signal is used after applying the negative PID requirements. Several affirmative cuts on the variable `ProbNNk` to kaon candidates and on the variable `ProbNNpi` to the pion candidate are applied simultaneously to this sample, which is shown in Figure B.3 in Appendix B. It was found that d1_`ProbNNk`>0.4, d3_`ProbNNk`>0.6 and d2_`ProbNNpi`>0.7 are the most efficient to a positive identification. The cross-feed is then controlled by combining both requirements. A summary is presented in Table 4.5. In Figure 4.5(b) is shown the $B^{\pm} \to K^{+}\pi^{\pm}K^{-}$ spectrum after apply the PID requirements.

4.9.3 $B^{\pm} \to \pi^{+}K^{\pm}\pi^{-}$

This mode has the largest branching fraction and after the BDT requirement, the signal is very clean, as can be seen from Figure 4.4(c). The main cross-feeds are $B^{\pm} \to K^{+}\pi^{\pm}K^{-}$ and $B^{\pm} \to \pi^{+}\pi^{\pm}\pi^{-}$ decay, which have lower branching fractions, therefore there is no need of tight requirements and the same PID requirement used in the Run 1 analysis [2] is kept, which are `ProbNNpi`>0.25 and `ProbNNk`<0.5 for pions and `ProbNNk`>0.2 for the kaon candidate. The mass spectrum after applying requirements is shown in Figure 4.5(c).

4.9.4 $B^{\pm} \to \pi^{+}\pi^{\pm}\pi^{-}$

The main cross-feed in the $B^{\pm} \to \pi^{+}\pi^{\pm}\pi^{-}$ is the decay $B^{\pm} \to \pi^{+}K^{\pm}\pi^{-}$, when the kaon is misidentified as pion and then populated the $B^{\pm} \to \pi^{+}\pi^{\pm}\pi^{-}$ spectrum. It is possible to control this cross-feed by applying cuts on the pion candidates with the same charge.

To determine the negative PID requirement, the $B \to \bar{D}^{0}(\to K^{+}\pi^{-})\pi^{-})$ signal from candidates selected as $B^{\pm} \to \pi^{+}\pi^{\pm}\pi^{-}$ is used. The BDT selection, muon and J/ψ vetoes are applied to the samples. By evaluating the impact of different negative

Decay	Daughter	PID selection cuts
$B^{\pm} \to K^{+}K^{\pm}K^{-}$	all	ProbNNk > 0.2
$B^{\pm} \to \pi^{+}K^{\pm}\pi^{-}$	pions	ProbNNpi > 0.25 & ProbNNk < 0.5
	Kaon	ProbNNk > 0.2
$B^{\pm} \to K^{+}\pi^{\pm}K^{-}$	Kaons	d1_ProbNNk > 0.4 & d3_ProbNNk > 0.6 & ProbNNpi < 0.2
	Pion	ProbNNpi > 0.7 & ProbNNk < 0.05
$B^{\pm} \to \pi^{+}\pi^{\pm}\pi^{-}$	all	ProbNNpi > 0.5 & ProbNNk < 0.1

TABLE 4.5: PID selection criteria for $B^{\pm}$ decays.

cuts on the pion candidates, and it was found that the requirement `ProbNNk` <0.1 has the better performance to reduce the mis-identification of kaon as a pion. The same cut is applied to pion candidate with odd charge. The plot distribution for each negative cut applied can be found in the Figure B.4 (a) of the Appendix B.

To estimate the impact of affirmative PID cuts on the $B^{\pm} \to \pi^{+}\pi^{\pm}\pi^{-}$ signaL, the $B \to \bar{D}^{0}(\to \pi^{+}\pi^{-})\pi^{-})$ signal is used. By applying the requirement `ProbNNk` <0.1 in all tracks and the selection described above, the $\pi^{+}\pi^{-}$ invariant mass distribution from $B^{\pm} \to \pi^{+}\pi^{\pm}\pi^{-}$ candidates is analysed, by looking at the D^{0} region. After different affirmative PID cuts being it was found `ProbNNpi`>0.5 requirement for all pion candidates has the better performance. It is shown in Figure B.4 (b) of the Appendix B. In the Figure 4.5(d) can be found a comparison before and after the final PID requirements. The list of cuts is summarised in Table 4.5.

4.10 Removing charmed background contribution

Even after the explicit veto on D^{0} and final PID requirements, misidentified D^{0} contributions from $B^{\pm} \to Dh^{\pm}$ candidates pass through the selection. To eliminate those contributions vetoes of ± 35 MeV/c around D^{0} mass are applied. It is summarised below:

- $B^{+} \to K^{+}K^{+}K^{-}$ receives contributions from $B^{+} \to D^{0}K^{+}$, where $D^{0} \to K^{+}K^{-}$. Thus a D^{0} veto is applied on the $K^{+}K^{-}$ invariant mass. Due to the mis-identification of a kaon as a pion, it is removed the region around D^{0} mass on the $K^{+}\pi^{-}$ invariant mass mis-identification hypothesis.

- $B^{+} \to K^{+}\pi^{+}K^{-}$ receives contribution from both $B^{+} \to D^{0}K^{+}$, with $D^{0} \to K^{+}\pi^{-}$ and $B^{+} \to D^{0}\pi^{+}$, with $D^{0} \to K^{+}K^{-}$ The veto is applied on the $K^{+}\pi^{-}$ and $K^{+}K^{-}$ invariant mass. The mis-identification contribution is negligible.

- $B^{+} \to \pi^{+}K^{+}\pi^{-}$ also receives contribution from both $B^{+} \to D^{0}K^{+}$, where $D^{0} \to pi^{+}\pi^{-}$ and $B^{+} \to D^{0}\pi^{+}$, where $D^{0} \to K^{+}\pi^{-}$. The D^{0} veto is applied on $K^{+}\pi^{-}$ and $\pi^{+}\pi^{-}$ invariant mass. To remove the mis-identification of a kaon as a pion, a veto is applied on $K^{+}K^{-}$ and $\pi^{+}\pi^{-}$ invariant mass mis-identification hypothesis.

- $B^{+} \to \pi^{+}\pi^{+}\pi^{-}$ receives contributions from , with $D^{0} \to \pi^{+}\pi^{-}$, thus the veto is applied on the $\pi^{+}\pi^{-}$ invariant mass. To remove mis-identification of a pion as a kaon, the veto is applied on the $K^{+}\pi^{-}$ invariant mass mis-identification hypothesis.

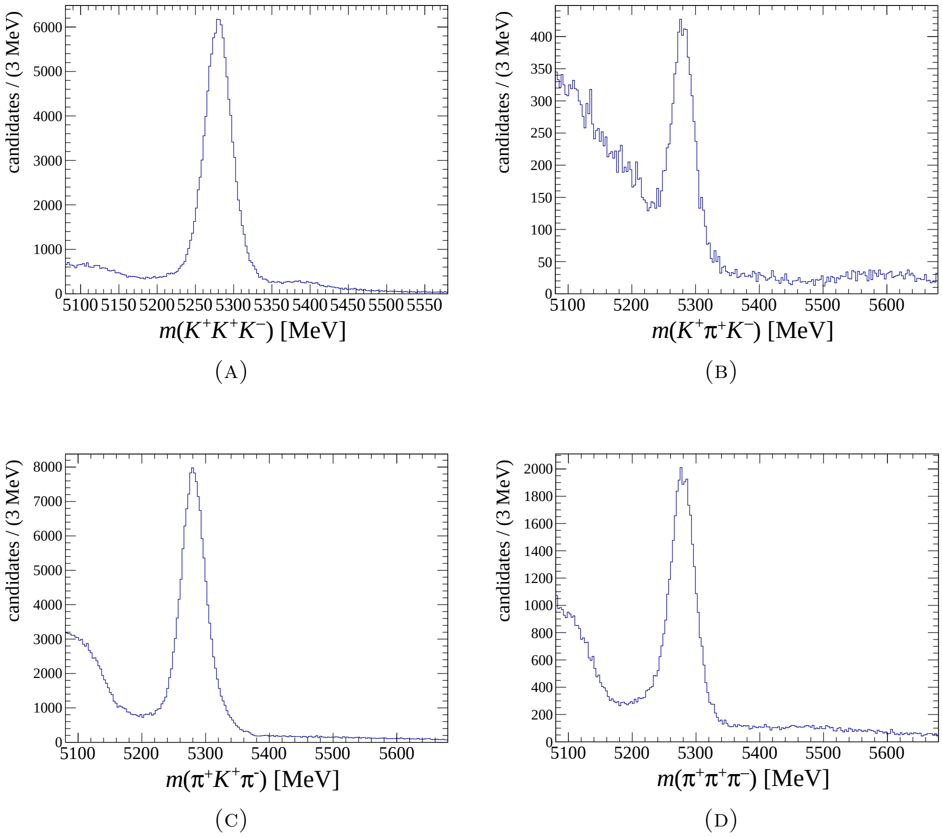

FIGURE 4.5: Invariant B mass distribution with PID final requirement in (A) $B^\pm \to K^+K^\pm K^-$, (B) $B^\pm \to K^+\pi^\pm K^-$, (C) $B^\pm \to K^+\pi^\pm K^-$ and (D) $B^\pm \to \pi^+\pi^\pm\pi^-$.

4.11 The remaining background contributions

After the final selection, some background contributions are still present in the signal spectrum and thus for the determination of the signal yields, each contribution must be taken into account in invariant B mass fit. Below it is described the remaining background contributions that will be modelled in the fit.

4.11.1 Background contributions to $B^\pm \to K^+K^\pm K^-$

- Partially reconstructed: the largest contributions comes from modes with a missing π^0. The main contribution is from $B^\pm \to K^{*\pm}K^+K^-$, $K^{*\pm} \to K^\pm\pi^0$ with a combined branching fraction of 1.8×10^{-5}.
- Cross-feed contribution from $B^\pm \to \pi^+K^\pm\pi^-$ and $B^\pm \to K^+\pi^\pm K^-$ decays.

4.11.2 Background contributions to $B^\pm \to \pi^+K^\pm\pi^-$

- Partially reconstructed backgrounds: the most relevants channels for this case are the $B^\pm \to \bar{D}^0(D^0)\pi^\pm$, $\bar{D}^0(D^0) \to K^\pm\pi^\mp\pi^0$ with a combined branching fraction of 6.67×10^{-4} $B^\pm \to K^{*\pm}\pi^+\pi^-$, $K^{*\pm} \to K^\pm\pi^0$ with a combined branching fraction of 7.49×10^{-5};

- $B^\pm \to \eta' K^\pm$, $\eta' \to \rho^0\gamma$ and $\rho^0 \to \pi^+\pi^-$ with a combined branching fraction of 2.05×10^{-5}, in which a photon is lost. Its shape was obtained from the analysis of the Ref. [65] to be fixed in the fit to data.

- Cross-feed contributions from $B^\pm \to \pi^+\pi^\pm\pi^-$ and $B^\pm \to K^+\pi^\pm K^-$ decays.

4.11.3 Background contributions to $B^\pm \to K^+\pi^\pm K^-$

- Partially reconstructed backgrounds: B_s^0 decays with a missed charged pion, including $B_s^0 \to D_s^-(K^+K^-\pi^-)\pi^+$, $B_s^0 \to \overline{K}^{*0}K^{*0}$ and possibly other modes; and B decays with a missed charged or neutral pion, including $B^0 \to D^-(K^+K^-\pi^-)\pi^+$, $B^\pm \to D^0(K^+K^-\pi^0)\pi^\pm$, $B^\pm \to K^{*\pm}(K^\pm\pi^0)\pi^\pm K^\mp$ and $B^0 \to K^+K^-\pi^+\pi^-$. The shape of B_s^0 partially reconstructed background contribution was obtained from the analysis of the Ref. [65], which is then fixed in the fit to data.

- Cross-feed contributions from $B^\pm \to K^+K^\pm K^-$ and $B^\pm \to \pi^+K^\pm\pi^-$ decays.

4.11.4 Background contributions to $B^\pm \to \pi^+\pi^\pm\pi^-$

The two main decay channels that contribute in the $B^\pm \to \pi^+\pi^\pm\pi^-$ mass spectrum as backgrounds are the cross-feed from $B^\pm \to \pi^+K^\pm\pi^-$ and the partially reconstructed background $B^\pm \to \pi^\pm\pi^+\pi^-\pi^0$.

4.12 $B^\pm$ invariant mass fit

The key information for the $\mathcal{A}_{CP}$ measurement is the event yield extracted from the B mass fit of the signals and backgrounds. In this section, it is provided the fits for the four decay channels.

The total signal yields and raw asymmetries $A_{\rm raw}$ are extracted from a simultaneous unbinned extended maximum likelihood fit of the B^+ and B^- invariant mass distributions in the range $5080-5580$ MeV$/c^2$.

4.12.1 Fit model

We perform a simultaneous unbinned extended maximum likelihood fit to the invariant masses of the B^+ and B^- mass distribution. The probability density functions (PDF) are implemented and fitted using the RooFit C++ data modelling package [66]. The mass fit model ($F^\pm$) for B$^\pm$ events samples is defined as:

$$F^\pm = \left[\frac{N_S}{2}(1 \mp A_{\rm raw})\right] F_S^\pm + \tag{4.8}$$

$$+\left[\frac{N_{comb}}{2}\left(1 \mp A_{raw}^{comb}\right)\right] F_{comb}^\pm + \tag{4.9}$$

$$+\sum_{i=1}\left[\frac{(f_{bkg_i}N_S)}{2}\left(1 \mp A_{raw}^{bkg_i}\right)\right] F_{bkg_i}^\pm \tag{4.10}$$

where $A_{\rm raw}$ is the term related to the CP asymmetry (including also detection and production asymmetries) of the decay channel, $A_{raw}^{bkg_i}$ is related to the charge asymmetry of the peaking background component, A_{raw}^{comb} is related to asymmetry that can exist in the combinatorial background, N_S is the total number of signal events, N_{comb} is the total number of combinatorial background events and F is used to define the PDF function (F_S for signal, F_{comb} for combinatorial and F_{bkgi} for peaking and partial background). The sum in i is used to indicate the peaking or partially reconstructed background component.

4.12.2 Signal fit model

$B^{\pm} \to h^{+}h^{\pm}h^{-}$ decays are affected by radiative energy loss and detector resolution effects. Thus, the signal fit model uses the Crystal Ball functions, that account for both effects.

The Crystal Ball function ($CB(m;\mu,n,a,\sigma)$ [67] consists of a Gaussian with an exponential tail that starts at a sigma away from the mean of the Gaussian, and a n parameter that controls the exponential slope. It is used to describe the typical low-mass tail as well as the subtle high-mass suppression due to radiative decays. It is defined as:

$$CB(m;\mu,n,a,\sigma) = \begin{cases} \exp\left(-\frac{1}{2}t^2\right), & \text{se} \quad (t \geq -|a|) \\ \left(\frac{A}{(B-t)^n}\right), & \text{se} \quad (t < -|a|) \end{cases} \tag{4.11}$$

where

$$t = \frac{m-\mu}{\sigma}, \qquad A = \left(\frac{n}{|a|}\right)^2 \exp(-\frac{1}{2}|a|^2) \quad \text{e} \quad B = \frac{n}{|a|} - |a| \tag{4.12}$$

The μ parameter represents the mean of the Crystal Ball and σ is the width. The parameters a and n were determined from the fit to the signal MC sample and fixed in the data fit.

The signal fit model uses two Crystal-Ball ($CB_1(m;\mu_1,n_1,a_1,\sigma_1)$ and $CB_2(m;\mu_2,n_2,a_2,\sigma_2)$) for the signal PDF ($F_S^{\pm}$), with common parameters for the B^+ and B^- samples. These functions are combined as follow, where f_{CBs} are the Crystal-Ball fractions,

$$\begin{aligned} F_S^+ = F_S^- &= f_{CBs} \cdot CB_1(m;\mu_1,n_1,a_1,\sigma_1) \\ &\quad +(1-f_{CBs}) \cdot CB_2(m;\mu_2,n_2,a_2,\sigma_2). \end{aligned} \tag{4.13}$$

4.12.3 Background fit models

The background which could not be eliminated by the selection have to be modelled in the mass fit. The remaining contribution involved are: combinatorial background, partially reconstructed background and signal cross-feed.

Combinatorial background

The combinatorial background is parametrized with an exponential PDF

$$F_{comb}(m;b) = \exp\left[b \cdot (m - 5080\,\text{MeV}/c^2)\right], \tag{4.14}$$

with one free parameter b for the slope.

Partially-reconstructed background

The partially reconstructed backgrounds are parametrized by an Argus function [68], convolved with a Gaussian resolution. The Argus function has the form:

$$\mathcal{A}(m;m_t,c,p) = \frac{2^{-p}c^{2(p+1)}}{\Gamma(p+1) - \Gamma(p+1,c^2/2)} \cdot \frac{m}{m_t^2}\left(1 - \frac{m^2}{m_t^2}\right)^p \exp\left[-\frac{1}{2}c^2(1 - \frac{m^2}{m_t^2})\right] \tag{4.15}$$

	Fraction from MC
Cross-feed contributions to $B^{\pm} \to K^{+}K^{\pm}K^{-}$ mode	
$B^{\pm} \to \pi^{+}K^{\pm}\pi^{-}$	0.035 ± 0.003
$B^{\pm} \to K^{+}\pi^{\pm}K^{-}$	0.021 ± 0.003
Cross-feed contributions to $B^{\pm} \to K^{+}\pi^{\pm}K^{-}$ mode	
$B^{\pm} \to K^{+}K^{\pm}K^{-}$	0.054 ± 0.009
$B^{\pm} \to \pi^{+}K^{\pm}\pi^{-}$	0.098 ± 0.016
$B^{\pm} \to \pi^{+}\pi^{\pm}\pi^{-}$	0.003 ± 0.0006
Cross-feed contributions to $B^{\pm} \to \pi^{+}K^{\pm}\pi^{-}$ mode	
$B^{\pm} \to K^{+}K^{\pm}K^{-}$	0.027 ± 0.002
$B^{\pm} \to K^{+}\pi^{\pm}K^{-}$	0.012 ± 0.002
$B^{\pm} \to \pi^{+}\pi^{\pm}\pi^{-}$	0.1 ± 0.011
Cross-feed contributions to $B^{\pm} \to \pi^{+}\pi^{\pm}\pi^{-}$ mode	
$B^{\pm} \to \pi^{+}K^{\pm}\pi^{-}$	0.029 ± 0.003
$B^{\pm} \to K^{+}\pi^{\pm}K^{-}$	negligible

TABLE 4.6: Estimation of the fraction of the cross-feed contributions for each of $B^{\pm} \to h^{+}h^{\pm}h^{-}$ modes.

with three parameters for the mass threshold m_t upper limit, the curvature c and the power p which controls the falling of its slope. The threshold parameter is fixed to the difference between the B and pion masses, and the Gaussian resolution is fixed to that of the signal. The rest of the Argus shape parameters, as well as its fractional yield with respect to the signal, are left free in the fit.

Signal cross-feed

The shape of the cross-feed from other $B^{\pm} \to h^{+}h^{\pm}h^{-}$ decays is parametrized with the same PDF function as the signal, i.e. two Crystall functions. The parameters are determined from the MC and fixed in the fit.

The number of events which belong to a given background can be estimated as $N^{bkg} = f_{bkg}N_S$, the label S stands for the signal, bkg for the related background and f_{bkg} is the fraction of the background component, calculated from:

$$f_{bkg} = \frac{N_{bkg}}{N_S} = \frac{\mathcal{B}_{bkg}}{\mathcal{B}_S} \times \frac{\epsilon_{bkg}}{\epsilon_S} \tag{4.16}$$

where $\mathcal{B}_{bkg}$ and $\mathcal{B}_S$ are the branching fraction taken from the PDG and ϵ_{bkg} and ϵ_S are the efficiencies which the background and the signal MC samples. The efficiencies are estimated from the fraction of MC samples that passed all the selection criteria. The ϵ_S is the ratio between the number of signal MC events after all selection criteria and the number of generated events. The efficiency ϵ_{bkg} is the ratio between the number of background MC events after all selection criteria and the number of generated background events.

The decay modes that can contribute due to a single or double mis-identification of pion/kaon and its correspondent fraction are listed in Table 4.6, and their fitted distribution in the reconstructed B mass, as determined from simulation, are shown in Figures 4.6, 4.7, 4.8 and 4.9. The fraction of a given cross-feed contribution in the final sample is fixed to the estimate value in the mass fit.

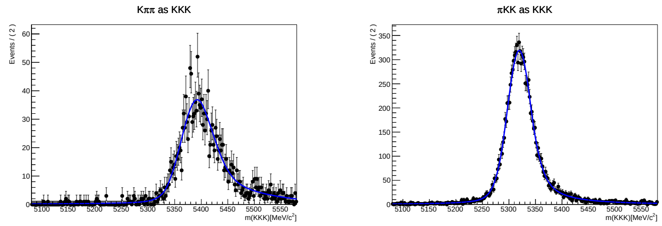

(A) (B)

FIGURE 4.6: Fits to the reconstructed m(KKK) distributions obtained from MC samples that passed the selection criteria for each cross-feed contribution to $B^{\pm} \to K^{+}K^{\pm}K^{-}$ mode. (A) $B^{\pm} \to \pi^{+}K^{\pm}\pi^{-}$ and (B) $B^{\pm} \to K^{+}\pi^{\pm}K^{-}$

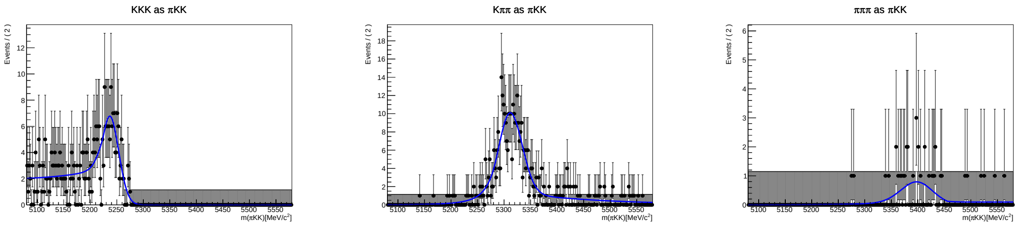

(A) (B) (C)

FIGURE 4.7: Fits to the reconstructed m(πKK) distributions obtained from MC samples that passed the selection criteria for each cross-feed contribution to $B^{\pm} \to K^{+}\pi^{\pm}K^{-}$ mode. (A) $B^{\pm} \to K^{+}K^{\pm}K^{-}$, (B) $B^{\pm} \to \pi^{+}K^{\pm}\pi^{-}$ and (C) $B^{\pm} \to \pi^{+}\pi^{\pm}\pi^{-}$.

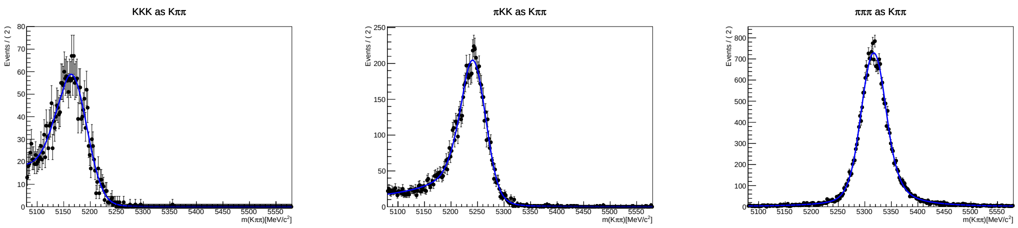

(A) (B) (C)

FIGURE 4.8: Fits to the reconstructed m($K\pi\pi$) distributions obtained from MC samples that passed the selection criteria for each cross-feed contribution to $B^{\pm} \to \pi^{+}K^{\pm}\pi^{-}$ mode. (A) $B^{\pm} \to K^{+}K^{\pm}K^{-}$, (B) $B^{\pm} \to K^{+}\pi^{\pm}K^{-}$ and (C) $B^{\pm} \to \pi^{+}\pi^{\pm}\pi^{-}$

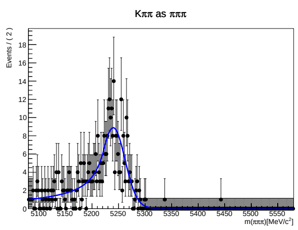

(A)

FIGURE 4.9: Fits to the reconstructed m($\pi\pi\pi$) distributions obtained from MC samples that passed the selection criteria for each cross-feed contribution to $B^{\pm} \to \pi^{+}\pi^{\pm}\pi^{-}$ mode. (A) $B^{\pm} \to \pi^{+}K^{\pm}\pi^{-}$

2015+2016 data sample	Yield (N_S)	$A_{\rm raw}$
$B^\pm \to \pi^+K^\pm\pi^-$	226475 ± 634	+0.005 ± 0.002
$B^\pm \to K^+K^\pm K^-$	110002 ± 367	-0.057 ± 0.003
$B^\pm \to \pi^+\pi^\pm\pi^-$	30729 ± 221	+0.089 ± 0.007
$B^\pm \to K^+\pi^\pm K^-$	9373 ± 147	-0.157 ± 0.013
2011+2012 data sample [65]	Yield (N_S)	$A_{\rm raw}$
$B^\pm \to \pi^+K^\pm\pi^-$	181074 ± 556	+0.010 ± 0.002
$B^\pm \to K^+K^\pm K^-$	109240 ± 354	-0.056 ± 0.003
$B^\pm \to \pi^+\pi^\pm\pi^-$	24907 ± 222	+0.074 ± 0.008
$B^\pm \to K^+\pi^\pm K^-$	6161 ± 172	-0.135 ± 0.017

TABLE 4.7: Signal yields (N_S) and A_{raw} extracted from the mass fit to the 2015+2016 data. For comparison, it is presented N_S) and A_{raw} extracted from the mass fit to the 2011+2012 data [65].

4.12.4 Fit Results

The mass fit plots of B^+ and B^- samples are shown in Figures 4.10 and 4.11 for the $B^\pm \to \pi^+K^\pm\pi^-$, $B^\pm \to K^+K^\pm K^-$, $B^\pm \to \pi^+\pi^\pm\pi^-$ and $B^\pm \to K^+\pi^\pm K^-$ performed with 2015 and 2016 data samples.

In Figure 4.10(A) is shown the invariant mass fit of $B^- \to \pi^+K^-\pi^-$ on the left and $B^+ \to \pi^+K^+\pi^-$ on the right , where it can be seen the relevant background contribution: combinatorial background (in dotted-dashed line), $B \to$4-body partially reconstructed background (light green line), the background due to mis-identification of kaon as pion $B^\pm \to \pi^+\pi^\pm\pi^-$ and the $B^\pm \to \eta'(\rho^0\gamma)K^\pm$ contribution. The total signal yield obtained is about 220 k candidates, which corresponds to a increase of 25% in the signal yield in comparison with result from Run I data.

In Figure 4.10 (B) shows the invariant mass fit of $B^- \to K^+K^-K^-$ on the left and $B^+ \to K^+K^+K^-$ on the right with the combinatorial and partially reconstructed background. Due to the very low contributions of the $B^\pm \to K^+\pi^\pm K^-$ and $B^\pm \to \pi^+K^\pm\pi^-$ cross-feed, they are only visible in the logarithmic plot as shown in Figure C.1 (B) in the Appendix C. The total signal yield is about 110 k which correspond to same statistics from the Run I, shown in Table 4.7.

For the $B^\pm \to \pi^+\pi^\pm\pi^-$ decay channel, the Figure 4.11 (A) shows the invariant mass fit for $B^- \to \pi^+\pi^-\pi^-$ on the left and $B^+ \to \pi^+\pi^+\pi^-$ on the right. In the green filled curve, it shows a significant contribution from partially reconstructed and in red the cross-feed contribution from $B^\pm \to \pi^+K^\pm\pi^-$ due to mis-identification of kaon as a pion. The total signal yield is about 30 k candidates, that corresponds to a increase of 20% in the signal yield in comparison with the previous analysis.

The invariant mass fit of the $B^\pm \to K^+\pi^\pm K^-$ channel is shown in Figure 4.11 (B). The partially reconstructed background of both the B and B_s decay modes have a significant contribution, as shown in light green dotted-dashed line and green filled curves. The background contribution due to the mis-identification of pions and kaons are shown in red for the $B^\pm \to \pi^+K^\pm\pi^-$ cross-feed and in cyan for the $B^\pm \to K^+K^\pm K^-$ cross-feed. The total signal yields is around 10 k candidates in total, which is almost 2 times greater than the signal yields obtained with Run I data.

The total signal yield (N_S) and the raw asymmetry($A_{\rm raw}$) obtained with 2015 and 2016 samples for each decay channel are listed in Table 4.7. Logarithmic plots and residuals as well as the complete fit results for each channels can be found in Appendix C.

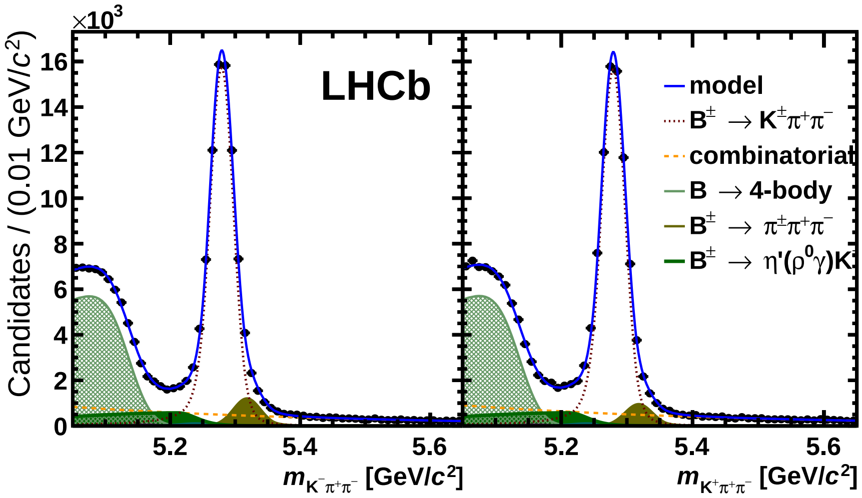

(A) $B^{\pm} \to \pi^{+} K^{\pm} \pi^{-}$

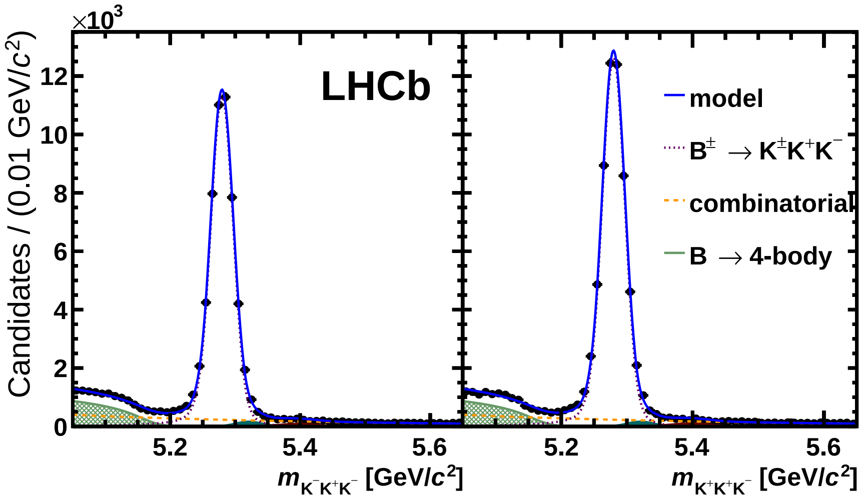

(B) $B^{\pm} \to K^{+} K^{\pm} K^{-}$

FIGURE 4.10: Results for the fits to the invariant mass distribution of reconstructed $B^{\pm}$ for full 2015 and 2016 data sample. In each pair of distributions, the plot on the left B^{-} and on the right B^{+}.

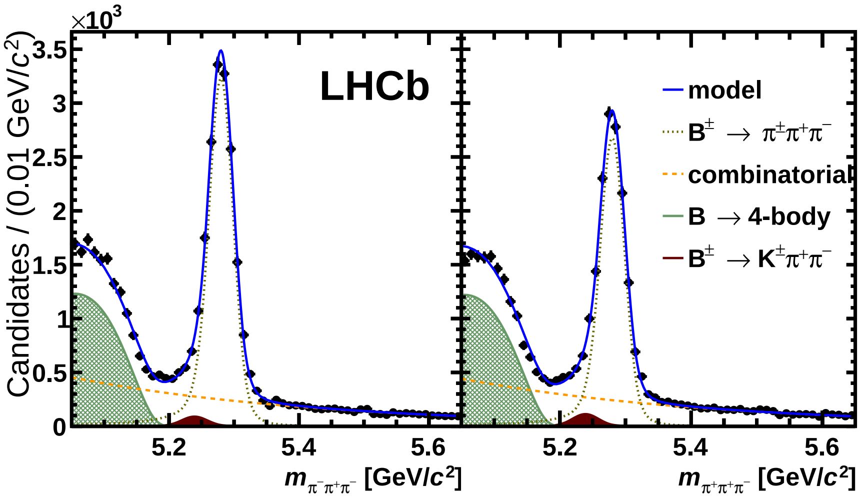

(A) $B^{\pm} \to \pi^{+}\pi^{\pm}\pi^{-}$

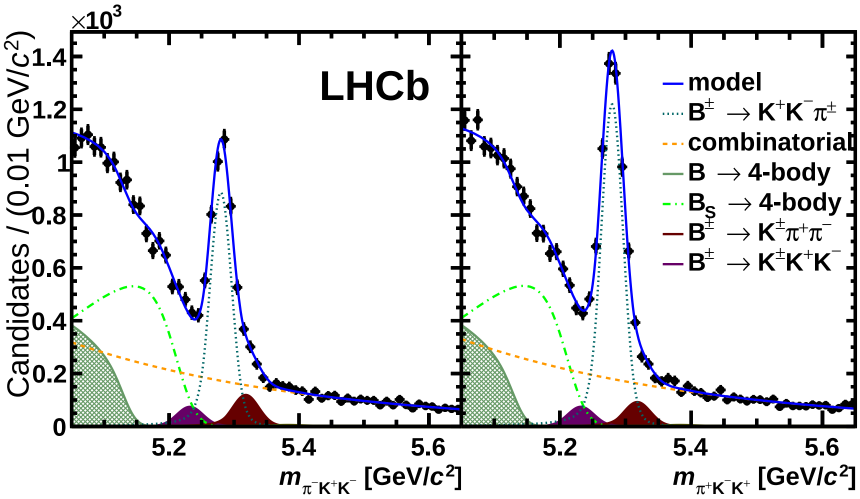

(B) $B^{\pm} \to K^{+}\pi^{\pm}K^{-}$

FIGURE 4.11: Results for the fits to the invariant mass distribution of reconstructed $B^{\pm}$ for full 2015 and 2016 data sample. In each pair of distributions, the plot on the left B^{-} and on the right B^{+}.

4.13 Phase-space acceptance

Three-body decays are dominated for several intermediate contributions, which can interfere with each other leading to structures in the phase-space. Those structures are related to the dynamics of the decay, which is not known a priori and thus not well represented by the simulation. In addition, the selection cuts can distorts the signal, which leads to a non-uniform efficiency and A_{raw} distribution across the Dalitz plot. As the signal efficiency may be not correctly represented in MC simulation, an acceptance correction needs to be performed.

A common feature of $B^{\pm} \to h^{+}h^{\pm}h^{-}$ decays is that both the signal events and the background events populate the kinematic boundaries of the Dalitz plot. Thus, the variation of the efficiency occurring over small areas of the Dalitz plot become difficult to describe in detail. A solution that was adopted by some analyses is to apply a transformation to the kinematic variables that maps the Dalitz plot into a rectangle: the so-called *square Dalitz plot* (SDP). Such transformation improve the resolution in the areas with great variation of efficiency by expanding the corner and the border of the Dalitz plot relative to the less populated region. Thus the phase-space acceptance correction is performed by obtaining the acceptance maps in the SDP representation.

4.13.1 Square Dalitz Plot

$B^{\pm} \to h^{+}h^{\pm}h^{-}$ decays are dominated by resonates states which lead to a non uniform event distribution in the Dalitz plot. Most resonances that contribute to these decays have low mass relative to the B mass and thus populate the boundaries of the Dalitz plot region, (which can be seen in Figure X where the events are concentrated in the borders and corners of DP and less events in the central region). Those regions are great of interest since interference effects, which are responsible for the CP violation, occur in those regions. In order to expand these regions in relation to the central area, a coordinate transformation of the standard Dalitz plot to a square Dalitz plot [69] [70] is performed:

$$dm_{ij}^2 dm_{kj}^2 \to |detJ| dm' d\theta' \tag{4.17}$$

where J is the Jacobian of the transformation and m' and θ' ,the square Dalitz plot coordinates, defined as:

$$m' = \frac{1}{\pi} \arccos\left(2\frac{m_{ij} - m_{ij}^{min}}{m_{ij}^{max} - m_{ij}^{min}} - 1\right) \tag{4.18}$$

$$\theta' = \frac{1}{\pi}\theta_{ij} \tag{4.19}$$

where $m_{ij}^{max} = (m_B - m_k)$ and $m_{ij}^{min} = (m_i + m_j)$, which represent the kinematic limits permitted in the decay, and θ' is the helicity angle defined in Section X. Those new variables are dimensionless and range from 0 to 1. Figure 4.12 show a comparison with the standard Dalitz plot (left) and the SDP one (right) with the highlighted regions mapped after m' and θ' transformation.

4.13.2 Acceptance correction

For each decay channel, the acceptances maps are obtained in the SDP representation for B^{+} and B^{-} MC samples separately, and each $B^{\pm}$ acceptance histograms are built

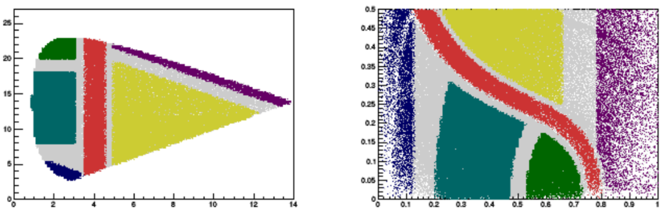

(A) $B^{\pm} \to K^{+}K^{\pm}K^{-}$

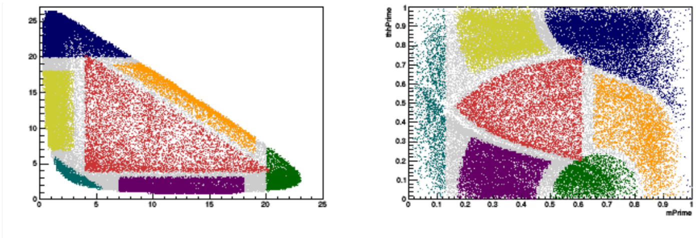

(B) $B^{\pm} \to K^{+}\pi^{\pm}K^{-}$

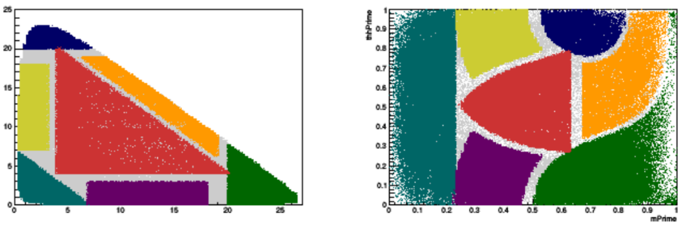

(C) $B^{\pm} \to \pi^{+}K^{\pm}\pi^{-}$

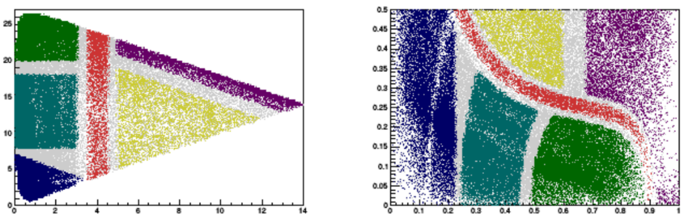

(D) $B^{\pm} \to \pi^{+}\pi^{\pm}\pi^{-}$

FIGURE 4.12: Dalitz Plot view on the left, and SDP view on the right for each decay channel.

up from the following individual contribution:

- **Year**: The acceptance maps are generated separated by year (2015 and 2016) to taking into account the difference between the two data taking.
- **Polarity**: The acceptance maps are obtained separately for each magnet polarity to taking into account the left-right asymmetry of the detector.
- **Trigger configuration**: This separation is performed in order to apply the trigger correction. The correction need to be performed due to differences between the `L0Hadron_TOS` trigger efficiency in data and MC simulation. As the correction is needed to be applied on MC subsamples TOS and TISnotTOS, the maps are generated separetely for each trigger subsample. Although in this thesis no trigger corrections is performed, it was chosen to keep this separation as the analysis will be improved by including all data collected by the LHCb.

The acceptance maps of each subsample are generated with reconstructed MC sample with kinematics, trigger and TrueID cuts, corrected by the efficiency weights for the detection asymmetries and PID cuts divided by a flat generated MC:

$$Acc_{B^{\pm}} = \frac{Histo^{final}_{B^{\pm}}}{Histo^{GEN}_{B^{\pm}}} \tag{4.20}$$

where,

- $Histo^{final}_{B^{\pm}}$: Binned histogram of the reconstructed large MC samples generated flat in SDP, reported in Table 4.2, with selection requirements and corrections.
- $Histo^{GEN}_{B^{\pm}}$: Binned histogram of large simulated samples generated around the solid angle 4π, with no cuts at the generator level to reproduce the phase-space distribution before any acceptance and selection cuts, then scaled to the total estimated number of generated MC.

The binning scheme was chosen to be 15×15 bins in the square Dalitz plot representation.

4.13.3 PID efficiency

Since the PID variables are not well described in MC simulation PID efficiency is obtained through a package called PIDCalib. The package provide the PID efficiency for the PID selection in Table 4.5 by using *golden decay* samples produced in the experiment that were reconstructed without the RICH detector. The efficiency is obtained as weight for each final state track and each magnet polarity, and then added event per event in the acceptance maps. The PIDCalib implementation scheme used is standard and detailed in References [71, 65].

4.13.4 Detection asymmetries correction

For each decay channel the kaon and pion detection asymmetries are included as a weight in the acceptance maps correction event per event. The detection asymmetry weight, $w_i^{A_D}$ for each event i is given by

$$w_i^{A_D}(h^+h^{'+}h^-) = (1 + A_D(h^+))(1 + A_D(h^{'+}))(1 - A_D(h^-)) \tag{4.21}$$

and for its complex conjugate

$$w_i^{A_D}(h^-h^{'-}h^+) = (1 - A_D(h^-))(1 - A_D(h^{'-}))(1 + A_D(h^+)) \tag{4.22}$$

where $A_D(h = K, \pi)$ is the kaon and pion detection asymmetry.

Kaon detection asymmetry

It is known that the interaction of kaons with the detector can be different for K^+ and K^-. This asymmetry is dependent on the momentum and lead to difference in $K^{\pm}$ detection efficiency [59]. Therefore, $A_D(K^{\pm})$ is measured in different ranges of kaon momentum. The method to determine the asymmetry is the same as the one described in [58], which uses the following definitions of $A_D(K^{\pm})$:

$$A_D(K^-) = A_D(K^-\pi^+) - A_D(\pi^+) \tag{4.23}$$

where

- $A_D(K^-\pi^+)$ is obtained from two calibration samples, $D^+ \to K^-\pi^+\pi^+$ and $D^+ \to \bar{K}^0\pi^+$ decays channel.
- $A_D(\pi^+)$ is estimate from the calibration sample $D^{*+} \to (K^-\pi^+\pi^-\pi^+)\pi^+$ decay.

The values of $A_D(K^-\pi^+)$ are taken from the LHCb analysis note [59]. To determine $A_D(K^-\pi^+)$, they considered the raw asymmetries of the two calibration samples cited above. The raw asymmetry of $D^+ \to K^-\pi^+\pi^+$ decay is given by:

$$A_{raw}(K^-\pi^+\pi^+) = A_P(D^+) + A_D(K^-\pi^+) + A_D(\pi^+) \tag{4.24}$$

and the raw asymmetry of $D^+ \to \bar{K}^0\pi^+$ decay given by:

$$A_{raw}(\bar{K}^0\pi^+) = A_P(D^+) + A_D(\pi^+) - A_D(K^0) \tag{4.25}$$

By subtracting 4.24 and 4.25 equations, $A_D(K^+\pi^-)$ can be written as[4]

$$A_D(K^-\pi^+) = A_{raw}(K^-\pi^+\pi^+) - A_{raw}(\bar{K}^0\pi^+) - A_D(K^0) - A_{PID}(K^+\pi^-) \tag{4.26}$$

where the raw asymmetries are obtained from the fit to the D invariant mass of their respective decays channel, $A_{PID}(K^+\pi^-)$ is the asymmetry due to the PID cuts on $K^+\pi^-$ and is obtained using PIDCalib and $A_D(K^0)$ is a constant reported to be:

$$A(\bar{K}^0) = -A(K^0) = (-0.054 \pm 0.014) \tag{4.27}$$

The note [59] provides $A_D(K^-\pi^+) + A_D(K^0)$ corrected by the PID asymmetries as a function of the kaon momentum, shown in Table D.2 in Appendix D. For this analysis $A_D(K^-\pi^+)$ is obtained by subtracting the values from the table by $A_D(K^0)$. Thus, the kaon detection asymmetry in each momentum range i is obtained from:

$$A_D^i(K^-) = (A_D(K^-\pi^+) + A_D(K^0))^i - A_D(K^0) - A_D^i(\pi^-) \tag{4.28}$$

where$A_D^i(\pi^+)$ is the pion detection asymmetry as a function of the kaon momentum[5]. Their values are taken from the analysis [58] and reported in Table D.1 in Appendix D.

Pion detection asymmetry

For the pion detection asymmetry $A_D^i(\pi^-)$ in equations 4.21 and 4.22, it is used the values provided in the LHCb analysis note [58], which were obtained using the Run I data, i.e. 2011 and 2012 data. As at the present moment there is no measurement of the pion detection asymmetry available for Run II data, this analysis uses the values provided using the 2012 data. Their values are reported in Table D.3 in Appendix D. It is not considered a major problem as the pion detection asymmetry was measured to be approximately zero.

4.13.5 Combining Acceptance Maps

To combine the subsamples acceptances in a single map, for each year the TOS and TISnotTOS histograms are added weighted in order to reproduce the TOS/TISnotTOS

[4] $A_P(D^+)$ and $A_D(\pi^+)$ only cancel out if their kinematic distributions are equal, otherwise a re-weighting procedure is needed.

[5] It is the pion detection asymmetry, $A_D(\pi^+)$, measured in bins of pion momentum and re-weighted by the kaon momentum of the $D^+ \to K^-\pi^+\pi^+$ decay.

ratio from the data while keeping the overall normalisation. The weight for the TOS sample is given by

$$w_{TOS}^{year} = R_{TOTAL}^{year} \times \frac{N_{TOS}^{DATA^{year}}}{N_{TOS}^{MC^{year}}} \tag{4.29}$$

where *year* is each year data taking (2015 or 2016), R_{TOTAL} is the total number of events MC/data ratio, $N_{TOS}^{DATA^{year}}$ is the number of data TOS events from 1D mass fit and $N_{TOS}^{MC^{year}}$ is the number of MC TOS events from 1D mass fit. Similarly for TISnotTOS configuration. The magnet up and magnet down subsamples are also added weigted take into account the following factor:

$$w_{Up}^{year} = \frac{N_{Up}^{year}}{N_{total}^{year}} \tag{4.30}$$

where N_{Up}^{year} is the number of magnet up data events for a certain year data taking and N_{total}^{year} is the total number of data events. Thus combination by year and by charge is given by:

$$Acc_{charge}^{year} = w_{TOS} \times Acc_{TOS}^{(Up+Down)} + w_{TISnotTOS} \times Acc_{TISnotTOS}^{(Up+Down)} \tag{4.31}$$

where,

$$Acc_{TOS}^{(Up+Down)} = w_{Up} Acc_{TOS}^{Up} + (1 - w_{Up}) Acc_{TOS}^{Down} \tag{4.32}$$

$$Acc_{TISnotTOS}^{(Up+Down)} = w_{Up} Acc_{TISnotTOS}^{Up} + (1 - w_{Up}) Acc_{TISnotTOS}^{Down} \tag{4.33}$$

To obtain the overall final acceptance maps an average 2015 and 2016 with 1:2 weights is performed. An illustration of how the acceptance is combined can be found in Fig. E.6 in Appendix E.

Figure 4.13 shows the final acceptance maps for B^+ and B^- for each decay channel. In the appendix E can be found the total acceptance maps per year for B^+ and B^- for each decay channel.

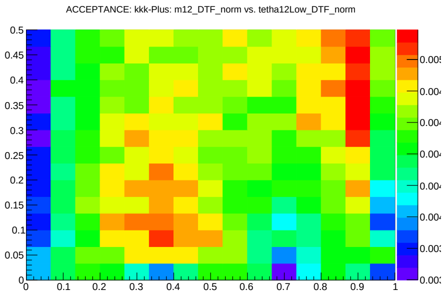

(A)
$B^{+} \to K^{+}K^{+}K^{-}$

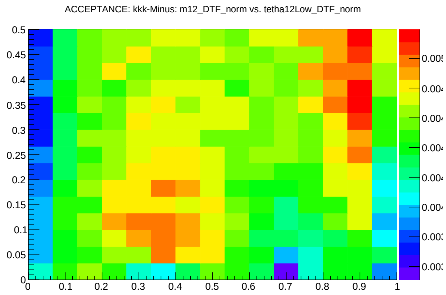

(B)
$B^{-} \to K^{+}K^{-}K^{-}$

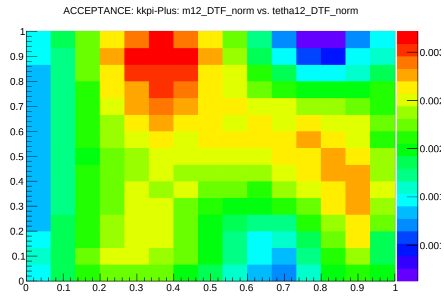

(C)
$B^{+} \to K^{+}\pi^{+}K^{-}$

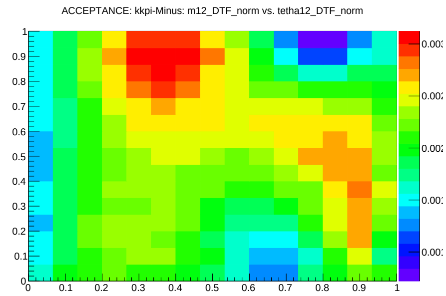

(D)
$B^{-} \to K^{+}\pi^{-}K^{-}$

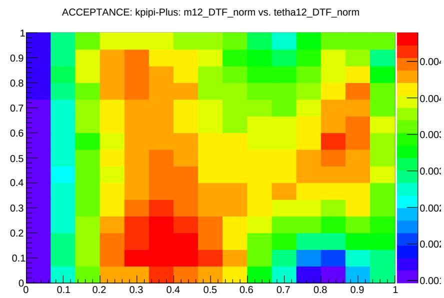

(E)
$B^{+} \to \pi^{+}K^{+}\pi^{-}$

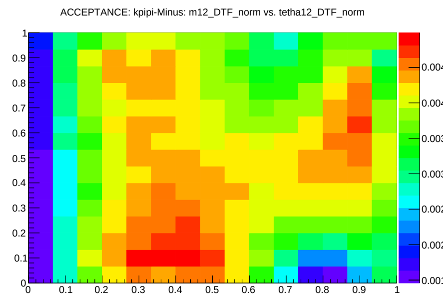

(F)
$B^{-} \to K^{+}\pi^{-}K^{-}$

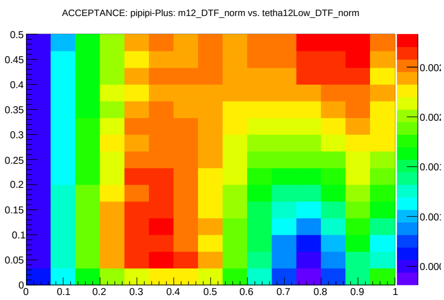

(G)
$B^{+} \to \pi^{+}\pi^{+}\pi^{-}$

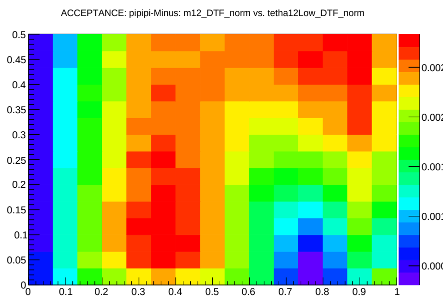

(H)
$B^{-} \to \pi^{+}\pi^{-}\pi^{-}$

FIGURE 4.13: Final combined acceptance B^{+}(right) B^{-}(left) 2015+2016 for the four $B^{\pm} \to h^{+}h^{\pm}h^{-}$ decay channels.

Decay channel	$<\epsilon^{+}>$	$<\epsilon^{-}>$	R $\pm\Delta$R
$B^{\pm}\to K^{+}K^{\pm}K^{-}$	0.00466	0.00464	0.996 $\pm$ 0.001
$B^{\pm}\to K^{+}\pi^{\pm}K^{-}$	0.00227	0.00220	0.969 $\pm$ 0.005
$B^{\pm}\to \pi^{+}K^{\pm}\pi^{-}$	0.00383	0.00390	1.016 $\pm$0.003
$B^{\pm}\to \pi^{+}\pi^{\pm}\pi^{-}$	0.00173	0.00180	1.042 $\pm$ 0.005

TABLE 4.8: Average efficiency for B^{+} and R for the binned acceptance for all decay channels with 2015+2016 data;

4.13.6 Average Efficiency

For the determination of the $\mathcal{A}_{CP}$ asymmetry, the A_{raw} needs to be corrected by the average efficiency of the acceptance. The efficiency is then corrected by data distribution as the MC samples used in the acceptance maps don't describe the dynamics of the decays. It is done through the *Splot* technique [72], where each MC event is weighted according to the signal data distribution in order to reproduce the population in the Dalitz plot signal data. Thus the harmonic averages of the efficiency separately for B^{+} and B^{-} is given by:

$$< \epsilon^{\pm} >= \frac{\sum_{i=1}^{events} w_i^{\pm}}{\sum_{i=1}^{events} \frac{w_i^{\pm}}{\epsilon_i}} \tag{4.34}$$

where w are the signal data weights and ϵ_i is the efficiency for each event i obtained from the final acceptance maps. The A_{raw} value is corrected by the ratio:

$$R = \frac{<\epsilon^{-}>}{<\epsilon^{+}>} \tag{4.35}$$

Table 4.8 reports $<\epsilon^{+}>$, $<\epsilon^{-}>$ and R for 2015+2016 data. The acceptance correction on A_{raw} is given by [2]:

$$A_{\text{raw}}^{ACC} = \frac{(N_{B^-}/R) - N_{B^+}}{(N_{B^-}/R) + N_{B^+}} \tag{4.36}$$

To propagate the MC statistics errors to the acceptance, we varied the acceptance histogram content of each bin according to a Gaussian centred at the original value and with width given by the error.

4.14 $\mathcal{A}_{CP}$ measurement

To determine the inclusive *CP* asymmetries, the raw asymmetries measured from the fits, shown in Table 4.7, must be corrected for effects induced by detector efficiency, interactions of final state particles with matter and any asymmetry in the forward production rates between B^{+} and B^{-}. The raw asymmetry is written in terms of the B^{+} event yields, and the number of signal events N_{B^-} and N_{B^+} are related to the asymmetries by

$$N_{B^+} = (1 - A_{CP})(1 - A_P)\frac{N_S}{2} \tag{4.37}$$

$$N_{B^-} = (1 + A_{CP})(1 + A_P)\frac{N_S}{2}R \tag{4.38}$$

Substituting the above Equation into Equation 4.36, the raw asymmetry can be expressed in terms of A_{CP} and A_P:

$$A^{ACC}_{RAW} = \frac{(A_{CP} + A_P)}{(1 + A_{CP}A_P)} \tag{4.39}$$

For small asymmetries the term with product of two asymmetries is negligible, and the raw asymmetry corrected by the acceptance becomes:

$$A^{ACC}_{RAW} \approx A_{CP} + A_P. \tag{4.40}$$

$$A_{CP} \approx A^{ACC}_{RAW} - A_P. \tag{4.41}$$

In the cases of large asymmetries, such as the ones measured in selected regions of phase space, the above approximation no longer holds and the A_{CP} asymmetry need to be calculated as:

$$A_{CP} = \frac{A^{ACC}_{RAW} - A_P}{(1 - A^{ACC}_{RAW}A_P)} \tag{4.42}$$

The total integrated *CP* asymmetry measured using 2015 and 2016 data samples for the four channels are:

- $\mathcal{A}_{CP}$ $(B^{\pm} \to \pi^+K^{\pm}\pi^-)$ = +0.004 ± 0.003(stat).
- $\mathcal{A}_{CP}$ $(B^{\pm} \to K^+K^{\pm}K^-)$ = -0.047 ± 0.003(stat).
- $\mathcal{A}_{CP}$ $(B^{\pm} \to \pi^+\pi^{\pm}\pi^-)$= +0.076 ± 0.007(stat).
- $\mathcal{A}_{CP}$ $(B^{\pm} \to K^+\pi^{\pm}K^-)$ = -0.134 ± 0.013(stat).

where the uncertainty is due to the statistical uncertainties of A^{ACC}_{RAW} of the signal channel. The quantities used for the calculation for each decay channel are summarised in Table 4.9. The integrated *CP* asymmetries is aproximately zero for $B^{\pm} \to \pi^+K^{\pm}\pi^-$, positive for $B^{\pm} \to \pi^+\pi^{\pm}\pi^-$ and negative for $B^{\pm} \to K^+K^{\pm}K^-$ and $B^{\pm} \to K^+\pi^{\pm}K^-$ decays. Apart from the $B^{\pm} \to \pi^+K^{\pm}\pi^-$ channel, the result is in agreement with the previous measurement [2].

	$B^{\pm} \to \pi^{+}K^{\pm}\pi^{-}$	$B^{\pm} \to K^{+}K^{\pm}K^{-}$	$B^{\pm} \to \pi^{+}\pi^{\pm}\pi^{-}$	$B^{\pm} \to K^{+}\pi^{\pm}K^{-}$
A_{raw}	0.005±0.003	-0.057±0.003	0.089±0.007	-0.157±0.013
R	1.016±0.003	0.994±0.003	1.042±0.005	0.969±0.005
$A_{\text{raw}}^{\text{ACC}}$	-0.003±0.003	-0.054±0.003	0.069±0.007	-0.142±0.013
A_{Prod}	-0.0074±0.0015			
A_{CP}	0.004±0.003	-0.047±0.003	0.076±0.007	-0.134±0.013

Table 4.9

4.15 Summary and Prospects

In this chapter it was presented the measurement of the phase-space integrated *CP* asymmetry for four charmless three-body B decays $B^{\pm} \to \pi^{+}K^{\pm}\pi^{-}$, $B^{\pm} \to K^{+}K^{\pm}K^{-}$, $B^{\pm} \to K^{+}\pi^{\pm}K^{-}$ and $B^{\pm} \to \pi^{+}\pi^{\pm}\pi^{-}$,

- $\mathcal{A}_{CP}$ $(B^{\pm} \to \pi^{+}K^{\pm}\pi^{-})$ = +0.004 ± 0.003(stat).
- $\mathcal{A}_{CP}$ $(B^{\pm} \to K^{+}K^{\pm}K^{-})$ = -0.047 ± 0.003(stat).
- $\mathcal{A}_{CP}$ $(B^{\pm} \to \pi^{+}\pi^{\pm}\pi^{-})$= +0.076 ± 0.007(stat).
- $\mathcal{A}_{CP}$ $(B^{\pm} \to K^{+}\pi^{\pm}K^{-})$ = -0.134 ± 0.013(stat).

where the uncertainty is due to the statistical uncertainties of A^{ACC}_{RAW} of the signal channel. The measurement were performed using data collected with the LHCb detector at a centre-of-mass energy of 13 TeV in 2015 and 2016 of the LHC Run 2, corresponding to an integrated luminosity of 1.9 fb^{-1}. The results obtained are consistent with the previous LHCb analysis based on 3.0 fb^{-1} at centre-of-mass energy of 7 TeV and 8 TeV (2011 and 2012)[2].

The $B^{\pm} \to h^{\pm}h^{+}h^{-}$ candidates were selected through an inclusive selection criteria based on the topology and kinematic of the decays. The background was reduced by using a multivariate analysis and particle identification requirements. In order to obtain the number of B candidates, a simultaneous fit to the sample of B^{+} and B^{-} invariant mass distribution were performed in each decay channel. The results for the signal yields were found to be about 220 k candidates for the $B^{\pm} \to \pi^{+}K^{\pm}\pi^{-}$ channel, 110 k candidates for the $B^{\pm} \to K^{+}K^{\pm}K^{-}$ channel, 30 k for the $B^{\pm} \to \pi^{+}\pi^{\pm}\pi^{-}$ channel and 9 k candidates for the $B^{\pm} \to K^{+}\pi^{\pm}K^{-}$ channel. Those values correspond to an increase of 25% in the number of signal events for $B^{\pm} \to \pi^{+}K^{\pm}\pi^{-}$, 20% for $B^{\pm} \to \pi^{+}\pi^{\pm}\pi^{-}$ and 50% for the $B^{\pm} \to K^{+}\pi^{\pm}K^{-}$ decay in comparison with the previous measurement.

The raw asymmetry was determined from the signal yields of B^{+} and B^{-} candidates obtained in the B mass fit. The inclusive *CP* asymmetry was obtained by correcting the raw asymmetry by the asymmetries introduced by the detector: detection asymmetry of pions-kaons and the production asymmetry of B^{+}/B^{-} at the LHCb experiment.

The *CP* asymmetry measured was found to be compatible with zero for $B^{\pm} \to \pi^{+}K^{\pm}\pi^{-}$, positive for $B^{\pm} \to \pi^{+}\pi^{\pm}\pi^{-}$ and negative for $B^{\pm} \to K^{+}K^{\pm}K^{-}$ and $B^{\pm} \to K^{+}\pi^{\pm}K^{-}$ decays. Apart from the $B^{\pm} \to \pi^{+}K^{\pm}\pi^{-}$ mode, the results are in agreement with the previous measurement [2]. The measurement presented in this chapter is a preliminary result of the analysis that has been performed by the LHCb group at CBPF, in which the inclusive *CP* asymmetry will be obtained with full Run II (2015+2016+2017+2018) data samples. The same procedure used in this thesis for the selection requirement, background reduction, fit model and acceptance correction has been applied to the measurement with full Run II LHCb dataset. The analysis note for the review of the LHCb collaboration is in preparation and the expectation is to be released next year (2020).

Chapter 5

Phase-space inspection of $B^{\pm} \to h^+h^{\pm}h^-$ decays

The purpose of this chapter is to localise source of *CP* violation in the Dalitz plot of the $B^{\pm} \to h^+h^{\pm}h^-$ decays by using the data collected by the LHCb in 2011, 2012, 2015 and 2016, which, in the signal mass region, provide samples with amount of:

- $B^{\pm} \to \pi^+K^{\pm}\pi^-$: 258727 events.
- $B^{\pm} \to K^+K^{\pm}K^-$: 178339 events.
- $B^{\pm} \to K^+\pi^{\pm}K^-$: 12480 events.
- $B^{\pm} \to \pi^+\pi^{\pm}\pi^-$: 57361 events.

The signal mass region definitions for the four channels are shown in Figure 5.1. It is defined within 34 MeV/c^2 of the fitted mass, except for the $B^{\pm} \to K^+\pi^{\pm}K^-$ decay, for which the mass window is restricted to ± 17 MeV/c^2. The background subtraction nor the acceptance correction are included in this study. This corresponds to samples of approximately 3 times larger than the ones from the Run 1.

5.1 Introduction

Each of four modes $B^{\pm} \to h^+h^{\pm}h^-$ can decay into many different intermediates states, where each contribution can interfere coherently with one another. The distribution of events in the Dalitz plot reflects this interference and an amplitude analysis is required to measure each component. In this thesis, only a simple Dalitz plot inspection is performed. The objective is to provide an insight about the CP asymmetry observed and examine how the asymmetry is spread over the phase space.

The study of the Dalitz plot of $B^{\pm} \to h^+h^{\pm}h^-$ decays may bring to light new mechanisms responsible for *CP* violation that can not be revealed by measuring the inclusive $\mathcal{A}_{CP}$ alone. The Figures 5.2 and 5.3 show the Dalitz plot for the four decay channels (2011,2012,2015 and 2016 data combined) [1]. The event distributions are concentrated at low mass region, as expected due to the dominance of light resonant contributions. In addition, the interference between these components can be used to study *CP* violation.

From the amplitude analysis of $B^{\pm} \to h^+h^{\pm}h^-$ decays, the following resonances can be identified in the Dalitz plot:

- $B^{\pm} \to \pi^+K^{\pm}\pi^-$: In the region $1 < m^2(K\pi) < 3.3$, there are contributions from higher K^* resonances, such as $K^{*0}(892)$ and $K^{*0}_{0,2}(1430)$. In the $\pi\pi$ projection,

[1] The vetoes applied on J/ψ and D^0 mass appear as gaps in the Dalitz plot distribution

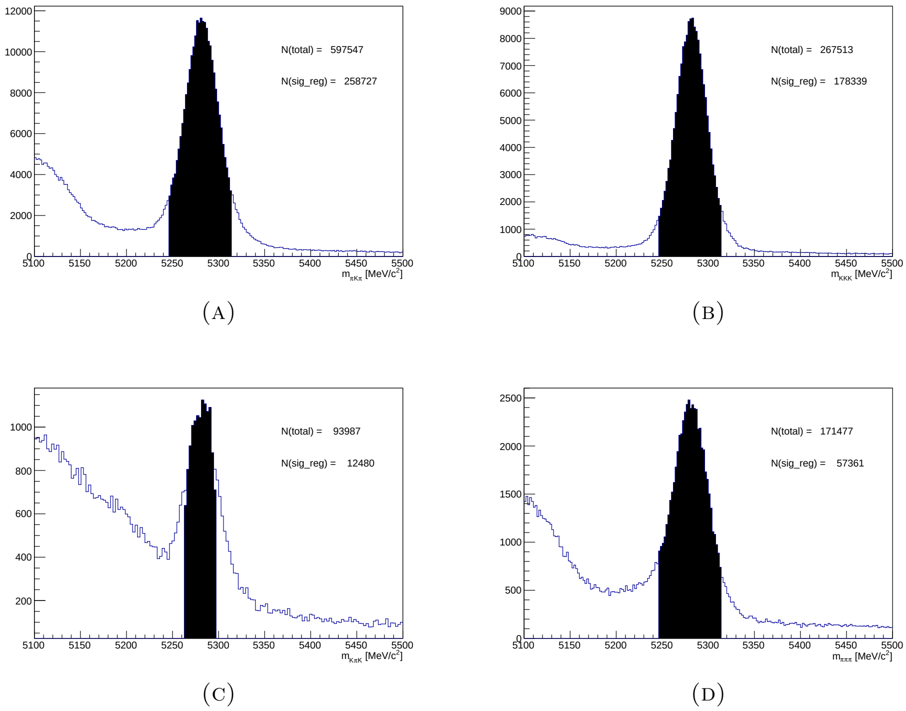

FIGURE 5.1: $B^{\pm} \to \pi^{+}K^{\pm}\pi^{-}$ in (A), $B^{\pm} \to K^{+}K^{\pm}K^{-}$ in (B), $B^{\pm} \to K^{+}\pi^{\pm}K^{-}$ in (C) and $B^{\pm} \to \pi^{+}\pi^{\pm}\pi^{-}$ in (D) visualisation of the signal (black filled). The signal region is defined within 34 MeV/c^2 of the fitted mass for $B^{\pm} \to \pi^{+}K^{\pm}\pi^{-}$, $B^{\pm} \to K^{+}K^{\pm}K^{-}$ and $B^{\pm} \to \pi^{+}\pi^{\pm}\pi^{-}$, while the $B^{\pm} \to K^{+}\pi^{\pm}K^{-}$ has a tighter definition, within 17 MeV/c^2, since there is a significant background contribution in this region

the region $m^2(\pi\pi) < 1$ has contributions from $\rho^0(770)$ and $f_0(980)$, also around 11 GeV/c^2, above $m^2(K\pi) > 3.6$ the $\chi_{c0}(1P)$ resonance is evident.

- $B^{\pm} \to K^{+}K^{\pm}K^{-}$: The region of $m^2(KK)_{low}$ around 1.0 GeV/c^2 correspond to the $\phi(1020)$ and around 11.5 GeV/c^2 to the $\chi_{c0}(1P)$ resonance. In the region $2.1 < m^2(KK)_{low} < 3.4$ is expected contribution of $f_0(1500)$ and $f_2'(1525)$. The region $3.9 < m^2(KK)_{low} < 6$ could have higher mass resonances and non-resonant contributions. In addition, the $B^{\pm} \to J/\psi K^{\pm}$ with $J/\psi \to K^{+}K^{-}$ is visible around 9.6 GeV/c^2.

- $B^{\pm} \to \pi^{+}\pi^{\pm}\pi^{-}$: The resonances are $\rho^0(770)$ and $f_0(980)$ at $m^2(\pi\pi)_{low} < 1$ GeV/c^2. In the region of $1.5 < m^2(\pi\pi)_{low} < 2$ GeV/c^2, also could correspond to the $\rho^0(1450)$ and the $f_2(1270)$ resonances. A subtle structure can be seen in the region of $10 < m^2(\pi\pi)_{high} < 13$, which could correspond to the $\chi_{c0}(1P)$ resonance.

- $B^{\pm} \to K^{+}\pi^{\pm}K^{-}$: The region $m^2(K\pi) < 1$ is dominated by $K*(892)^0$ and non-resonant contribution. In the region $1.8 < m^2(K\pi) < 2.2$ contribution from the $K^{*}(1430)^0$ resonance. Above this region, may higher K^{*} could contribute. Onto KK projection, in $1.8 < m^2(KK) < 2.2$ region, the resonance $\rho^0(1450)$ can contribute. Also, in the $8 < m^2(KK) < 14$ region, charmonium states χ_{c0} and J/ψ may be dominant.

To inspect the phase-space of the $B^{\pm} \to h^{+}h^{\pm}h^{-}$ decays it is used an approach described in detail in Ref. [73]. In a few words, it considers two Dalitz plot surfaces (B^{+} and B^{-}) divided into bins, by using an *adaptive binning* algorithm. Taking the total sample, it obtains bins with different size but with approximately the same number of events. In each bin, the variable $\mathcal{A}_{CP}^{bin} \equiv \frac{N_{B^-}-N_{B^+}}{N_{B^-}+N_{B^+}}$ is computed from the number of $B^{\pm}$ events candidate. The resulting $\mathcal{A}_{CP}^{bin}$ distribution across the Dalitz plots is refereed here as *Mirandizing* plot. The integration over the phase-space results in the observable global $\mathcal{A}_{CP}$. This method allow us to identify the fraction of events that violate CP and thus localise the source of asymmetry in the Dalitz plot.

In Figure 5.4 the variation of the raw asymmetry $\mathcal{A}_{raw}^{bin}$ [2] over the Dalitz plot for the four channels are shown, the red colours stand for positive asymmetries whereas the blue colours for negative ones. Larger asymmetries are found compared to the previous analysis [2], such as the region around ρ^0 resonance in $B^{\pm} \to \pi^{+}K^{\pm}\pi^{-}$ decay and the region of the re-scattering $\pi\pi \leftrightarrow KK$ in the four channels (region between 1 and 3 GeV^2/c^4). [3]

In addition, one can observe new regions with high asymmetries, such as the structure in the region of the χ_{c0} resonance (around 11.6 GeV/c^2) in the $B^{\pm} \to \pi^{+}\pi^{\pm}\pi^{-}$ and $B^{\pm} \to K^{+}\pi^{\pm}K^{-}$ channels[4] (see section 5.3.2). Also, in the region between 2 and 3 GeV/c^2 of the $m^2(KK)_{low}$, the CP asymmetry has a change of sign.

By looking at the Dalitz-plot dependence of the CP violation asymmetry as a function of various two-body invariant, one can find localised CP signatures involving different contribution. A phenomenological description of those local CP asymmetries is presented in Ref.[3] where an explicit expression for the CP asymmetry was obtained, and through fast Monte Carlo simulation it was explored the partner of the local asymmetries observed experimentally. Three types of dynamics related to CP violation in the Dalitz plot were considered:

i. Direct CP violation due to the interference of tree and penguin amplitudes with the same final state. This mechanism occur at the quark level and it is based on BSS model. This mechanism was set to be zero in the model, as the contribution locally violates CPT constraint.

ii. CP asymmetry produced through the interference between two different final states with different weak phases coupled by the final state interaction. This type of asymmetry is the so called *Compound* CP violation, in which the CP violation flows from one channel to the another coupled channel as a consequence of the CPT invariance. If the asymmetry has positive CP violation across the phase in a certain region, it is observed a negative CP violation across the phase in the same region of its coupled channels.

iii. CP violation that comes from the interference of two resonances in the Dalitz plot, which share the same phase space and the same final state. If the interference occurs between resonances with different angular momentum, such as vector and scalar, the CP asymmetry becomes dependent on $\cos\theta_H$ and changes sign when $\cos\theta_H$ cross the zero. In the Dalitz plot it is seem two regions related to the asymmetry, with positive and another one with negative CP violation.

[2] $\mathcal{A}_{raw}^{bin}$ is used as no correction on raw asymmetry is applied to obtain solely the physical asymmetry.

[3] m($\pi\pi$) for $B^{\pm} \to K^{\pm}\pi^{+}\pi^{-}$, low m($\pi\pi$) for $B^{\pm} \to K^{\pm}\pi^{+}\pi^{-}$, low m($KK$) for $B^{\pm} \to K^{\pm}K^{+}K^{-}$ and m(KK) $B^{\pm} \to \pi^{\pm}K^{+}K^{-}$.

[4] high m($\pi\pi$) for $B^{\pm} \to \pi^{+}\pi^{\pm}\pi^{-}$ and m(KK) for $B^{\pm} \to K^{+}\pi^{\pm}K^{-}$.

Combining the present knowledge of the resonant contributions with the plots of asymmetries in bins of the Dalitz plot, an inspection of *CP* violation partners can be made by looking at specific regions of the two-body invariant mass projections.

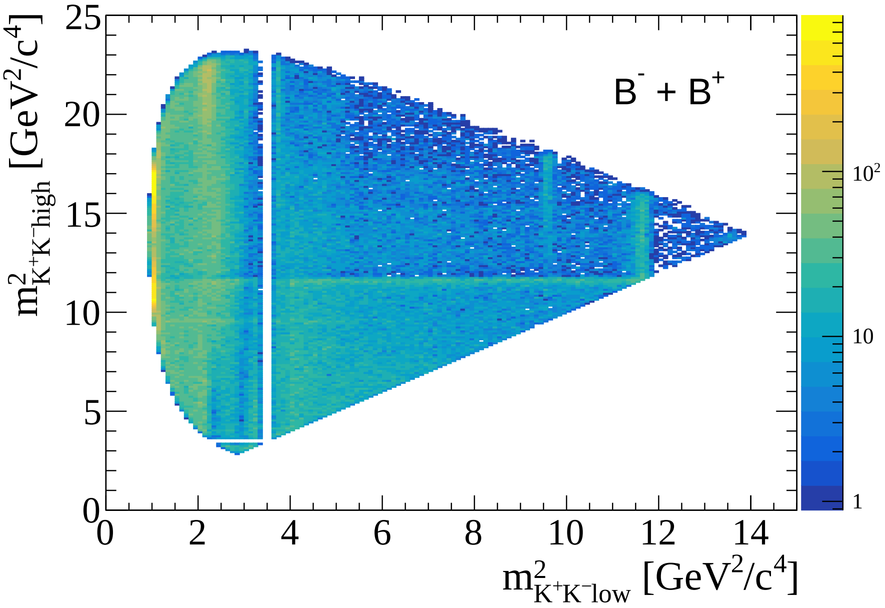

(A) $B^{\pm} \to K^{+}K^{\pm}K^{-}$

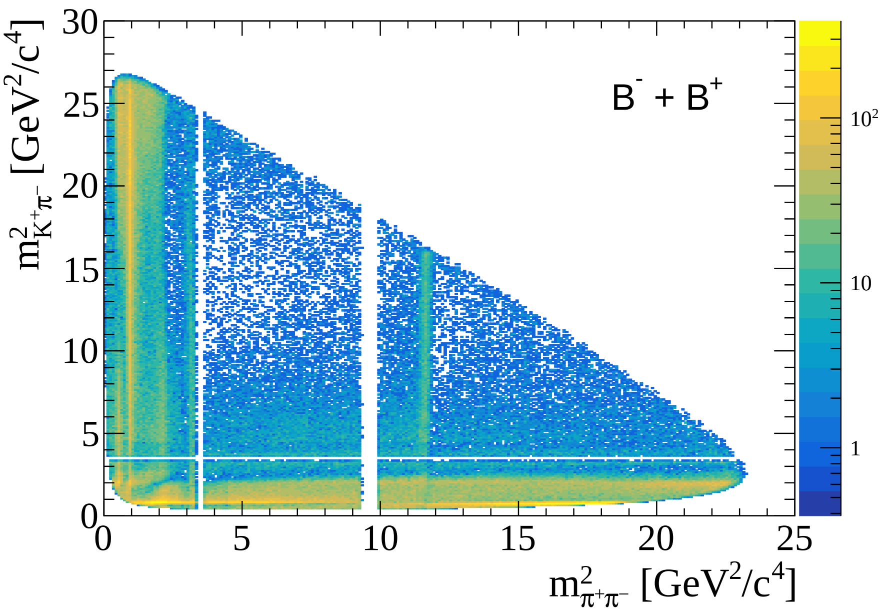

(B) $B^{\pm} \to \pi^{+}K^{\pm}\pi^{-}$

FIGURE 5.2: Dalitz plot of $B^{\pm} \to \pi^{+}K^{\pm}\pi^{-}$ (top) and $B^{\pm} \to K^{+}K^{\pm}K^{-}$ (bottom) with 2011+2012+2015+2016 data sample.

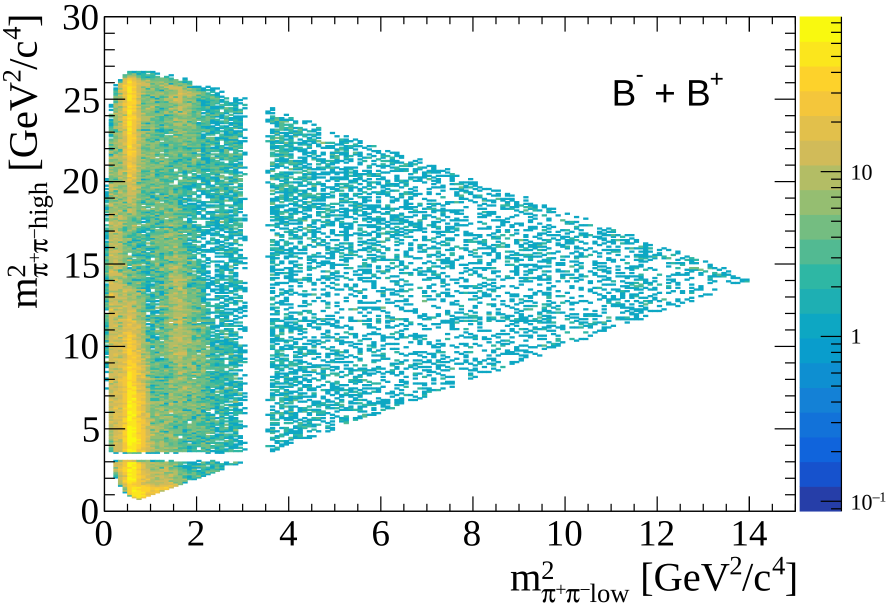

(A) $B^{\pm} \to \pi^+\pi^{\pm}\pi^-$

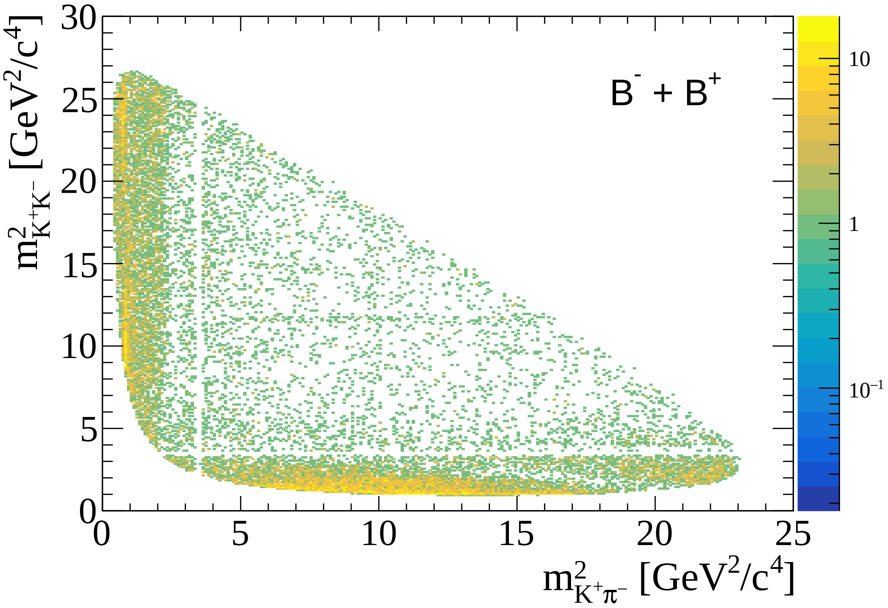

(B) $B^{\pm} \to K^+\pi^{\pm}K^-$

FIGURE 5.3: Dalitz plot of $B^{\pm} \to \pi^+\pi^{\pm}\pi^-$ (top) and $B^{\pm} \to K^+\pi^{\pm}K^-$ (bottom) with 2011, 2012, 2015 and 2016 combined data sample.

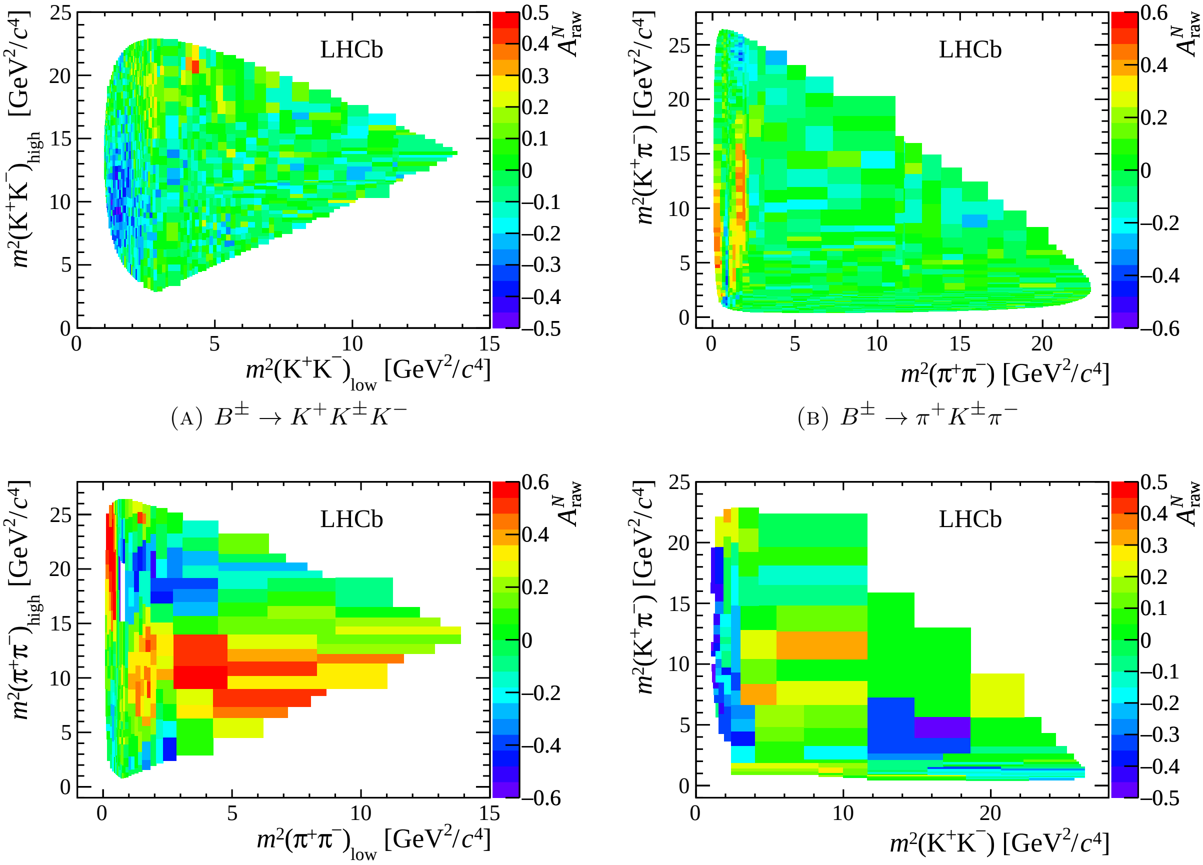

(A) $B^{\pm} \to K^{+}K^{\pm}K^{-}$

(B) $B^{\pm} \to \pi^{+}K^{\pm}\pi^{-}$

(C) $B^{\pm} \to \pi^{+}\pi^{\pm}\pi^{-}$

(D) $B^{\pm} \to K^{+}\pi^{\pm}K^{-}$

FIGURE 5.4: $\mathcal{A}_{CP}^{bin}$ in Dalitz plot bins with equal number of events for the four $B^{\pm} \to h^{+}h^{\pm}h^{-}$ decay channels with 2011, 2012, 2015 and 2016 combined data sample.

5.2 Two-body invariant mass projection

5.2.1 $B^{\pm} \to \pi^{+}K^{\pm}\pi^{-}$

The resonances which coupled to $\pi^{+}\pi^{-}$ invariant mass of $B^{\pm} \to \pi^{+}K^{\pm}\pi^{-}$ decay are $\rho^{0}(770)$ and $f_{0}(980)$, located below to 1 GeV/c^{2}, as shown in Figure 5.5, where the projections are split according to the sign of $\cos\theta$. The clear pattern of interference has also been observed in the previous measurement with Run 1 data. In the $\cos\theta_{H} < 0$ region there is a zero around the ρ mass and another zero around $f_{0}(980)$ mass, where there is a change of sign. In Ref. [3] has suggested that the dynamics behind the asymmetry observed is due to the interference between the vector and scalar amplitudes.

5.2.2 $B^{\pm} \to K^{+}K^{\pm}K^{-}$

In the $B^{\pm} \to K^{+}K^{\pm}K^{-}$ decay, Figure 5.6 shows the Dalitz plot projection of $m(K^{+}K^{-})_{low}$ in the $\phi(1020)$ region, split according to the sign of $\cos\theta_{H}$. In both plots can be seen a small asymmetry that changes sign around the ϕ mass ($\sim$ 1.02 GeV/c^{2}). The asymmetry observed has a interference pattern which was not clear observed in previous analysis. In adittion, the pattern is similar to the one shown in Figure 5.7 in $B^{\pm} \to \pi^{+}\pi^{\pm}\pi^{-}$ decay, in which the Ref.[3] suggests the asymmetry produced may be due to the interference between the vector resonant and non-resonant amplitude. Following the same idea, it is possible that the origin of *CP* violation partner observed in 5.6 may comes from the interference between the vector (ϕ, in this case) and non-resonant amplitude, as in this region, the ϕ is the only resonant contribution.

5.2.3 $B^{\pm} \to \pi^{+}\pi^{\pm}\pi^{-}$

The Figure 5.7 shows the low $\pi^{+}\pi^{-}$ invariant mass plot in the region below 1.8 GeV/c^{2}. It can be seen a bump bellow 1 GeV/c^{2} corresponding to the $\rho^{0}(770)$ and $f_{0}(980)$ resonances. Between 1.1 and 1.5 GeV/c^{2}, a smaller peak can be seen, which could corresponds to the region of the $f_{2}(1270)$ and $\rho^{0}(1450)$ resonances. The projections are split according to the sign of $\cos\theta$. It shows the same interference pattern observed in previous analysis [2]. In both plots, there is a zero and a change of sign around the $\rho^{0}(770)$ mass (0.770 GeV/c^{2}). This *CP* violation pattern has been interpreted as a result of the interference between the non-resonant and the vector resonance ρ^{0} amplitudes.

5.2.4 $B^{\pm} \to K^{+}\pi^{\pm}K^{-}$

In Figure 5.8 shows the projection of $B^{\pm} \to K^{+}\pi^{\pm}K^{-}$ onto invariant mass $K\pi$ the where the first bump is in the mass region of $K^{*}(892)^{0}$ and $K_{0}^{*}(1430)^{0}$ resonances. No significant asymmetry is observed in this region.

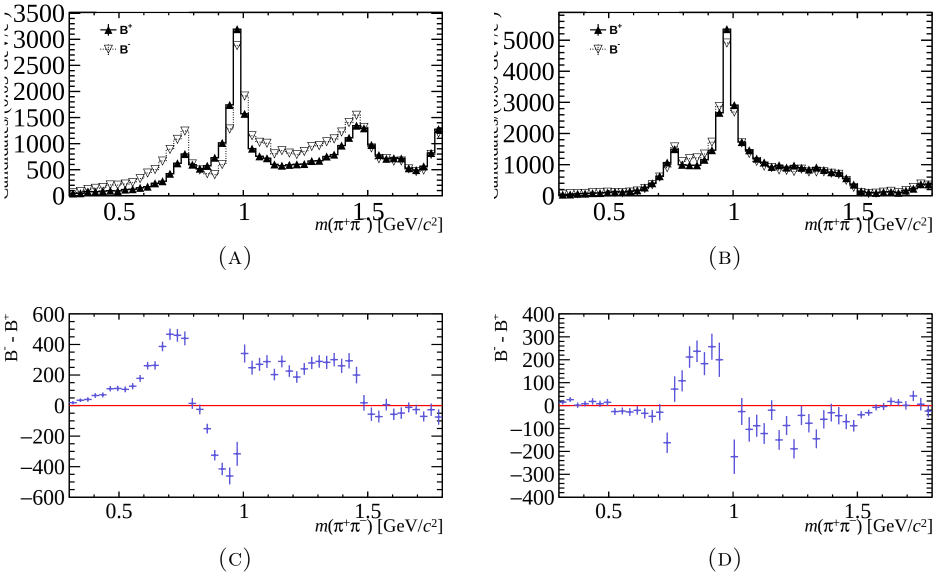

FIGURE 5.5: $B^{\pm} \to \pi^{+}K^{\pm}\pi^{-}$ zoom of in the $\rho^{0}(770)$ and $f_0(980)$ region. Projections are separated for events with $\cos\theta < 0$ (left) and $\cos\theta > 0$ (right). Candidates distributions of events in (a) and (b). The difference between B^{+} and B^{-} candidates in (c) and (d).

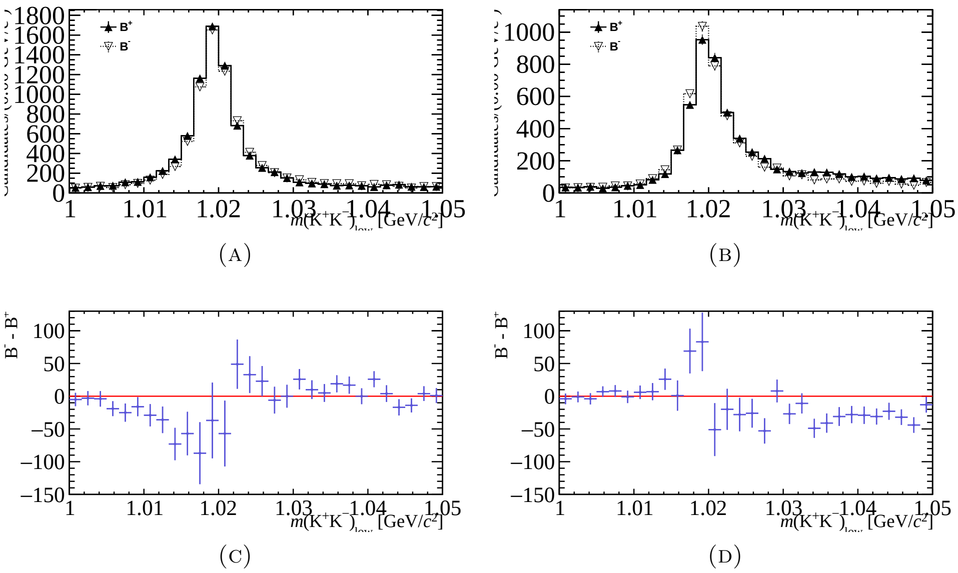

FIGURE 5.6: $B^{\pm} \to K^{+}K^{\pm}K^{-}$ zooms in the region of $\phi(1020)$. Projections are separated for events with $\cos\theta < 0$ (left) and $\cos\theta > 0$ (right). Candidates distributions of events in (a) and (b). The difference between B^{+} and B^{-} candidates in (c) and (d).

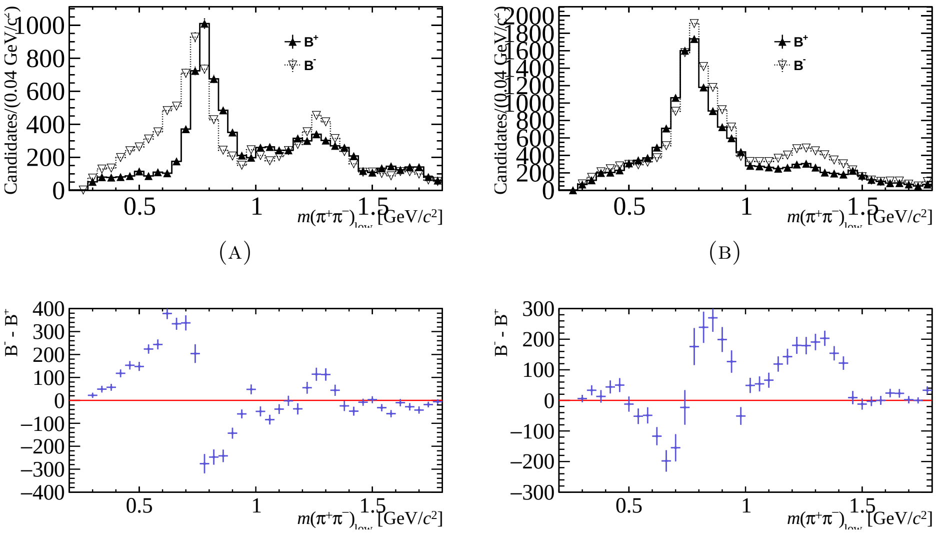

(A) (B)

(C) (D)

FIGURE 5.7: $B^{\pm} \to \pi^{+}\pi^{\pm}\pi^{-}$ mass projections in the region of $\rho^0(770)$. The projections are separated for events with $\cos\theta < 0$ (left) and $\cos\theta < 0$ (right). The difference between B^+ and B^- candidates are presented in the last column.

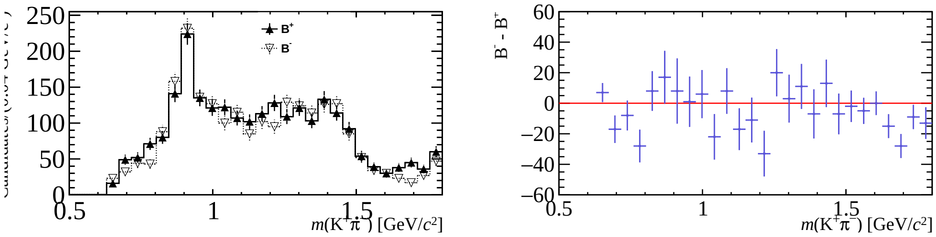

(A) (B)

FIGURE 5.8: Projection of $B^{\pm} \to K^{+}\pi^{\pm}K^{-}$ Dalitz plot in the region of K^*, separated by charge in (a) and the difference between B^+ and B^- candidates in (b).

5.3 Regions with high asymmetries

5.3.1 Comment about the re-scattering region

An interesting find in the previous analysis was a large *CP* asymmetry located in the region between 1 and 1.5 GeV/c^2 of the K^+K^- and $\pi^+\pi^-$ invariant mass in the four decay channels. In this range, the $\mathcal{A}_{CP}$ measured in each channel was found to be [2]:

- $\mathcal{A}_{CP}$ $(B^{\pm} \to K^+K^{\pm}K^-)$ = -0.211 $\pm$ 0.011 $\pm$ 0.004 $\pm$ 0.007
- $\mathcal{A}_{CP}$ $(B^{\pm} \to \pi^+K^{\pm}\pi^-)$ = +0.121 $\pm$ 0.012 $\pm$ 0.017 $\pm$ 0.007
- $\mathcal{A}_{CP}$ $(B^{\pm} \to K^+\pi^{\pm}K^-)$ = -0.328 $\pm$ 0.028 $\pm$ 0.029 $\pm$ 0.007
- $\mathcal{A}_{CP}$ $(B^{\pm} \to \pi^+\pi^{\pm}\pi^-)$ = +0.172 $\pm$ 0.021 $\pm$ 0.015 $\pm$ 0.007

The source of these asymmetries has been attribute to the rescattering effect $\pi\pi \leftrightarrow KK$, where a pair produced in one channel appear in the final state of the coupled channel. As pointed out before, the *CP* asymmetry induced by the re-scattering is based on the idea of *Compound CP* asymmetry, in which the asymmetry in one channel flows to another coupled channels in order to have the sum of partial width of a family of decays identical for particle and antiparticle. Thus, positive *CP* asymmetry in a channel implies negative *CP* asymmetries in its coupled channel.

This correlation between the asymmetries can be observed above, where the asymmetry is positive for channels with a $\pi^+\pi^-$ pair and negative for those with a K^+K^- pair. The large data sample in the present study allows us to visualise this effect more evident.

In Figure 5.9 is shown the projection of $m(K^+K^-)_{low}$ between 1.05 and 1.8 GeV/c^2. The ϕ resonance region is excluded in this plot in order to better observe other contributions in this region. The projections are split according to the cosine of the helicity. The high asymmetry observed in Figure 5.9 (d) is has been attributed to the re-scattering process. The same structure with opposite sign is observed in the same region of the $m(\pi^+\pi^-)$ of its couple decay $B^{\pm} \to \pi^+K^{\pm}\pi^-$, as can be seen in Figure 5.10 (d). The same goes to the channel $B^{\pm} \to K^+\pi^{\pm}K^-$, where the projection onto K^+K^- projection in the re-scattering region is shown in Figure 5.11 and for its coupled decay $B^{\pm} \to \pi^+\pi^{\pm}\pi^-$ in Figure 5.12.

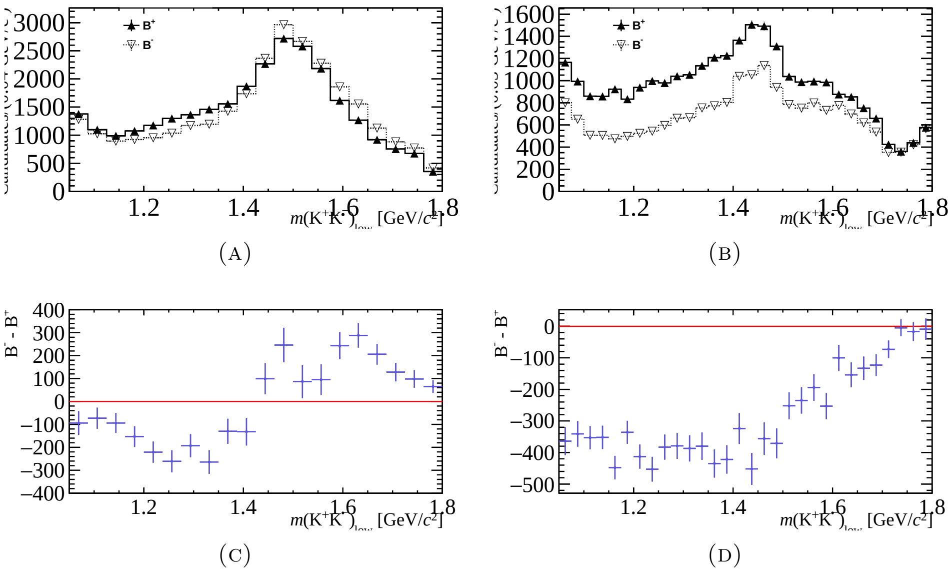

FIGURE 5.9: $B^{\pm} \to K^{+}K^{\pm}K^{-}$ zooms in the re-scattering region, where the $\phi(1020)$ is removed. Candidates distributions of events in the signal region with (a),(c) $\cos(\theta) < 0$ and (b),(d) $\cos(\theta) > 0$.

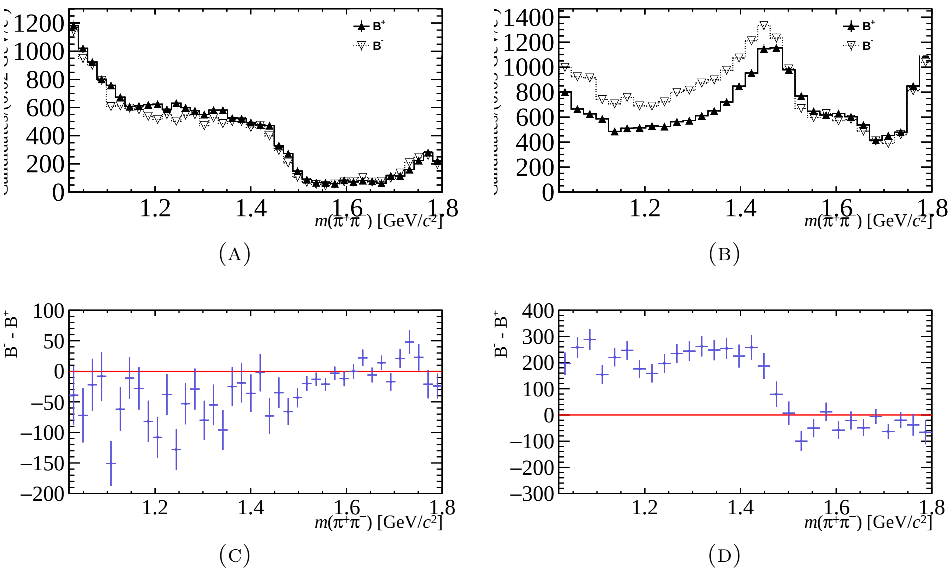

FIGURE 5.10: A zoom of in the re-scattering region for the $B^{\pm} \to \pi^{+}K^{\pm}\pi^{-}$ decay, for events with (a) $\cos_{\theta} < 0$ and (b) $\cos_{\theta} > 0$ and the $B^{-} - B^{+}$ distributions, (c) and (d)

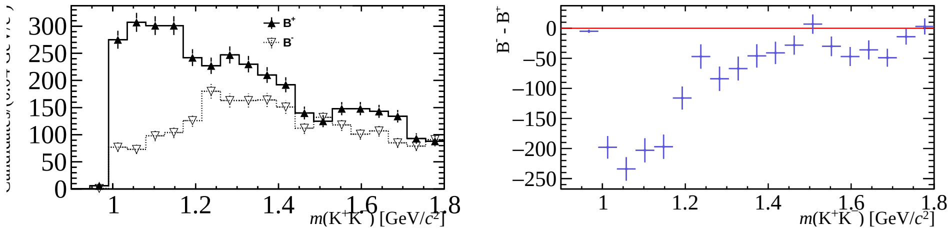

(A) (B)

FIGURE 5.11: $B^{\pm} \to K^{+}\pi^{\pm}K^{-}$ zoom in the region of the rescattering. Projections are separated by the B meson charge (a) and the difference of these two distributions (b).

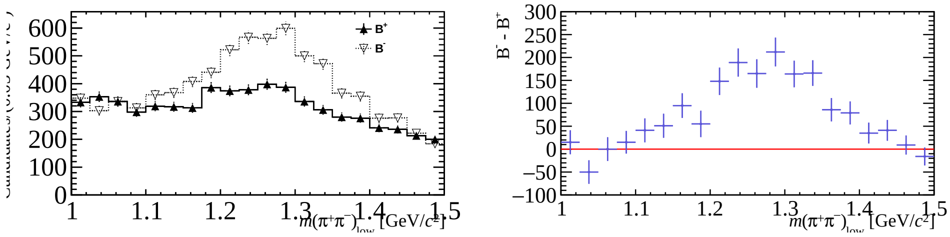

(A) (B)

FIGURE 5.12: Projection onto low $\pi\pi$ invariant mass of $B^{\pm} \to \pi^{+}\pi^{\pm}\pi^{-}$ in the region of the rescattering.

5.3.2 Region of $\chi_{c0}(1P)$ resonance

The χ_{c0} meson is a spin-zero charmonium state, which is composed of $c\bar{c}$ quarks. Its rest mass is $\sim$ 3.414 GeV/c^2 and width around 0.01 GeV/c^2 (10 MeV/c^2). In B charged decays, the $c\bar{c}$ resonance is formed through the $b \to c\bar{c}d(s)$ transition [8]. This resonance is well established in the $B^\pm \to \pi^+K^\pm\pi^-$ and $B^\pm \to K^+K^\pm K^-$, with measured branching fraction. For $B^\pm \to K^+\pi^\pm K^-$ and $B^\pm \to \pi^+\pi^\pm\pi^-$ this process has never been observed before.

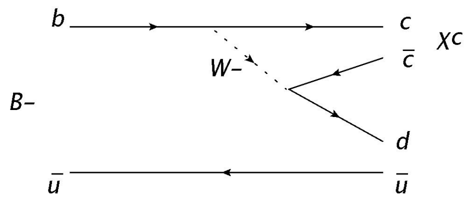

FIGURE 5.13: $B^\pm \to (\chi_{c0})\pi^\pm$, $\chi_{c0} \to \pi^+\pi^-$ tree diagram.

In Figures 5.14 and 5.15 are shown the projections onto the two-body invariant mass in the region of mass of the $\chi_{c0}(1P)$ resonance for $B^\pm \to \pi^+\pi^\pm\pi^-$ and $B^\pm \to K^+\pi^\pm K^-$, respectively. In both modes, the bump is the region of the $\chi_{c0}(1P)$ resonance. In particular, we draw attention to the $B^\pm \to \pi^+\pi^\pm\pi^-$ decay due to the clear high asymmetry between B^+ and B^- events.

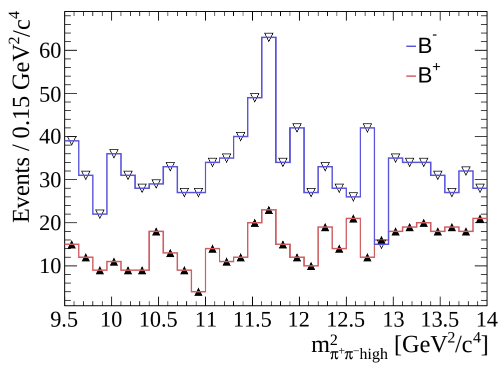

FIGURE 5.14: $B^\pm \to \pi^+\pi^\pm\pi^-$ event distribution in the region of the $\chi_{c0}(1P)$ resonance. Projection onto $m^2(\pi\pi)_{high}$ above the region $m^2(\pi\pi)_{low} > 3$.

The $B^\pm \to (\chi_{c0})\pi^\pm \to \pi^\pm\pi^+\pi^-$ decay is a tree level decay driven by the $b \to c\bar{c}d$ transition, the tree diagram is shown in Figure 5.13. The process $B^\pm \to (\chi_{c0})\pi^\pm$ was reported by Babar collaboration with an upper limit of $\mathcal{B}(B^\pm \to (\chi_{c0})\pi^\pm) < 1.5 \times 10^{-5}$ [74]. The $B^\pm \to (\chi_{c0})\pi^\pm$, $\chi_{c0} \to \pi^+\pi^-$ has even a more suppressed branching fraction, with an upper limit of ($< 1 \times 10^{-7}$).

The study of this decay was first pointed out in Ref.[75], one investigates the possibility of having CP asymmetry in $B^\pm \to (\chi_{c0})\pi^\pm \to \pi^\pm\pi^+\pi^-$. The basic idea is that the CP asymmetry could arise from the interference of the resonance χ_{c0} and non-resonant decay amplitude. As it carries the CKM coefficients V_{bc} and V_{cd}^*, its amplitude has no CP violating phase (γ). Therefore when the $\chi_{c0}\pi$ interfere with a direct B decay amplitude going through $b \to u\bar{u}d$ transition (with different CKM phase) the resonance width provides the necessary phase to produce the CP asymmetry. This model describes also predicts that the an observed CP asymmetry

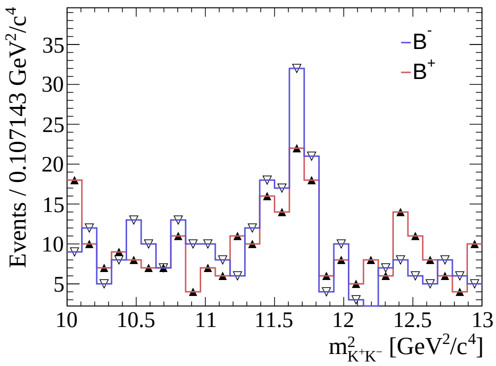

FIGURE 5.15: $B^{\pm} \to K^{+}\pi^{\pm}K^{-}$ event distribution in the region of the $\chi_{c0}(1P)$ resonance. Projection onto $m^2(KK)$ above the region $m^2(K\pi) > 4$ GeV/c^2.

in $B^{\pm} \to (\chi_{c0})\pi^{\pm} \to \pi^{\pm}\pi^{+}\pi^{-}$ would be of the order of 10%. In addition, this process can be used to extract the CKM phase $\gamma = arg(V_{ub}^{*})$, as suggested in Ref.[76].

The significant difference between B^{+} in B^{-} candidates suggests that CP violation should be large in this region. However, further studies are required, as the precise measurement of the localised CP asymmetry. Also, a fast Monte Carlo study, considering the interference between the non-resonant and scalar amplitude, would be a interesting study to probe the source of the asymmetry observed.

Chapter 6

Measurement of the lifetime difference in charmless $B^{\pm}$ decays

In this chapter a measurement of the lifetime difference between B^+ and B^- in $B^{\pm} \to K^+K^{\pm}K^-$ and $B^{\pm} \to K^+\pi^{\pm}K^-$ decays is presented. For this analysis the data collected by LHCb at two different pp collision energies is used: $\sqrt{s} = 7$ TeV during 2011 and $\sqrt{s} = 8$ TeV in 2012 with a total integrated luminosities of $1005.72 \pm 35.20\,\mathrm{pb}^{-1}$ and $2032.93 \pm 101.65\,\mathrm{pb}^{-1}$ respectively. In the following sections the motivation and the analysis performed to obtain the lifetime difference are presented.

6.1 Motivation

The recent measurements of *CP* violation in $B^{\pm} \to h^{\pm}h^+h^-$, discussed in the previous chapter, motivate an experimental search for other violations related to the CPT theorem.

The *CPT* theorem is a theoretical result linking Lorentz and *CPT* symmetries, which are two of the most fundamental symmetries in physics and their violation have not yet been observed. It states that local quantum field theories with Lorentz symmetry must also have *CPT* symmetry. These theories include the Standard Model (SM) and Grand Unified Theories, for example. Thus the SM of particles physics is expected to obey *CPT* invariance. Indeed, violations of all symmetries (C, P, T, CP) are predicted by the SM and have already been observed in experiments. Only the combination *CPT* is required to be a symmetry of Nature and no evidence of its violation has been observed despite numerous experimental tests [77].

One question that one may ask is if *CPT* symmetry seems to be an exact symmetry which is hard to break, why do we have to bother to test *CPT* invariance, given that all our phenomenology to date has been based on it? To answer this question we can call upon three considerations. First, since all of our phenomenology has been based on the *CPT* invariance, it is paramount that we confirm its invariance at all possible process. Any process that breaks *CPT* invariance would represent a window to physics beyond the SM. Therefore test of the *CPT* symmetry is still an important topic in particle physics to probe new physics. Second, the proof of the *CPT* theorem assumes the existence of asymptotic states, which, however, is not be applicable for QCD as quarks and gluons are confined. Thus, the fundamental nature of the *CPT* theorem can be questioned [78]. Third, a signal of *CPT* violation could be found in deviations from the SM predictions on the *CP* violation observable since the SM does not provide the dynamic origin of the *CP* violation. Thus, *CP*-violating systems are a likely place for a possible *CPT* violation show up [79].

Given those three considerations above, we can motivate a search for *CPT* violation in the $B^{\pm} \to h^{+}h^{\pm}h^{-}$ decays, since *CP* violation has been observed in these channels with good precision. As discussed above, the Standard Model is *CPT* invariant and given *CPT* invariance, *CP* violation and T violation are equivalent. Therefore any observed *CP* violation in a decay implies a violation of T, as otherwise *CPT* would be broken. So a natural path to test *CPT* symmetry in decays with *CP* violation is to check the T violation.

Although T violation is expected (given that *CP* is violated), it has not been observed, because T symmetry is not a practical symmetry to be tested experimentally. For any unstable particle, we can observe both production and decay process, however, we can rarely measure the inverse production process, mostly due to the experimental difficulty in preparing the initial state [4]. As an example, consider the $B^{\pm} \to K^{+}K^{\pm}K^{-}$ decay, which is a rare decay with a branching fraction of the order of 10^{-5}. At the LHCb, we can produce a sufficient number of B meson to observe it, and indeed we have shown the measurement of its *CP* asymmetry in the previous chapter. The *CP* violation is characterised by the difference between the rate R_1 for the $B^{+} \to K^{+}K^{+}K^{-}$ and the rate R_2 for $B^{-} \to K^{+}K^{-}K^{-}$. Thus, *CPT* states that the rates for the inverse processes (R_1 for $K^{+}K^{+}K^{-} \to B^{+}$ and R_2 for $K^{-}K^{-}K^{+} \to B^{-}$) have to be equal. By comparing each B process with its inverse, if *CPT* is preserved, it is expected a T-violation. However, there are no prospects of an experiment that can provide the measurement of these inverse rates. Thus, it is necessary to consider another observable to check *CPT* symmetry.

The *CPT* theorem has some physical implications that can be used as a direct test for *CPT* symmetry; it implies that particles and antiparticles have the same mass, the same total lifetime and that all their quantum numbers are opposite but equal in magnitude. Therefore, the simplest test to verify *CPT* invariance is to check the equality of lifetime or masses for particles and antiparticles.

However, our motivation is to test *CPT* invariance in a given *CP* violating environment and, in principle, for charged B decays, the comparison between B^{+} and B^{-} would not be sensitive to a possible *CPT* violation due to *CP* violation. Since any measurement of the lifetime in charged B meson decays is independent of the decay mode. A general test of *CPT* invariance through the measurement of the total lifetime is usually performed in charged B decays with high branching ratio, such as the $B^{\pm} \to J/\psi K^{\pm}$ decay, which is two orders of magnitude higher than decays under study in this thesis. The LHCb has already measured with high precision the lifetime ratio between B^{+} and B^{-} in the $B^{\pm} \to J/\psi K^{\pm}$ mode. It has been reported to be $1.002 \pm 0.004 \pm 0.002$ [80], which is consistent with the Standard Model expectation.

Another consequence of *CPT* theorem that can be taken into account is the connection between *CPT* and Lorentz symmetry. It has been demonstrated that if *CPT* violation occurs, it necessarily implies that Lorentz symmetry is also violated. On the other hand, the violation of Lorentz symmetry does not necessarily lead to the violation of the *CPT* theorem [81]. However, if somehow Lorentz is broken in a process, it may indicate a possible *CPT* violation. By exploring the latter assumption, an attempt to probe *CPT* violation in $B^{\pm} \to h^{+}h^{\pm}h^{-}$ decays is made by considering some models that have included explicit broken Lorentz symmetry. Those models propose an experimental search for violation of the Lorentz symmetry in charged decays by testing the time dilation formula. Two models are considered in this thesis and described below.

6.1.1 The Redei Model

The Redei Model [82] is a model associated with the sensitivity to new physics at a small distance scale to test time dilation, a small deviation from the standard model prediction could indicate a new physics.

The Redei Model is a specific model describing the Lorentz non-invariant interaction. The size of the lifetime deviation can be related to the distance scale on which the new Lorentz invariant interaction is taking place. In the Redei model, microcasuality is broken below some small fundamental distance scale α. The resulting weak interaction Hamiltonian contains a non-causality form factor that permits interaction between simultaneous space-time events in the laboratory frame provided their spatial separation is less than α.

In this model, the time dilation formula ($\tau_{Lab} = \gamma\tau$) for the decay of a particle of mass m and energy E is then modified:

$$\tau_{Lab} = \gamma\tau(1 + 0.2(m \cdot c/\hbar)^2\gamma^2\alpha^2) = \gamma\tau(1 + 0.2(E/\hbar c)^2\alpha^2) \tag{6.1}$$

From this formula, it is expected that the lifetime measured at the laboratory frame be longer than the expected by an amount Δ:

$$\Delta \equiv 0.2(E/\hbar c)^2\alpha^2 \tag{6.2}$$

In GeV:

$$\Delta \equiv 5 \times 10^{26} E^2\alpha^2 \tag{6.3}$$

An important consequence of this model is that the lifetime becomes dependent on the energy of the particle and the deviation would increase for higher energies.

6.1.2 Nielsen and Picek Model

In the Nielsen and Picek model [83] the standard theory of electroweak is modified by the addition of a Lorentz non-invariant interaction. This model implies a modification of the Dirac equation for electrons, which is hard to be acceptable. However, the general approach has some interesting features which provide a framework for searching for Lorentz non-invariant interaction.

The model modifies the weak propagators by adding a non-Lorentz invariant term in the normal metric tensor, changing the weak interaction Hamiltonian. This adding term is dependent on a parameter δ which characterises the size the adding term. This implies many consequences in Lorentz invariant terms, one, for example, is in the mass term that becomes dependent on the velocity. In the case of the lifetime, the model obtains a formula for the dilation formula:

$$\tau \sim \gamma\tau_0(1 - (4/3)\delta\gamma^2) \tag{6.4}$$

Thus the lifetime would be different than the expected by an amount:

$$\Delta \equiv -(4/3)\delta\gamma^2 \tag{6.5}$$

The model proposes to measure the δ parameter, non-zero δ would indicate a violation of the Lorentz invariance.

6.1.3 A proposal to test Lorentz symmetry and *CPT* symmetry in $B^{\pm} \to h^{+}h^{\pm}h^{-}$ decays

The two models presented above propose to test the time dilation as a way to investigate broken Lorentz symmetry. Also, they suggest that the presence of a Lorentz non-invariant interaction could also be probed by checking the dependence of the lifetime measurement on the momentum of the decaying particle. In the Redei model, the adding term in the dilation formula is dependent on the energy-momentum and in the Nielsen and Picek model, the deviation is proportional to γ^2. Thus it motivates a lifetime measurement as a way to search for other violations.

In the LHCb experiment the decay time variable, t, is obtained by a Lorentz transformation from the laboratory frame to the centre-of-mass of the particle. In its rest frame, t is given by:

$$t = L\frac{m}{|\vec{p}|}, \tag{6.6}$$

where p is the reconstructed three-momentum, L is the flight distance of the particle between the production and the decay vertices and m is its reconstructed invariant mass. The decay time distribution, for an ideal detector, is an exponential function decreasing with the inverse of the lifetime of the particle, τ:

$$F_I(t) = e^{-t/\tau} \tag{6.7}$$

Thus, the lifetime τ of the particle (proper-time) is obtained by fitting the decay time distribution with the equation above. The variable t is obtained by performing a Lorentz transformation through the time dilation formula $t_{Lab} = \gamma t$. However, if somehow Lorentz symmetry is broken in a process, the transformation would not be valid anymore and the use of the dilation formula would give us a decay time distribution different from the standard one, in other words, we would measure a longer or smaller lifetime than the one expected. Therefore, according to the models presented above, any significant deviation in the lifetime measurement would indicate a possible violation of Lorentz symmetry in the process.

In this thesis, it is proposed two measurements of the $B^{\pm}$ lifetime in the coupled decays channel $B^{\pm} \to \pi^{+}K^{\pm}\pi^{-}$ and $B^{\pm} \to K^{+}K^{\pm}K^{-}$ to investigate both *CPT* and Lorentz violation. The choice of those two decays was motivated due to the higher statistics compared with the other two decay modes ($B^{\pm} \to \pi^{+}\pi^{\pm}\pi^{-}$ and $B^{\pm} \to K^{+}\pi^{\pm}K^{-}$), which are also studied in this thesis. The two proposals are described below:

1. We propose to measure the lifetime difference between B^{+} and B^{-} in decays with *CP* violation to probe other violation of invariance in weak decays. If Lorentz symmetry is violated it may could be manifested in a difference between the measured B^{+} and B^{-} lifetime, in addition any difference measured would indicate the presence of *CPT* violating interaction. Within the framework of the models considered above, we expect this measurement to be sensitive to a Lorentz non-invariant or CPT violating interaction as the sensitive of the particle lifetime to a new interaction is proportional to the square of the energy of the decaying particle.

2. We propose to search for a sign of Lorentz violation by measuring the B lifetime in bins of momentum. As discussed above, the two models considered, have a Lorentz violation term introduced in the time dilation formula dependent on the momentum-energy of the decaying particle. Therefore any deviation in the

measured lifetime in different regions of momentum would indicate a broken Lorentz symmetry.

In this thesis, it is presented an analysis performed considering the first proposal, which concerns to measure the lifetime difference between B^+ and B^- in the $B^\pm \to K^+K^\pm K^-$ and $B^\pm \to \pi^+K^\pm\pi^-$ decays.

6.2 Analysis Strategy

In this thesis, to measure the lifetime difference bewteen B^+ and B^- we use the same analysis strategy as the one described in the Ref. [84]. As discussed in the previous section, the decay time distribution of a particle follows an exponential and thus the lifetime can be obtained by fitting its distribution. However, as any other measurement, the lifetime measurement suffers from experimental uncertainties that needs to take into account.

The measured decay time distribution for a realistic detector is then defined as exponential function (Equation 6.7) convolved with a decay time resolution function, $G(t,\sigma)$, and multiplied by an acceptance function, A(t):

$$F_R(t) = A(t) \times [e^{-t'/\tau} \otimes G(t-t',\sigma)]. \tag{6.8}$$

As we are interested in obtaining a measurement of the lifetime difference between B^+ and B^-, we perform a ratio of the two measured decay time distributions to obtain the lifetime difference, by doing this most of systematic uncertainties and the background cancel. The ratio between B^+ and B^- decay time distributions can be written as:

$$r(t) = \frac{A_{B^+}(t) \times [e^{-t'/\tau_{B^+}} \otimes G(t-t',\sigma_{B^+})]}{A_{B^-}(t) \times [e^{-t'/\tau_{B^-}} \otimes G(t-t',\sigma_{B^-})]}. \tag{6.9}$$

As shown in chapter 4, the acceptance for both $B^\pm \to K^+K^\pm K^-$ and $B^\pm \to K^+\pi^\pm K^-$ decay are not uniform in the phase space and in addition, it was observed to be different for B^+ and B^-. Thus a correction is implemented when perform the ratio. In the case of the resolution function, it is expected not to be different for B^+ and B^- and we assume that the resolution effects cancel in the ratio. The equation above can be rewritten as:

$$r(t) = A_r(t) R_0 e^{-t'\Delta_{B^+B^-}} \tag{6.10}$$

where $A_r(t)$ is the acceptance function correction, $\Delta_{B_+B_-} = \frac{1}{\tau_{B+}}$ - $\frac{1}{\tau_{B-}}$ is the difference of the inverse of the lifetimes and R_0 is a normalisation. Then the lifetime difference can be calculated from $\Delta_{B^+B^-}$.

The procedure to measure $\Delta_{B^+B^-}$ can be roughly divided into two steps: (i) obtaining the ratio of the decay time distribution and (ii) the fit to the ratio distribution to extract $\Delta_{B^+B^-}$.

The ratio of the decay time distribution is obtained through the number of signal yields in different bins of decay time, and for each decay time bin i, the ratio below is performed:

$$R(t_i) = \frac{N_{B+}(t_i)}{N_{B_-}(t_i)} \tag{6.11}$$

The ratio distribution $r(t)$ is then constructed by summing over all the decay time bins

Decay		2011	2012
$B^{\pm} \to \pi^{+}K^{\pm}\pi^{-}$	MagUp	1053319	1007386
	MagDown	1061187	1016546
$B^{\pm} \to K^{+}K^{\pm}K^{-}$	MagUp	1009257	1027433
	MagDown	1064125	1004594

TABLE 6.1: MC signal statistics.

$$r(t) \equiv \sum_{i} \frac{N_{B+}(t_i)}{N_{B\_}(t_i)} \tag{6.12}$$

Thus, the lifetime difference $\Delta_{B^{+}B^{-}}$ is extracted by performing a fit with the equation 6.10 to the ratio of the signal yields. The signal yields are obtained through a fit to the $B^{\pm}$ invariant mass. First we fit the $B^{\pm}$ invariant mass in the full range of the decay time, then we perform the mass fit in each decay bin by fixing the parameter shape to those found in the total fit. The fit procedure is described in details in section 6.5.

6.3 Data and Simulation

The measurement of the lifetime difference presented in this thesis is performed with the data sample collected by the LHCb in 2011 and 2012 at centre-of-mass energy $\sqrt{s}$ = 7 TeV and 8 TeV, respectively. The 2011 sample consists of a integrated luminosity of $1005.72 \pm 35.20\,\text{pb}^{-1}$, and the 2012 sample consists of a integrated luminosity of $2032.93 \pm 101.65\,\text{pb}^{-1}$.

The MC simulated samples for $B^{\pm} \to K^{+}K^{\pm}K^{-}$ and $B^{\pm} \to \pi^{+}K^{\pm}\pi^{-}$ were generated without *CP* violation and flat in the Squared Dalitz plot representation (described in section 4.13.1). The events were generated with similar conditions as the data takings and and reflect the detector acceptance. In Table 6.1 MC statistics is summarised for each magnet polarity.

6.4 Selection of $B^{\pm} \to \pi^{+}K^{\pm}\pi^{-}$ and $B^{\pm} \to K^{+}K^{\pm}K^{-}$ decays

The selection of $B^{\pm} \to K^{+}K^{\pm}K^{-}$ and $B^{\pm} \to \pi^{+}K^{\pm}\pi^{-}$ candidates follow a similar strategy as the one described in section 4.3 of the chapter 4. The trigger and stripping selection are common for both Run I and Run II, thus the same requirements described in 4.4 and 3.5 are applied in this analysis. To further refine the $B^{\pm}$ candidate, an offline selection consisting of three steps is performed. First, a multivariate analysis selection to reduce the combinatorial background, followed by a particle identification selection and invariant mass cuts to remove charm contribution.

6.4.1 Trigger and Stripping selection

As discussed previously, the trigger and stripping selection are general requirements used to select different B decays that have common features. Hence, in this analysis it is used the same trigger and stripping requirements as the ones described in chapter 4. The only exception is in the L0 trigger lines, in which the threshold of the transverse energy is different for each year data taking. The trigger requirement is summarized below:

- `L0Hadron_TOS` or `L0Global_TIS`: selects the hadron candidate with high transverse energy ($E_T > 3.5$ GeV for 2011 and $E_T > 3.7$ GeV for 2012) and others particle not belong to the signal candidate fired any L0 trigger line.
- `HLT1TrackALL_TOS`: perform the partial reconstruction of the decay by selecting hadron candidates with $p_T > 1.6$ GeV and significant displacement from the primary vertex.
- `HLT2Topo(2-,3-,4-Body)_TOS`: perform the full reconstruction of the decay by selecting B decays candidates with two, three or four charged particles in the final state and a with significant displaced decay vertex and transverse momentum.

The stripping line used to select $B^\pm \to K^+K^\pm K^-$ and $B^\pm \to \pi^+K^\pm\pi^-$ data samples is presented in section 4.5, where a summary of the selection requirements can be found in Table 4.3. The definitions of the variables and more details about the stripping process were already described in the chapter 4.

6.4.2 Offline selection

In order to separate the $B^\pm \to K^+K^\pm K^-$ and $B^\pm \to \pi^+K^\pm\pi^-$ events from the physical background, a further selection stage is needed. This stage is refereed as offline selection and aims to reduce the combinatorial background, cross-feed background and remove charm contributions.

The combinatorial background is reduced through a multivariate analysis selection and the contamination from other b-hadron decays is suppressed by applying particle identification requirements in all final states particles. It is also applied vetoes around the D^0 and J/ψ mass to reject charm contributions. It is also discard events with more than one candidate that passed the final selection, since it is not expect more than one signal B candidate per event due to the low branching ratios of the decay channels. Table 6.2 list the number of candidates excluded in the cut of multiple candidates. For $B^\pm \to \pi^+K^\pm\pi^-$ $2-3\%$ of the candidates in the data and simulated samples are excluded. For $B^\pm \to K^+K^\pm K^-$ we excluded less than 1% of the candidates.

Multivariate Analysis selection

The method used to perform the multivariate analysis (MVA) selection is the Boosted Decision Tree (BDT), which was already described in section 4.8.

The procedure used in this thesis is the same as the one described in [85], which was performed aiming the selection of the four $B^\pm \to h^+h^\pm h^-$ channels. For the BDT training it was used data and simulation samples described in section 6.3. The training was performed common to all $B^\pm \to h^+h^\pm h^-$ decay channels included in the stripping selection (i.e. $B^\pm \to K^+K^\pm K^-$, $B^\pm \to \pi^+K^\pm\pi^-$, $B^\pm \to K^+\pi^\pm K^-$ and $B^\pm \to \pi^+\pi^\pm\pi^-$), as the combinatorial background distribution in the signal spectrum is similar for the $B^\pm \to h^+h^\pm h^-$ modes. The signal and the background samples are defined as :

- Signal sample: Simulated samples of all $B^\pm \to h^+h^\pm h^-$ decays channels
- Background sample: Reconstructed events of $B^\pm \to \pi^+\pi^\pm\pi^-$ data sample in the region of $5400 < m(\pi\pi\pi) < 5580$ MeV$/c^2$. In the high sidebands of the other $B^\pm \to h^+h^\pm h^-$ decays, are contamined by the signal cross-feed of the other $B^\pm \to h^+h^\pm h^-$ decays. The only exception is the $B^\pm \to \pi^+\pi^\pm\pi^-$ decay, for which the cross-feed of all modes lies below the B mass.

Sample	Decay	Year	Mag. Polarity	Candidates excluded	Total of candidates	
Data	$B^{\pm} \to \pi^{+}K^{\pm}\pi^{-}$	2011	Mag. Down	2180	74975	2.91%
Data	$B^{\pm} \to \pi^{+}K^{\pm}\pi^{-}$	2011	Mag. Up	1582	54096	2.92%
Data	$B^{\pm} \to \pi^{+}K^{\pm}\pi^{-}$	2012	Mag. Down	4636	156057	2.97%
Data	$B^{\pm} \to \pi^{+}K^{\pm}\pi^{-}$	2012	Mag. Up	4676	152879	3.06%
Data	$B^{\pm} \to K^{+}K^{\pm}K^{-}$	2011	Mag. Down	83	27206	0.31%
Data	$B^{\pm} \to K^{+}K^{\pm}K^{-}$	2011	Mag. Up	62	19879	0.31%
Data	$B^{\pm} \to K^{+}K^{\pm}K^{-}$	2012	Mag. Down	206	59230	0.35%
Data	$B^{\pm} \to K^{+}K^{\pm}K^{-}$	2012	Mag. Up	277	58522	0.47%
Data	$B^{\pm} \to \pi^{+}\pi^{\pm}\pi^{-}$	2011	Mag. Down	302	13461	2.24%
Data	$B^{\pm} \to \pi^{+}\pi^{\pm}\pi^{-}$	2011	Mag. Up	230	9365	2.46%
Data	$B^{\pm} \to \pi^{+}\pi^{\pm}\pi^{-}$	2012	Mag. Down	613	25931	2.36%
Data	$B^{\pm} \to \pi^{+}\pi^{\pm}\pi^{-}$	2012	Mag. Up	565	25177	2.24%
Data	$B^{\pm} \to K^{+}\pi^{\pm}K^{-}$	2011	Mag. Down	94	5605	1.68%
Data	$B^{\pm} \to K^{+}\pi^{\pm}K^{-}$	2011	Mag. Up	54	3768	1.43%
Data	$B^{\pm} \to K^{+}\pi^{\pm}K^{-}$	2012	Mag. Down	153	11277	1.36%
Data	$B^{\pm} \to K^{+}\pi^{\pm}K^{-}$	2012	Mag. Up	159	11121	1.43%
MC	$B^{\pm} \to \pi^{+}K^{\pm}\pi^{-}$	2011	Mag. Down	219	10549	2.08%
MC	$B^{\pm} \to \pi^{+}K^{\pm}\pi^{-}$	2011	Mag. Up	206	10062	2.05%
MC	$B^{\pm} \to \pi^{+}K^{\pm}\pi^{-}$	2012	Mag. Down	523	18600	2.81%
MC	$B^{\pm} \to \pi^{+}K^{\pm}\pi^{-}$	2012	Mag. Up	464	18303	2.54%
MC	$B^{\pm} \to K^{+}K^{\pm}K^{-}$	2011	Mag. Down	142	20288	0.70%
MC	$B^{\pm} \to K^{+}K^{\pm}K^{-}$	2011	Mag. Up	112	20067	0.56%
MC	$B^{\pm} \to K^{+}K^{\pm}K^{-}$	2012	Mag. Down	260	37409	0.70%
MC	$B^{\pm} \to K^{+}K^{\pm}K^{-}$	2012	Mag. Up	302	37644	0.80%
MC	$B^{\pm} \to \pi^{+}\pi^{\pm}\pi^{-}$	2011	Mag. Down	248	10310	2.41%
MC	$B^{\pm} \to \pi^{+}\pi^{\pm}\pi^{-}$	2011	Mag. Up	253	12000	2.11%
MC	$B^{\pm} \to \pi^{+}\pi^{\pm}\pi^{-}$	2012	Mag. Down	367	19723	1.86%
MC	$B^{\pm} \to \pi^{+}\pi^{\pm}\pi^{-}$	2012	Mag. Up	430	19784	2.17%
MC	$B^{\pm} \to K^{+}\pi^{\pm}K^{-}$	2011	Mag. Down	30	4593	0.65%
MC	$B^{\pm} \to K^{+}\pi^{\pm}K^{-}$	2011	Mag. Up	58	4629	1.25%
MC	$B^{\pm} \to K^{+}\pi^{\pm}K^{-}$	2012	Mag. Down	89	8209	1.08%
MC	$B^{\pm} \to K^{+}\pi^{\pm}K^{-}$	2012	Mag. Up	83	8182	1.01%

TABLE 6.2: List of candidates excluded in the cut of multiple candidates.

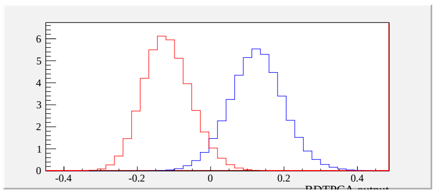

FIGURE 6.1: Discriminating variable BDT output by the optimization common to the four channels studied in [85]

.

Aiming a common optimization for the four channels with a focus on rejecting combinatorial background, the BDT is trained with a combination of all four simulation samples for the signal, and data from $B^{\pm} \to \pi^+ \pi^{\pm} \pi^-$ candidates in the mentioned B mass range for the background.

In Figure 6.1, it is shown the BDT output for these events for signal events (blue) and background events (red). In order to choose the cut on the BDT output variable, the significance is maximized $S/\sqrt{S+B}$, where S stands for signal and B for background for each channel and are extracted from fits to data for a given BDT cut.

The optimum cut on the BDT output variable from the common optimization is aproximately the same and it was decided to use $BDT > 0$ for the modes[1].

In Figure 6.2, it is shown the B mass distributions for each channel, before (black) and after (blue) the cut on the BDT output variable. As can be seen, the combinatorial background is significantly reduced.

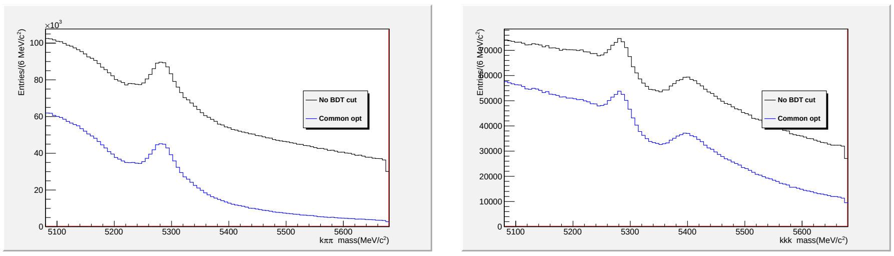

(A) $B^{\pm} \to \pi^+ K^{\pm} \pi^-$

(B) $B^{\pm} \to K^+ K^{\pm} K^-$

FIGURE 6.2: B mass distributions for 2012 data before and after a cut on the BDT discriminating variable $BDT > 0$ for $B^{\pm} \to \pi^+ K^{\pm} \pi^-$ and $B^{\pm} \to K^+ K^{\pm} K^-$.

Particle Identification selection

In the previous selection stages, no particle identification requirement was applied and thus the remaining background is rich in signal cross-feed from $B^{\pm} \to h^+ h^{\pm} h^-$ decays. The level of contamination from other B decays vary for the different modes. For this reason, different criteria for the identification of pions and kaons is adopted, depending on the final state. For the PID requirements it is used the PID variables `ProbNNk` for the identification of particle as kaon and `ProbNNpi` for the identification of a particle as pion (described in section 4.3).

[1] To simplify systematics errors and make easier to compare the results among the different channels we decided to unity the selection as much as possible. We choose the same set of variables, a single MVA training sample and finally the same BDT cut for all channels.

Decay	Daughter	PID selection cuts
$B^\pm \to K^+K^\pm K^-$	all	`ProbNNk`>0.2
$B^\pm \to \pi^+K^\pm\pi^-$	pions	`ProbNNpi`>0.25 & `ProbNNk`<0.35
	Kaon	`ProbNNk`>0.2

TABLE 6.3: Particle identification criteria to select $B^\pm \to K^+K^\pm K^-$ and $B^\pm \to \pi^+K^\pm\pi^-$ decay modes.

The basic source of contamination is the kaon misidentified as pion ($K-\pi$ mis-ID) and the pion misidentified as kaon ($\pi - K$ mis-ID). The PID selection criteria for $B^\pm \to K^+K^\pm K^-$ and $B^\pm \to \pi^+K^\pm\pi^-$ channels are shown in Table 6.3. Also, to reject muons contribution, a veto is applied in each final state track by impose a requirement on the variable for muon identification (`isMuon=0`). Details about the process of choosing these cut values and further PID studies for each channel can be found in [85].

Charm vetoes

The most dominant contribution to the $B^\pm \to K^+K^\pm K^-$ $B^\pm \to \pi^+K^\pm\pi^-$ decays are charmed contributions. To reject those contributions it is excluded the regions of $\pm 30\,\mathrm{MeV}/c^2$ around the D^0 mass (1895 MeV/c^2) in each axis of the Dalitz plot. For $B^\pm \to K^+K^\pm K^-$ we require m_{KK}, $m_{K\pi}$ and $m_{\pi K}$ not to be in the region ([1.834, 1.894] GeV/c^2. For $B^\pm \to \pi^+K^\pm\pi^-$ we also require $3.05 < m_{\pi\pi} < 3.15\,\mathrm{GeV}/c^2$ to exclude $B^\pm \to J/\psi K^\pm$ contributions.

6.4.3 Selection for the simulated samples

The $B^\pm \to \pi^+K^\pm\pi^-$ and $B^\pm \to K^+K^\pm K^-$ simulated samples passed through the same selection as for the data (same cuts, trigger lines and PID selection). These samples will be used in the next section to compute the fractions and shapes of the background component due to the cross-feed among the various $B^\pm \to h^+h^\pm h^-$.

6.5 Determination of the Signal Yields

To measure the lifetime difference between B^+ and B^-, we first have to obtain the ratio of signal yields in each decay time bin i:

$$R(t_i) = \frac{N_{B+}(t_i)}{N_{B-}(t_i)} \tag{6.13}$$

where $N_{B+}(t_i)$ and $N_{B-}(t_i)$ are the number of signal yields extracted from fit to the B invariant mass in a given decay time bin i. The mass fit in each bin is performed by fixing all signal and background shape parameters from those found in the total B mass fit (full decay time range).

In this section the total fit to the B^+ and B^- invariant mass distributions in the range $5080 - 5580$ MeV/c^2 is presented.

The main background contribution, that will be modelled in the mass fit, is the same as the ones described in section 4.11. They are classified as combinatorial background, partially reconstructed backgrounds (mostly from four-body decays with a missing particle) and the signal cross-feed among the $B^\pm \to K^+K^\pm K^-$ and $B^\pm \to \pi^+K^\pm\pi^-$ decays, that have one or more particles misidentified. The signal cross-feed and partially reconstructed backgrounds are parametrized using the MC simulations described in the Ref. [85].

6.5.1 Fit model

For each final state it is performed a simultaneous unbinned extended maximum likelihood fit to the invariant masses of the B^+ and B^- mass distribution. The PDFs are implemented and fitted using the RooFit C++ data modeling package [66]. The ratio of signal yields R is defined as

$$R = \frac{N^+}{N^-} \tag{6.14}$$

where N^+ and N^- are the number B^+ and B^- decays, respectively. We can represent N^+ and N^- as a function of R and $N_S \equiv N^+ + N^-$ in the following way:

$$N^+ = N_S \frac{R}{(R+1)} \tag{6.15}$$

$$N^- = N_S \frac{1}{(R+1)} \tag{6.16}$$

Using this definition, the mass fit model ($F^\pm$) for $B^\pm$ events samples is defined as

$$F^+ = \left[N_S \frac{R}{(1+R)}\right] F_S^+ + \left[N_{comb} \frac{R^{comb}}{(1+R^{comb})}\right] F_{comb}^+ + \sum_{i=1} \left[(f_{bkg_i} N_S)\, \frac{R^{bkg_i}}{(1+R^{bkg_i})}\right] F_{bkg_i}^+ \tag{6.17}$$

$$F^- = \left[N_S \frac{1}{(1+R)}\right] F_S^- + \left[N_{comb} \frac{1}{(1+R^{comb})}\right] F_{comb}^- + \sum_{i=1} \left[(f_{bkg_i} N_S)\, \frac{1}{(1+R^{bkg_i})}\right] F_{bkg_i}^- \tag{6.18}$$

where R^{comb} is the ratio of yields of the combinatorial background, R^{bkg_i} is the ratio of yields of the peaking background component, N_S is the total number of signal events, N_{comb} is the total number of combinatorial background events and F is used to define the PDF function (F_S for signal, F_{comb} for combinatorial and F_{bkgi} for peaking and partial background). The sum in i is used to indicate the peaking or partially reconstructed background component.

The following subsections define the PDFs used for the $B^\pm \to K^+K^\pm K^-$ and $B^\pm \to \pi^+K^\pm\pi^-$ decays.

6.5.2 Signal fit model

The fit model uses a sum of a Crystal Ball and a Gaussian for the signal PDF ($F_S(m)$), with common mean and different widths for the B^+ and B^- samples. The choice of this function for the signal PDF was determined from Monte Carlo studies to best describe the signal shape and was found to give the best fit stability for data.

The Crystal Ball function $\mathcal{C}(m)$ is described in section 4.12.2 and the parametrisation of the signal PDF for $B^\pm \to K^+K^\pm K^-$ and $B^\pm \to \pi^+K^\pm\pi^-$ is given by :

$$F_S(m) = f_{sig} \exp\left[\frac{-(m-m_0)^2}{2\sigma_1^2}\right] + (1-f_{sig})\mathcal{C}(m)\,. \tag{6.19}$$

where m_0 is the common mean of the Crystal Ball and the Gaussian, σ_1 is the width of the Gaussian, σ_2 of the Crystal Ball, and f_{sig} gives the fraction of the Gaussian in the sum of the two functions.

6.5.3 Background fit models

Combinatorial background : parameterised with an exponential PDF with one free parameter for the slope.

Cross-feed contribution : the shape are parameterized by a Cruijff function $\mathcal{C}(m)$, which is defined as a Gaussian function with different left-right resolutions (σ_1, σ_2) and non-Gaussian tails (a_1, a_2). Its expression is given by:

$$\mathcal{C}(m; m_0, \sigma_1, \sigma_2, a_1, a_2) = \exp\left[\frac{-(m-m_0)^2}{2\sigma_i^2 + a_i(m-m_0)^2}\right] \quad \text{where} \begin{cases} i=1 & \text{if} \quad \leq m_0 \\ i=2 & \text{if} \quad m > m_0 \end{cases} \tag{6.20}$$

Each cross-feed contribution was parameterised from MC studies performed in Ref. [85] and fixed in the mass fit. The procedure is the same as the one described in chapter 4.

Partially reconstructed backgrounds : are parameterized by an Argus function convolved with a Gaussian resolution (defined in section 4.12.3). The parameters are freely varied in the fit.

6.5.4 Mass fit procedure

The same mass fit procedure as described in Ref. [85] is used. The Crystal Ball parameters a and n of the signal component are extracted from the fit of the MC samples described in section 6.3 (passing the full event selection criteria) and fix them in the data mass fit. The widths of the Crystal Ball and the Gaussian are determined from the simultaneous fit to the full data sample of B^- and B^+ decays.

The MC sample is divided in 10 sub-samples with the same statistics as the data and the MC fits are performed using the signal model function described in the previous section. In order to decrease statistical fluctuations we used the range $5080 - 5400$ MeV/c^2. The mass fit plots of the MC sub-samples as well as the parameter results extracted from the fit for $B^\pm \to K^+K^\pm K^-$ and $B^\pm \to \pi^+K^\pm\pi^-$ modes can be found in Appendix F. The MC values that were used to fix in the data fit are shown in the tables 6.4 and 6.5, which were obtained calculating the average of the results from the MC subsamples.

6.5.5 Fit results

In Figures 6.3 and 6.4 are shown the mass fit plots of the B^- (on the left) and B^+ (on the right) data samples for $B^\pm \to K^+K^\pm K^-$ and $B^\pm \to K^+\pi^\pm K^-$ decays, respectively. In each figure is presented fits performed with 2011 (first row), 2012 (second row) and the combined 2011 and 2012 data sample (third row). The fit results can be found in Table 6.6 for $B^\pm \to K^+K^\pm K^-$ and Table 6.7 for $B^\pm \to \pi^+K^\pm\pi^-$. The parameters found for the signal and background will be fixed in the mass fit performed in each decay time bin.

$B^{\pm} \to K^{+}K^{\pm}K^{-}$ MC sample		
	2011	2012
Signal component - the average		
m_0[MeV/c^2]	5280.48 ± 0.049	5280.49 ± 0.051
σ_1[MeV/c^2]	31.302 ± 0.620	31.164 ± 0.593
σ_2[MeV/c^2]	15.096 ± 0.079	15.394 ± 0.086
a	2.366 ± 0.035	2.362 ± 0.0361
f_{sig}	0.104 ± 0.0076	0.117 ± 0.008
n	0.966 ± 0.056	0.968 ± 0.058
N_S	129035 ± 359	129032 ± 359
R	1.015 ± 0.006	1.014 ± 0.006

Table 6.4: The average of the parameters extracted from the fit of the $B^{\pm} \to K^{+}K^{\pm}K^{-}$ MC subsamples.

$B^{\pm} \to K^{+}K^{\pm}K^{-}$ MC sample		
	2011	2012
Signal component - the average		
m_0[MeV/c^2]	5280.19 ± 0.059	5280.21 ± 0.063
σ_1[MeV/c^2]	34.548 ± 0.757	34.05 ± 0.750
σ_2[MeV/c^2]	16.299 ± 0.092	16.475 ± 0.093
a	2.123 ± 0.029	2.131 ± 0.0283
f_{sig}	0.102 ± 0.008	0.110 ± 0.008
n	1.049 ± 0.049	1.037 ± 0.048
N_S	116986 ± 342	126712 ± 356
R	1.019 ± 0.006	1.014 ± 0.006

Table 6.5: The average of the parameters extracted from the fit of the $B^{\pm} \to \pi^{+}K^{\pm}\pi^{-}$ MC subsamples.

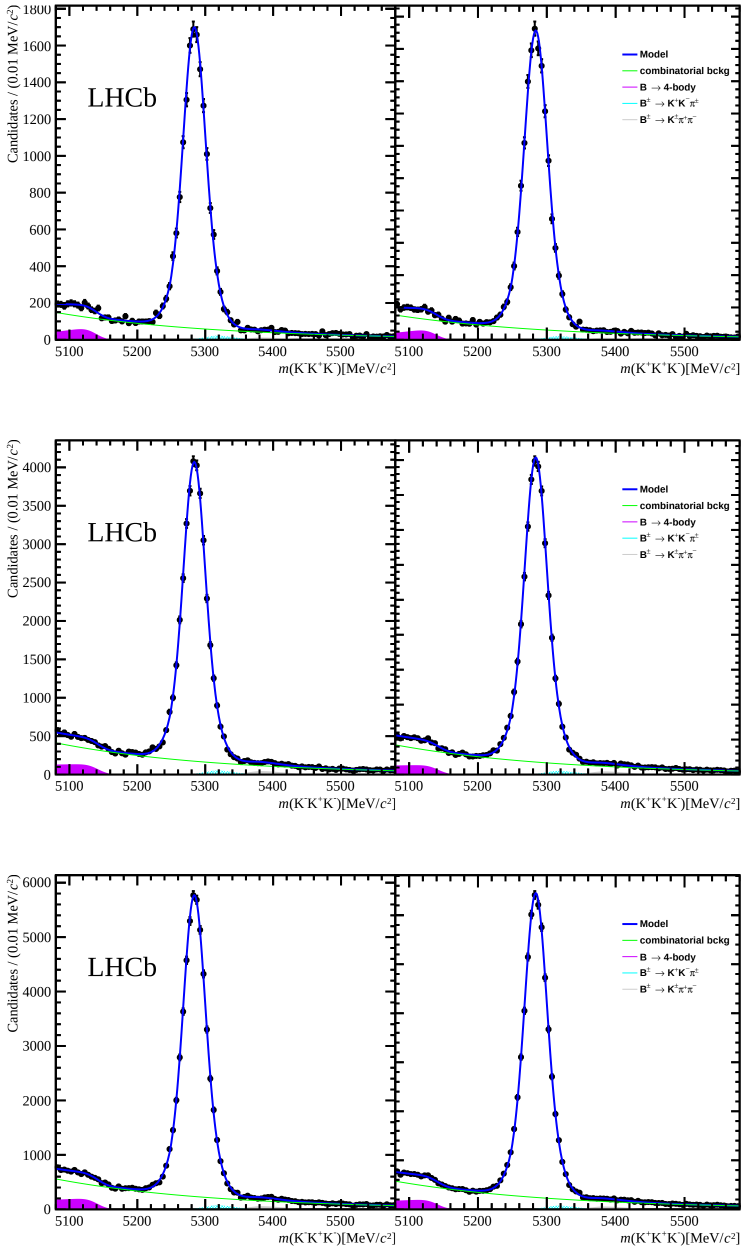

FIGURE 6.3: $B^{\pm} \to K^{+}K^{\pm}K^{-}$ candidates with final selection for 2011 data sample (first row), 2012 data sample (second row) and 2011+2012 data sample (last row). In each pair of distributions, the plot on the left is B^{-} and on the right is B^{+}. The pull distributions and the fit parameters results are in Appendix F.

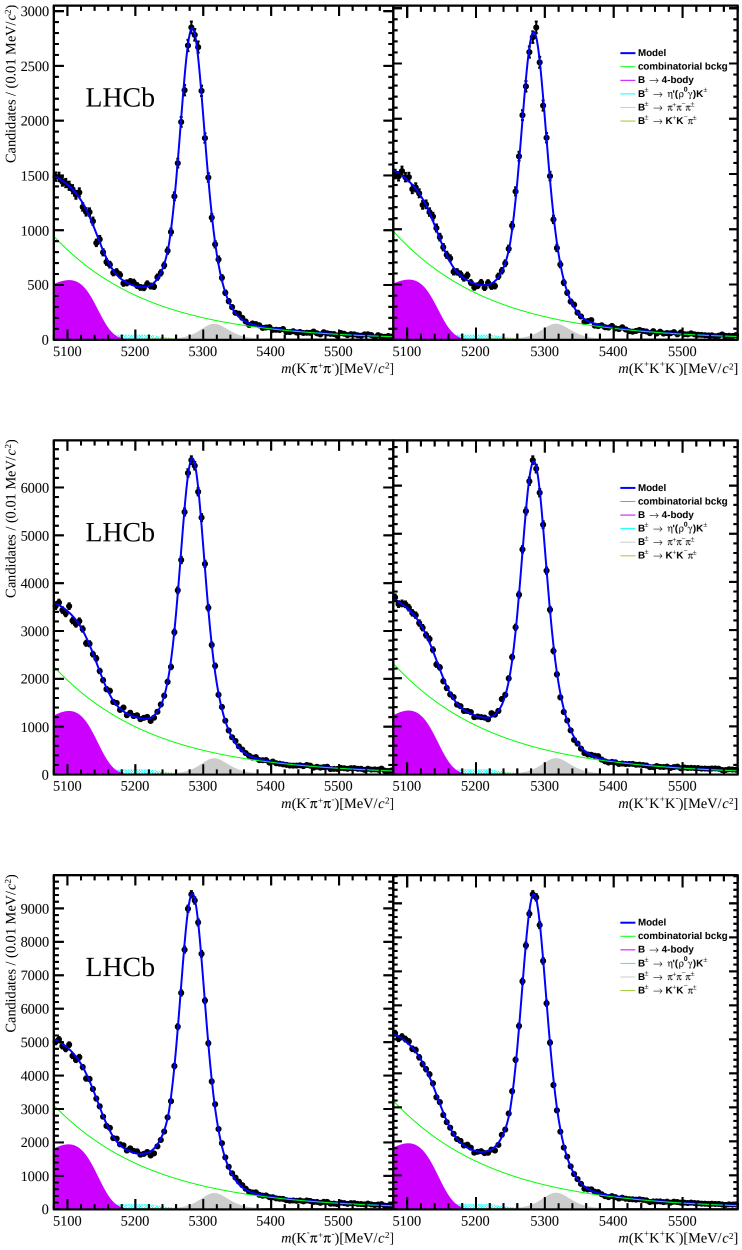

FIGURE 6.4: $B^\pm \to \pi^+ K^\pm \pi^-$ candidates with final selection for 2011 data sample (first row), 2012 data sample (second row) and 2011+2012 data sample (last row). In each pair of distributions, the plot on the left is B^- and on the right is B^+. The pull distributions and the fit parameters results are in Appendix F.

$B^{\pm} \to K^{+}K^{\pm}K^{-}$ data sample			
	2011	2012	2011+2012
Signal component			
m_0[MeV/c^2]	5284.0 ± 0.11908	5283.9 ± 0.065719	5283.9 ± 0.065889
σ_1[MeV/c^2]	22.438 (C)	23.648 (C)	23.299 (C)
σ_2[MeV/c^2]	14.811 (C)	14.597 (C)	14.682 (C)
a	2.4000 (C)	2.4000 (C)	2.4000 (C)
f_{sig}	0.47915 ± 0.013642	0.46965 ± 0.0064393	0.46889 ± 0.0068321
n	0.97000 (C)	0.97000 (C)	0.97000 (C)
N_S	31474 ± $^{(-191.93,}_{+191.17)}$	74545 ± $^{(-299.24,}_{+298.48)}$	106126 ± $^{(-355.85,}_{+355.87)}$
R	1.1304 ± 0.013666	1.1178 ± 0.0073119	1.1216 ± 0.0074170
Combinatorial component			
b	-0.00424449 ± 0.00011411	-0.00424477 ± 0.000048853	-0.00423151 ± 0.000059398
N_{comb}	12503 ± 220.69	34715 ± 257.26	47043 ± 439.25
R_{comb}	1.0290 ± 0.022898	1.0283 ± 0.0073119	1.0282 ± 0.011763
$B \to$ 4-body (partially rec. component)			
σ [MeV/c^2]	12.732 (C)	12.732 (C)	12.732 (C)
m_t [MeV/c^2]	5138.4 ± 3.5615	5142.2 ± 3.6144	5141.2 ± 2.1633
c	-23.0618 ± 21.371	-2.37318 ± 88.337	-7.25258 ± 9.0365
p	0.0000009 ± 0.71985	0.00070637 ± 0.84337	0.00026076 ± 0.089069
$Fraction$[%]	0.042244 ± 0.0040234	0.044924 ± 0.0023173	0.044565 ± 0.0023937
R_{bkg}	1.00 (C)	1.00 (C)	1.00 (C)
$B^{\pm} \to K^{+}\pi^{\pm}K^{-}$ component			
m_0[MeV/c^2]	5317.9 (C)	5317.9 (C)	5317.9 (C)
σ_1[MeV/c^2]	17.560 (C)	17.560 (C)	17.560 (C)
σ_2[MeV/c^2]	22.300 (C)	22.300 (C)	22.300 (C)
a_1	0.1600 (C)	0.1600 (C)	0.1600 (C)
a_2	0.1920 (C)	0.1920 (C)	0.1920 (C)
$Fraction$[%]	0.0176 (C)	0.0176 (C)	0.0176 (C)
R_{bkg}	1.00 (C)	1.00 (C)	1.00 (C)
$B^{\pm} \to \pi^{+}K^{\pm}\pi^{-}$ component			
m_0[MeV/c^2]	5382.3 (C)	5382.3 (C)	5382.3 (C)
σ_1[MeV/c^2]	19.18 (C)	19.18 (C)	19.18 (C)
σ_2[MeV/c^2]	31.64 (C)	31.64 (C)	31.64 (C)
a_1	0.184 (C)	0.184 (C)	0.184 (C)
a_2	0.230 (C)	0.230 (C)	0.230 (C)
$Fraction$[%]	0.012631 ± 0.0022343	0.019630 ± 0.0011345	0.017677 ± 0.0013050
R_{bkg}	1.00 (C)	1.00 (C)	1.00 (C)

TABLE 6.6: List of the $B^{\pm} \to K^{+}K^{\pm}K^{-}$ mass fit model parameters extracted from the 2011, 2012 and 2011+2012 data sample. The numbers followed by a "(C)" were fixed in the corresponding fit.

$B^{\pm} \to \pi^{+}K^{\pm}\pi^{-}$ data sample			
	2011	2012	2011+2012
Signal component			
m_0[MeV/c^2]	5283.7 ± 0.11730	5283.9 ± 0.066794	5283.9 ± 0.058502
σ_1[MeV/c^2]	25.530 (C)	16.043 (C)	27.351 (C)
σ_2[MeV/c^2]	16.018 (C)	28.698 (C)	16.275 (C)
a	2.1000 (C)	2.1000 (C)	2.1000 (C)
f_{sig}	0.45827 ± 0.011765	0.56236 ± 0.0051242	0.41056 ± 0.0051860
n	1.0400 (C)	1.0400 (C)	1.0400 (C)
N_S	50500 ± $^{(-265.80,}_{+264.19)}$	117901 ± 332.29	169386 ± 414.45
R	0.97474 ± 0.010019	0.98022 ± 0.0056694	0.97882 ± 0.0049771
Combinatorial component			
b	-0.00704448 ± 0.00007148	-0.00680180 ± 0.000034448	-0.00678918 ± 0.000028721
N_{comb}	53100 ± 652.90	129667 ± 622.65	179519 ± 758.14
R_{comb}	1.0398 ± 0.011755	1.0204 ± 0.0062924	1.0263 ± 0.0057264
$B \to$ 4-body (partially rec. component)			
σ [MeV/c^2]	16.322 (C)	16.322 (C)	16.322 (C)
m_t [MeV/c^2]	5154.0 ± 7.3032	5156.5 ± 3.6673	5158.0 ± 2.2964
c	-40.4035 ± 26.646	-49.7877 ± 42.959	-49.9826 ± 49.809
p	0.71893 ± 0.82919	0.94909 ± 0.15642	1.00000 ± 0.68628
$Fraction$[%]	0.28000 ± 0.0097987	0.29156 ± 0.0040641	0.29895 ± 0.0033506
R_{bkg}	1.00 (C)	1.00 (C)	1.00 (C)
$B^{\pm}\to\eta'(\rho^0\gamma)K^{\pm}$ component			
m_0[MeV/c^2]	5211.0 (C)	5211.0 (C)	5211.0 (C)
σ_1[MeV/c^2]	196.10 (C)	196.10 (C)	196.10 (C)
σ_2[MeV/c^2]	27.500 (C)	27.500 (C)	27.500 (C)
a_1	0.0000 (C)	0.0000 (C)	0.0000 (C)
a_2	0.0863 (C)	0.0863 (C)	0.0863 (C)
$Fraction$[%]	0.0596 (C)	0.0596 (C)	0.0596 (C)
R_{bkg}	1.00 (C)	1.00 (C)	1.00 (C)
$B^{\pm} \to \pi^{+}\pi^{\pm}\pi^{-}$ component			
m_0[MeV/c^2]	5315.9 (C)	5315.9 (C)	5315.9 (C)
σ_1[MeV/c^2]	19.470 (C)	19.470 (C)	19.470 (C)
σ_2[MeV/c^2]	20.830 (C)	20.830 (C)	20.830 (C)
a_1	0.1770 (C)	0.1770 (C)	0.1770 (C)
a_2	0.1910 (C)	0.1910 (C)	0.1910 (C)
$Fraction$[%]	0.0734 (C)	0.0734 (C)	0.0734 (C)
R_{bkg}	1.00 (C)	1.00 (C)	1.00 (C)
$B^{\pm} \to K^{+}\pi^{\pm}K^{-}$ component			
m_0[MeV/c^2]	5243.3 (C)	5243.3 (C)	5243.3 (C)
σ_1[MeV/c^2]	24.640 (C)	24.640 (C)	24.640 (C)
σ_2[MeV/c^2]	18.380 (C)	18.380 (C)	18.380 (C)
a_1	0.3200 (C)	0.3200 (C)	0.3200 (C)
a_2	0.1170 (C)	0.1170 (C)	0.1170 (C)
$Fraction$[%]	0.0112 (C)	0.0112 (C)	0.0112 (C)
R_{bkg}	1.00 (C)	1.00 (C)	1.00 (C)

TABLE 6.7: List of the $B^{\pm} \to \pi^{+}K^{\pm}\pi^{-}$ mass fit model parameters extracted from the 2011, 2012 and 2011+2012 data sample. The numbers followed by a "(C)" were fixed in the corresponding fit.

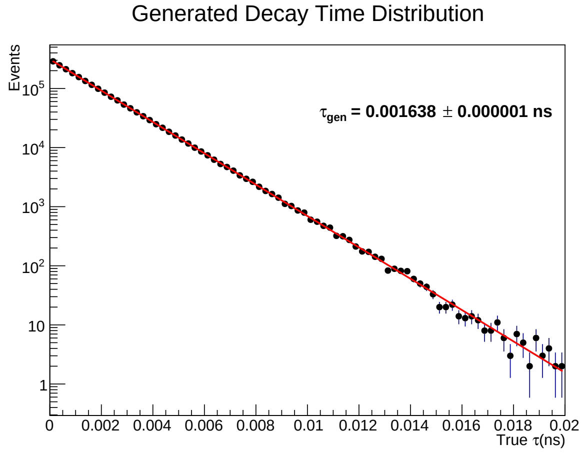

FIGURE 6.5: True lifetime distributions used as a normalisation to extract lifetime acceptances in MC. Curves are fitted with a single exponential.

	$B^{\pm} \to K^{+}K^{\pm}K^{-}$	$B^{\pm} \to \pi^{+}K^{\pm}\pi^{-}$
(2011 MC sample)		
a	0.0025 ± 0.0012	0.0029 ± 0.0012
(2012 MC sample)		
a	0.0015 ± 0.0011	0.0020 ± 0.0012
(2011 + 2012 MC sample)		
a	0.0021 ± 0.0008	0.0025 ± 0.0009

TABLE 6.8: The values of the slope extracted from the acceptance ratio fit.

6.6 Acceptance function

The acceptance function introduced in section 6.2 is obtained from simulated samples through the decay time acceptance distribution. The decay time acceptance is defined as the ratio between the reconstructed decay time distribution for selected events and the generated one. The latter represents the decay time distribution before any selection requirement and is named here as the *true* decay time distribution.

The reconstructed decay time distribution are obtained from MC samples described in section 6.1. The *true* decay time distribution is generated by using the equation 6.7 with the B lifetime τ given by the PDG, which is 1.638 ps. Also, the same statistics of the MC 2012 and 2011 samples. The generated true decay time distribution is shown in Figure 6.5.

Thus, by performing the ratio of the decay time acceptance of B^{+} and B^{-}, we obtain the acceptance ratio. In Figure 6.6 shows the acceptance ratio distributions fitted by a linear function $(1 + at)$, where a is the slope. The values of the slope for each mode are shown in Table 6.8. For both decays can be seen that the acceptance of B^{+} and B^{-} have a slight difference. Thus, our acceptance function is defined as $A_r(t) = (1 + at)$, where the slope is used as a correction when fitting the measured decay time ratio:

$$r(t) = R_0(1 + at)e^{-t\Delta_{B_{+}B_{-}}} \tag{6.21}$$

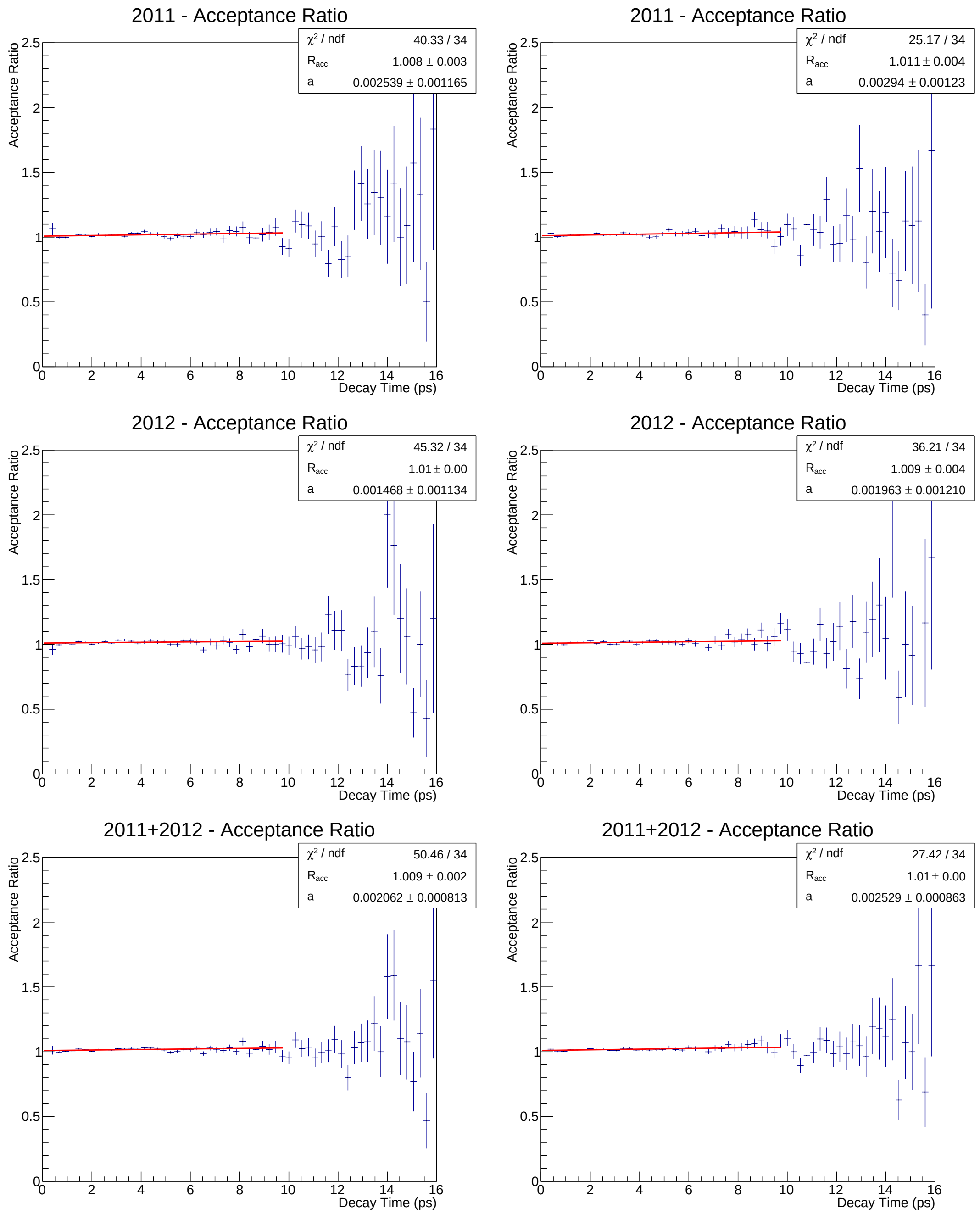

FIGURE 6.6: Ratio of the decay time acceptances between B^+ and B^- for the $B^\pm \to K^+K^\pm K^-$ channel (first column) and the $B^\pm \to \pi^+K^\pm\pi^-$ channel (second column).

6.7 Measurement of the lifetime difference

The procedure consist in performing a mass fit in each decay time bin i in view of obtaining the ratio of the yields as a function of the decay time. The distribution of the ratio of the yields should follow an exponential, therefore it is fitted in the following way in order to obtain $\Delta_{B_+B_-}$:

$$[N_{B+}/N_{B_-}]_i = A_r(t)R_0e^{-t\Delta_{B_+B_-}} \tag{6.22}$$

where R_0 is a normalisation, $\Delta_{B_+B_-} = \frac{1}{\tau_{B+}}$ - $\frac{1}{\tau_{B-}}$ is the difference of the inverse of the lifetimes and $A_r(t)$ the acceptance function. As shown previously, the correction with acceptance ratio should be included, therefore the equation 6.21 is used in the fit ratio. Furthermore, we use the second order exponential approximation :

$$r = R_0(1+at)(1-t\Delta_{B_+B_-} + \frac{t^2\Delta^2_{B_+B_-}}{2}) \tag{6.23}$$

We divide the data into bins of width of 0.7 ps. Each time bin is fit, fixing the signal and background shape to those obtained from full fit mass, showed in the section 6.5.5. Only the yields of the signal and backgrounds are freely varied in the fit to each time bin. The mass distributions of the fits in each time bins can be found in the Appendix H.

In this analysis we use bin width of 0.7 ps and a fit range of 0.0 - 9.8 ps for the two modes. We also performed the ratio for different binning widths, it can be found in Appendix G.

6.7.1 MC results

The fit to the distribution of the ratio of signal yields obtained with MC samples are shown in Figures 6.7 and the results in Table 6.9. In case that there is no significant lifetime difference between B^+ and B^-, the fitted value of $\Delta_{B_+B_-}$ is expected to be zero for all cases. For the MC11 and MC12 results, the $\Delta_{B_+B_-}$ obtained are consistent with the expectation. The R_0 is the ratio between the total number of B^+ and B^- signal yields, therefore we expect for the MC that R_0 obtained to be one, as the MC samples are generated without CP asymmetry. The results obtained show R_0 compatible with one, within the statistical uncertainties, for all cases.

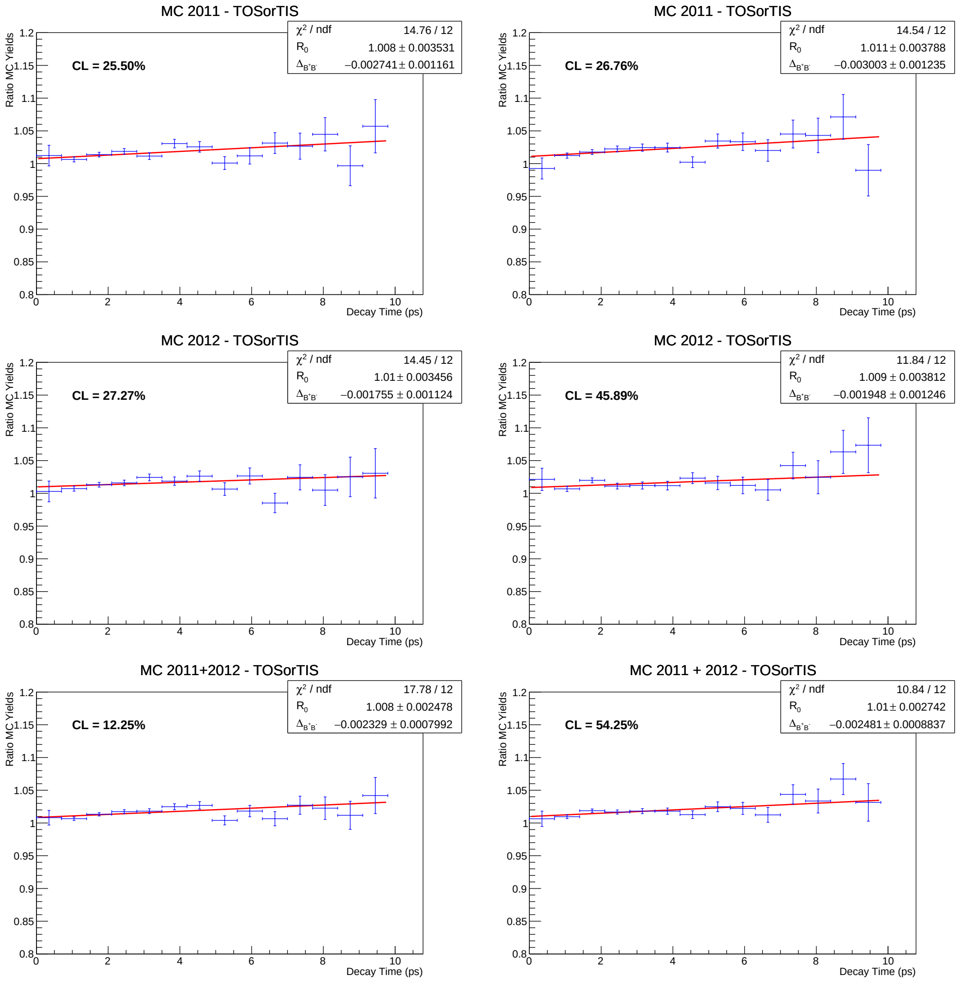

FIGURE 6.7: B^+/B^- ratio of the yields for MC11 (first row), MC12 (second row) and MC11+MC12 (third row) for the $B^\pm \to K^+K^\pm K^-$ decay (left column) and $B^\pm \to \pi^+K^\pm\pi^-$ decay (right column).

6.7.2 Data results

The fit to the distribution of the ratio of signal yields obtained with the data samples are shown in Figures 6.8 and 6.9, for $B^\pm \to K^+K^\pm K^-$ decay and $B^\pm \to \pi^+K^\pm\pi^-$ decay respectively.

The results obtained for the $B^\pm \to K^+K^\pm K^-$ data sample show a slight difference between the fitted value of $\Delta_{B_+B_-}$ from 2011 and 2012. However, in the Figure 6.8 it is also shown the ratio for 2011+2012, for this case no discrepancy with respect the expected is observed. Thus, this result suggest that the small discrepancy observed between 2011 and 2012 data is likely due to statistical fluctuation. The R_0 obtained for both data samples have a discrepancy larger than 3σ, as expected due to the *CP* asymmetry already observed in this decay channel.

In the case of $B^\pm \to \pi^+K^\pm\pi^-$, shown in Figure 6.9, no discrepancy in relation to $\Delta_{B_+B_-}$ was observed and the R_0 obtained shows an asymmetry between B^+ and B^- signal events, as expected. A summary of the measurements is shown in Table 6.10.

We also performed the fit to the ratio distribution separately for each L0 trigger requirements: `"L0Hadron_TOS"` (TOS) and `"L0Global_TIS"` (TIS). The plots as well as the results can be found in Appendix I.

$B^{\pm} \to K^{+}K^{\pm}K^{-}$ MC sample			
	2011	2012	2011+2012
$\Delta_{B_{+}B_{-}}$	-0.0027 ± 0.0012	-0.0017 ± 0.0011	-0.0023 ± 0.0008
R_0	1.0080 ± 0.0035	1.0100 ± 0.0034	1.0080 ± 0.0025
$B^{\pm} \to \pi^{+}K^{\pm}\pi^{-}$ MC sample			
	2011	2012	2011+2012
$\Delta_{B_{+}B_{-}}$	-0.0030 ± 0.0012	-0.0020 ± 0.0012	-0.0025 ± 0.0009
R_0	1.0110 ± 0.0038	1.009 ± 0.0038	1.0100 ± 0.0027

TABLE 6.9: Results for $\Delta_{B_{+}B_{-}}$ and R_0 extracted from the MC fit ratios.

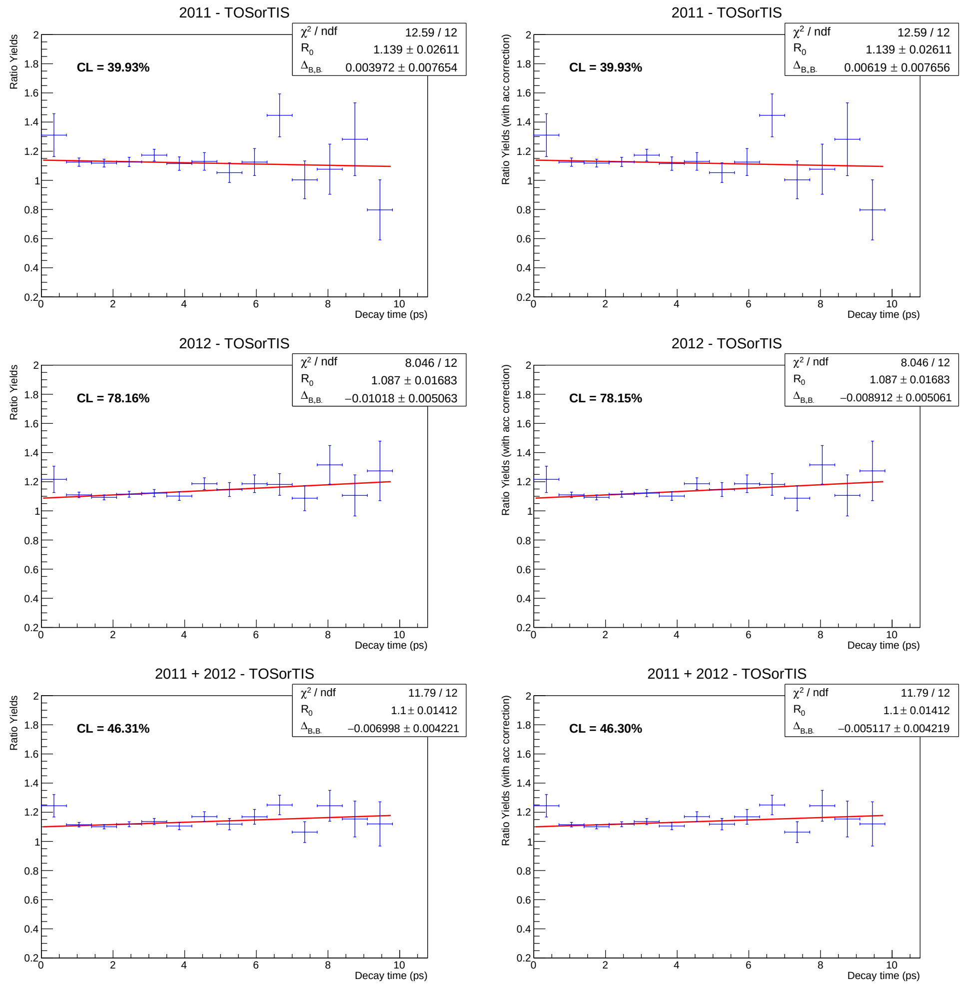

FIGURE 6.8: B^+/B^- ratio of the yields for 2011 (first row), 2012 (second row) and 2011+2012 (third row) data sample for the $B^\pm \to K^+K^\pm K^-$ channel, without (left column) and corrected with the MC acceptance (right column).

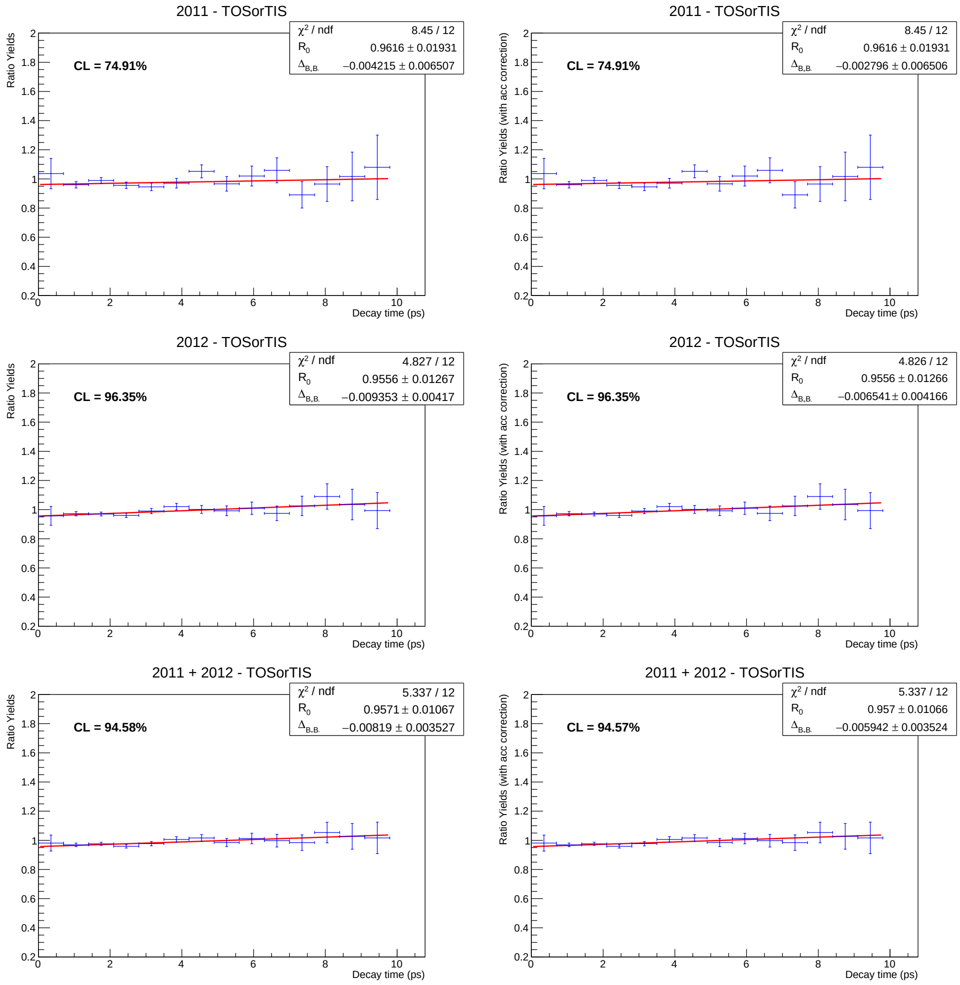

FIGURE 6.9: B^+/B^- ratio of the yields for 2011 (first row), 2012 (second row) and 2011+2012 (third row) data sample for the $B^{\pm} \to \pi^+ K^{\pm} \pi^-$ channel, without (left column) and corrected with the MC acceptance (right column).

$B^{\pm} \to K^{+}K^{\pm}K^{-}$ data sample			
	2011	2012	2011+2012
$\Delta_{B_+B_-}$	0.0062 ± 0.0077	-0.0089 ± 0.0051	-0.0051 ± 0.0042
R_0	1.139 ± 0.0261	1.087 ± 0.0168	1.100 ± 0.0141
$B^{\pm} \to \pi^{+}K^{\pm}\pi^{-}$ data sample			
	2011	2012	2011+2012
$\Delta_{B_+B_-}$	-0.0028 ± 0.0065	-0.0065 ± 0.0042	-0.0059 ± 0.0035
R_0	0.9616 ± 0.0193	0.9556 ± 0.0127	0.9570 ± 0.0107

TABLE 6.10: Results for $\Delta_{B_+B_-}$ and R_0 extracted from the data fit ratios corrected with MC acceptance.

$B^{\pm} \to K^{+}K^{\pm}K^{-}$ data sample		
	2011 data sample	2012 data sample
R	1.1304 ± 0.0137	1.1178 ± 0.0073
A_{raw}^{L}	-0.0612 ± 0.0064	-0.0556 ± -0.0035
A_{raw}^{P} - Ref.[85]	-0.06090 $\pm$ $^{(-0.0060,}_{+0.0059)}$	-0.05460 ± 0.00390
$B^{\pm} \to \pi^{+}K^{\pm}\pi^{-}$ data sample		
R	0.97474 ± 0.010019	0.98022 ± 0.0056694
A_{raw}^{L}	0.0128 ± 0.0051	0.0100 ± 0.0027
A_{raw}^{P} - Ref.[85]	0.0115 $\pm$ 0.0048	0.0093 ± 0.0031

TABLE 6.11: The values obtained from nominal mass fit.

6.8 Cross-checks

Some cross-checks have been performed to validate the results obtained.

Firstly, we checked the mass fit through the global raw charged asymmetry A_{raw} whose is defined as:

$$A_{raw} = \frac{N^{-} - N^{+}}{N^{-} + N^{+}} \tag{6.24}$$

where N^{-} and N^{+} are the number B^{-} and B^{+} decays, respectively, and it is obtained from thr mass fit. Using the results from total B invariant mass fit and the equation above, we can obtain A_{raw} from R, with $R = \frac{N^{+}}{N^{-}}$:

$$A_{raw} = \frac{1 - R}{1 + R} \tag{6.25}$$

The results are shown in the table 6.11, where the A_{raw} from R is denoted as A_{raw}^{L} and to comparison, we also present the A_{raw} published in [85] that is denoted by A_{raw}^{P}. The main purpose behind the calculation of A_{raw} is to check the mass fit function used, once the measurement of the charged asymmetry was published with the same channels and data set used in this analysis. Both results obtained are statistically compatible with the published one.

Another cross-check is a hypothesis test that consists in confronting two fit functions evaluating their confidence level. Since we have obtained $\Delta_{B_{+}B_{-}}$ compatible with zero, we can checked our results by calculating the confidence level for the null hypothesis and compare it with the one obtained previously. The null hypothesis, H_0, is the case where the function used to fit the ratio distribution is a constant function, which implies:

$$H_0 : \Delta_{B_{+}B_{-}} = 0 \tag{6.26}$$

The confidence levels calculated for the H_0 hypothesis can be found in Tables 6.12 and 6.13. The results show that the null hypothesis is accepted for all cases.

We also have checked the lifetime difference, $\Delta_{B_{+}B_{-}}$, for bins widths of 0.5 and 0.9 ps, the results can be found in the Table 6.14 and the plots in Appendix G. All the results are consistent with zero.

Confidence Level			
	2011	2012	2011 and 2012
$B^{\pm} \to K^{+}K^{\pm}K^{-}$			
H_0 hypothesis	48%	52%	34%
$B^{\pm} \to \pi^{+}K^{\pm}\pi^{-}$			
H_0 hypothesis	78%	70%	63%

TABLE 6.12: Confidence Level for the null hypothesis.

Confidence Level				
	Region I	Region II	Region III	Region I + Region III
$B^{\pm} \to K^{+}K^{\pm}K^{-}$				
H_0 hypothesis	24%	72%	19%	45%

TABLE 6.13: Confidence Level for the null hypothesis in the phase space region study.

	$B^{\pm} \to K^{+}K^{\pm}K^{-}$ (2011+2012)	$B^{\pm} \to \pi^{+}K^{\pm}\pi^{-}$ (2011+2012)
Nominal $\Delta_{B_{+}B_{-}}$	-0.0051 $\pm$ 0.0042	-0.0059 $\pm$ 0.0035
0-10 ps (0.5 ps bins) $\Delta_{B_{+}B_{-}}$	-0.0035 $\pm$ 0.0042	-0.0057 $\pm$ 0.0035
0.5-9.5 ps (0.5 ps bins) $\Delta_{B_{+}B_{-}}$	-0.0042 $\pm$ 0.0043	-0.0059 $\pm$ 0.0035
0-9.9 ps (0.9 ps bins) $\Delta_{B_{+}B_{-}}$	-0.0072 $\pm$ 0.0037	-0.0051 $\pm$ 0.0042

TABLE 6.14: Ratio fits using different binning schemes. The plots are shown in Appendix G.

6.9 Summary and Conclusions

In this chapter, the measurement of the lifetime difference between B^{+} and B^{-} in $B^{\pm} \to K^{+}K^{\pm}K^{-}$ and $B^{\pm} \to \pi^{+}K^{\pm}\pi^{-}$ decay modes was presented with data collected by the LHCb in 2011 and 2012. The CP asymmetries in these decays were already measured with the same dataset with significance 4.3σ for $B^{\pm} \to K^{+}K^{\pm}K^{-}$ and 2.8σ for $B^{\pm} \to \pi^{+}K^{\pm}\pi^{-}$ [85]. In addition, they are coupled channels connected by final state interactions.

The lifetime difference measurement was performed following the same strategy as in the Ref. [84]. The procedure is based on the calculation of the ratio between B^{+} and B^{-} signal yields as a function of the decay time. The ratio distribution is built through the B signal yields obtained in different decay time bin. In each bin, a simultaneous mass fit is performed with the signal and background shape fixed from those values found in the B mass fit in the full decay time range. Then, the ratio distribution, $r(t)$, is fitted with the function below:

$$r(t) = A_r(t) R_0 e^{-t\Delta_{B+B-}}$$

where Δ_{B+B-} give us the lifetime difference between B^{+} and B^{-}, R_0 is the total ratio of signal yields of B^{+} and B^{-} which measures the *CP* violation and $A_r(t)$ is the acceptance function correction obtained through the simulation.

For each data sample, the Δ_{B+B-} was found to be:

$$\Delta_{B+B-}(B^{\pm} \to K^{+}K^{\pm}K^{-})^{2011} = 0.0062 \pm 0.0077(\text{stat})$$

$$\Delta_{B+B-}(B^{\pm} \to K^{+}K^{\pm}K^{-})^{2012} = \text{-}0.0089 \pm 0.0051(\text{stat})$$

$$\Delta_{B+B-}(B^{\pm} \to K^{+}K^{\pm}K^{-})^{2011+2012} = \text{-}0.0051 \pm 0.0042(\text{stat})$$

$$\Delta_{B+B-}(B^{\pm} \to \pi^{+}K^{\pm}\pi^{-})^{2011} = \text{-}0.0028 \pm 0.0065(\text{stat})$$

$$\Delta_{B+B-}(B^{\pm} \to \pi^{+}K^{\pm}\pi^{-})^{2012} = \text{-}0.0065 \pm 0.0042(\text{stat})$$

$$\Delta_{B+B-}(B^{\pm} \to \pi^{+}K^{\pm}\pi^{-})^{2011+2012} = \text{-}0.0059 \pm 0.0035(\text{stat})$$

These results indicate that in both decay modes, there is no lifetime difference between B^{+} and B^{+}. In addition, all results are statistically compatible with the published one [85]. Even though no lifetime difference was observed, the measurement could be improved with a phase-space acceptance correction and a resolution study.

Chapter 7

Contributions to the LHCb Upgrade

During the period of 2019-2021, the LHCb experiment will be upgraded and many of its sub-detectors will be replaced. In particular, the current tracker detector will be replaced by a new technology made by scintillating fibres.

In this chapter, a brief overview of the new tracker detector is given, followed by the description of tests performed in some of its components to monitor their quality. The work presented in this chapter was performed during the period from May 2017 to January 2018 at the National Institute for Subatomic Physics (Nikhef) in Amsterdam, the Netherlands, as part of an exchange doctoral program.

7.1 The LHCb Upgrade

In order to obtain events which are clear and better reconstructible, LHCb works with lower luminosity in comparison with the others main experiments at the LHC[1]. The upgrade aims to enlarge the data sample significantly by increasing the LHCb instantaneous luminosity to $2 \times 10^{33}\mathrm{cm}^{-2}\mathrm{s}^{-1}$, which is a factor five higher than the current luminosity. With the upgrade, this is expected to increase the yield for hadronic channels by a factor 20 compared to the current experiment [86].

However this increased luminosity will lead to larger track densities as well as higher radiation dose and to maintain/improve the performance of LHCb in these conditions, the detector needs to be upgraded.

Another limitation concerns the trigger system. The current LHCb trigger consists of a hardware trigger (L0) and a software trigger (HLT). The L0 reduces the visible bunch crossings from 30MHz to 1MHz at which frequency the front-end electronics can be readout. The upgraded LHCb will operate at a factor of five times the current luminosity and at this luminosity the 1 MHz readout becomes a bottleneck, as the limited information available to the L0 trigger leads to an unacceptable loss of efficiency, particularly for hadronic final states [87]. To cope with the limitation, a new trigger paradigm will be adopted. The current hardware plus software trigger will be replaced by a full software trigger and all of the front-end devices will be upgraded in order to read the detector out at the LHC bunch crossing frequency of 40 MHz [86].

The current sub-detectors were designed for low multiplicity and with the increased luminosity, they have to deal with the higher particle densities as well as satisfy the requirements of finer granularity and better radiation hardness [88]. In the tracking system in which all tracking detectors will be replaced. The Vertex

[1] LHCb luminosity is a order of $4 \times 10^{32}\mathrm{cm}^{-2}\mathrm{s}^{-1}$ while LHC can provide a luminosity of order $10^{34}\mathrm{cm}^{-2}\mathrm{s}^{-1}$.

Locator (VELO) will be completely redesigned and equipped with electronics capable of reading out at 40 MHz data that will provide fast pattern recognition and track reconstruction to the software trigger. The rest of the current tracker system, which is composed of the Trigger Tracker (TT) and the T- stations will also be redesigned. The TT will be replaced by a detector with the same technology, i.e. silicon strips, but with finer granularity, especially in the inner part, in order to reduce the occupancy and ghost tracks rate; the new TT system is called Upstream Tracker (UT). The T-stations, currently using silicon strips in the inner part (IT) and straw tubes in the outer part (OT) will be replaced by a single technology using layers of scintillating fibres read out by silicon photo-multipliers (SiPMs) placed outside the acceptance [89, 90]. This new system is called Scintillating Fibre Tracker (SciFi) and its characteristics are presented in the next section.

The particle identification system, which is composed of two Ring Imaging Cherenkov (RICH) detectors, the electromagnetic and hadronic calorimeters, as well as five muon chambers, will also be upgraded. In the case of calorimeters, the detector modules and photo-multipliers of the ECAL and HCAL are going to be kept. Both calorimeters are going to be equipped with new readout electronics, compatible with 40 MHz readout. Both RICH detectors are going to occupy the same locations and employ the same gas radiators as the original detectors. In the case of the RICH placed upstream the magnet, the optics will be redesigned in order to cope with the higher expected occupancies. For the same reason and due to the removal of the L0 trigger, the Scintillating Pad Detector (SPD) and the Preshower detectors (PS), as well as the first muon chamber (M1), all placed in front of the electromagnetic calorimeter, will be removed [88][91].

A schematic side-view of the upgraded LHCb detector with the location of all new sub-detectors is shown in Figure 7.1.

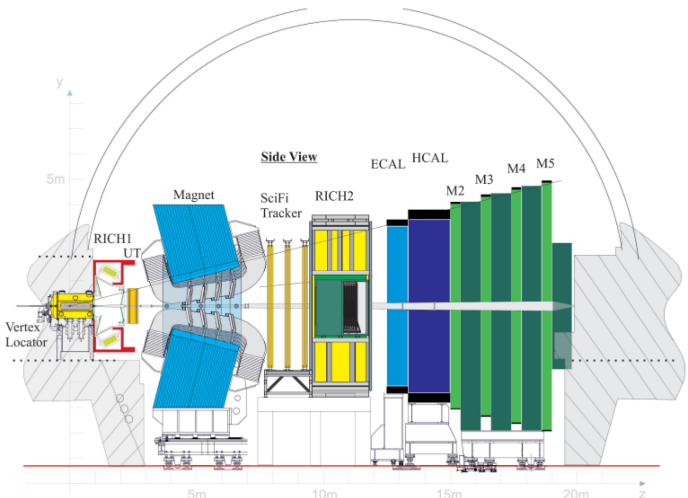

FIGURE 7.1: Schematic side-view of the upgraded LHCb detector, where UT stands for Upstream Tracker (the current TT station). and SciFi Tracker for Scintillating Fibre Tracker (the current T-stations) [92].

7.2 The Scintillating Fibre Tracker

The Scintillating Fibre Tracker (SciFi) consists of three stations (T1,T2,T3) composed of four detection layers each, as shown in Figure 7.2. There are 10 modules in T1-T2 and 12 modules in T3 in each detection layer, and a total of 128 modules for the complete detector. Each module (0.5 m × 4.8 m) is composed of 8 mats (4 on the top and 4 on the bottom) with a length of 2.4 m, and each mat is made of six layers of scintillating fibres.

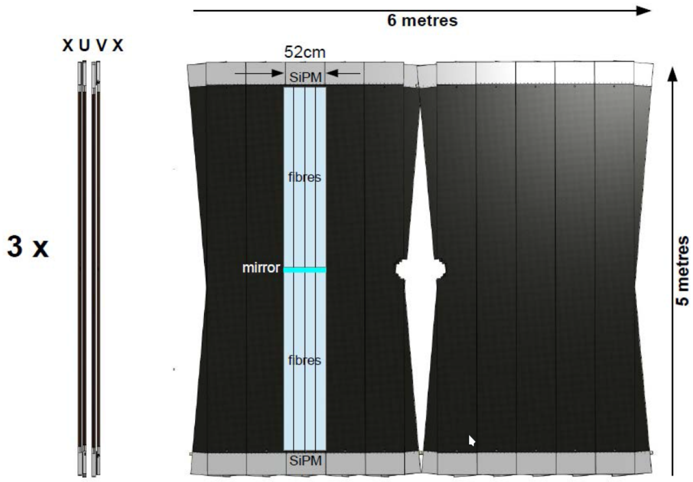

FIGURE 7.2: Schematic view of the SciFi Tracker. Highlighted in blue are the eight fibre mats with the mirror in the middle. Mirrors are glued to the end of the fibres mats to increase the light yield.

The scintillating fibres are the active material of the SciFi tracker. Each fibre has a circular cross-section with a nominal diameter of 250 μm and consists of a core surrounded by two claddings, which have descending refraction indices to enable the transport of light via internal reflection. An illustration of a fibre is shown in Figure 7.3.

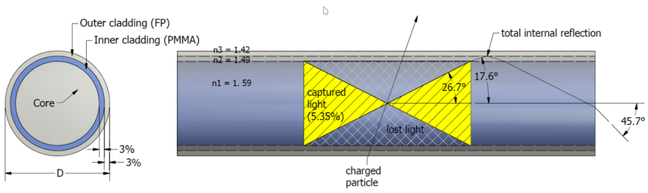

FIGURE 7.3: Transverse (left) and longitudinal (right) section of a double cladded fibre, with a schematic representation of the light generation and transport [93].

The scintillating photons are detected by multi-channel silicon photomultipliers (SiPM). Each fibre mat will be readout by 4 SiPMs and a module will be readout by 32 SiPMs. A SiPM consists of a matrix of pixels, where each pixel can detect a single photon. Each SiPM is made of 128 channels arranged into dies of 64 channels, each channel containing 96 pixels. The pixels themselves measure 62.5μm×57.5μm resulting in a rectangular channel of 250μm width, as shown in Figure 7.4 (A).

The working principle of the SciFi tracker is illustrated in Figure 7.4 (B): a particle that crosses the fibres produces scintillation photons, which propagate through the

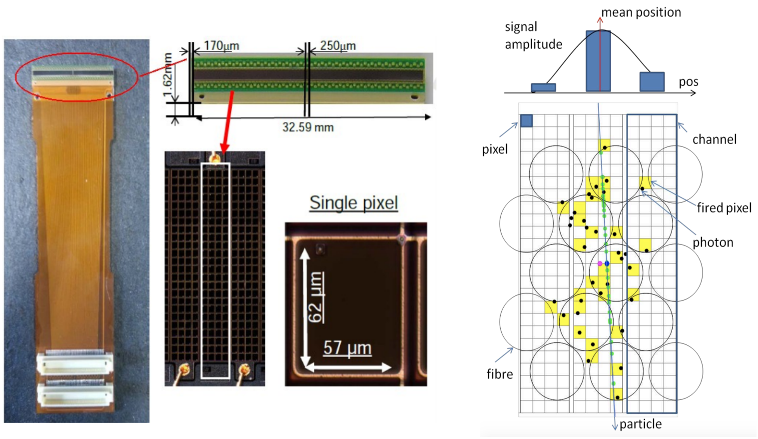

(A) (B)

FIGURE 7.4: In (A) overview of one silicon photomultiplier. The elpise denotes the 128 channels and the white rectangle shows one channel. In (B) the detection principle of the SciFi tracker. The fibres cross-sections are indicated in blue. The fired pixels are highlighted in yellow. Taken from [89].

fibres and are detected by multichannel SiPMs. The particle deposits energy in more than one fibre which results in a signal typically wider than one SiPM channel. The signals from those channels that pass a certain threshold are grouped together as a cluster. The position of the particle is then calculated as a weighted average of all the channels in a cluster.

Noise affect the SiPM performance. The major contribution comes from the Dark Count Rate (DCR), which is a signal generated in the SiPM by thermal agitation. The dark events are indistinguishable from the signal generated by a photon. Since the SiPM dark events decrease with temperature, it has been estimated that for a satisfactory tracking performance after irradiation the SiPMs need to be cooled to -40°C in order to reduce the DCR to an acceptable level. Thus, the SiPMs are mounted in so-called cold-boxes and cooled down by 3D-printed titanium cold-bars to -40°C [93]. An illustration is shown in Figure 7.5. Each cold-box will cool 16 SiPMs connected to a read-out box (ROB) housing the front-end electronics. Each module will have two identical ROBs, at the top and at the bottom, where the fibres are interfaced with the SiPMs [94].

7.2.1 Detector requirements

Several requirements for the SciFi tracker need to be achieved in order to assure a satisfactory detector performance. The two most important are the hit detection efficiency and the spacial resolution.

Hit efficiency is strongly dependent on the amount of photon produced in the scintillating fibres that are detected by the SiPMs. The parameter that measures this quantity is called light yield and its unit is photo-electrons. Therefore to achieve a high hit efficiency, enough light yield must be produced and detected.

In the case of the spatial resolution, it is related to the mechanical precision to with which the modules are build. The single hit spatial resolution in the bending plane of the magnet (x- direction) is required to be better than 100 μm. In order to satisfy this requirement over the total area of 360 m^2, the construction of modules

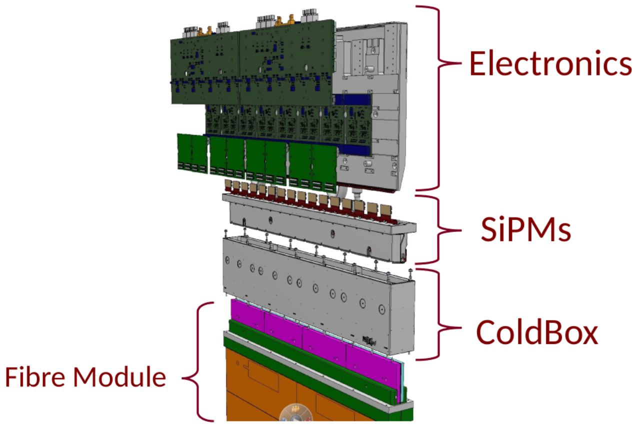

FIGURE 7.5: Schematic view of the SciFi layer composed of a module, cold-box, 16 SiPMs and the read-out electronics.

and mats have to ensure that the scintillating fibres inside a single module (8 mats) are straight and well aligned and with deviations smaller than 50 μm [92].

To build the LHCb SciFi Tracker 128 modules are needed, and as one module consist of 8 fibre mats, at least 1024 fibre mats have to be produced in total. The serial production of all fibre mats and modules needs to ensure a fast and reliable process of production in order to achieve the requirements presented in the LHCb Tracker Upgrade Technical Design Report [89].

In order to determine the performance of the detector with respect to the requirements, measurements to ensure the quality of each detector component need to be performed in the laboratories and in test beam campaigns.

In the next sections, a brief introduction of the production of fibre mats and modules are given, followed by the quality assurance procedures performed during the serial production of the SciFi components. Out of many quality assurances that are performed, this work is focused on two of them. One is the measurement of the light output of fibre mats and modules and the second is the measurement of the straightness of the scintillating fibres within the detector modules.

7.3 Fibre Mats

The scintillating fibres are the active component of the SciFi Tracker and must be assembled very precisely and with high quality. To achieve a sufficient light yield at the photo-detector, the scintillating fibres are arranged into multi-layers mats with 6 layers through a process called winding. A winding machine, shown in Figure 7.6, is used to place the fibre on a turning threaded wheel which guides the fibres. Before starting the winding, precision holes are drilled into the winding wheel and filled with glue producing alignment pins bonded to the bottom of the fibre, as shown in Figure 7.7. This process is made in order to assure the overall alignment of the fibre mats within the detector. Therefore the straightness of the mats during the module production is checked by measuring the pins positions attached to the mat. After producing the fibre matrix, end pieces and the mirror are glued and the fibres mats are ready to be assembled in module [92, 89]. Figure 7.7 (C) shows a picture of a finished fibre mat.

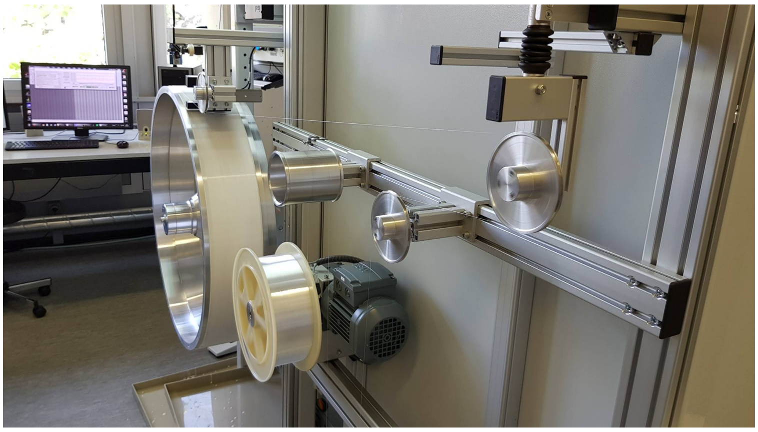

FIGURE 7.6: The winding machine which is used to lay and glue the 6 layers of fibre.

7.3.1 Quality Assurance of the Fibre Mats

Fibres mats and modules are produced in specialised Winding and Module Centres. Fibre mats are wound, finalized and characterised in the Winding Centre before getting shipped to the Module Centre. There are 4 Winding Centres (Aachen, Dortmund, Lausanne and Moscow) and two Module Centres (Nikhef and Heidelberg).

After the winding process, the light yield needs to be measured for all the fibre mats before and after the cut, which it is done in the Winding Centres. After the fibre mats are finished, they are transported to the Modules Centres. Before integrating fibre mats in detector modules the light yield is measured, where only a sample 1 out of 8 is checked. To ensure that the fibre mat did not get damaged during the transportation. The procedure used to perform the light yield measurement in the Module Centre is described below.

Light Yield measurement

To measure the light yield of a fibre mat, the scintillation process is stimulated by the use of a ^{90}Sr source (beta particles) and the response is measured with SiPMs. In Figure 7.8 shows a scheme of the setup used to meausure the light yield of one fibre mat, which consists of:

- A template to place the fibre mat.
- ^{90}Sr source.
- Trigger system to select ^{90}Sr events.
- 4 SiPMs.
- Readout electronics.

The light produced in the fibres is detected by SiPMs connected to the read-out electronics. The trigger uses a scintillator to select the events. The signal of the SiPMs is sent via USB board to the PC and dedicated software is used to analyse the data.

In Figure 7.9 a typical result obtained for one fibre mat tested is presented. What is shown is the light yield for each event in every single channel, where each event is going through a clustering algorithm (average of photon yield). The light yield for

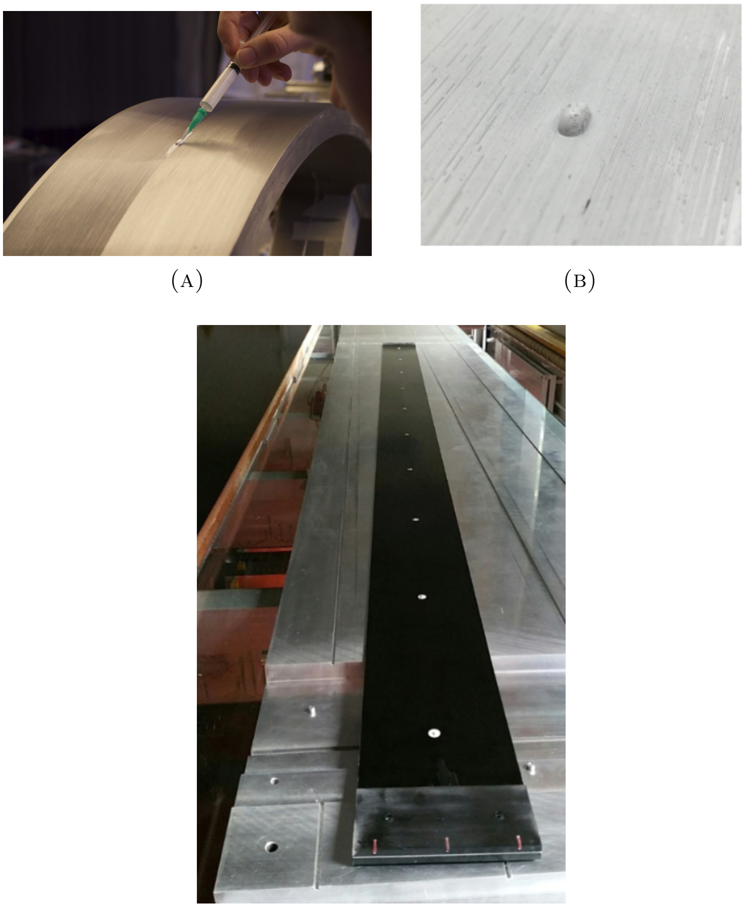

(A) (B)

(C)

FIGURE 7.7: (A) pin hole being filled with glue in the winding wheel, (A) pin hole on fibre mat and (C) a finished fibre mat, where in white are the alignment pins.

this particular fibre mat is homogeneous over the full width of the fibre. In addition, the average photon yield is compatible with the other measurements, which indicates that the mat suffered no damage in transport. A drop in light yields occurs every 64 channels due to the gaps between the SiPM dies as well as the gaps between the SiPM arrays. The edges of the fibre mats also have a drop in light yield due to the missing charge of the neighbouring channel. The measurement is performed for one out of 8 fibre mats that arrive at the Module Centre.

7.4 Fibre Modules

Each full SciFi tracker detector plane is divided into 12 individual detector components, called fibre module. A fibre module is the assembly of 8 fibre mats (4 on the top and 4 on the bottom) sandwiched between honeycomb and carbon fibre components to provide stability and support. The end of the modules are read out by 16 SiPMs [89].

The Scifi tracker has 3 stations (T1-T3), with 4 detection layers each. As each detector layer can have 10 modules (T1/T2) or 12 modules (T3) with a size of 52cmx5m, 128 modules will be needed to build the detector. A schematic illustration of the modules components are shown in Figure 7.10.

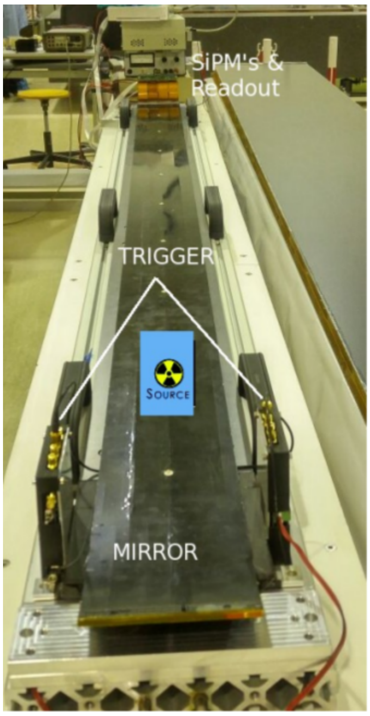

FIGURE 7.8: Setup to measure the light yield of a fibre mat.

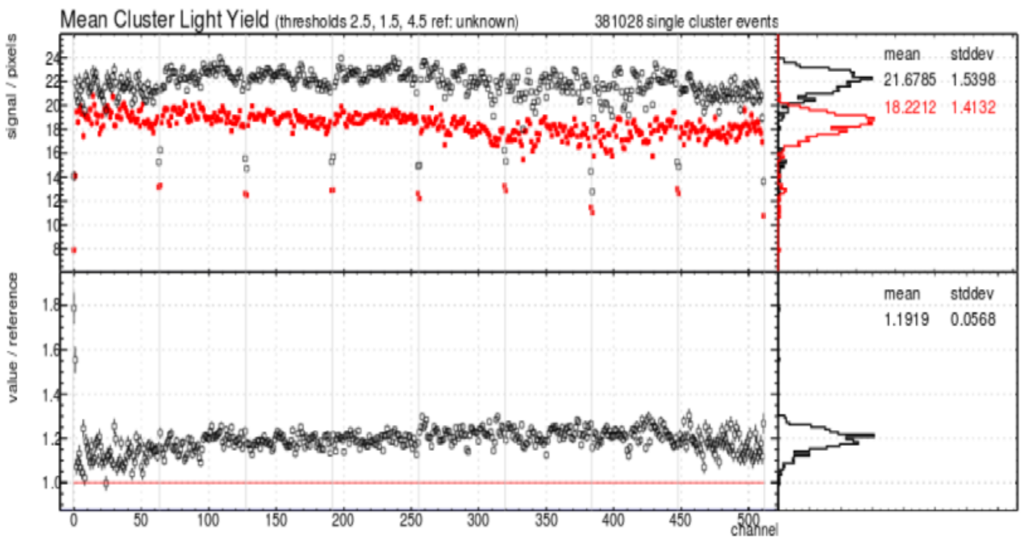

FIGURE 7.9: Light yield measurement for a single fibre mat as a function of the SiPMs channels (4×128). The light yield is homogenous over the full width of the fibre mat. The dips every 64 channels are due to the gaps between the SiPMs dies. In red is the measurement of the reference fibre mat and in black is the average measurement of other runs for comparison. On top right histograms with the mean light yield are displayed. On the bottom left is shown the ratio between the two measurements.

7.4.1 Module Assembly

The module assembly procedure has to ensure flatness and mechanical stability of the detector module as well as the correct alignment of fibre mats with respect to each

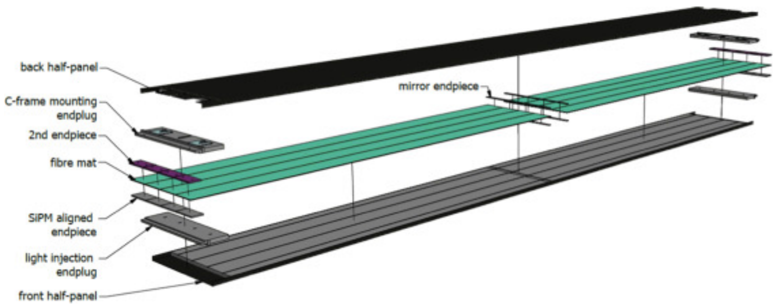

FIGURE 7.10: Schematic illustration of all fibre module components. Taken from [92].

other. It is done with the help of a high precision full size template (5 m × 0.53 m). The template gives the precision placement and alignment of the mats with respect to one another within the module.

The module assembly steps are briefly described below and showed in the Figure 7.11.

1. Fibre mats are placed onto the template.

2. Glue is applied to the surface of the fibre mats. The carbon fibre is placed on top of the fibre mats. The panels are pressed to the fibre mats by means of vacuum.

3. The bonded half-module is removed from the template and turned over.

4. Quality test to ensure straightness of the mats is made by measuring the pins positions attached to the mat.

5. Step 2 is repeated.

6. The module is cleaned and checked. In addition, side walls are glued to the detector module, in order to create a mechanical protection.

7. Quality assurance with cosmic rays is performed to check the light yield.

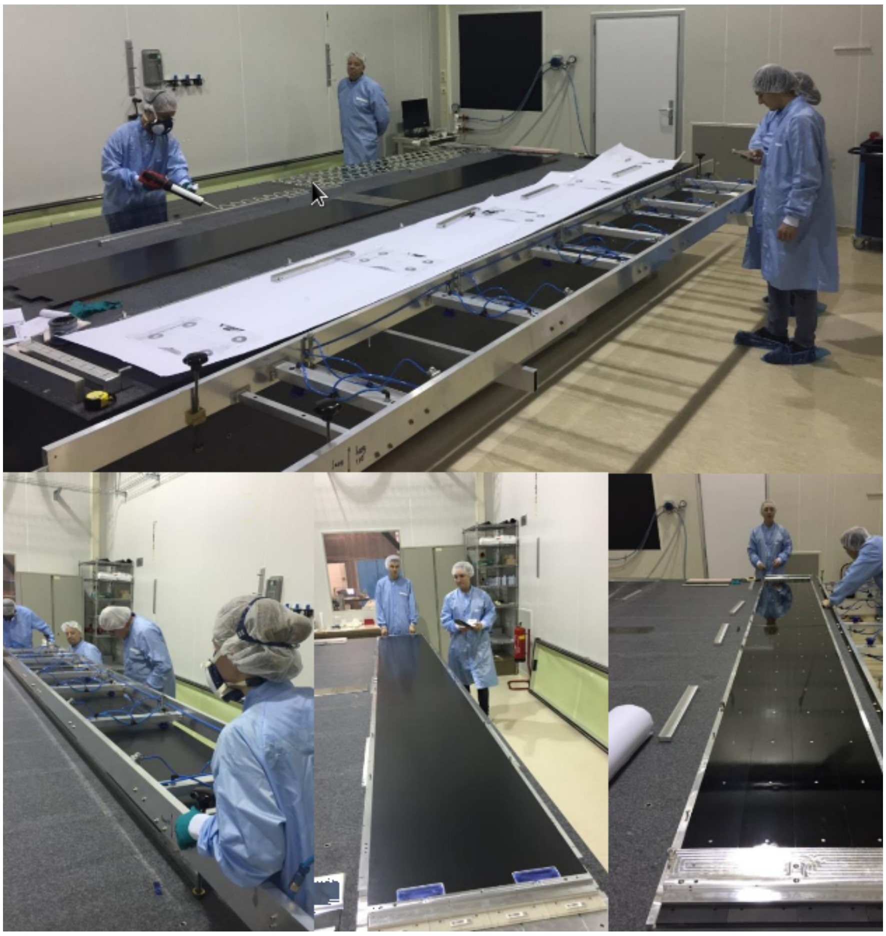

FIGURE 7.11: The photo on top shows the glue being applied to the surface of the 8 mats. Bottom left, the panels on top of the mats pressed with vacuum bump. Bottom right shown the bonded half-module turned, where after the quality test the second half-panel must be glued.

7.4.2 Quality Assurance- Straightness and Flatness of the fibre mats within the module

To check if the fibres are straight in the module, a measurement of the alignment pins position is performed. For this, a laser system that reflects the straightness and the flatness of the modules was developed. The experimental setup is shown in Figure 7.12 (B) and consists of:

- A position sensing detector, which allows determining x-position and y-position at the same time, where the z-direction is defined in the fibre direction in the mat and y-direction perpendicular to the plane of the mat.
- A laser.
- A custom-made support for the sensor, made of aluminium and with a cavity in the middle of 5 mm, which allows very accurate positioning with respect the pins.
- Acquisition software.

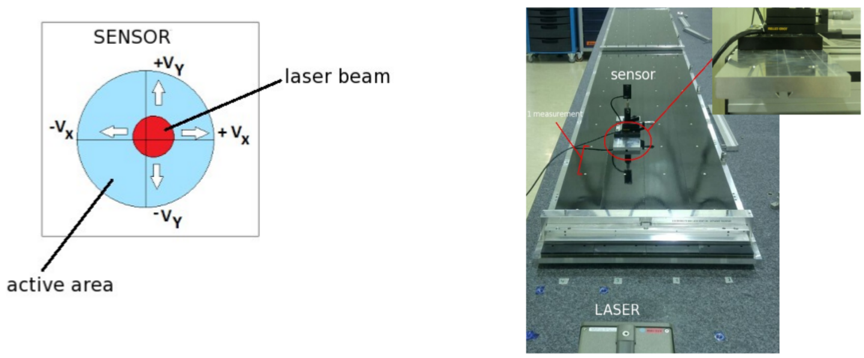

(A) (B)

FIGURE 7.12: In (A) an illustration of the sensor working principle. In (B) the experimental setup to measure the alignment pins on fibre mat. The support for the sensor with the cavity to allow the passage of the pins is highlighted.

The sensor determine the x and y position from measurement of the incident light that hits the surface, as illustrated in Figure 7.12 (A). Once the voltage output is measured for a certain position, a calibration in order to obtain a corrected transformation from voltage to position can be done.

An acquisition software was developed in order to obtain a precision measurement of each pin position. A summary of the measurements of the straightness and flatness of mats for 3 modules are shown in Figure 7.13. It shows a standard deviation of 46 μm for the straightness (x-direction) and 26 μm for the flatness (y-direction), well within the SciFi requirements. This procedure has to be performed for all finished modules and the expectation is to obtain a similar result to ensure a good spatial resolution of the detector.

7.4.3 Test stand for Light Yield measurement

The light yield measurement for the module is performed just after the assembly (similarly to the fibre mat) to ensure that the fibre mats have not been damaged during the module assembly which could lead to a reduction of the light yield.

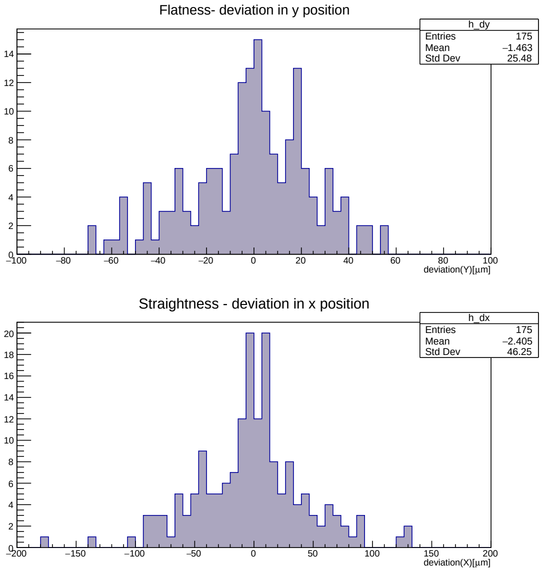

FIGURE 7.13: Deviation from a linear function of all pins measured for 3 Module.

The measurement is performed by using cosmic rays. Due to the dimension of the module, cosmic rays rather than a radioactive source are more appropriated for the full module measurement. In addition, studies comparing both sources were done and showed that quality assurance measurements with cosmic rays is possible if enough data is taken [95].

The experimental setup is shown in Figure 7.14 and consists of:

- A full size fibre module.
- Two scintillation counters used to trigger the cosmic rays pass through the module.
- 16 SiPMs (for each module side) and their readout for the full width of the module.
- Light injection system to calibrate the SiPMs.

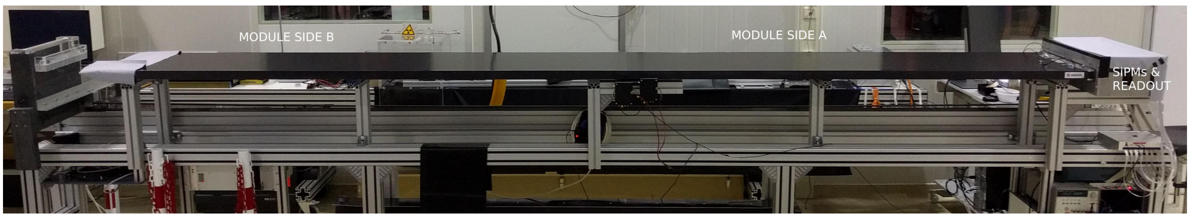

FIGURE 7.14: The experimental setup for the modules to measure the light yield using cosmic rays.

The light yield measurement for each SiPM channel using the cosmic setup for one full-size module is shown in Figure 7.15. The data was collected for 12 hours and the result obtained is a measurement of the light yield homogeneous over the full width of the module. In the middle of each SiPM the light yield drops due to the gap between dies. For this module, no damage or dead channel were observed. This is a typical result obtained for one module, the same procedure has to be done for all finished modules and a similar result to the one showed is expected to be obtained to guarantee a good performance of the detector.

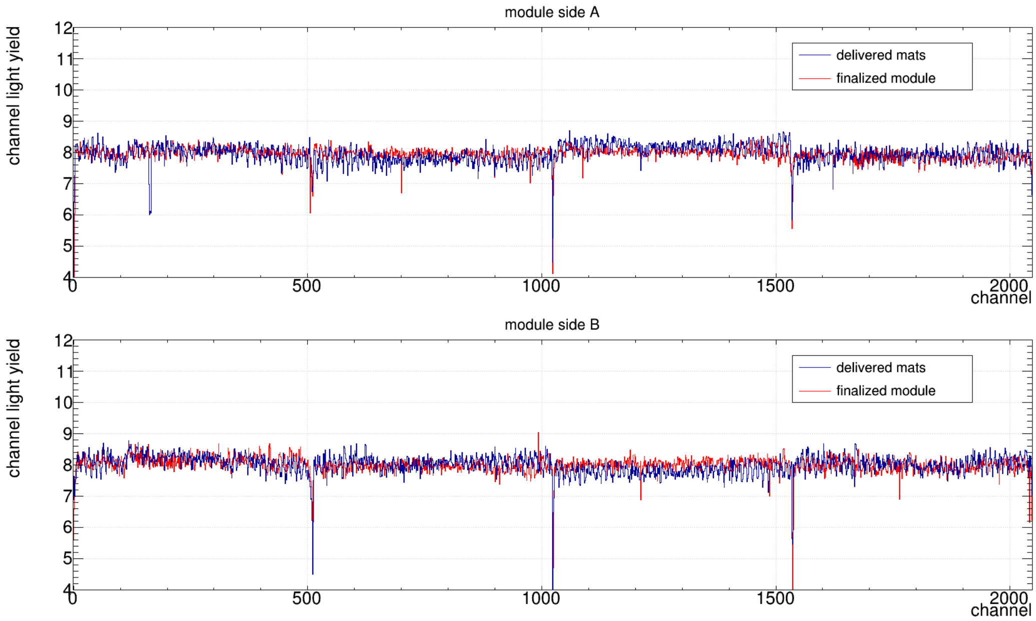

FIGURE 7.15: Light yield measured with cosmic rays for a full size detector module. Side A measurement corresponds to the four fibres mats placed of the top of the module while Side B measurement correspond to fibres mats of the bottom of the module. In both measurements, the light yield is homogeneous with no apparent damages.

7.5 Summary

The SciFi tracker will replace the current LHCb tracker detector during the LS2 in 2019-2021. It is based on scintillating fibres read out with silicon photomultipliers. The two key parameters of the SciFi tracker are the hit efficiency, related to the light yield produced by the scintillating fibres and the spacial resolution, connected to the straightness of the fibres. Both parameters have to satisfy requirements to ensure a good performance of the detector.

In this chapter were presented the quality tests related with the hit efficiency and the spacial resolution. Those were performed in fibres mats and modules of the SciFi tracker in order to check the light yield and the position of the fibres in the detector.

The setups presented were used to assure the quality of about a hundred modules and thousands of fibre mats in the Module Centres. At the current moment, the serial production of the detector components is successfully completed and the detector is being assembled at CERN since the beginning of 2019.

Chapter 8

Conclusions

The studies presented in this thesis, focused on physics analyses of charmless three-body B decays and the detector upgrade of the LHCb experiment.

Experimental results of CP violation in charmless three-body B decays have been shown interesting features related to CP violation effects, mainly in localised regions of the phase space of these decays. Those effects have been attributed to new sources of CP violation, which is of fundamental importance to the phenomenological study of heavy flavour physics. To understand these effects further large data sample is needed to perform precise measurements. In this thesis, four charmless B decays modes have been studied using either the Run II 1.9 fb^{-1} data collected at $\sqrt{s} = 13$ TeV in 2015 and 2016 or the full Run I data sample which are the 1 fb^{-1} data collected at $\sqrt{s} = 7$ TeV in 2011 and 2 fb^{-1} data collected at $\sqrt{s} = 8$ TeV in 2012. We also perform a qualitative study with the combination of the full Run I and 2015 and 2016 Run II data samples.

The first analysis of this thesis presents the measurement of the inclusive CP asymmetry for four charmless three-body B decays: $B^{\pm} \to K^{+}K^{\pm}K^{-}$, $B^{\pm} \to \pi^{+}K^{\pm}\pi^{-}$, $B^{\pm} \to K^{+}\pi^{\pm}K^{-}$ and $B^{\pm} \to \pi^{+}\pi^{\pm}\pi^{-}$, performed with data collected by LHCb in 2015 and 2016 (Run II). The CP violation in these channels was observed in previous LHCb analyses with Run I data, this measurement aims to update the previous LHCb results. The selection of $B^{\pm} \to h^{+}h^{\pm}h^{-}$ decays was improved with a multivariate analysis performed specifically for each channel, applying tighter particle identification requirements and more completed acceptance correction. The number of signal candidates increased in 25% for $B^{\pm} \to \pi^{+}K^{\pm}\pi^{-}$, 20% for $B^{\pm} \to \pi^{+}\pi^{\pm}\pi^{-}$ and 50% for the $B^{\pm} \to K^{+}\pi^{\pm}K^{-}$ decay channel. The inclusive CP asymmetry was obtained by correcting the charge raw asymmetry ($\mathcal{A}_{raw}$) by the acceptance and non-physical asymmetries,

- $\mathcal{A}_{CP}$ ($B^{\pm} \to \pi^{+}K^{\pm}\pi^{-}$) = +0.004 ± 0.003(stat).
- $\mathcal{A}_{CP}$ ($B^{\pm} \to K^{+}K^{\pm}K^{-}$) = -0.047 ± 0.003(stat).
- $\mathcal{A}_{CP}$ ($B^{\pm} \to \pi^{+}\pi^{\pm}\pi^{-}$)= +0.076 ± 0.007(stat).
- $\mathcal{A}_{CP}$ ($B^{\pm} \to K^{+}\pi^{\pm}K^{-}$) = -0.134 ± 0.013(stat).

Those values, apart from the $B^{\pm} \to \pi^{+}K^{\pm}\pi^{-}$, are consistent with the previous LHCb analysis that was based on a luminosity of 3.0 fb^{-1}. These represent the preliminary results of the work being performed by the LHCb group at CBPF, in which the inclusive CP asymmetry will be obtained with full Run II (2015-2018) data sample. The same procedures for the selection requirement, background reduction, fit model and acceptance correction have been applied to the measurement with full Run II dataset, in which the total integrated luminosity corresponds to approximately 6 fb^{-1}. It is expected to increase the number of signal yields by a factor 4 compared to the to Run I measurement, so the statistical error is expected, on average, to decrease a factor 2. We aim to publish the results with full Run II dataset next year (2020).

Besides the inclusive *CP* asymmetry, it was also presented a study of the phase-space of these decays. By using a qualitative method, we attempted to localise new sources of localised *CP* asymmetry with the data collected by LHCb in 2011, 2012, 2015 and 2016. By exploring the two-body invariant mass projections, we have shown that the CP asymmetry patterns have become more evident in some regions with observed *CP* asymmetry, such as the region of the $\phi(1020)$ resonance in $B^{\pm} \to K^{+}K^{\pm}K^{-}$ decay and the re-scattering region for the four decay channels studied. Also, regions with intriguingly high asymmetry have been observed for the first time, such as the region around the $\chi_{c0}(1P)$ resonance in the $B^{\pm} \to \pi^{+}\pi^{\pm}\pi^{-}$ decay channel. This could indicate the presence of the $B^{\pm} \to (\chi_{c0})\pi^{\pm} \to \pi^{\pm}\pi^{+}\pi^{-}$ process, which has been recently quoted in Ref. [96] as a process to be accessible only in the LHCb upgrade II (2030). This study demonstrates that the use of a qualitative method to analyse the *CP* violation in the phase-space can be very useful to locate the Dalitz plot regions with large asymmetries and thus assisting in the choice of the regions to measure the localised *CP* asymmetries.

The second analysis performed in this thesis aimed to investigate other types of violation in decays with observed *CP* violation. We explored the $B^{\pm} \to K^{+}K^{\pm}K^{-}$ and $B^{\pm} \to \pi^{+}K^{\pm}\pi^{-}$ decay channels with full 2011 and 2012 statistics. The search is based on the framework of some models with explicit Lorentz violation, which suggest that a Lorentz non-invariant interaction could be probed by measuring the lifetime of a high energy particle. Thus, we measured the lifetime difference between B^{+} and B^{-} to investigate other violations. The procedure is to obtain the ratio of the decay time distribution of B^{+} and B^{-} and then perform a fit to extract the lifetime difference Δ_{B+B-}. For each data sample, Δ_{B+B-} was measured to be:

$$\Delta_{B+B-}(B^{\pm} \to K^{+}K^{\pm}K^{-})^{2011} = 0.0062 \pm 0.0077(\text{stat})$$

$$\Delta_{B+B-}(B^{\pm} \to K^{+}K^{\pm}K^{-})^{2012} = \text{-}0.0089 \pm 0.0051(\text{stat})$$

$$\Delta_{B+B-}(B^{\pm} \to K^{+}K^{\pm}K^{-})^{2011+2012} = \text{-}0.0051 \pm 0.0042(\text{stat})$$

$$\Delta_{B+B-}(B^{\pm} \to \pi^{+}K^{\pm}\pi^{-})^{2011} = \text{-}0.0028 \pm 0.0065(\text{stat})$$

$$\Delta_{B+B-}(B^{\pm} \to \pi^{+}K^{\pm}\pi^{-})^{2012} = \text{-}0.0065 \pm 0.0042(\text{stat})$$

$$\Delta_{B+B-}(B^{\pm} \to \pi^{+}K^{\pm}\pi^{-})^{2011+2012} = \text{-}0.0059 \pm 0.0035(\text{stat})$$

These results are compatible with the SM theoretical predictions. They represent the first measurement of lifetime difference in these decays with the purpose to investigate *CPT* and Lorentz violation. These measurements will be improved by the LHCb group at CBPF with the full Run I and Run II data, also, it is foreseen to include another measurement proposed in this thesis, which is the measurement of the lifetime as a function of the B momentum.

The LHCb experiment has a wider upgrade program to improve significantly its luminosity and thus achieve larger data samples to provide unprecedented precision in heavy flavour studies; in a long-term plan is foreseen 4 upgrades until 2034. The next LHCb upgrade (2019-2021) aims to increase the current LHCb luminosity to a factor five and to deal with the higher densities of particles, most of its sub-detector will be replaced. The tracker system will be completely redesigned, in particular, the T-stations will be replaced by the SciFi tracker, a detector made by scintillating fibres and readout by silicon-photo multipliers, which aims to provide high hit efficiency and spatial resolution better than 100 μm. In this thesis, it was presented some quality tests developed to ensure the good performance of the SciFi tracker components. The same tests were used in serial production, which is now successfully completed.

Appendix A

BDT optimization

A.1 Specific for each channel

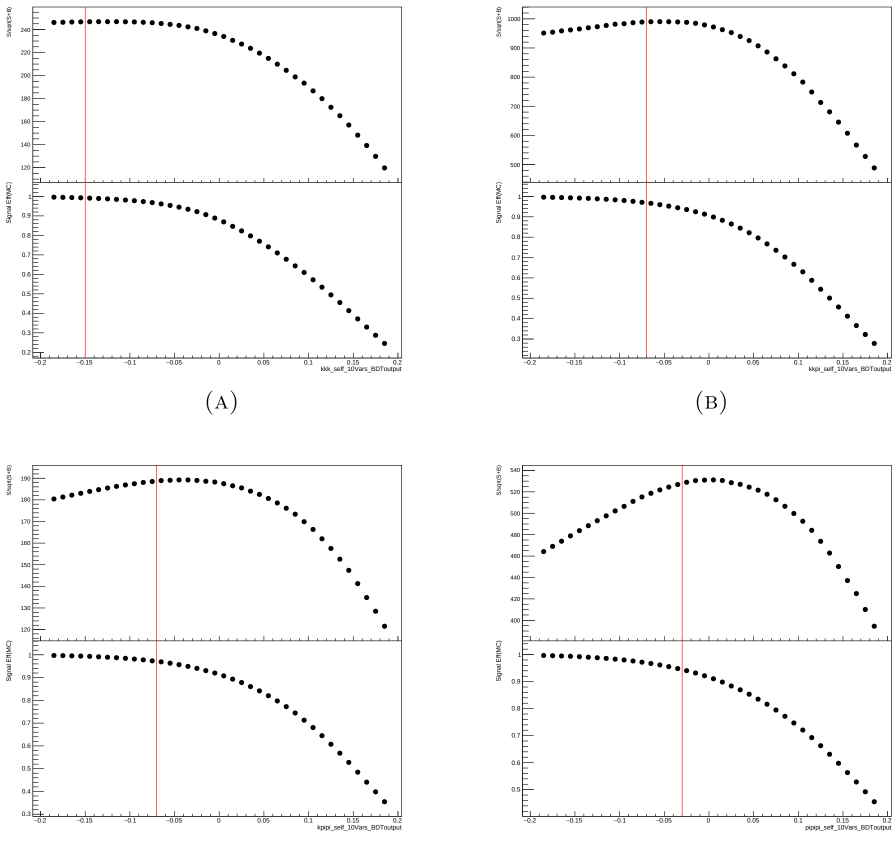

FIGURE A.1: The significance $S/\sqrt{(S+B)}$ (top) and signal efficiency from MC (bottom) as a function of the BDT output for the optimization specific for each channel. The red line indicates the location of the cut on the BDT output variable was choosen. (A) $B^{\pm} \to K^{+}K^{\pm}K^{-}$ mode, (B) $B^{\pm} \to K^{+}\pi^{\pm}K^{-}$, (C) $B^{\pm} \to K^{+}\pi^{\pm}K^{-}$ and (D) $B^{\pm} \to \pi^{+}\pi^{\pm}\pi^{-}$.

A.2 Common to all channel

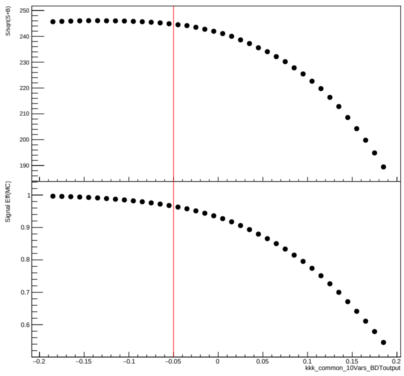

(A)

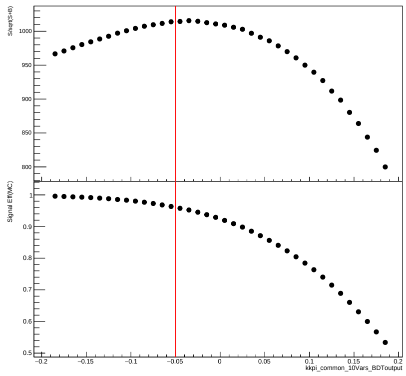

(B)

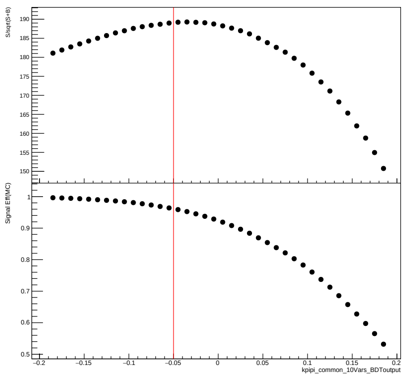

(C)

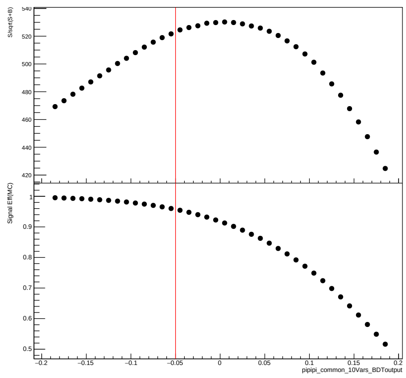

(D)

FIGURE A.2: The significance $S/\sqrt{(S+B)}$ (top) and signal efficiency from MC (bottom) as a function of the BDT output for the optimization common to all channel. (A) $B^{\pm} \to K^{+}K^{\pm}K^{-}$ mode, (B) $B^{\pm} \to K^{+}\pi^{\pm}K^{-}$, (C) $B^{\pm} \to K^{+}\pi^{\pm}K^{-}$ and (D) $B^{\pm} \to \pi^{+}\pi^{\pm}\pi^{-}$.

Appendix B

PID selection

B.1 $B^{\pm} \to K^{+}\pi^{\pm}K^{-}$

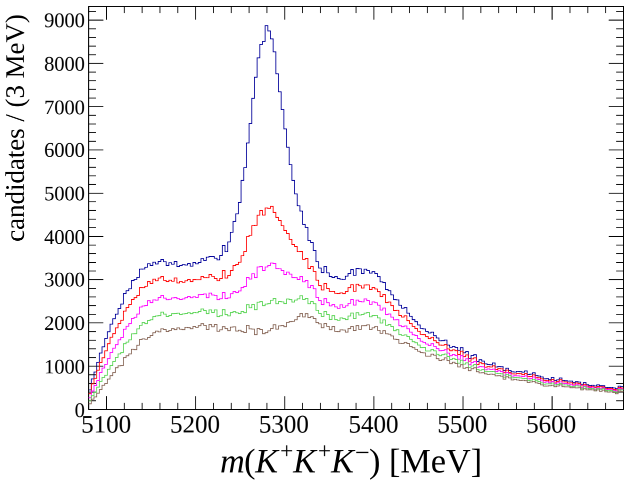

FIGURE B.1: The $B^{+} \to K^{+}K^{+}K^{-}$ signal from the $B^{+} \to K^{+}\pi^{+}K^{-}$ sample. Histograms in red, magenta, green and brown correspond to the requirement of `ProbNNk`<0.4, 0.3, 0.2 and 0.1, respectively. The plot has the 2015+2016 data and includes both polarities.

B.2 $B^{\pm} \to \pi^{+}\pi^{\pm}\pi^{-}$

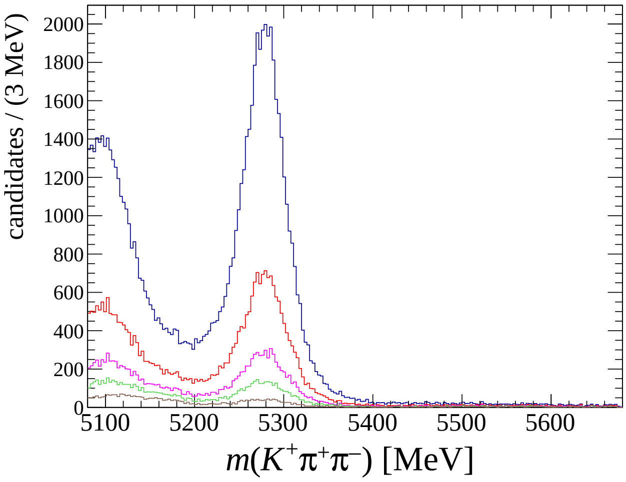

FIGURE B.2: The $B^+ \to \pi^+ K^+ \pi^-$ signal from the $B^+ \to K^+ \pi^+ K^-$ sample. Histograms in red, magenta, green and brown correspond to the requirement of `ProbNNpi`<0.4, 0.3, 0.2 and 0.1, respectively. The plot has the 2015+2016 data and includes both polarities.

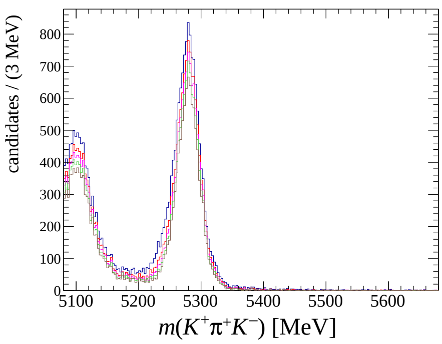

FIGURE B.3: The $B^+ \to \overline{D}^0(\to K^- K^+)\pi^+$ signal from the $B^\pm \to K^+ \pi^\pm K^-$ sample. Histograms in red, magenta, green and brown correspond to the simultaneous requirement of `ProbNNpi`, `ProbNNk`>0.3, 0.4, 0.5 and 0.6, respectively, after the negative PID is applied.

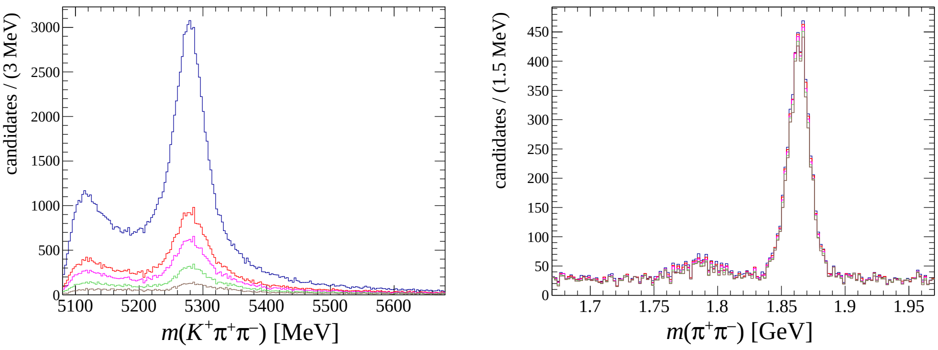

(A)

(B)

FIGURE B.4: (A) The $\overline{D}^0(\to \pi^- K^+)\pi^+$ invariant mass distribution of candidates from the $B^\pm \to \pi^+\pi^\pm\pi^-$ sample. The red, magenta, green and brown histograms illustrate the impact of the `d1,2,3_ProbNNk`< 0.4, 0.3, 0.2 , 0.1 requirements, respectively. (B) The $\pi^+\pi^-$ invariant mass distribution from $B^\pm \to \pi^+\pi^\pm\pi^-$ candidates, with `d1,2,3_ProbNNk`<0.1 for all three tracks (blue), and with the additional cut showing the impact of the cut `d1,2,3_ProbNNpi`>0.2 (red), 0.3 (magenta), 0.4 (green) and 0.5(brown).

Appendix C

Logarithmic and residual of the plots

In this appendix is presented the mass fits plot of B^+ and B^- samples in the logarithmic scale and the residuals for the $B^\pm \to \pi^+ K^\pm \pi^-$, $B^\pm \to K^+ K^\pm K^-$, $B^\pm \to \pi^+ \pi^\pm \pi^-$ and $B^\pm \to K^+ \pi^\pm K^-$ with 2015 and 2016 data samples. In addition, Tables C.1-C.4 A.1-A.8 present the complete parameters results obtained from the fit.

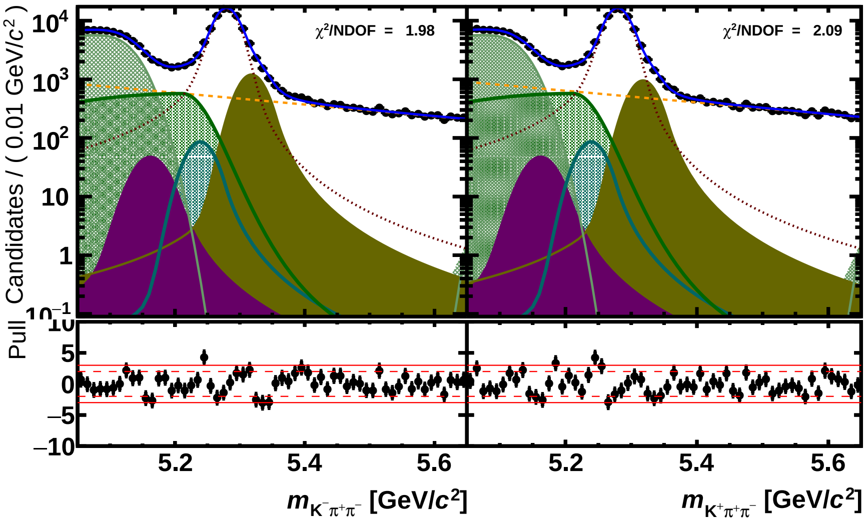

(A) $B^{\pm} \to \pi^{+}K^{\pm}\pi^{-}$

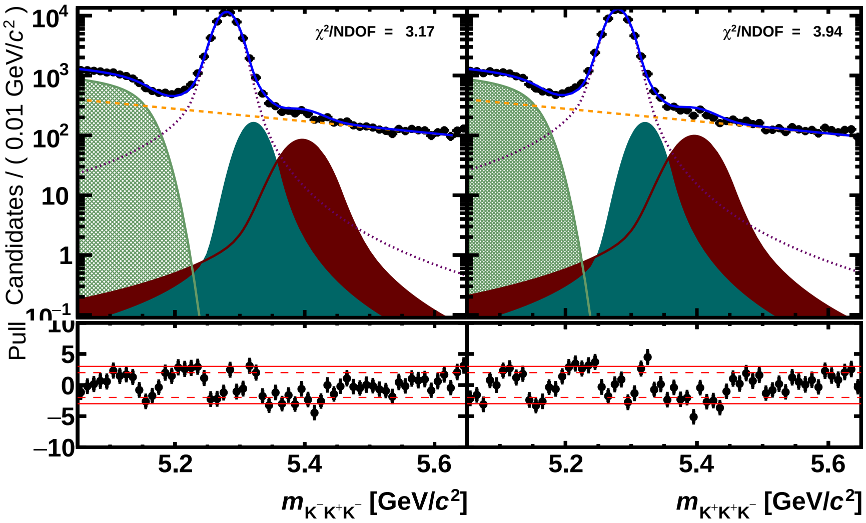

(B) $B^{\pm} \to K^{+}K^{\pm}K^{-}$

FIGURE C.1: Results for the fits to the invariant mass distribution of reconstructed $B^{\pm}$ for full 2015 and 2016 data sample. In each pair of distributions, the plot on the left B^{-} and on the right B^{+}.

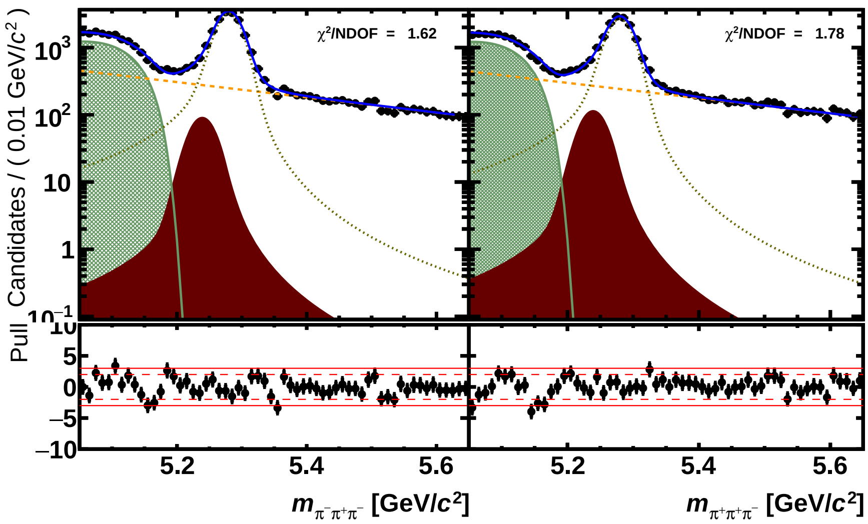

(A) $B^{\pm} \to \pi^+\pi^{\pm}\pi^-$

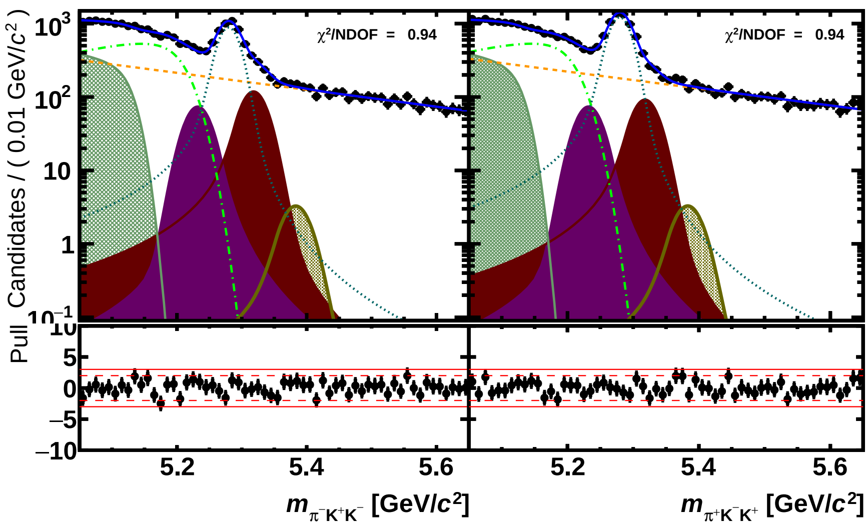

(B) $B^{\pm} \to K^+\pi^{\pm}K^-$

FIGURE C.2: Results for the fits to the invariant mass distribution of reconstructed $B^{\pm}$ for full 2015 and 2016 data sample. In each pair of distributions, the plot on the left B^- and on the right B^+.

$B^{\pm} \to \pi^{+}K^{\pm}\pi^{-}$ (2015+2016 data)	
Signal component	
m_0[MeV/c^2]	5280.8 ± 0.039128
σ[MeV/c^2]	16.579 ± 0.036595
a_1	1.3753 ± 0.037159
n_1	1.6833 ± 0.031936
a_2	-1.82740 ± 0.032658
n_2	2.7076 ± 0.064633
f_{CB}	0.52231 ± 0.026174
N_S	226475 ± 634
A_{raw}	0.0047 ± 0.0025
Combinatorial component	
b	-0.00231214 ± 0.000087237
A_{comb}	0.0000 (C)
N_{comb}	56386 ± 1094.6
$B \to$ 4-body (partially rec. component)	
σ [MeV/c^2]	26.670 ± 1.1976
m_t [MeV/c^2]	5138.3 ± 2.8906
c	-8.85358 ± 1.2713
p	0.13452 ± 0.088942
N_{bkg}	100434 ± 533.09
A_{bkg}	0.0000 (C)
$B^{\pm} \to \pi^{+}\pi^{\pm}\pi^{-}$ component	
m_0[MeV/c^2]	5318 (C)
σ[MeV/c^2]	21.00 (C)
a_1	1.60 (C)
n_1	1.38 (C)
a_2	-0.96 (C)
n_2	2.09 (C)
f_{CB}	0.05 (C)
$Fraction$[%]	0.076 (C)
A_{bkg}	0.000 (C)
$B^{\pm} \to K^{+}\pi^{\pm}K^{-}$ component	
m_0[MeV/c^2]	5239 (C)
σ[MeV/c^2]	21.00 (C)
a_1	0.50 (C)
n_1	0.00 (C)
a_2	-2.48 (C)
n_2	1.66 (C)
f_{CB}	0.03 (C)
$Fraction$[%]	0.006 (C)
A_{bkg}	0.000 (C)
$B^{\pm} \to K^{+}K^{\pm}K^{-}$ component	
m_0[MeV/c^2]	5162 (C)
σ[MeV/c^2]	25.00 (C)
a_1	0.60 (C)
n_1	0.00 (C)
a_2	-2.24 (C)
n_2	3.34 (C)
f_{CB}	0.12 (C)
$Fraction$[%]	0.004 (C)
A_{bkg}	0.000 (C)
$B^{\pm} \to \eta'(\rho^0\gamma)K^{\pm}$ component	
m_0 [MeV/c^2]	5211.0 (C)
σ_1 [MeV/c^2]	196.10 (C)
σ_2 [MeV/c^2]	27.500 (C)
a_1	0.0000 (C)
a_2	0.086300 (C)
$Fraction$[%]	0.135 ± 0.004
A_{bkg}	0.0000 (C)

TABLE C.1: List of the $B^{\pm} \to \pi^{+}K^{\pm}\pi^{-}$ mass fit model parameters extracted from the 2015+2016 sample fit. The numbers followed by a (C) were fixed in the corresponding fit.

$B^{\pm} \to K^{+}K^{\pm}K^{-}$ (2015+2016 data)	
Signal component	
m_0[MeV/c^2]	5281.0 ± 0.049
σ[MeV/c^2]	15.318 ± 0.045
a_1	1.402 ± 0.071
n_1	1.782 ± 0.062
a_2	-2.010 ± 0.037
n_2	2.871 ± 0.104
f_{CB}	0.369 ± 0.037
N_S	110002 ± 367
$A_{\rm raw}$	-0.057 ± -0.003
Combinatorial component	
b	0.00239 ± 0.00008
A_{comb}	0.0000 (C)
N_{comb}	25324 ± 436
$B \to$ 4-body (partially rec. component)	
σ [MeV/c^2]	20.234 ± 10.066
m_t [MeV/c^2]	5172.5 ± 14.991
c	4.311 ± 0.768
p	0.601 ± 0.340
N_{bkg}	14745 ± 295
A_{bkg}	0.0000 (C)
$B^{\pm} \to K^{+}\pi^{\pm}K^{-}$ component	
m_0[MeV/c^2]	5321 (C)
σ[MeV/c^2]	20.00 (C)
a_1	1.90 (C)
n_1	1.31 (C)
a_2	-0.73 (C)
n_2	2.03 (C)
f_{CB}	0.08 (C)
$Fraction$[%]	0.015 (C)
A_{bkg}	0.000 (C)
$B^{\pm} \to \pi^{+}K^{\pm}\pi^{-}$ component	
m_0[MeV/c^2]	5396 (C)
σ[MeV/c^2]	30.00 (C)
a_1	1.90 (C)
n_1	0.87 (C)
a_2	-1.24 (C)
n_2	0.45 (C)
f_{CB}	0.30 (C)
$Fraction$[%]	0.013 (C)
A_{bkg}	0.000 (C)

TABLE C.2: List of the $B^{\pm} \to K^{+}K^{\pm}K^{-}$ mass fit model parameters extracted from the 2015+2016 sample fit. The numbers followed by a (C) were fixed in the corresponding fit.

$B^{\pm} \to K^{+}\pi^{\pm}K^{-}$ (2015+2016 data)	
Signal component	
m_0[MeV/c^2]	5281.1 +/- 0.086640
σ[MeV/c^2]	16.023 +/- 0.082680
a_1	1.4728 +/- 0.079307
n_1	1.7199 +/- 0.075183
a_2	-1.86261 +/- 0.076993
n_2	2.9133 +/- 0.18563
f_{CB}	0.52271 +/- 0.061100
N_S	9372.7 +/- 147.18
A_{raw}	-0.157320 +/- 0.013242
Combinatorial component	
b	-0.00265741 +/- 0.00013782
A_{comb}	0.0000 (C)
N_{comb}	19459 +/- 590.73
$B \to$ 4-body (partially rec. component)	
σ [MeV/c^2]	14.698 +/- 4.2881
m_t [MeV/c^2]	5136.6 +/- 4.5556
c	-0.498704 +/- 98.269
p	0.41908 +/- 0.91135
N_{bkg}	4808.4 +/- 205.00
A_{bkg}	0.0000 (C)
$B_s^0 \to$ 4-body (partially rec. component)	
σ [MeV/c^2]	22.00 (C)
m_t [MeV/c^2]	5220 (C)
c	-18.7998 (C)
p	0.50 (C)
N_{bkg}	16093 +/- 412.90
A_{bkg}	0.0000 (C)
$B^{\pm} \to \pi^{+}K^{\pm}\pi^{-}$ component	
m_0[MeV/c^2]	5318 (C)
σ[MeV/c^2]	20.00 (C)
a_1	1.60 (C)
n_1	1.47 (C)
a_2	-0.38 (C)
n_2	5.73 (C)
f_{CB}	0.75 (C)
$Fraction$[%]	0.123 (C)
A_{bkg}	0.000 (C)
$B^{\pm} \to K^{+}K^{\pm}K^{-}$ component	
m_0[MeV/c^2]	5232 (C)
σ[MeV/c^2]	20.00 (C)
a_1	0.00 (C)
n_1	15.5 (C)
a_2	-2.04 (C)
n_2	1.88 (C)
f_{CB}	0.10 (C)
$Fraction$[%]	0.082 (C)
A_{bkg}	0.000 (C)
$B^{\pm} \to \pi^{+}\pi^{\pm}\pi^{-}$ component	
m_0[MeV/c^2]	5383 (C)
σ[MeV/c^2]	21.00 (C)
a_1	1.40 (C)
n_1	1.43 (C)
a_2	-0.27 (C)
n_2	4.32 (C)
f_{CB}	0.71 (C)
$Fraction$[%]	0.004 (C)
A_{bkg}	0.000 (C)

TABLE C.3: List of the $B^{\pm} \to K^{+}\pi^{\pm}K^{-}$ mass fit model parameters extracted from the 2015+2016 sample fit. The numbers followed by a (C) were fixed in the corresponding fit.

$B^{\pm} \to \pi^{+}\pi^{\pm}\pi^{-}$ (2015+2016 data)	
Signal component	
m_0[MeV/c^2]	5280.9± 0.084
σ[MeV/c^2]	17.015± 0.081
a_1	1.216± 0.069
n_1	1.764± 0.072
a_2	-1.812± 0.049
n_2	2.652± 0.115
f_{CB}	0.487± 0.041
N_S	30729± 221
A_{raw}	0.089397 ± 0.0069898
Combinatorial component	
b	-0.00262± 0.00007
A_{comb}	0.0000 (C)
N_{comb}	27122± 379
$B \to$ 4-body (partially rec. component)	
σ [MeV/c^2]	9.020± 10.029
m_t [MeV/c^2]	5189.3± 6.043
c	-41.432± 10.204
p	2.143± 0.149
N_{bkg}	20645± 273.82
A_{bkg}	0.0000 (C)
$B^{\pm} \to \pi^{+}K^{\pm}\pi^{-}$ component	
m_0[MeV/c^2]	5239 (C)
σ[MeV/c^2]	20.00 (C)
a_1	0.10 (C)
n_1	1.30 (C)
a_2	-1.99 (C)
n_2	2.80 (C)
f_{CB}	0.20 (C)
$Fraction$[%]	0.035 (C)
A_{bkg}	0.000 (C)

TABLE C.4: List of the $B^{\pm} \to \pi^{+}\pi^{\pm}\pi^{-}$ mass fit model parameters extracted from the 2015+2016 sample fit. The numbers followed by a (C) were fixed in the corresponding fit.

Appendix D

Values of pion and kaon detection asymmetry

	$A^i_D(\pi)$	
kaon momentum [GeV/c]	2012 Mag. Up	2012 Mag. Down
2 - 10	-0.0012± 0.0010	-0.0015 ± 0.0010
10 - 17.5	0.0001± 0.0011	-0.0028 ± 0.0011
17.5 - 22.5	0.0009 ± 0.0013	-0.0039 ±0.0013
22.5 - 30	0.0014 ± 0.0015	-0.0047 ± 0.0015
30 - 50	0.0022 ± 0.0019	-0.0058 ± 0.0019
50 - 70	0.0030 ± 0.0023	-0.0069 ±0.0023

TABLE D.1: Values of the pion detection asymmetry weighted in range of kaon momentum of the $D^+ \to K^-\pi^+\pi^+$ decay. Take from table 36 of the Ref. [58].

	$A_D(K\pi) + A_D(K^0)$	
Kaon momentum[GeV/c]	2015 Mag. Up	2015 Mag. Down
3 - 5	-3.01 ± 0.52	-1.68 ± 0.42
5 - 8	-1.95 ± 0.38	-0.41 ± 0.31
8 - 11	-0.81 ± 0.39	-1.52 ± 0.35
11 - 14	-1.12 ± 0.51	-0.58 ± 0.42
14 - 17	-1.85 ± 0.61	-1.00 ± 0.50
17 - 20	-0.99 ± 0.73	-1.04 ± 0.59
20 - 25	-0.78 ± 0.70	-0.87 ± 0.57
25 - 30	0.01 ± 0.93	-0.99 ± 0.75
30 - 40	-2.11 ± 0.92	1.21 ± 0.75
40 - 50	-1.67 ± 1.40	-0.03 ± 1.15
50 - 70	-2.52 ± 1.66	0.01 ± 1.36
Kaon Momentum [GeV/c]	2016 Mag. Up	2016 Mag. Down
3 - 5	-1.79 ± 0.26	-1.31 ± 0.24
5 - 8	-1.87 ± 0.17	-1.14 ± 0.15
8 - 11	-1.82 ± 0.18	-1.18 ± 0.17
11 - 14	-1.78 ± 0.22	-1.07 ± 0.20
14 - 17	-1.69 ± 0.25	-1.18 ± 0.24
17 - 20	-1.82 ± 0.30	-0.66 ± 0.28
20 - 25	-1.34 ± 0.29	-0.87 ± 0.27
25 - 30	-0.70 ± 0.37	-0.21 ± 0.35
30 - 40	-1.43 ± 0.37	-1.10 ± 0.35
40 - 50	-1.34 ± 0.56	-0.01 ± 0.53
50 - 70	-0.97 ± 0.66	-0.49 ± 0.64

TABLE D.2: Values of $A_D(K\pi) + A_D(K^0)$ divided by year and magnet polarity, corrected for the PID asymmetries. Values are reported in Tab. 13 of the analysis note [59].

	$A_D(\pi)$	
pion momentum [GeV/c]	2012 Mag. Up	2012 Mag. Down
2 - 6	-0.0121$\pm$ 0.0021	0.0032 $\pm$ 0.0022
6 - 15	-0.0052$\pm$ 0.0015	-0.0000 $\pm$ 0.0015
15 - 20	0.0008 $\pm$ 0.0021	-0.0012 $\pm$0.0021
20 - 30	0.0004 $\pm$ 0.0022	-0.0012 $\pm$ 0.0022
30 - 40	0.0015 $\pm$ 0.0033	-0.0073 $\pm$ 0.0033
40 - 50	0.0015 $\pm$ 0.0048	-0.0050 $\pm$0.0048
50 - 100	0.0062 $\pm$ 0.0051	-0.0107 $\pm$0.0051

TABLE D.3: Values of the pion detection asymmetry of various ranges of momentum, divided by magnet polarity. Take from table 34 of the Ref. [58].

Appendix E

Acceptance Maps

E.1 $B^- \to K^+\pi^-K^-$ acceptance map for TOS configuration-2016

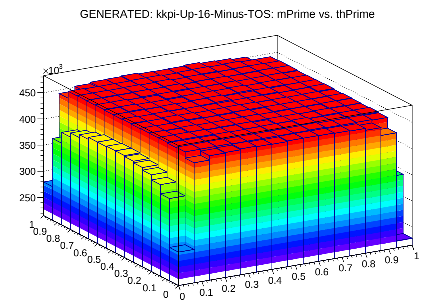

(A)

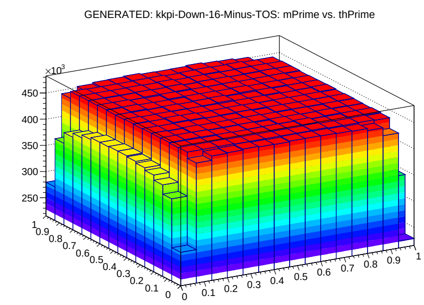

(B)

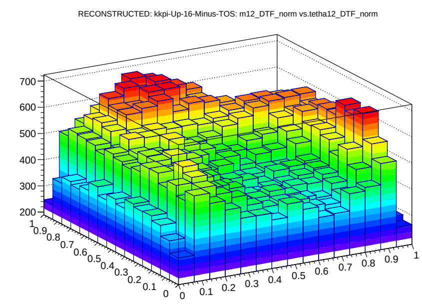

(C)

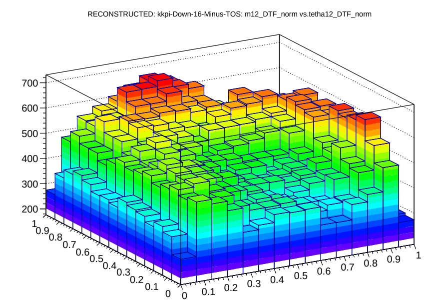

(D)

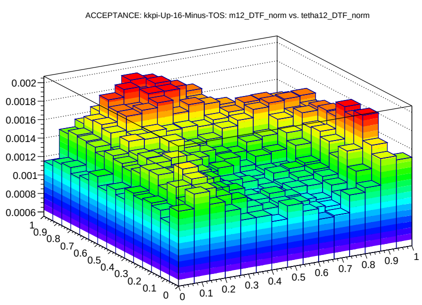

(E)

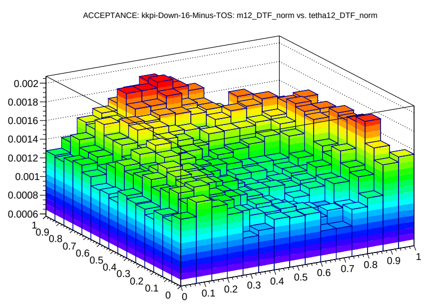

(F)

FIGURE E.1: (A),(C) and (E) show the generated histogram, reconstructed and the acceptance map respectively for B^-, TOS configuration-2016 and magnet up for the $B^- \to K^+\pi^-K^-$ channel. Similarly to (B),(D) and (F) histograms for the magnet down.

E.2 $B^{\pm} \to K^+K^{\pm}K^-$ acceptance maps for 2015 and 2016

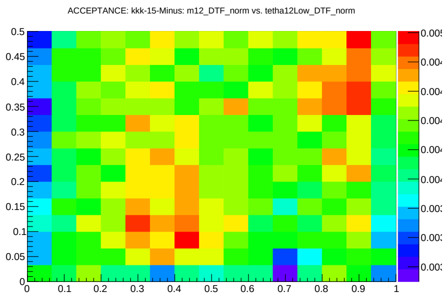

(A)

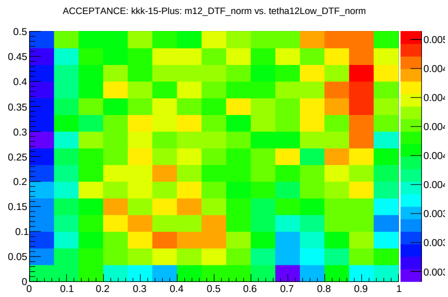

(B)

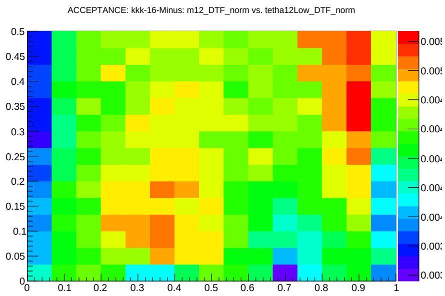

(C)

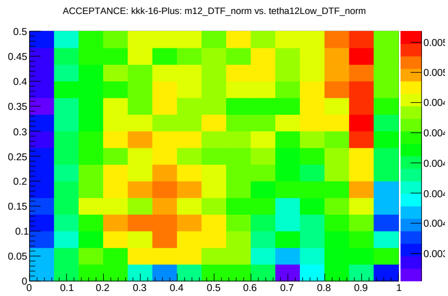

(D)

FIGURE E.2: $B^{\pm} \to K^+K^{\pm}K^-$ acceptance maps, (A) and (B) show the acceptance map for B^- and B^+ 2015 data, respectively. (C) and (D) show the acceptance map for B^- and B^+ 2016 data, respectively.

E.3 $B^{\pm} \to K^{+}\pi^{\pm}K^{-}$ acceptance maps for 2015 and 2016

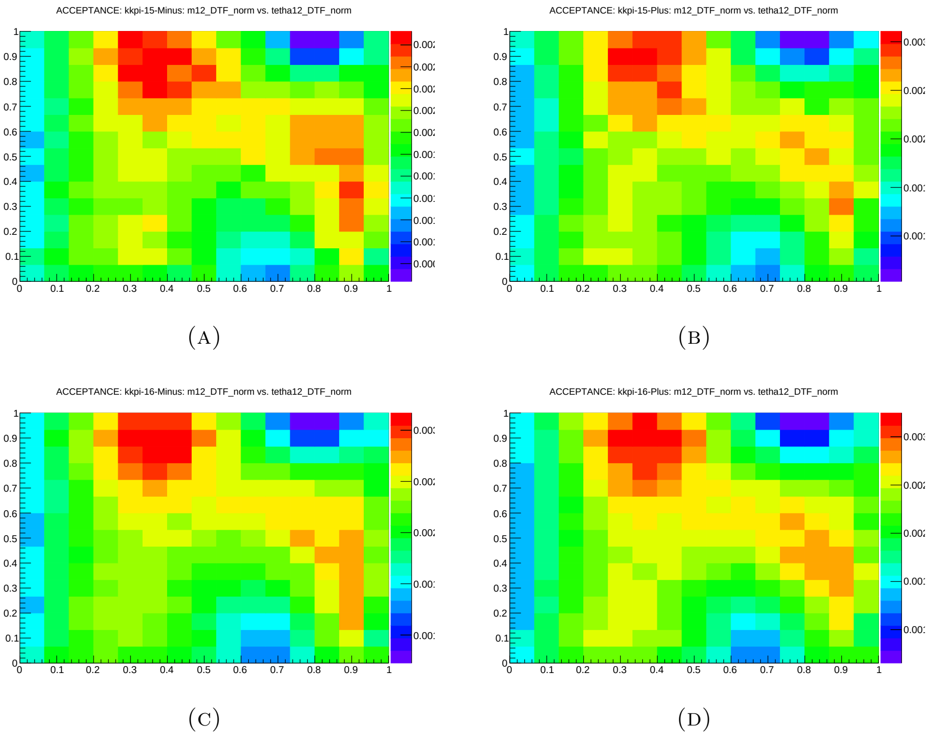

Figure E.3: $B^{\pm} \to K^{+}\pi^{\pm}K^{-}$ acceptance maps,(A) and (B) show the acceptance map for B^{-} and B^{+} 2015 data, respectively. (C),(D) show the acceptance map for B^{-} and B^{+} 2016 data, respectively.

E.4 $B^{\pm} \to \pi^+ K^{\pm} \pi^-$ acceptance maps for 2015 and 2016

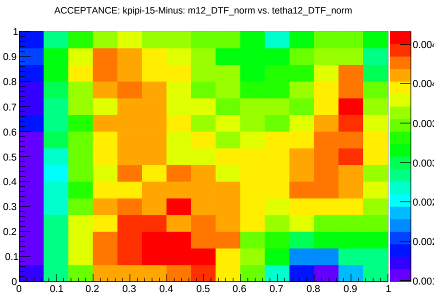

(A)

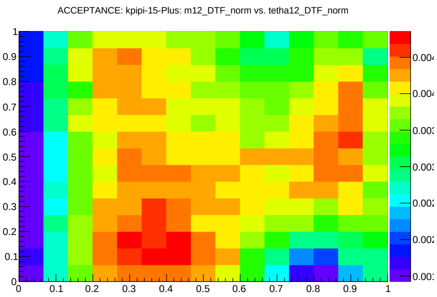

(B)

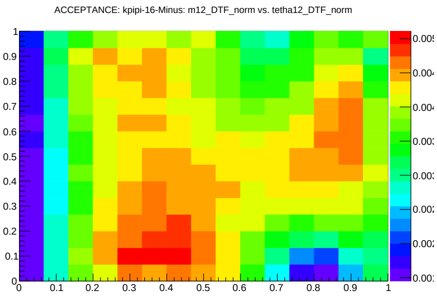

(C)

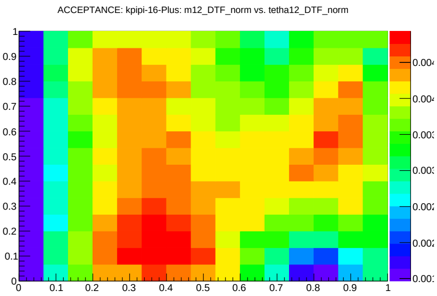

(D)

FIGURE E.4: $B^{\pm} \to \pi^+ K^{\pm} \pi^-$ acceptance maps, (A) and (B) show the acceptance map for B^- and B^+ 2015 data, respectively. (C) and (D) show the acceptance map for B^- and B^+ 2016 data, respectively.

E.5 $B^{\pm} \to \pi^{+}\pi^{\pm}\pi^{-}$ acceptance maps for 2015 and 2016

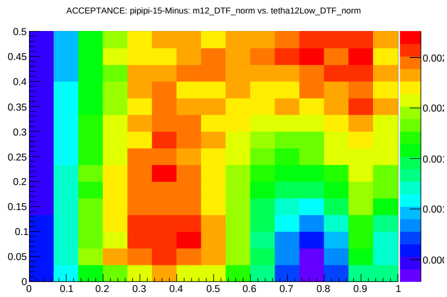

(A)

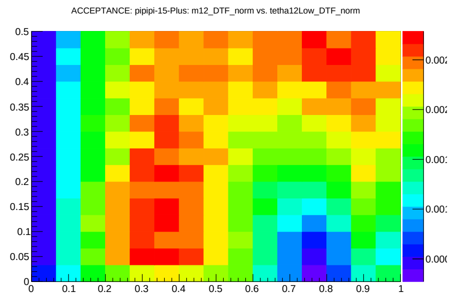

(B)

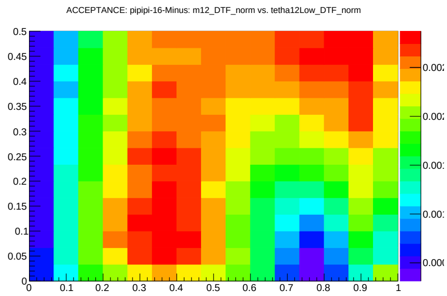

(C)

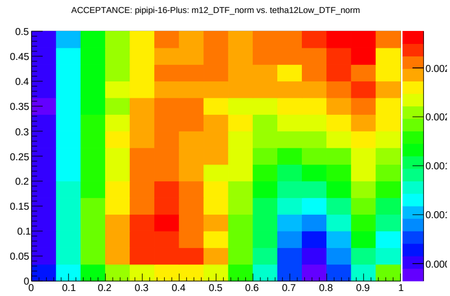

(D)

FIGURE E.5: $B^{\pm} \to \pi^{+}\pi^{\pm}\pi^{-}$ acceptance maps, (A) and (B) show the acceptance map for B^{-} and B^{+} 2015 data, respectively. (C) and (D) show the acceptance map for B^{-} and B^{+} 2016 data, respectively.

E.6 Combining Acceptance Maps

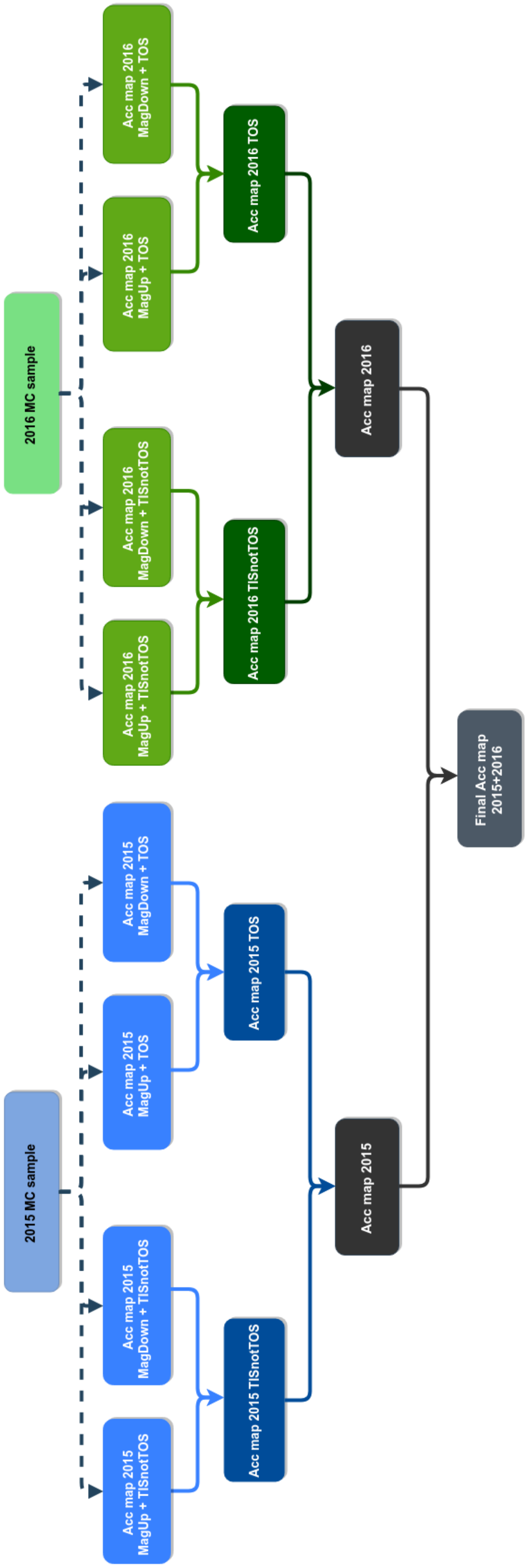

Figure E.6: Schematic diagram to illustrate how the acceptance subsamples are combined.

Appendix F

MC mass fits, Logarithmic and pulls of the plots

In this appendix it is presented the parameters results, logarithmic and pull plots related to the mass fit.

F.1 MC

F.1.1 Mass fit plots

F.1.2 Logaritmic and pull plots

F.2 Data

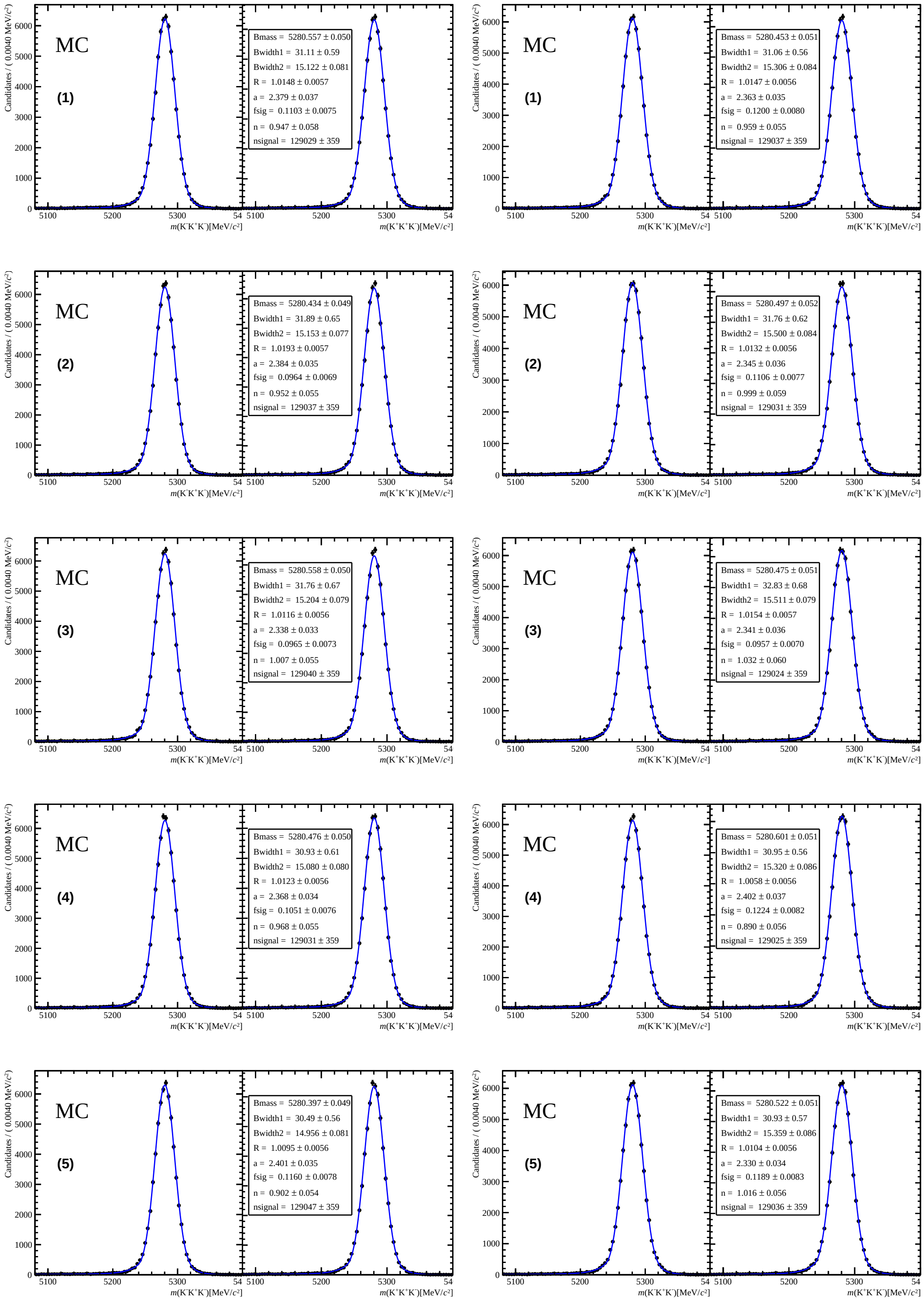

FIGURE F.1: Fits to the MC invariant mass distributions $B^{\pm} \to K^{+}K^{\pm}K^{-}$; 2011 (left column) and 2012 (right column) MC subsamples (from 1 to 5). In each pair of distributions, the plot on the left is B^{-} and on the right is B^{+}.

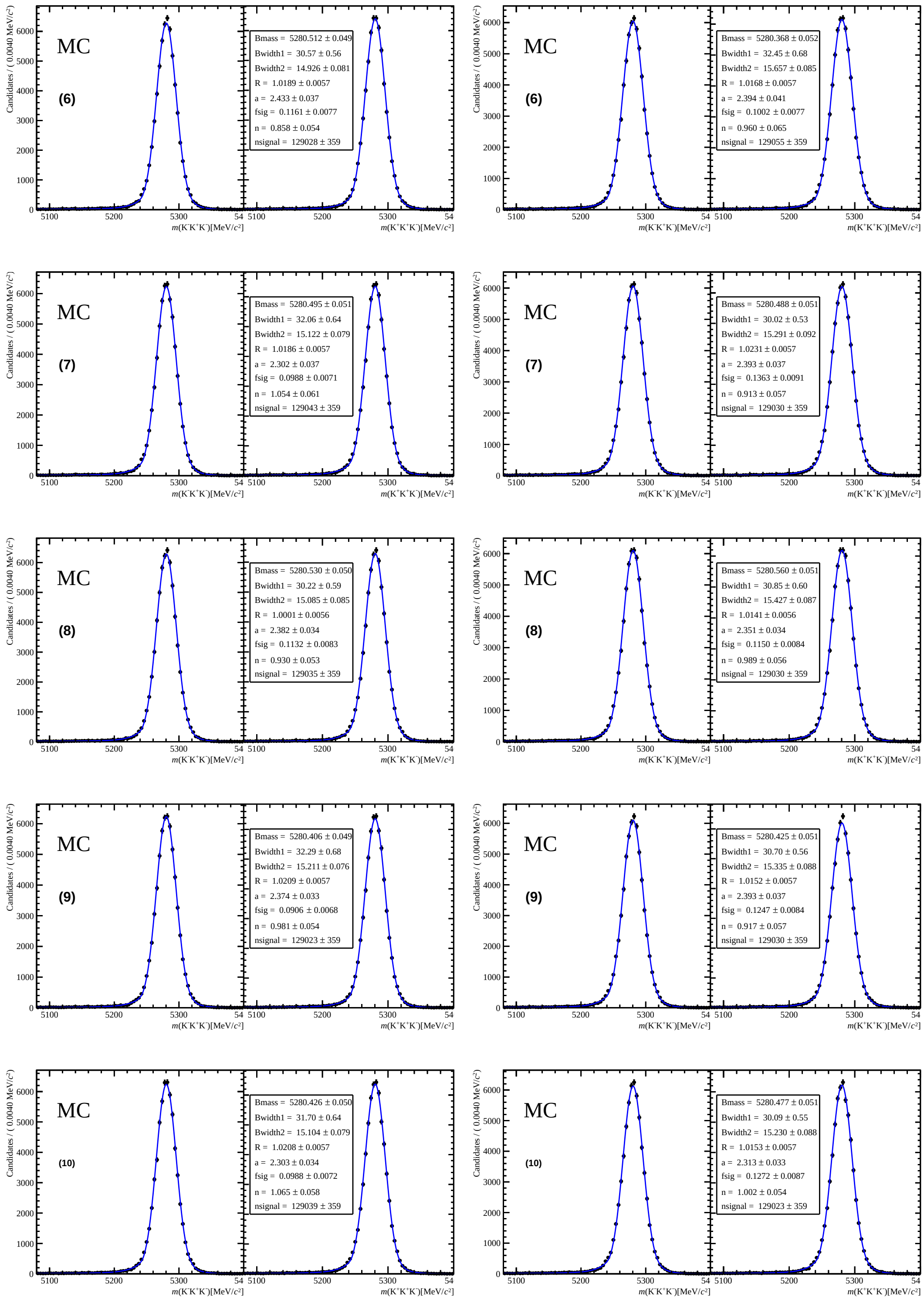

FIGURE F.2: Fits to the MC invariant mass distributions $B^{\pm} \to K^{+}K^{\pm}K^{-}$; 2011 (left column) and 2012 (right column) MC subsamples (from 6 to 10). In each pair of distributions, the plot on the left is B^{-} and on the right is B^{+}.

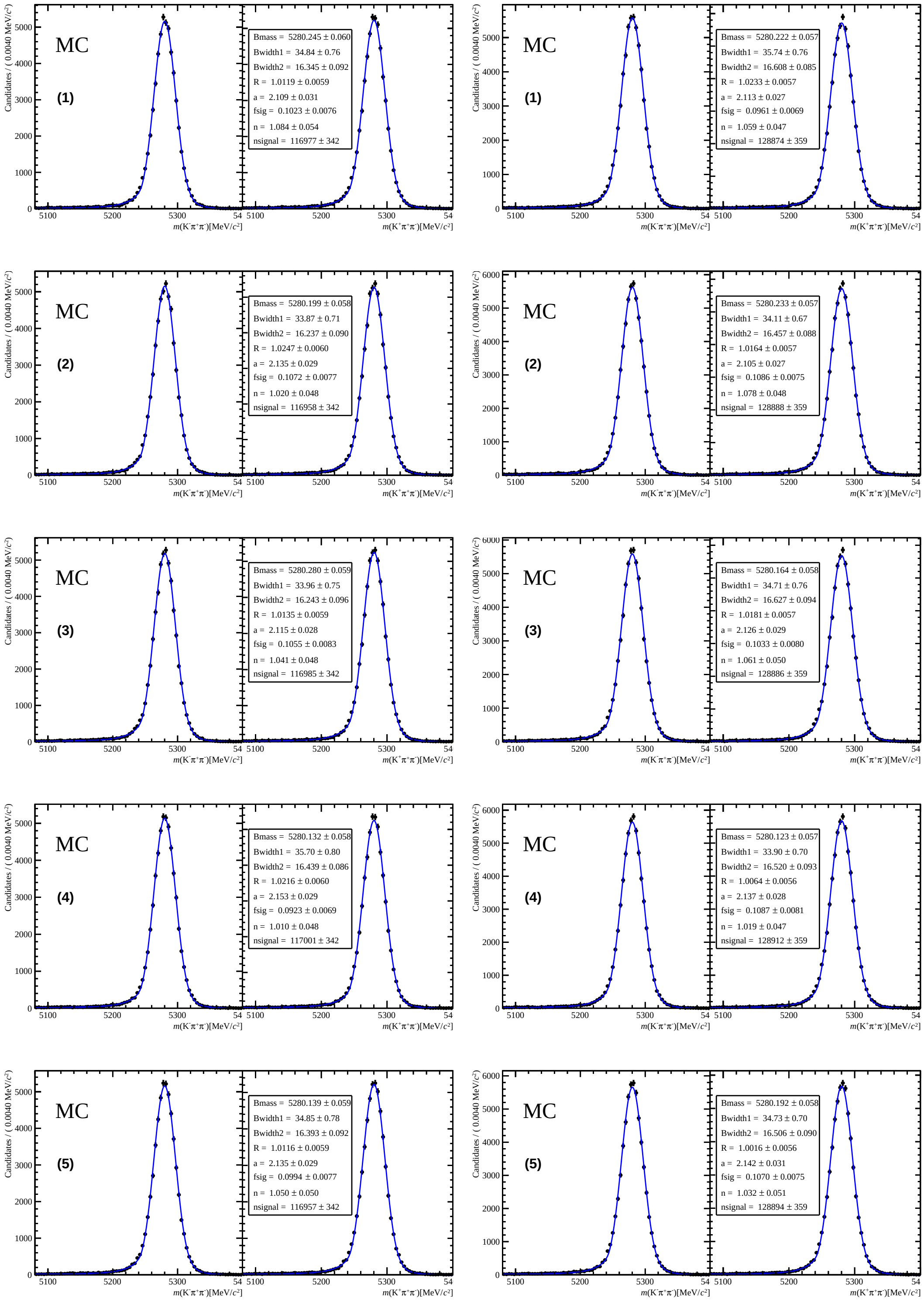

FIGURE F.3: Fits to the MC invariant mass distributions $B^{\pm} \to \pi^{+}K^{\pm}\pi^{-}$; 2011 (left column) and 2012 (right column) MC subsamples (from 1 to 5). In each pair of distributions, the plot on the left is B^{-} and on the right is B^{+}.

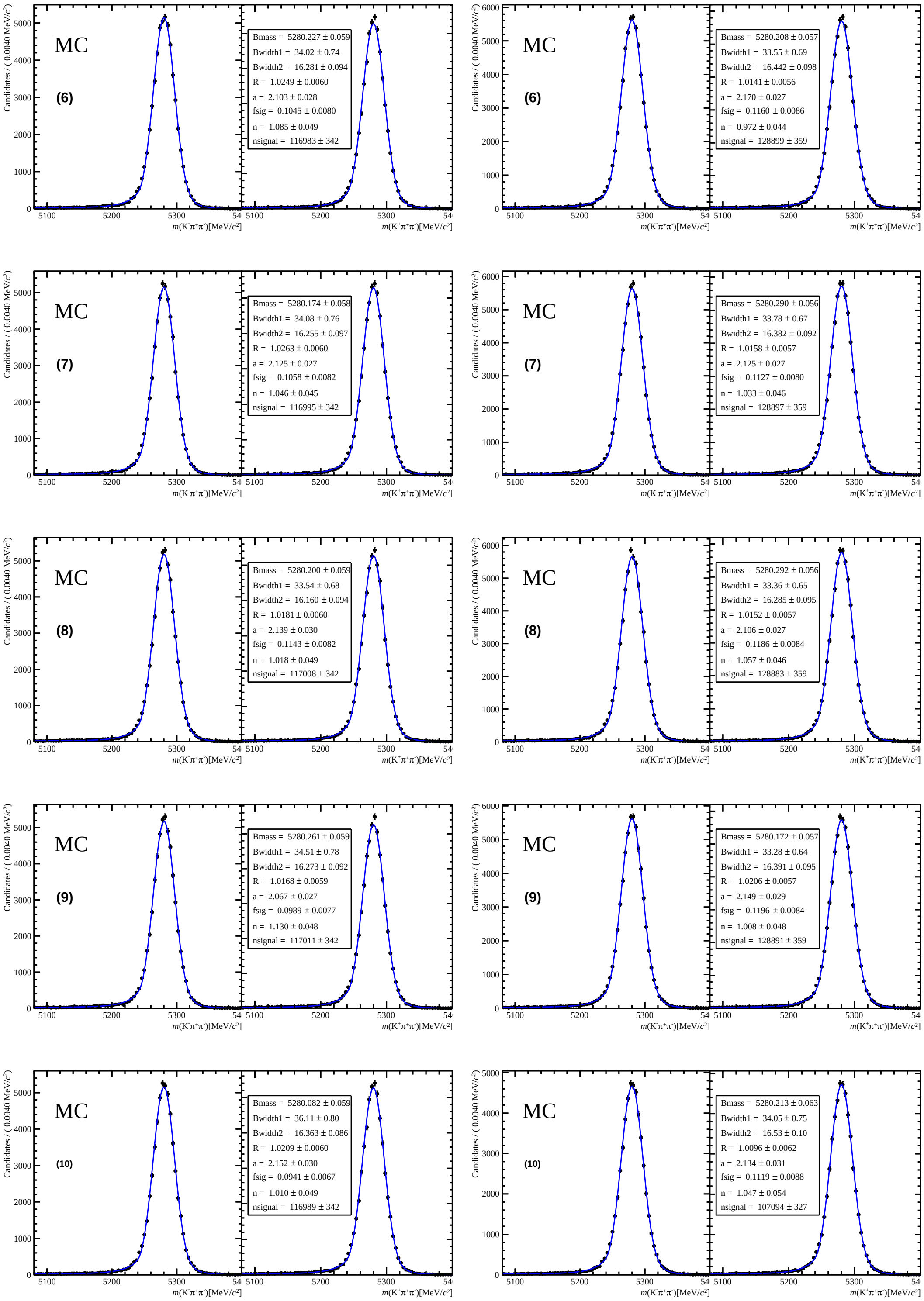

FIGURE F.4: Fits to the MC invariant mass distributions $B^{\pm} \rightarrow \pi^{+}K^{\pm}\pi^{-}$; 2011 (left column) and 2012 (right column) MC subsamples (from 6 to 10). In each pair of distributions, the plot on the left is B^{-} and on the right is B^{+}.

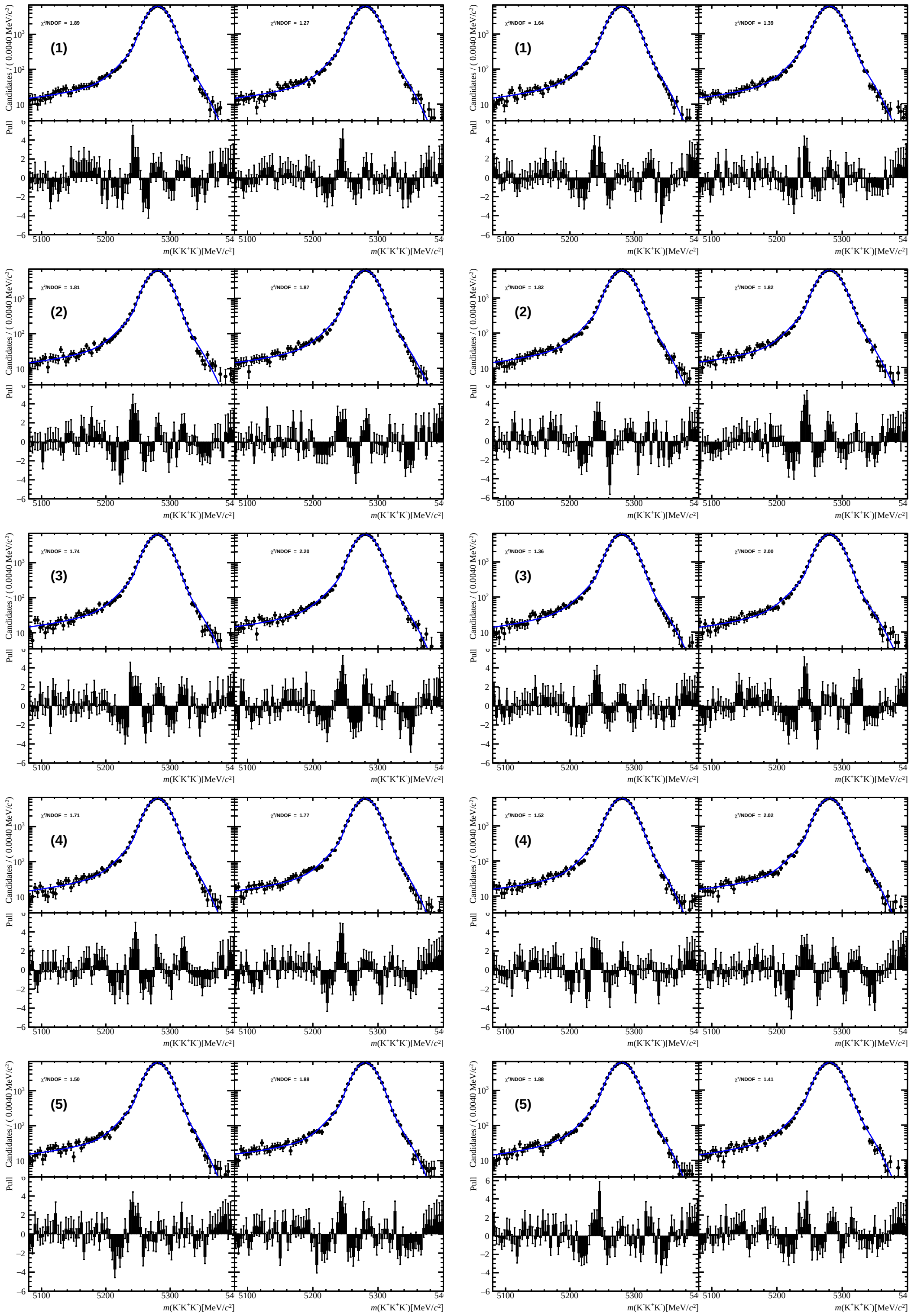

FIGURE F.5: Fits to the MC invariant mass distributions $B^{\pm} \to K^{+}K^{\pm}K^{-}$; 2011 (left column) and 2012 (right column) MC subsamples (from 1 to 5). In each pair of distributions, the plot on the left is B^{-} and on the right is B^{+}.

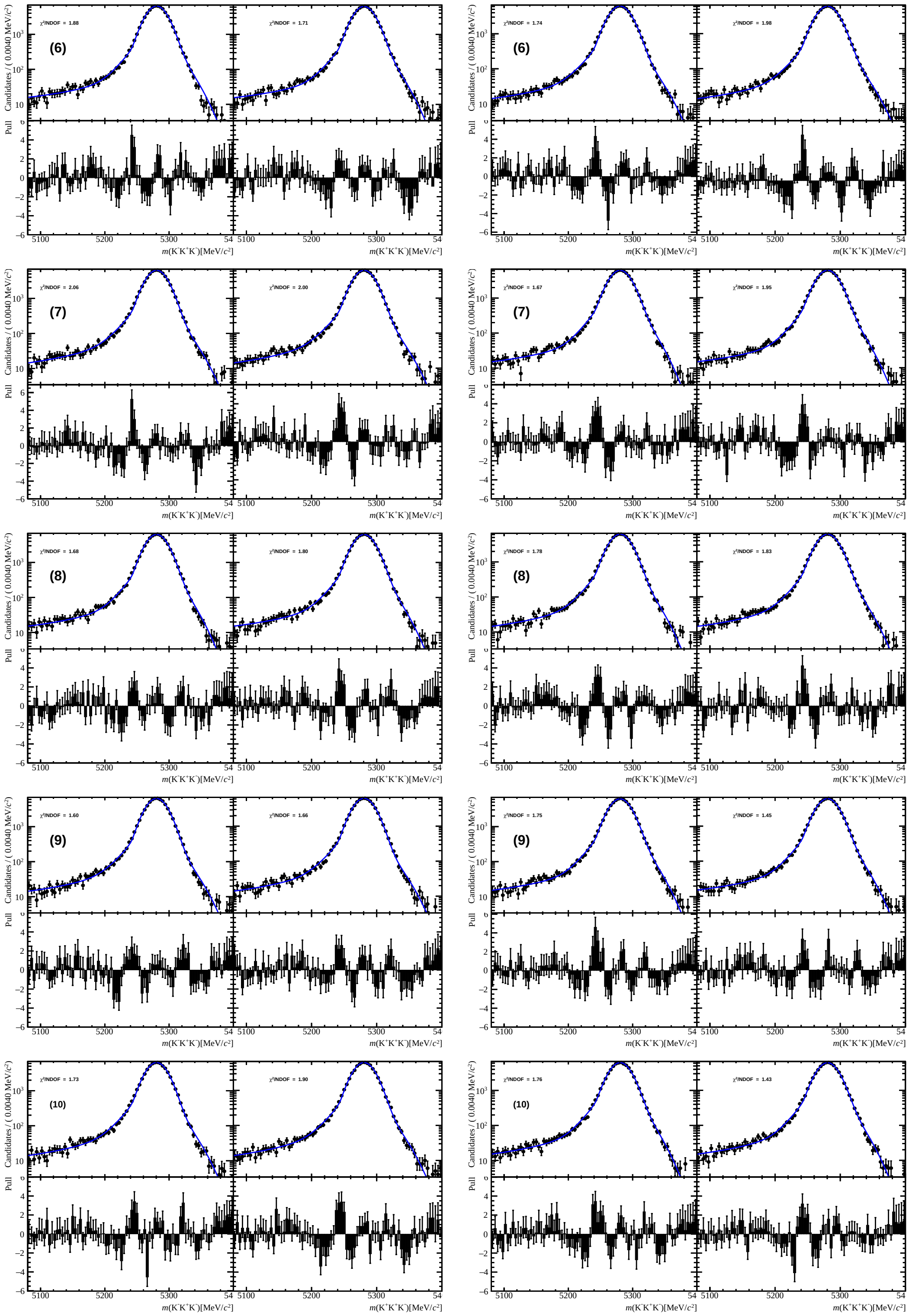

FIGURE F.6: Fits to the MC invariant mass distributions $B^{\pm} \to K^{+}K^{\pm}K^{-}$; 2011 (left column) and 2012 (right column) MC subsamples (from 6 to 10). In each pair of distributions, the plot on the left is B^{-} and on the right is B^{+}.

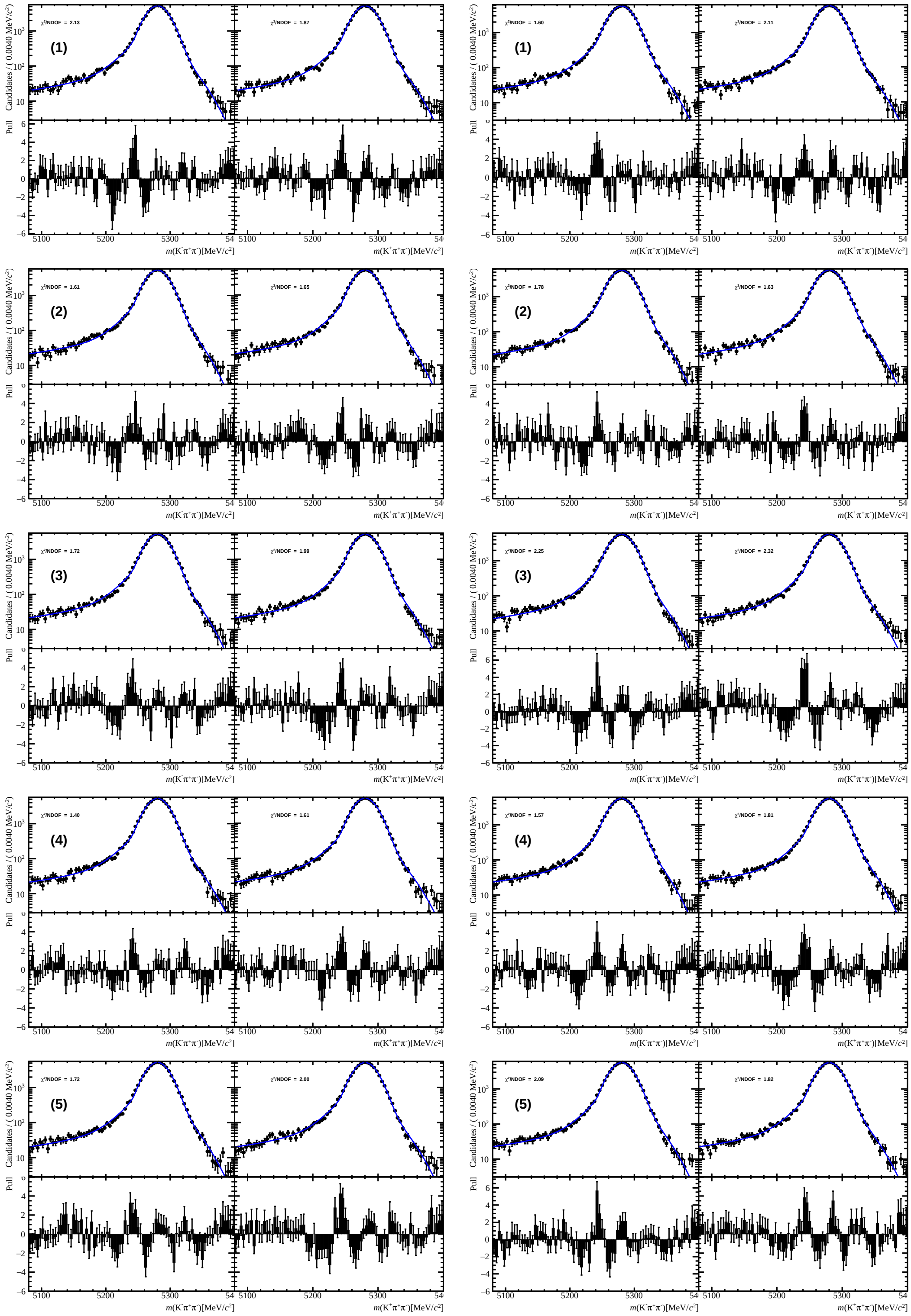

FIGURE F.7: Fits to the MC invariant mass distributions $B^{\pm} \to \pi^{+}K^{\pm}\pi^{-}$; 2011 (left column) and 2012 (right column) MC sub-samples (from 1 to 5). In each pair of distributions, the plot on the left is B^{-} and on the right is B^{+}.

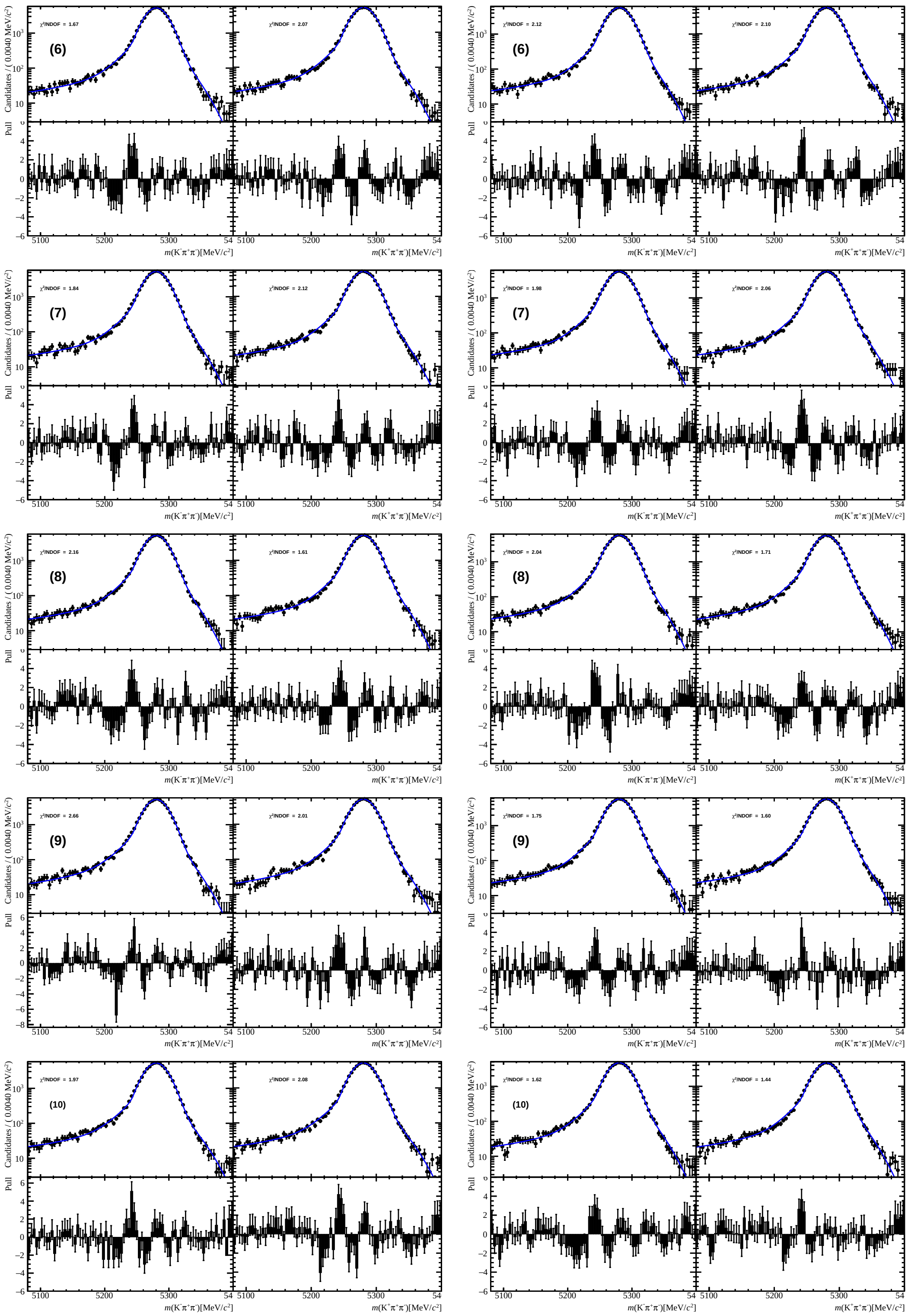

FIGURE F.8: Fits to the MC invariant mass distributions $B^{\pm} \to \pi^{+}K^{\pm}\pi^{-}$; 2011 (left column) and 2012 (right column) MC subsamples (from 6 to 10). In each pair of distributions, the plot on the left is B^{-} and on the right is B^{+}.

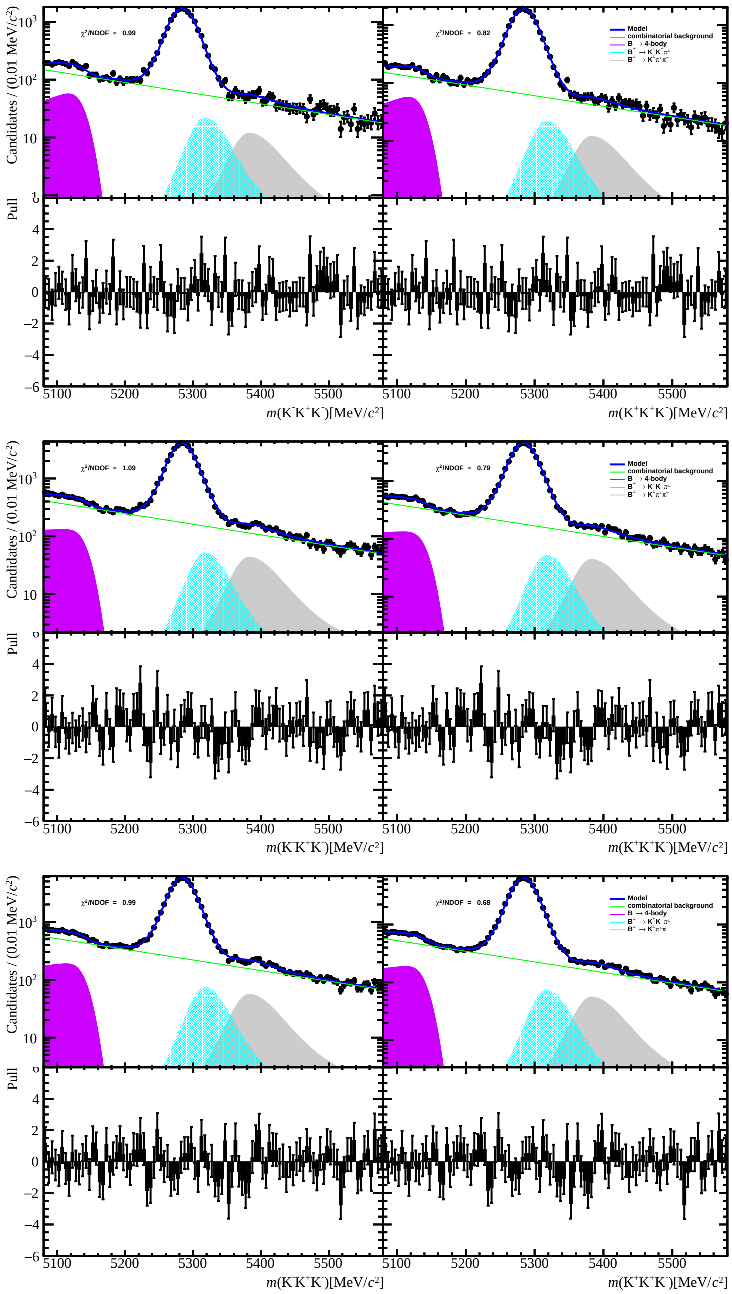

FIGURE F.9: The pull distributions for $B^{\pm} \to K^{+}K^{\pm}K^{-}$ candidates with final selection for 2011 data sample (first row), 2012 data sample (second row) and 2011+2012 data sample (last row). In each pair of distributions, the plot on the left is B^{-} and on the right is B^{+}.

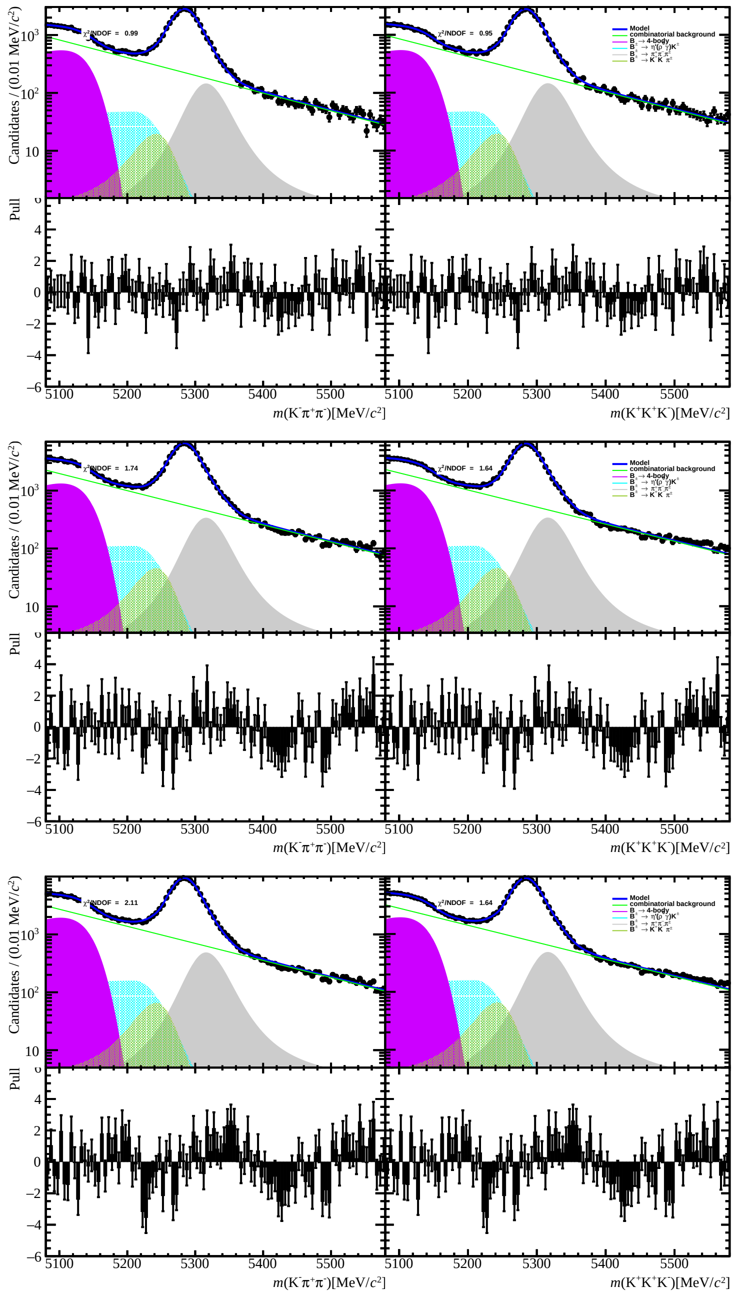

FIGURE F.10: The pull distributions for $B^{\pm} \to \pi^{+} K^{\pm} \pi^{-}$ candidates with final selection for 2011 data sample (first row), 2012 data sample (second row) and 2011+2012 data sample (last row). In each pair of distributions, the plot on the left is B^{-} and on the right is B^{+}.

Appendix G

Different binning schemes

We have performed the ratio for different bin widths, here we report bins widths of 0.5 and 0.9 ps.

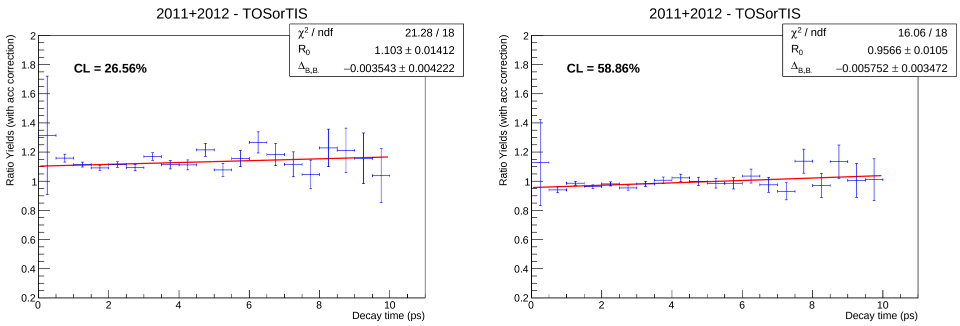

FIGURE G.1: Fit range: 0 - 10.0 ps - Bin width of 0.5 ps - $B^{\pm} \to K^{+}K^{\pm}K^{-}$ decay (on the left) and $B^{\pm} \to \pi^{+}K^{\pm}\pi^{-}$ decay (on the right).

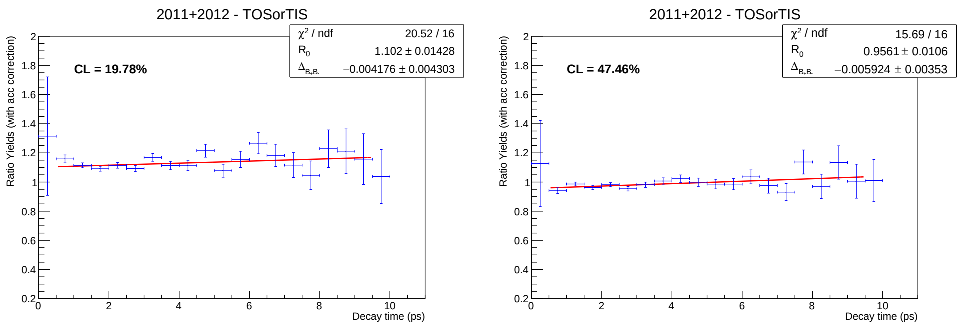

FIGURE G.2: Fit range: 0.5 - 9.5 ps - Bin width of 0.5 ps - $B^{\pm} \to K^{+}K^{\pm}K^{-}$ decay (on the left) and $B^{\pm} \to \pi^{+}K^{\pm}\pi^{-}$ decay (on the right).

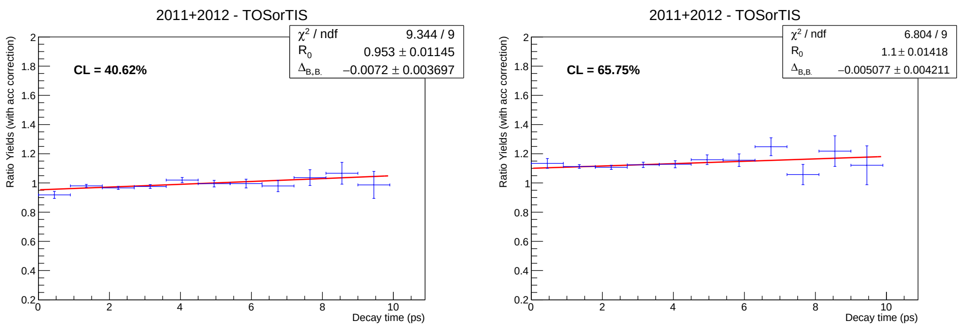

FIGURE G.3: Fit range: 0 - 9.9 ps - Bin width of 0.9 ps - $B^{\pm} \to K^+K^{\pm}K^-$ decay (on the left) and $B^{\pm} \to \pi^+K^{\pm}\pi^-$ decay (on the right).

Appendix H

Data fits in time bins

The results of the fits to the individual bins are presented in the following sections.

H.1 $B^{\pm} \to K^{+}K^{\pm}K^{-}$ data sample

H.1.1 2011

H.1.2 2012

H.1.3 2011+2012

H.2 $B^{\pm} \to \pi^{+}K^{\pm}\pi^{-}$ data sample

H.2.1 2011

H.2.2 2012

H.2.3 2011+2012

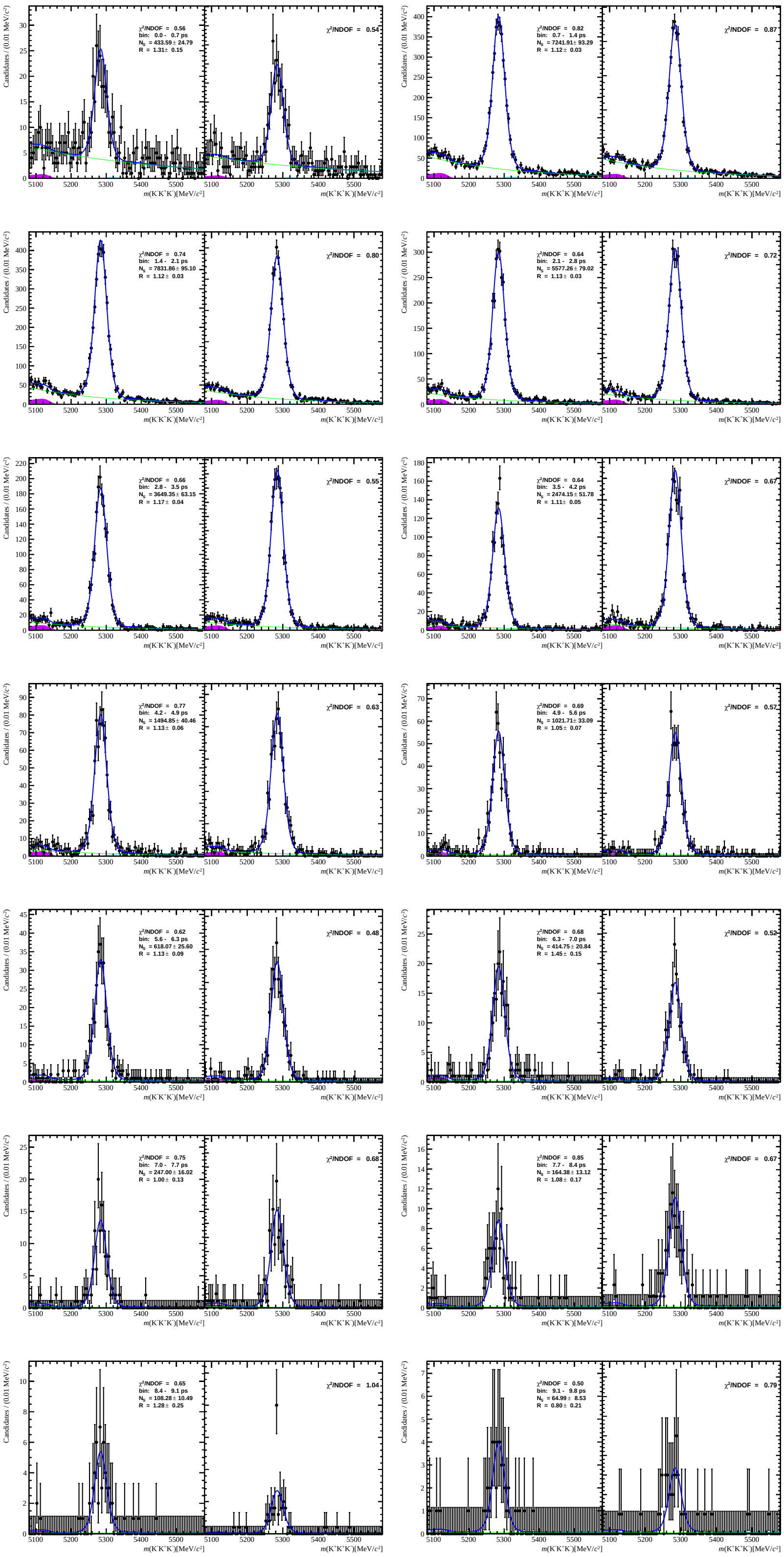

FIGURE H.1: Mass fits results for the 2011 $B^{\pm} \to K^{+}K^{\pm}K^{-}$ in the 14 time bins.

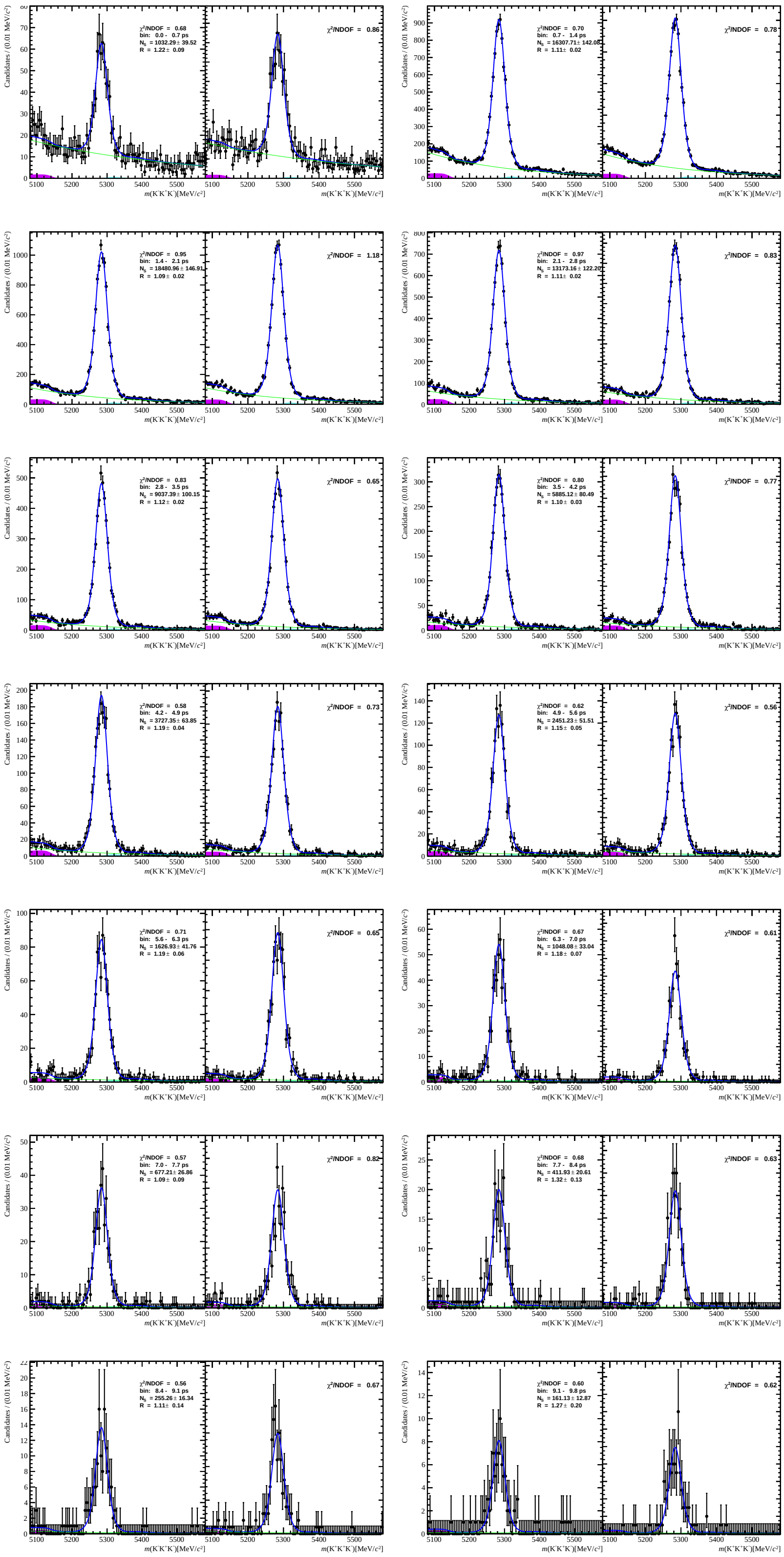

FIGURE H.2: Mass fits results for the 2012 $B^{\pm} \to K^{+}K^{\pm}K^{-}$ in the 14 time bins.

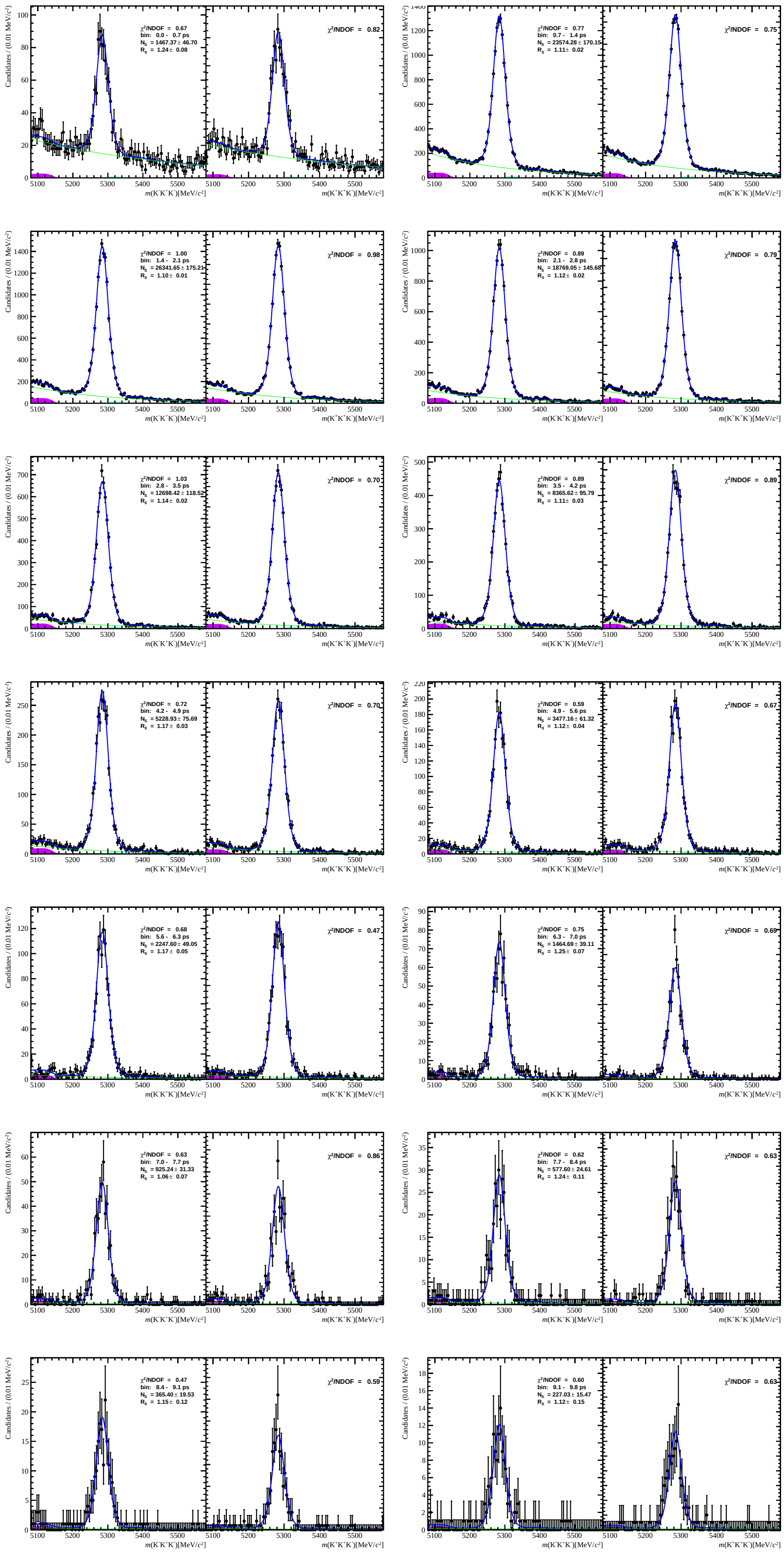

FIGURE H.3: Mass fits results for the 2011+2012 $B^{\pm} \to K^{+}K^{\pm}K^{-}$ in the 14 time bins.

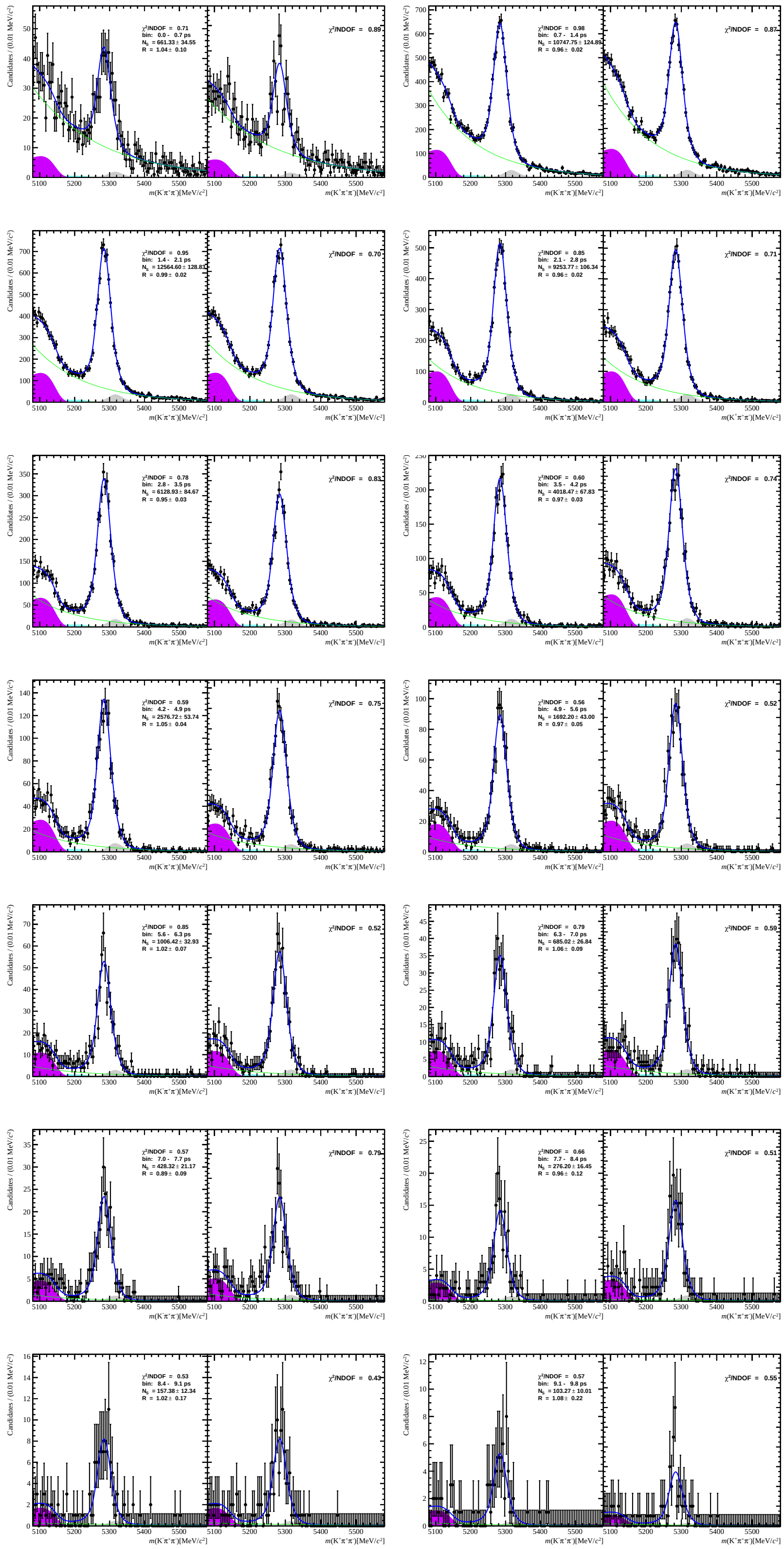

FIGURE H.4: Mass fits results for the 2011 $B^{\pm} \to \pi^{+}K^{\pm}\pi^{-}$ in the 14 time bins.

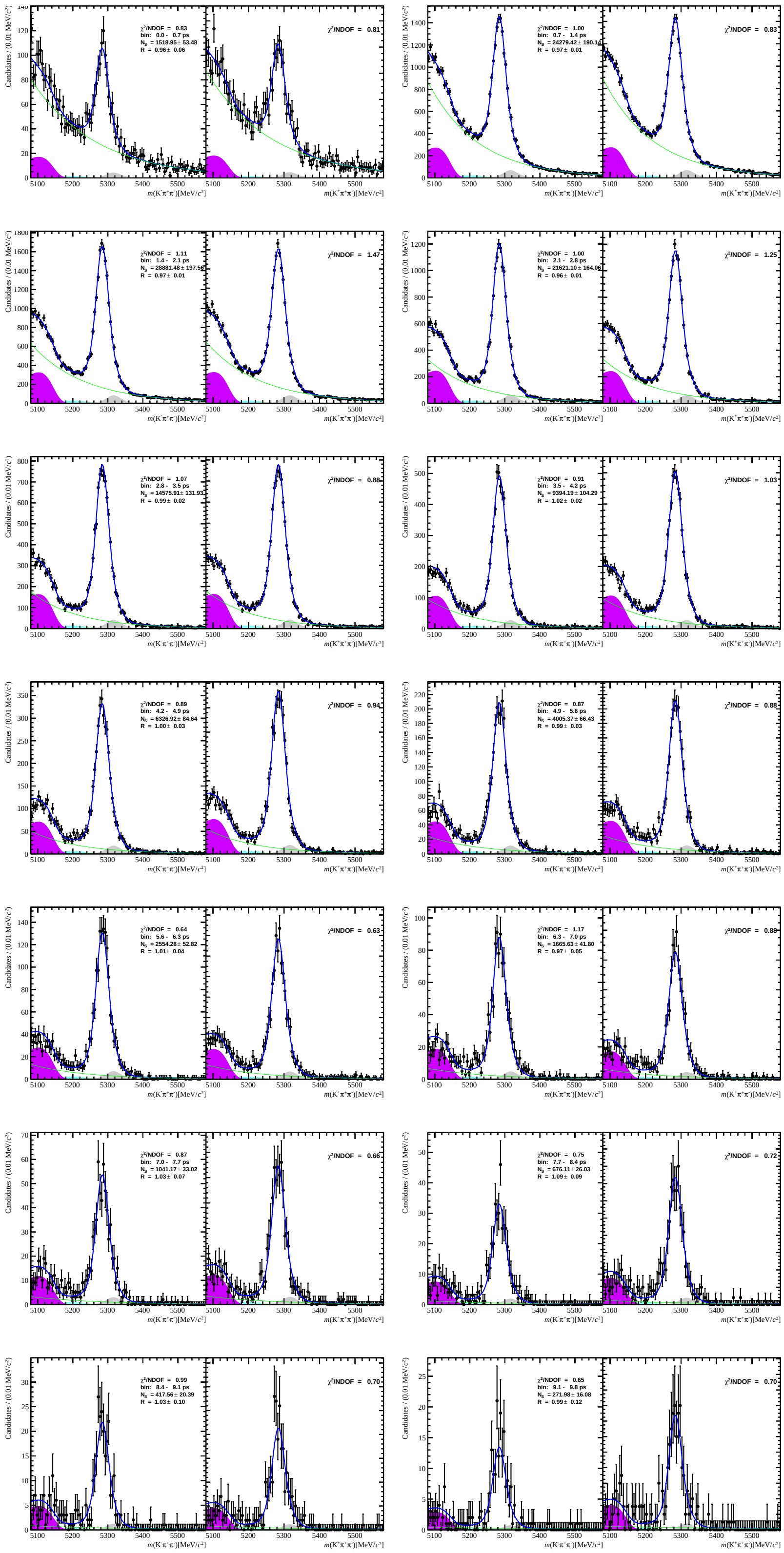

FIGURE H.5: Mass fits results for the 2012 $B^{\pm} \to \pi^{+}K^{\pm}\pi^{-}$ in the 14 time bins.

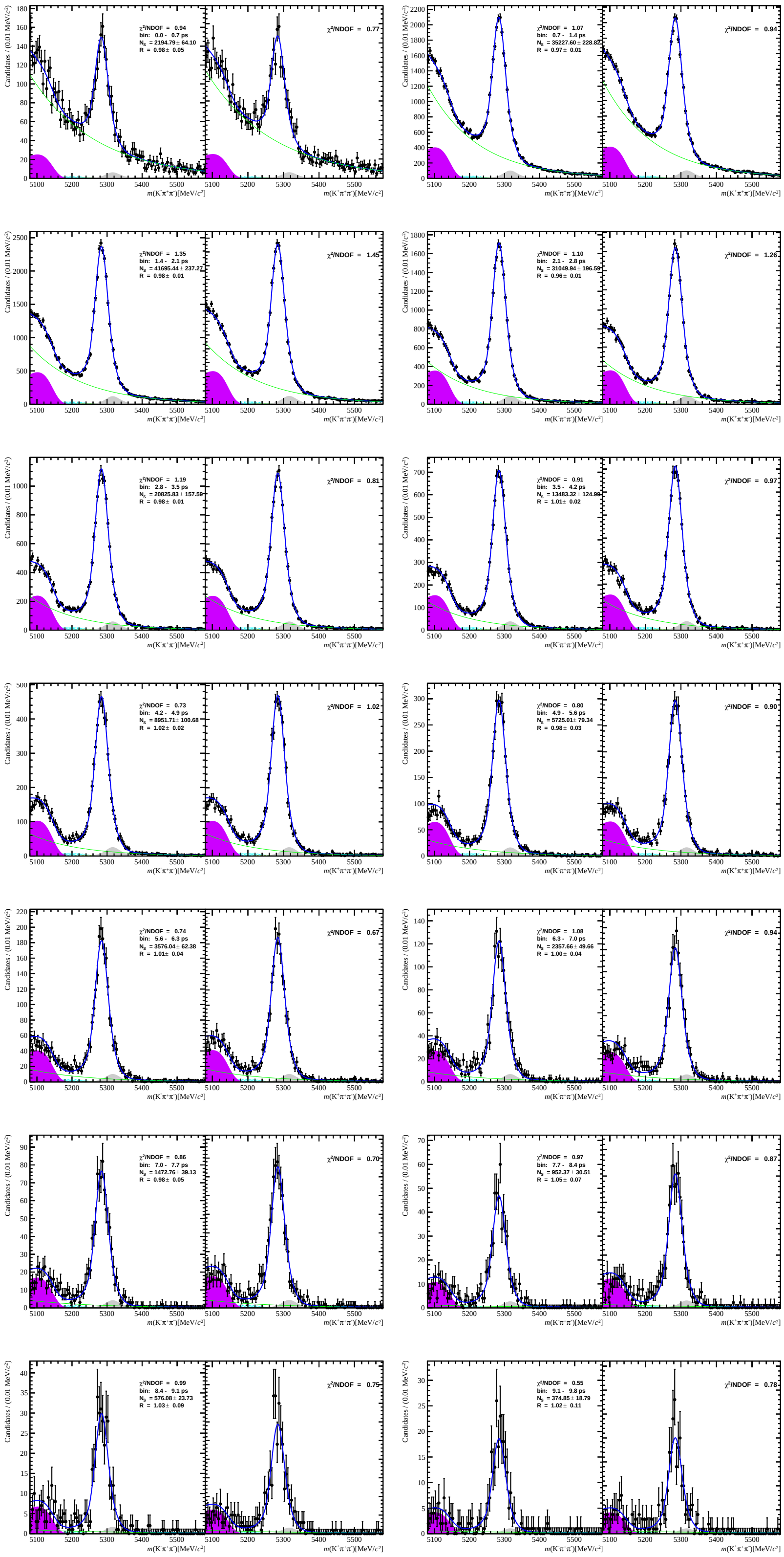

FIGURE H.6: Mass fits results for the 2011+2012 $B^{\pm} \to \pi^+ K^{\pm} \pi^-$ in the 14 time bins.

Appendix I

Ratio of the yields for different trigger requirements

Plots of the ratio fits for the different L0 trigger requirement are shown in figures I.1, I.2, I.3 and I.4. The parameters results are summarized in the tables I.1 and I.2.

I.0.1 MC

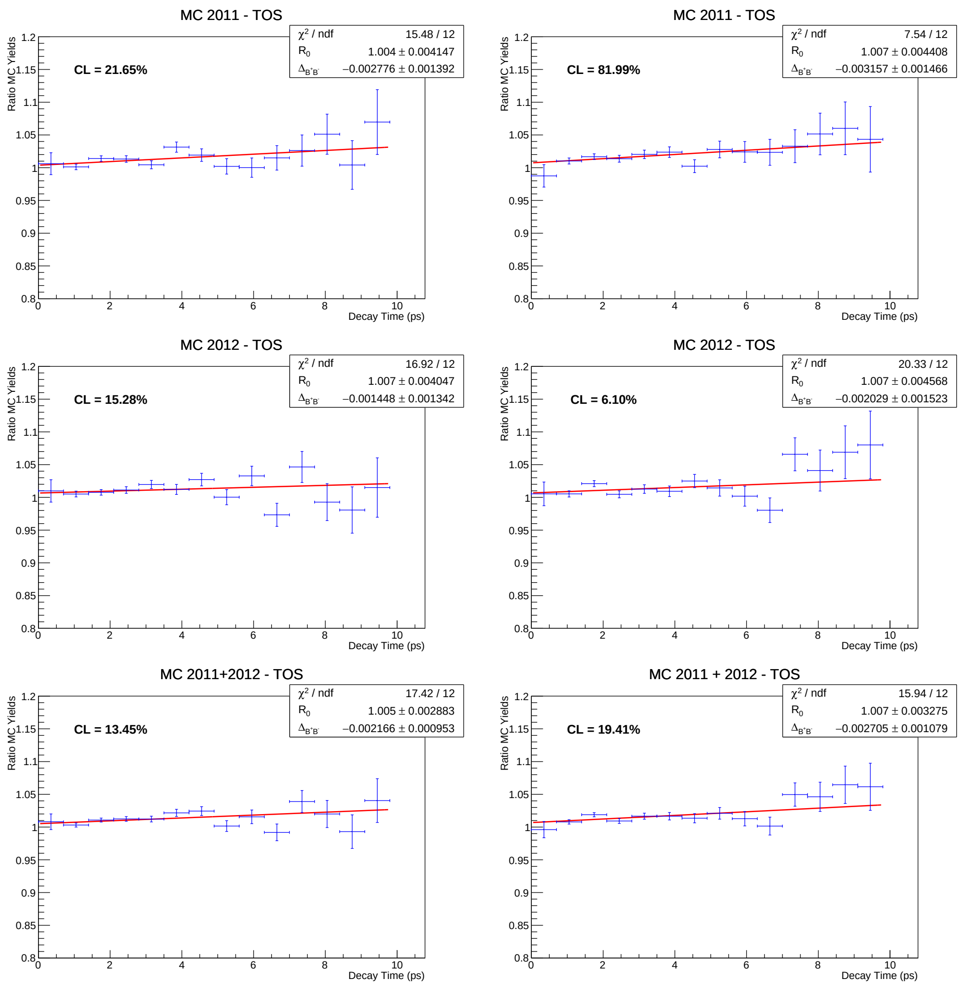

FIGURE I.1: B^+/B^- ratio of the yields for MC sample for $B^\pm \to K^+K^\pm K^-$ decay (left column) and $B^\pm \to \pi^+K^\pm\pi^-$ decay (right column), for the "Hadron_TOS" L0 trigger requirement.

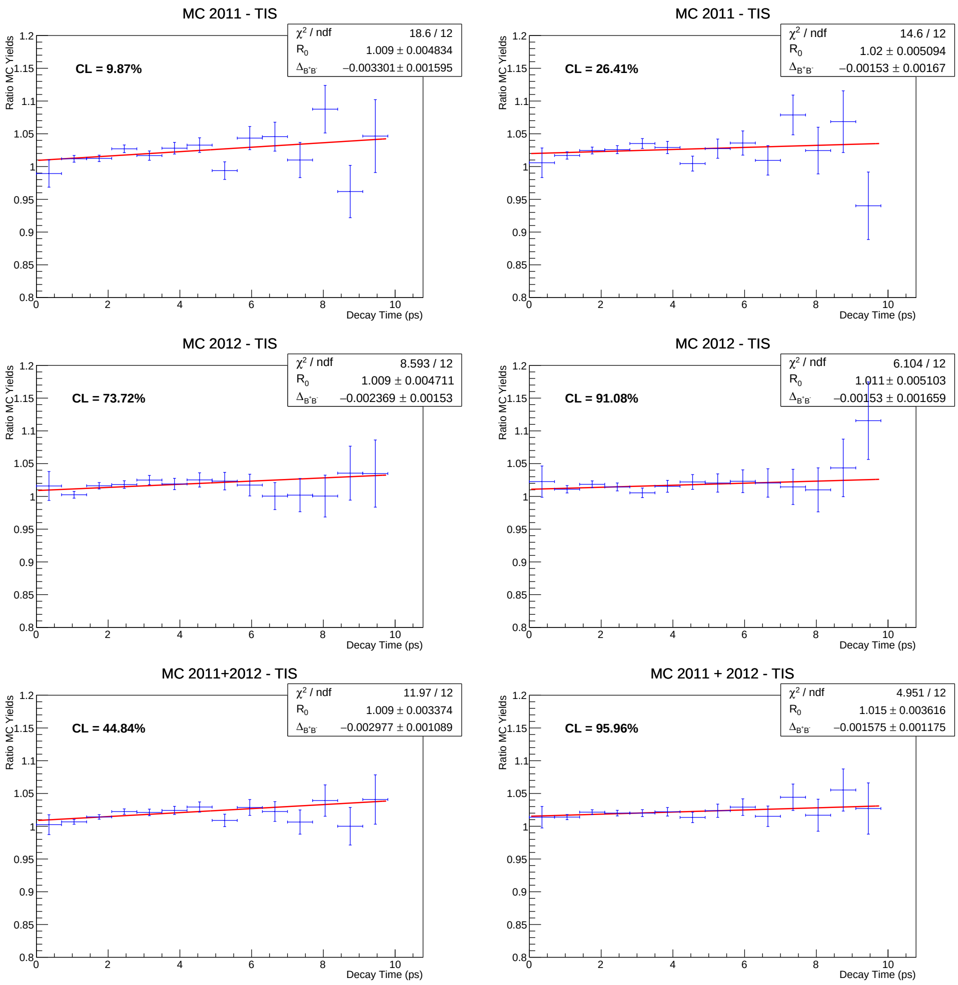

FIGURE I.2: B^+/B^- ratio of the yields for MC sample for $B^\pm \to K^+K^\pm K^-$ decay (left column) and $B^\pm \to \pi^+K^\pm\pi^-$ decay (right column), for the "Global_TIS" L0 trigger requirement.

I.0.2 Data

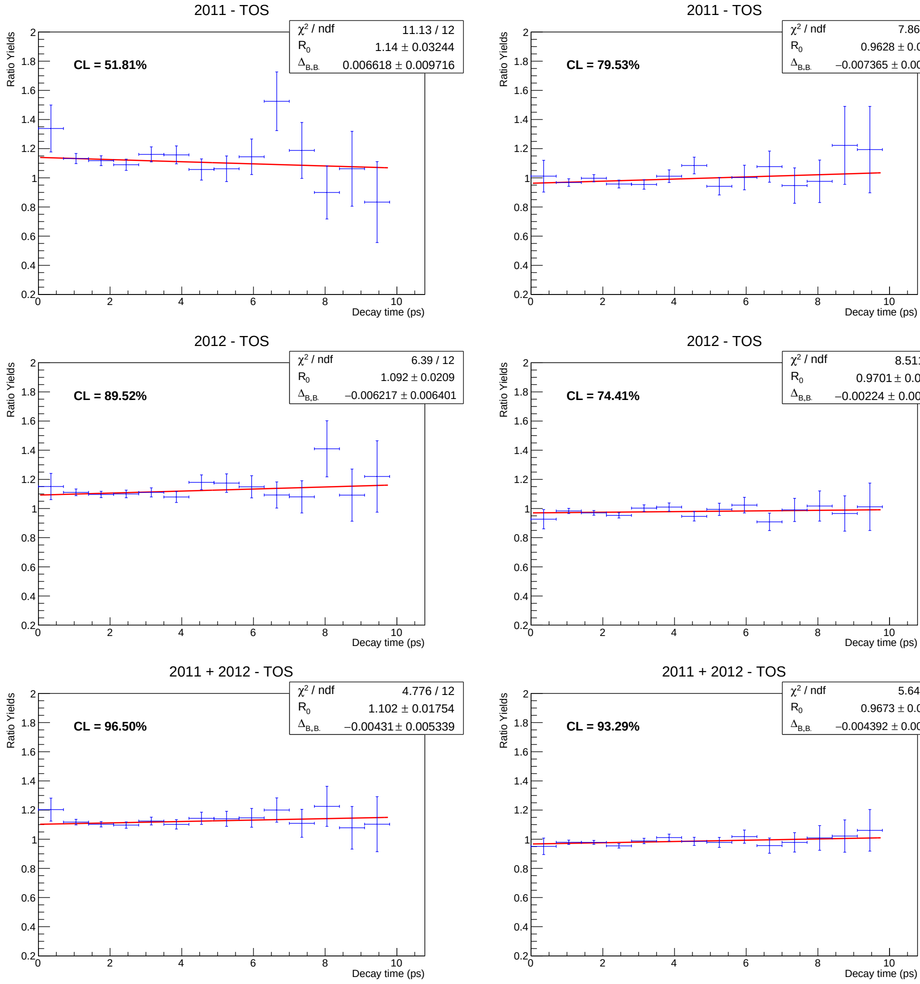

FIGURE I.3: B^+/B^- ratio of the yields for $B^\pm \to K^+K^\pm K^-$ decay (left column) and $B^\pm \to \pi^+K^\pm\pi^-$ decay (right column), for the "Hadron_TOS" L0 trigger requirement.

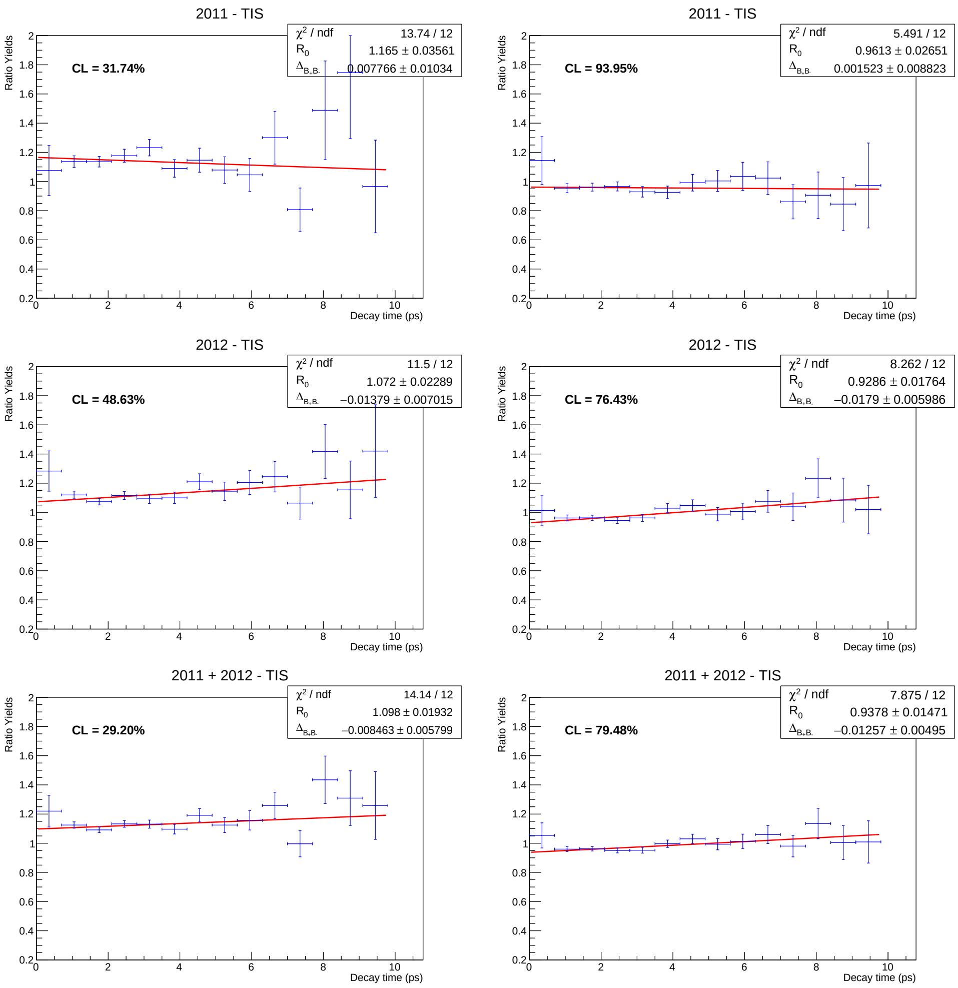

FIGURE I.4: B^+/B^- ratio of the yields for $B^\pm \to K^+K^\pm K^-$ decay (left column) and $B^\pm \to \pi^+K^\pm\pi^-$ decay (right column), for the "Global_TIS" L0 trigger requirement.

($B^\pm \to K^+K^\pm K^-$ MC sample): L0 Hadron TOS			
	2011	2012	2011+2012
$\Delta_{B_+B_-}$	-0.002776 ± 0.001392	-0.001448 ± 0.001342	-0.002166 ± 0.000953
R_0	1.004 ± 0.004147	1.007 ± 0.004047	1.005 ± 0.002883
($B^\pm \to K^+K^\pm K^-$ MC sample): L0 Global TIS			
$\Delta_{B_+B_-}$	-0.003301 ± 0.001595	-0.002369 ± 0.00153	-0.002977 ± 0.001089
R_0	1.009 ± 0.004834	1.009 ± 0.004711	1.009 ± 0.003374
($B^\pm \to \pi^+K^\pm\pi^-$ MC sample): L0 Hadron TOS			
	2011	2012	2011+2012
$\Delta_{B_+B_-}$	-0.003157 ± 0.001466	-0.002029 ± 0.001523	-0.002705 ± 0.001079
R_0	1.007 ± 0.004408	1.007 ± 0.004568	1.007 ± 0.003275
($B^\pm \to \pi^+K^\pm\pi^-$ MC sample): L0 Global TIS			
$\Delta_{B_+B_-}$	-0.00153 ± 0.00167	-0.00153 ± 0.001659	-0.001575 ± 0.001175
R_0	1.02 ± 0.005094	1.011 ± 0.005103	1.015 ± 0.003616

TABLE I.1: Results for $\Delta_{B_+B_-}$ and R_0 extracted from the MC ratio fits for different L0 requirements.

($B^{\pm} \to K^{+}K^{\pm}K^{-}$ data sample): L0 Hadron TOS			
	2011	2012	2011+2012
$\Delta_{B_{+}B_{-}}$	0.00662 ± 0.00972	-0.00622 ± 0.00640	-0.00431 ± 0.00534
R_0	1.140 ± 0.034	1.092 ± 0.021	1.102 ± 0.017
($B^{\pm} \to K^{+}K^{\pm}K^{-}$ data sample): L0 Global TIS			
$\Delta_{B_{+}B_{-}}$	0.00777 ± 0.01034	-0.01379 ± 0.00701	-0.00846 ± 0.00580
R_0	1.165 ± 0.036	1.072 ± 0.023	1.098 ± 0.019
($B^{\pm} \to \pi^{+}K^{\pm}\pi^{-}$ data sample): L0 Hadron TOS			
	2011	2012	2011+2012
$\Delta_{B_{+}B_{-}}$	-0.00736 ± 0.00799	0.00224 ± 0.00512	-0.00439 ± 0.00430
R_0	0.9628 ± 0.0232	0.9701 ± 0.0154	0.967 ± 0.0128
($B^{\pm} \to \pi^{+}K^{\pm}\pi^{-}$ data sample): L0 Global TIS			
$\Delta_{B_{+}B_{-}}$	0.00152 ± 0.00882	-0.0179 ± 0.00599	-0.01257 ± 0.00495
R_0	0.9613 ± 0.0265	0.929 ± 0.0176	0.9378 ± 0.0147

TABLE I.2: Results for $\Delta_{B_{+}B_{-}}$ and R_0 extracted from the data ratio fits for the different L0 trigger requirements.

Bibliography

[1] Andrej Dmitrievich Sakharov. “Violation of *CP* invariance, *C* asymmetry, and baryon asymmetry of the universe”. In: *JETP lett.* 5 (1967), pp. 24–27.

[2] Roel Aaij et al. “Measurements of *CP* violation in the three-body phase space of charmless $B^{\pm}$ decays”. In: *Physical Review D* 90.11 (2014), p. 112004.

[3] JH Alvarenga Nogueira et al. “CP violation: Dalitz interference, CPT, and final state interactions”. In: *Physical Review D* 92.5 (2015), p. 054010.

[4] Helen R Quinn. “Time reversal violation”. In: *Journal of Physics: Conference Series*. Vol. 171. 1. IOP Publishing. 2009, p. 012001.

[5] James H Christenson et al. “Evidence for the 2π Decay of the K_2^0 Meson”. In: *Physical Review Letters* 13.4 (1964), p. 138.

[6] Robert V Kowalewski. “*B* physics and *CP* violation”. In: *Particles And The Universe*. World Scientific, 2004, pp. 91–117.

[7] Makoto Kobayashi and Toshihide Maskawa. “*CP*-violation in the renormalizable theory of weak interaction”. In: *Progress of Theoretical Physics* 49.2 (1973), pp. 652–657.

[8] C. Patrignani et al. “Review of Particle Physics”. In: *Chin. Phys.* C40.10 (2016), p. 100001. DOI: 10.1088/1674-1137/40/10/100001.

[9] Lincoln Wolfenstein. “Parametrization of the Kobayashi-Maskawa matrix”. In: *Physical Review Letters* 51.21 (1983), p. 1945.

[10] David London and Amarjit Soni. “Measuring the CP angle β in hadronic $b \to s$ penguin decays”. In: *Physics Letters B* 407.1 (1997), pp. 61–65.

[11] P Gambino and A Stocchi. “The CKM Matrix and the unitarity triangles”. In: *arXiv preprint hep-ph/0304132* (2003).

[12] Thomas E Browder and Klaus Honscheid. “*B* mesons”. In: *Progress in Particle and Nuclear Physics* 35 (1995), pp. 81–219.

[13] Matthew Barrett and U Birmingham. *Dalitz Plot Analysis of the Charmless Three Body Decay* $B^{\pm} \to K^{\pm}K^{\pm}K^{\mp}$ *Utilising Data Recorded by the BaBar Experiment*. Tech. rep. SLAC National Accelerator Lab., Menlo Park, CA (United States), 2013.

[14] Helen Quinn. “*B* physics and *CP* violation”. In: *Fundamental Interactions*. World Scientific, 2005, pp. 47–84.

[15] Robert Fleischer. “*B* physics and *CP* violation”. In: *Heavy Quark Physics*. Springer, 2004, pp. 42–77.

[16] Paul F Harrison, Helen R Quinn, et al. *The BaBar physics book: Physics at an asymmetric B factory*. Tech. rep. SLAC National Accelerator Lab., Menlo Park, CA (United States), 2010.

[17] Gustavo C Branco, Luis Lavoura, and Joao Paulo Silva. *CP violation*. Vol. 103. Oxford University Press, 1999.

[18] L Wolfenstein. “L. Wolfenstein, Nuovo Cimento 63A, 269 (1969)”. In: *Nuovo Cimento* 63 (1969), p. 269.

[19] Myron Bander, D Silverman, and A Soni. “CP noninvariance in the decays of heavy charged quark systems”. In: *Physical Review Letters* 43.4 (1979), p. 242.

[20] Hai-Yang Cheng, Chun-Khiang Chua, and Amarjit Soni. “Final state interactions in hadronic B decays”. In: *Physical Review D* 71.1 (2005), p. 014030.

[21] Jean-Marc Gerard and Wei-Shu Hou. “*CP* violation in inclusive and exclusive charmless B decays”. In: *Physical Review D* 43.9 (1991), p. 2909.

[22] Ikaros I Bigi and A Ichiro Sanda. *CP violation*. Cambridge University Press, 2009.

[23] Alexey A Petrov. “Final state interactions: from strangeness to beauty”. In: *arXiv preprint hep-ph/9909312* (1999).

[24] David Atwood and Amarjit Soni. “Possibility of large direct CP violation in $B \to K\pi$-like modes because of long distance rescattering effects and implications for the angle γ”. In: *Physical Review D* 58.3 (1998), p. 036005.

[25] AJ Bevan et al. “The physics of the B factories”. In: *The European Physical Journal C* 74.11 (2014), p. 3026.

[26] David J Griffiths. *Introduction to elementary particles; 2nd rev. version*. Physics textbook. New York, NY: Wiley, 2008.

[27] A Garmash et al. “Dalitz analysis of the three-body charmless decays $B^+ \to K^+\pi^+\pi^-$ and $B^+ \to K^+K^+K^-$”. In: *Physical Review D* 71.9 (2005), p. 092003.

[28] BABAR Collaboration. and ZHITANG YU. “Dalitz plot analyses of charmless B decays”. In: *International Journal of Modern Physics A* 20.15 (2005), pp. 3559–3561.

[29] Hai-Yang Cheng. “Charmless 3-body B decays: resonant and nonresonant contributions”. In: *International Journal of Modern Physics A* 23.21 (2008), pp. 3229–3236.

[30] Roel Aaij et al. “Amplitude analysis of the $B^\pm \to \pi^\pm\pi^+\pi^-$ decay”. In: *arXiv preprint arXiv:1909.05212* (2019).

[31] Roel Aaij et al. *arXiv: Amplitude analysis of $B^\pm \to K^\pm K^+\pi^-$ decays*. Tech. rep. 2019.

[32] CERN. *CERN’s mission*. URL: https://public-archive.web.cern.ch/public-archive/en/About/Mission-en.html. (accessed: 01.08.2019).

[33] CERN. *The History of CERN*. URL: https://timeline.web.cern.ch/timeline-header/89#371. (accessed: 01.08.2019).

[34] Lyndon Evans and Philip Bryant. “LHC machine”. In: *Journal of instrumentation* 3.08 (2008), S08001.

[35] Giorgio Apollinari et al. *High-luminosity large hadron collider (HL-LHC): Preliminary design report*. Tech. rep. Fermi National Accelerator Lab.(FNAL), Batavia, IL (United States), 2015.

[36] CERN. *LHC Machine Outreach*. URL: http://lhc-machine-outreach.web.cern.ch/lhc-machine-outreach/images/lhc-schematic.jpg. (accessed: 01.09.2019).

[37] Jeroen Van Tilburg. “Track simulation and reconstruction in LHCb”. PhD thesis. NIKHEF, Amsterdam, 2005.

[38] A Augusto Alves Jr et al. "The LHCb detector at the LHC". In: *Journal of instrumentation* 3.08 (2008), S08005.

[39] LHCb experiment. *LHCb facts*. URL: https://twiki.cern.ch/twiki/bin/view/Main/LHCb-Facts. (accessed: 01.09.2016).

[40] LHCb. *Dipole Magnet*. URL: http://lhcb-magnet.web.cern.ch/lhcb-magnet/. (accessed: 01.09.2019).

[41] T Latham. "Performance of the LHCb Vertex Locator". In: *Phys. Procedia* 37.LHCb-PROC-2012-054. CERN-LHCb-PROC-2012-054 (Nov. 2012), 830–837. 8 p. DOI: 10.1016/j.phpro.2012.02.424. URL: https://cds.cern.ch/record/1491236.

[42] Roel Aaij et al. "Performance of the LHCb vertex locator". In: *Journal of Instrumentation* 9.09 (2014), P09007.

[43] Daniel Esperante. "The LHCb Silicon Tracker, first operational results". In: *2010 IEEE Instrumentation & Measurement Technology Conference Proceedings*. IEEE. 2010, pp. 1057–1062.

[44] Jeroen J van Hunen. "The LHCb tracking system". In: *Nuclear Instruments and Methods in Physics Research Section A: Accelerators, Spectrometers, Detectors and Associated Equipment* 572.1 (2007), pp. 149–153.

[45] TDR LHCb. *RICH technical design report*. Tech. rep. CERN-LHCC-2000-037, 2000.

[46] Eduardo Picatoste Olloqui, LHCb Collaboration, et al. "LHCb PreShower (PS) and Scintillating Pad Detector (SPD): Commissioning, calibration, and monitoring". In: *Journal of Physics: Conference Series*. Vol. 160. 1. IOP Publishing. 2009, p. 012046.

[47] M Chefdeville. "Operation and performance of the LHCb calorimeters". In: *Journal of Instrumentation* 13.03 (2018), p. C03021.

[48] Pascal Perret et al. "First years of running for the LHCb calorimeter system". In: *arXiv preprint arXiv:1407.4289* (2014).

[49] R Antunes Nobrega et al. "LHCb Trigger System: Technical Design Report". In: (2002).

[50] T Head. "The LHCb trigger system". In: *Journal of Instrumentation* 9.09 (2014), p. C09015.

[51] R Aaij et al. "The LHCb trigger and its performance in 2011". In: *Journal of Instrumentation* 8.04 (2013), P04022.

[52] Eduardo Rodrigues, LHCb Collaboration, et al. "The LHCb trigger system". In: *Nuclear Physics B-Proceedings Supplements* 170 (2007), pp. 298–302.

[53] B Adeva et al. "Roadmap for selected key measurements of LHCb". In: *arXiv preprint arXiv:0912.4179* (2009).

[54] J Albrecht. "The LHCb Trigger System". In: *Nucl. Phys. B, Proc. Suppl.* 187 (2009), pp. 237–244. DOI: 10.1016/j.nuclphysbps.2009.01.033. URL: https://cds.cern.ch/record/1245164.

[55] Siim Tolk. "Discovery Of Rare B decays. First observation of the $B_s \to \mu^+\mu^-$ decays, first evidence of the $B^0 \to \mu^+\mu^-$ decays." Presented 08 Apr 2016. Dec. 2015. URL: https://cds.cern.ch/record/2148631.

[56] S. Tolk et al. *Data driven trigger efficiency determination at LHCb*. Tech. rep. LHCb-PUB-2014-039. CERN-LHCb-PUB-2014-039. Cited on page 2. Geneva: CERN, May 2014. URL: https://cds.cern.ch/record/1701134.

[57] Irina Nasteva et al. "Search for CP violation in $B^{\pm} \to K^{\pm}\pi^{+}\pi^{-}$ and $B^{\pm} \to K^{+}K^{-}K^{\pm}$ decays in 2011 data". In: (July 2012). URL: https://cds.cern.ch/record/1432502.

[58] Angelo Carbone et al. "Measurement of B^0, B_s^0, B^+ and Λ_b^0 production asymmetries in 7 TeV and 8 TeV pp collisions". In: (May 2016). URL: https://cds.cern.ch/record/2156564.

[59] Adam Davis et al. *Measurement of the $K^-\pi^+$ two-track detection asymmetry in Run 2 using the Turbo stream*. Tech. rep. LHCb-INT-2017-023. CERN-LHCb-INT-2017-023. Geneva: CERN, Sept. 2017. URL: https://cds.cern.ch/record/2284097.

[60] LHCb Collaboration. "LHCb detector performance". In: *International Journal of Modern Physics A* 30.07 (2015), p. 1530022.

[61] Johannes Albrecht et al. "Performance of the LHCb High Level Trigger in 2012". In: *Journal of Physics: Conference Series*. Vol. 513. 1. IOP Publishing. 2014, p. 012001.

[62] M. Williams et al. *The HLT2 topological lines*.

[63] Alvaro Gomes dos Santos Neto. "Identificação de Violação de CP em Decaimentos do Méson B em Três Hádrons". presented in Sep 2010. 2010. URL: https://cds.cern.ch/record/2679497.

[64] P Speckmayer et al. "The toolkit for multivariate data analysis, TMVA 4". In: *Journal of Physics: Conference Series*. Vol. 219. 3. IOP Publishing. 2010, p. 032057.

[65] I Bediaga et al. "$B^{\pm} \to h^{\pm}h^{+}h^{-}$ decays in 2011 and 2012 data". In: (Aug. 2014). Linked to LHCB-PAPER-2014-044. URL: https://cds.cern.ch/record/1695393.

[66] W. Verkerke and D. Kirkby. "The RooFit toolkit for data modeling". In: *arXiv:physics* 0306116v1 (2003).

[67] John Erthal Gaiser. *Charmonium Spectroscopy From Radiative Decays of the J/ψ and ψ'*. Tech. rep. 1982.

[68] Albrecht et al. "Measurement of the polarization in the decay $B \to J/\psi K$". In: *Physics Letters B* 340.3 (1994), pp. 217–220.

[69] Bernard Aubert et al. "Amplitude Analysis of the Decay $\mathrm{B}^{\pm} \to \pi^{\pm}\pi^{\pm}\pi^{\mp}$". In: *Physical Review D* 72.5 (2005), p. 052002.

[70] JP Lees, BaBar collaboration, et al. *Measurement of CP-violating asymmetries in $B^0 \to (\rho\pi)^0$ using a time-dependent Dalitz plot analysis*. Tech. rep. BABAR-PUB-12-026, 2013.

[71] Lucio Anderlini et al. *The PIDCalib package*. Tech. rep. 2016.

[72] Muriel Pivk. "sPLOT: A Quick introduction". In: *Presented at.* physics/0602023. 2006, pp. 173–177.

[73] I Bediaga et al. "Second generation of *Miranda procedure* for *CP* violation in Dalitz studies of B (and D and τ) decays". In: *Physical Review D* 86.3 (2012), p. 036005.

[74] Virginia Azzolini et al. "Dalitz plot analysis of $B^{\pm} \to \pi^{pm}\pi^{\pm}\pi^{\mp}$ decays". In: (2009).

[75] Gad Eilam, Michael Gronau, and Roberto R Mendel. "Large CP Asymmetries in $B^{\pm} \to \eta_c(\chi_{c0})\pi^{\pm}$ from the $\eta_c(\chi_{c0})$ Width". In: *Physical review letters* 74.25 (1995), p. 4984.

[76] I Bediaga et al. "Procedure for direct measurement of the Cabibbo-Kobayashi-Maskawa angle γ". In: *Physical review letters* 81.19 (1998), p. 4067.

[77] V. Alan Kostelecký and Neil Russell. "Data tables for Lorentz and *CPT* violation". In: *Reviews of Modern Physics* 83.1 (Mar. 2011), pp. 11–31. ISSN: 1539-0756. DOI: 10.1103/revmodphys.83.11. URL: http://dx.doi.org/10.1103/RevModPhys.83.11.

[78] M Kobayashi and AI Sanda. "On testing *CPT* symmetry in *B* decays". In: *Physical review letters* 69.22 (1992), p. 3139.

[79] M Hayakawa and AI Sanda. "Searching for T, CP, CPT, and $\Delta S = \Delta Q$ rule violations in the neutral K meson system: A guide". In: *Physical Review D* 48.3 (1993), p. 1150.

[80] Roel et al. Aaij. "Measurements of the B^{+}, B^{0}, B_s^0 meson and Λ_b^0 baryon lifetimes". In: *JHEP* 04.LHCB-PAPER-2013-065. LHCB-PAPER-2013-065. CERN-PH-EP-2014-018 (Feb. 2014). Comments: 28 pages, 4 figures. Updated references, 114. 26 p. URL: https://cds.cern.ch/record/1647708.

[81] Oscar W Greenberg. "*CPT* Violation Implies Violation of Lorentz Invariance". In: *Physical Review Letters* 89.23 (2002), p. 231602.

[82] LE Lundberg and LB Rédei. "Validity of Special Relativity at Small Distances and the Velocity Dependence of the Charged-Pion Lifetime". In: *Physical Review* 169.5 (1968), p. 1012.

[83] Holger Bech Nielsen and I Picek. "The Rédei-like model and testing Lorentz invariance". In: *Physics Letters B* 114.2-3 (1982), pp. 141–146.

[84] Paolo Gandini. "Measurement of the B_s^0 meson lifetime in the flavour specific hadronic decay $B_s^0 \to D_s^- \pi^+$". In: (Feb. 2014). URL: https://cds.cern.ch/record/1647586.

[85] I Bediaga et al. "$B^{\pm} \to h^{\pm}h^{+}h^{-}$ decays in 2011 and 2012 data". In: (Aug. 2014). Linked to LHCB-PAPER-2014-044. URL: https://cds.cern.ch/record/1695393.

[86] Alessio Piucci. "The LHCb Upgrade". In: *Journal of Physics: Conference Series*. Vol. 878. 1. IOP Publishing. 2017, p. 012012.

[87] Roel et al Aaij. *Upgrade trigger: Biannual performance update*. Tech. rep. LHCb-PUB-2017-005. CERN-LHCb-PUB-2017-005. Geneva: CERN, Feb. 2017. URL: https://cds.cern.ch/record/2244312.

[88] Olaf Steinkamp, LHCb Collaboration, et al. "LHCb Upgrades". In: *Journal of Physics: Conference Series*. Vol. 1271. 1. IOP Publishing. 2019, p. 012010.

[89] LHCb Collaboration et al. *LHCb tracker upgrade technical design report*. Tech. rep. 2014.

[90] Simon Akar, Lhcb Collaboration, et al. "The LHCb Upgrade". In: *Journal of Physics: Conference Series*. Vol. 556. 1. IOP Publishing. 2014, p. 012073.

[91] LHCb Collaboration et al. *LHCb PID upgrade technical design report*. Tech. rep. 2013.

[92] Christian Joram et al. *LHCb Scintillating Fibre Tracker Engineering Design Review Report: Fibres, Mats and Modules*. Tech. rep. LHCb-PUB-2015-008. CERN-LHCb-PUB-2015-008. Geneva: CERN, Mar. 2015. URL: https://cds.cern.ch/record/2004811.

[93] Plamen Hopchev et al. "SciFi: A large scintillating fibre tracker for LHCb". In: *arXiv preprint arXiv:1710.08325* (2017).

[94] Petr Gorbounov. "Cooling for the LHCb Upgrade Scintillating Fibre Tracker". In: *PoS* (2014), p. 220.

[95] Lukas Witola. "Comissioning of a test stand for quality assurance of fibre modules using cosmic rays for the scifi detector upgrade". An optional note. July 2016. URL: https://www.physi.uni-heidelberg.de//Publications/Thesis-Lukas.pdf.

[96] I Bediaga et al. "Physics case for an LHCb Upgrade II-Opportunities in flavour physics, and beyond, in the HL-LHC era". In: *arXiv preprint arXiv:1808.08865* (2018).